ABSTRACT

Title of Document: MECHANISTIC STUDIES OF PLASMA-SURFACE INTERACTIONS DURING NANOSCALE PATTERNING OF ADVANCED ELECTRONIC MATERIALS USING PLASMA

Xuefeng Hua, Doctor of Philosophy. 2006

Directed By: Professor Gottlieb S. Oehrlein, Department of Material Science and Engineering and Institute for Research in Electronics and Applied Physics

Photolithographic patterning of photoresist materials and transfer of these images into electronic materials using directional plasma etching techniques plays a critical role in the fabrication of integrated circuits. As critical device dimensions are reduced below 100 nm, precise control of the interactions of process plasmas with materials is required for successful integration. This requires a scientific understanding of plasma-surface interaction mechanisms that control the properties of the ultimate devices and ICs produced. Fluorocarbon discharges are commonly used for dielectric etching, e.g. SiO_2. In this work we have studied surface-chemical aspects of the interaction of C_4F_8/Ar discharges with SiO_2 and Si. Free fluorine atoms that are liberated from fluorocarbon species during ion bombardment are driven to the

surface and react with the substrate, a process called defluorination. The defluorination is dependent on the plasma properties and the penetration of reactive species is limited within 10nm below the surface. Future device requires novel materials, i.e. nanoporous silica, to replace conventional SiO_2.When some O atoms in Si-O matrix are replaced with nano cavities (pores), the plasma-induced modifications are extended to the deep subsurface region and the modification scale can be a few hundred nanometers. This modification is correlated with overall porosity and also strongly depends on plasma properties. O_2 N_2 and H_2 discharges likely induce carbon depletion and material densification on nanoporous silica. Novel approach, i.e. shutter approach, is employed to study the issues of plasma processing of advanced photoresist materials at nanometer dimension. Hydrogen depletion, material densification and graphitization of these polymers are important processes during short exposure time with the plasma. High roughening rates are also observed within this time range. Subsequently, dedensification, i.e. surface roughening, dominates in the plasma-photoresist interactions. Depending on the molecular structures, the roughness scale can be well beyond the molecular size and RMS roughness does not saturate even after a long exposure time. For the etching of features, rough edges induced by initial plasma exposure on the top of the lines in the features form local masks and striations are formed on the sidewalls during long exposure times, which could lead failures of the devices.

MECHANISTIC STUDIES OF PLASMA-SURFACE INTERACTIONS DURING NANOSCALE PATTERNING OF ADVANCED ELECTRONIC MATERIALS USING PLASMA

By

Xuefeng Hua

Dissertation submitted to the Faculty of the Graduate School of the University of Maryland, College Park, in partial fulfillment of the requirements for the degree of Doctor of Philosophy
2006

Advisory Committee:
Professor Gottlieb S. Oehrlein, Chair
Professor Ellen D. Williams
Professor Michael S. Fuhrer
Professor Thomas M. Antonsen
Professor Ichiro Takeuchi

© Copyright by
Xuefeng Hua
2006

Acknowledgements

First and foremost, I would like to acknowledge Professor Oehrlein for being a great advisor. His sincerity, guidance and ideas throughout the years are crucial for this thesis. I would like to thank you for developing my independent research ability. I am also thankful for providing us with facilities that are unique in the field of our research and great opportunities to interact with scientists in academia and industry.

Second, I would like to acknowledge my various research financial supports: Semiconductor Research Corporation (SRC) Center for Advanced Interconnect Science and Technology (CAIST), Department of Energy (Contract No. DE-FG0200ER54608), National Science Foundation (under award No. DMR-0406120) and Maryland Technology-Development Corporation (TEDCO).

I would also like to acknowledge the collaboration with companies and other research groups. I thank Ping Jiang (Texas Instruments)---my SRC industry mentor, who was responsible for scanning electron microscopy (SEM) characterizations of structures used in the work of this thesis, Paolo Lazzeri, Erica Iacob and Mariano Anderle (ITC-irst, Center for Scientific and Technological Research, Italy) for the characterizations using time of flight secondary ion mass spectroscopy (TOF SIMS), C. K. Inoki and T. S. Kuan, (University at Albany, SUNY) who contributed to the thesis with characterizations using transmission electron microscopy (TEM), Wen-li Wu (National Institute of Standards and Technology), Taesoon Kwon and R. Phaneuf (University of Maryland), David Humbird and David Graves (UC, Berkeley), and Ying Zhang (IBM).

I thank my colleagues, Li Ling, Xi Li, Sebastian Engelmann, Bryan Orf, Ming-shu Kuo, Christian Scholz, Roman Dabrowsky, Xiang Wang, Daphne Fuentevilla for helpful discussion and assistance in the work present in this thesis and maintenance of the lab. I appreciate technical support from Jay Pyle and John Rodgers (IREAP) for the maintenance of equipment.

I am grateful to the members of my dissertation committee for reading my thesis on such a short notice. Thank you Professor Williams, Professor Antonsen, Professor Fuhrer, and Professor Takeuchi.

Finally I would like to thank my family, especially my wife Lanyi. I know that without your love and support I would not have made it through my five and half year tour of duty in Maryland. Mom and Dad, I will always be grateful for the educational foundation you provided and the unwavering support.

Table of Contents

Acknowledgements ii

Table of Contents iv

List of Tables vi

List of Figures vii

Chapter 1: Introduction 1
- 1.1 Basics of Plasma Processing of Thin Films 1
  - 1.1.1 Plasma Sources for Plasma Processing of Thin Films 6
  - 1.1.2 Facility of Plasma Processing Laboratory 11
- 1.2 Patterning of Advanced Dielectrics Based on Plasma Processing 13
- 1.3 Challenges in Plasma Processing at Nanoscale Dimension 16
- 1.4 Thesis Overview 19

Chapter 2: Role of fluorocarbon radicals and ions in SiO_2 or Si surface etching mechanism with fluorocarbon-based discharges 22
- 2.1 Introduction 24
- 2.2 Experimental setup and procedure 26
- 2.3 Results 27
  - 2.3.1Ar addition effect on fluorocarbon plasma characteristics: Ion current density and surface polymerization rate 27
  - 2.3.2 SiO_2 or Si etching in C_4F_8/Ar discharges with fixed bias voltage 29
  - 2.3.3 SiO_2 or Si etching in C_4F_8/Ar discharges with various bias voltages 39
  - 2.3.4 FC film etching 43
  - 2.3.5 Physical sputtering of FC film with argon discharges 46
- 2.4 Modeling of the Data 48
  - 2.4.1 Mathematical Description 51
  - 2.4.2 The role of FC film thickness in SiO_2 and Si etching with fluorocarbon based plasmas 53
  - 2.4.3 Ion-induced Defluorination of FC film 57
- 2.5 Conclusions 62

Chapter 3: Study of C_4F_8/N_2 and $C_4F_8/Ar/N_2$ plasmas for highly selective organosilicate glass (OSG) etching over Si_3N_4 and SiC 63
- 3.1 Introduction 65
- 3.2 Experimental setup and procedures 66
- 3.3 Experimental Results 68
  - 3.3.1 C_4F_8/N_2 plasmas 68
  - 3.3.2 $C_4F_8/Ar/N_2$ plasmas 76

3.3.3 Comparison of O_2 addition and N_2 addition into C_4F_8 or C_4F_8/Ar plasma 83
3.4 Discussions 86
3.5 Conclusions 88

Chapter 4: Plasma-surface interactions of nanoporous silica during plasma-based pattern transfer using C_4F_8 and C_4F_8/Ar gas mixtures 90
4.1 Introduction 92
4.2 Experimental setup and procedure 93
4.3 Results and Discussions 99
4.3.1 Etching results in different discharges 99
4.3.2 Near surface characterization 108
4.3.3 Sub surface characterization 131
4.4 Conclusions 137

Chapter 5: Damage of ultra low k materials during photoresist stripping process 139
5.1 Introduction 141
5.2 Experimental setup and procedure 142
5.3 Results and discussions 147
5.3.1 Direct plasma exposure 147
5.3.2 Remote plasma photoresist stripping and ULK damage effects 152
5.4 Summary and Conclusions 169

Chapter 6: Studies of plasma surface interactions during short time plasma etching of 193nm and 248nm photoresist materials 170
6.1 Introduction 172
6.2 Experimental setup and procedure 174
6.3 Results and discussions 180
6.3.1Temporal Evolutions of 193 nm and 248 nm Photoresist Patterns 180
6.3.2 Surface Modifications of Photoresist Films During Argon Sputtering 192
6.3.3 Surface Roughness of Blanket Photoresist Films for C_4F_8/Ar Discharges 194
6.4 Conclusions 203

Chapter 7: General conclusions 205

References 210

List of Tables

Table 2.1: Summary of ionic or dominant neutral fluxes and surface chemistry information during processing conditions: C_4F_8 (ion-limited) or C_4F_8/90% Ar (neutral-limited) with a floating substrate or with a substrate biased –125V. 48

Table 4.1: Summary of ionic or dominant neutral fluxes and surface chemistry information during processing conditions: C_4F_8 (ion-limited) or C_4F_8/90% Ar (neutral-limited) with a floating substrate or with a substrate biased –125V. 98

Table 5.1: Dielectric constants and porosity of the materials used in this work. Toluene X-ray reflectivity porosimetry indicates overall porosity while the value revealed with perfluorohexane X-ray reflectivity porosimetry is believed to provide a measure of the proportion of interconnected pores. 144

List of Figures

Figure 1.1: An example of a multilevel interconnect structure (From JSR Microelectronics Inc.). 4

Figure 1.2: Patterning scheme for forming trenches and holes in dielectric materials that will be filled with metal to form the interconnecing wiring of an IC(called damascene processs). 6

Figure 1.3: Schematic of a capacitive plasma source. 8

Figure 1.4: Schematic of inductive coupled plasma reactor used in this work. 11

Figure 1.5: University of Maryland cluster system for plasma processing of materials 12

Figure 1.6: Schematic of time evolution of plasma properties as a function of time during conventional schedule of plasma processing of a substrate. For clarity, the durations of the various regimes have been exaggerated or diminished and are not to scale. 19

Figure 2.1: Ion current density (a) and fluorocarbon deposition rate (b) as a function of Ar addition in C_4F_8 discharge. Pressure, source power and total gas flow rate were fixed at 10mTorr, 1000w, 50sccm, respectively**.** 28

Figure 2.2: Etch rate a), selectivity b) and etch yield versus Ar addition into C_4F_8. Pressure, source power and total gas flow rate were fixed at 10mTorr, 1000w, 50sccm, respectively. RF bias voltage was –125V or – 200V. 31

Figure 2.3: C (1s) photoemission spectra of steady-state fluorocarbon films on Si or SiO_2thin films and passively deposited films produced in C_4F_8 or C_4F_8/90% Ar discharge. The spectra were obtained at a collection angle of 90^0. 32

Figure 2.4: Normalized Si (2p) photoemission spectra of partially etched Si samples in C_4F_8 or C_4F_8/90% Ar discharge. The spectra were obtained at a collection angle of 90^0. 34

Figure 2.5: F/C ratios in the steady-state fluorocarbon film on Si or SiO_2 samples at RF bias voltage –125V or –200V and passively deposited films at floating voltage processed by C_4F_8 with different argon addition discharges. 35

Figure 2.6: Angle resolved XPS analysis on the steady-state fluorocarbon film formed on Si (a) or SiO_2 (b). The electron emission angles were 90^0 or 20^0. 37

Figure 2.7: The steady-state FC film thickness formed on SiO_2 or Si etched by C_4F_8 with different argon addition discharges at RF bias voltage –125V or –200V. 38

Figure 2.8: SiO_2 or Si etch rate (positive values) and fluorocarbon deposition rate (negative values) processed in C_4F_8 or C_4F_8/80% Ar discharge with different RF bias voltages. 40

Figure 2.9: The thickness of the fluorocarbon film formed on SiO_2 or Si during steady-state etching with different RF bias voltages in C_4F_8 or C_4F_8/80% Ar discharge. 40

Figure 2.10: F/C ratios in the fluorocarbon film formed on SiO_2 or Si processed with C_4F_8 or C_4F_8/80% Ar discharge as a function of RF bias voltage. 41

Figure 2.11: a) The thickness of the SiFy layer formed on Si (a) and C-Si/C-C intensity from C(1s) spectra of the CFx film (b) during steady-state etching with different RF bias voltages in C_4F_8 or C_4F_8/80% Ar discharge. 43

Figure 2.12:A comparison of semi-infinite FC film etching rate with RF bias voltage:-125V and deposition rate on a floating sample. 45

Figure 2.13:A comparison of the F/C ratio of a partially etched semi-infinite FC film using an RF bias voltage of –125V with that of a passively deposited FC film (substrate at floating voltage relative to plasma). 45

Figure 2.14: Argon sputtering of FC film: (a) etch rates as a function of bias voltage; (b) XPS C1s spectra of FC film after argon plasma sputtering at floating potential. 47

Figure 2.15: Schematic of the model presented. The left-hand portion shows the basic processes in the FC layer and on the substrate. The right-hand portion indicates carbon or fluorine mass flux balance during the steady-state etching. 50

Figure 2.16: (a) Etch rate and (b) etch yield as a function of CFx film thickness.54

Figure 2.17: Modeling result of $ER \bullet \rho_{Sub} /(DR \bullet D_{F/C}) \sim 1/\sinh(\sqrt{\frac{k}{D}}d)$, 57
data in ellipse are obtained at high Ar addition conditions ($\geq$90%).
.
Figure 2.18: Etch rate (a) or the ratio of etch rate to deposition rate (b) versus 59
the defluorination in the CFx film.

Figure 2.19: SiO_2 or Si etching rate versus the parameter presented in the model 61

Figure 3.1: Schematic outline of the planar coil ICP. 66

Figure 3.2: Etch rate a) and selectivity b) as a function of N_2 addition 69
into C_4F_8. Pressure, source power and total gas flow rate were
fixed at 10mTorr, 1000w, 50sccm, respectively.

Figure 3.3: N_2 effect on the steady-state fluorocarbon film thickness on Si 70
sample when added into C_4F_8. Pressure, source power and total
gas flow rate were fixed at 10mTorr, 1000w, 50sccm, respectively.

Figure 3.4: a) C (1s), b) N (1s) and c) F (1s) photoemission spectra of 71
steady-state fluorocarbon films on SiC or Si_3N_4 thin films and
passively deposited films produced in C_4F_8 or C_4F_8/N_2 discharge.
The spectra were obtained at a collection angle of 90^0.

Figure 3.5: C(1s), Si(2p), F(1s) and N(1s) photoemission spectra of 73
steady state fluorocarbon film on Si_3N_4 processed by C_4F_8/N_2 plasma.

Figure 3.6: Etch rate as a function of the steady-state FC film thickness 74
of OSG, Si_3N_4, SiC, SiO_2 and Si etched by C_4F_8 or C_4F_8/N_2

Figure 3.7: F/C and N/C ratios in the fluorocarbon film on Si sample 75
processed by C_4F_8/N_2 or C_4F_8 discharge as a function of bias voltage.

Figure 3.8: Etch rate & deposition rate a) and selectivity b) as a function 77
of N_2 addition into C_4F_8/90% Ar. Pressure, source power and
total gas flow rate were fixed at 10mTorr, 1000w, 50sccm,
respectively.

Figure 3.9: N_2 effect on the steady-state fluorocarbon film thickness on 79
Si sample when added into C_4F_8/Ar. Pressure, source power
and total gas flow rate were fixed at 10mTorr, 1000w,
50sccm, respectively.

Figure 3.10: a) C (1s), b) N (1s) and c) F (1s) photoemission spectra of steady-state fluorocarbon films on SiC, Si_3N_4 and passively deposited samples in C_4F_8/Ar or C_4F_8/Ar/N_2 discharge. The spectra were obtained at a collection angle of 90^0. 80

Figure 3.11: Etch rate as a function of the steady-state FC film thickness of OSG, Si_3N_4, SiC, SiO_2 and Si etched by C_4F_8/Ar or C_4F_8/Ar/N_2 81

Figure 3.12: F/C and N/C ratios in the fluorocarbon film on Si sample processed by C_4F_8/Ar/N_2 or C_4F_8/Ar discharge as a function of bias voltage. 82

Figure 3.13: Etch rates of (a) OSG, Si_3N_4& SiO_2 and (b) SiC&Si for O_2 (the up row) and N_2 addition (the down row) into C_4F_8 or C_4F_8/Ar. Pressure, source power self-bias voltage and total gas flow rate were fixed at 10mTorr, 1000w, -125V and 50sccm, respectively. 83

Figure 3.14: O_2 effect on the steady-state fluorocarbon film thickness on Si sample when added into C_4F_8 or C_4F_8/Ar. Pressure, source power self-bias Voltage and total gas flow rate were fixed at 10mTorr, 1000w, -125V and 50sccm, respectively. 84

Figure 3.15: Comparison of important electron impact dissociation or ionization energies (for C_4F_8) and thermal dissociation or ionization energies (for N_2 and O_2). Ar^*: argon metastable. According to measurements by Cosby (J. Chem. Phys., Vol. 98 , No.12, 15 June 1993), the cross section for electron induced dissociation of N2 becomes significant (within the uncertainty of the measurement) above 18eV electron energy. 85

Figure 3.16: Ion current densities for N_2 and O_2 addition into C_4F_8 or C_4F_8/Ar discharges. Pressure, source power self-bias voltage and total gas flow rate were fixed at 10mTorr, 1000w, -125V and 50sccm, respectively. 86

Figure 4.1: Integrated photoemission intensity C1s (a), Si2p and O1s (b) from untreated NPS films. 94

Figure 4.2: NPS materials processed in different discharges: (a) Ar sputtering (600 W); (b) C_4F_8 (1000 W); (c) C_4F_8/90%Ar (1000 W). Pressure and total gas flow rate were fixed at 10 mTorr, 50 sccm, respectively. Self-bias voltage was set at –125 V. 100

Figure 4.3: Time resolved etching of NPS. The discharges are maintained at at 10 mTorr and 500 W source power. The self-bias voltage was set at –125 V. 105

Figure 4.4: (a) Trenches in 50% NPS film using a C_4F_8/90% Ar discharge maintained at 10 mTorr and 1000 W source power. The self-bias voltage was set at –125 V. (b) SEM image for Patterned film (from a) after O_2 plasma cleaning. 107

Figure 4.5: Etch rate ratios for different NPS to SiCN or Si_3N_4 using a C_4F_8 (a) or C_4F_8/90% Ar (b) discharge maintained at 10mTorr and 1000W source power. The self-bias voltage was set at –125 V. 108

Figure 4.6: Effective refractive index of NPS (30%) material upon different plasma treatments. 110

Figure 4.7: TEM cross-section images for partially etched NPS (~30%) samples with (a) C_4F_8 or (b) C_4F_8/90% Ar plasmas maintained at 10 mTorr and 1000 W source power. The self-bias voltage was set at –125 V. 112

Figure 4.8: Negative SSIMS spectrum of 30% NPS samples: (a) untreated; (b) partially etched with C_4F_8 discharges; (c) partially etched with C_4F_8/90% Ar discharges. The discharges are maintained at 10 mTorr and 1000 W source power. The self-bias voltage was set at –125 V. 113

Figure 4.9: Principal Component Analysis for untreated samples or partially etched samples with C_4F_8 or C_4F_8/90% Ar discharges. 115

Figure 4.10: Integrated photoemission intensity C1s, Si2p, O1s and F1s (a) (90° emission angle) from partially etched NPS film with C_4F_8 discharge. Angular dependent F/C or Δ F/C are shown in (b) or (c) respectively. 119

Figure 4.11: Integrated photoemission intensity C1s, Si2p, O1s and F1s (a) (90^0 emission angle) from partially etched NPS film with C_4F_8 /90% Ar discharge. Angular dependent F/C or Δ F/C are shown in (b) or (c) respectively. 121

Figure 4.12: Surface pores Vs bulk pores: surface pores will be filled with FC during fluorocarbon plasma etching. 125

Figure 4.13: Silicon 2p and C 1s model results as a function of pore size and experimental XPS data for etching of NPS using C_4F_8 discharges. 128

Figure 4.14: (a) Surface orientations (respected with horizontal surface) used in the model for C_4F_8/90% case; (b) Model results for C1s spectra; (c) Model results for Si2p spectra. Rough surface has been used for NPS materials, and for SiO_2 a smooth surface has been assumed. 130

Figure 4.15: A schematic picture for Ar sputtering of NPS films pretreated with fluorocarbon discharges. 132

Figure 4.16: (a) Removed thickness as a function of process time for NPS film (pretreated with C_4F_8 plasma) during argon plasma. (b) Depth (shown in Figure 5) Vs. NPS porosity. 132

Figure 4.17: DSIMS depth profiling results for NPS samples partially etched with (a) C_4F_8; (b) C_4F_8/90% Ar discharges. 136

Figure 5.1: A schematic of the gap structure: Samples placed in the region shielded by the roof primarily interact with neutrals, the remote plasma processing regime. For samples placed in the plasma exposed region, low energy ion bombardment assists in the plasma-surface interaction. 146

Figure 5.2: (a) Damage thickness as a function of process time of O_2, N_2, or H_2 discharges; (b) Influence of porosity on damage layer thickness after 10 s of either O_2 or H_2 discharge treatments. Discharges were generated using a source power of 500 W, pressure 100 mTorr, and total gas flow rate 50sccm. Damage thickness was determined with the 1 % HF dipping method and ellipsometry. 150

Figure 5.3: Process efficiency defined as NPS damage thickness per nm photoresist removal for different direct discharges examined in this work. Discharges were generated with source power 500 W, pressure 100 mTorr, and total gas flow rate 50 sccm. 151

Figure 5.4: Si2p and C1s intensities obtained using XPS with plasma-treated NPS films as a function of process time. Results for direct O_2, N_2 or H_2 plasma treatments are shown. Carbon depletion and densification are observed for all ashing processes. Discharges were generated with source power 500 W, pressure 100 mTorr, and total gas flow rate 50 sccm. 153

Figure 5.5: TOF SIMS depth profiles of OSG(a) and 3 2% NPS material(b) after 30 s direct plasma exposure employing O_2. The intensities obtained with untreated materials are shown for comparison. Discharges were generated with source power 500 W, pressure 100 mTorr, and total gas flow rate 50 sccm. 153

Figure 5.6: Thickness of damaged layers produced in NPS materials as a result of remote plasma exposures using O_2, N_2 or H_2 discharges. Discharges were generated with at a source power level of 1000 W, pressure of 100 mTorr, and total gas flow rate of 50 sccm. 157

Figure 5.7: The effect of substrate temperature on removed photoresist thickness and nanoporous ULK material damage layer thickness after 1 minute exposure to a remote H_2 plasma. Discharges were generated using 1000 W source power, a pressure of 100 mTorr, and a total gas flow rate of 50 sccm. 159

Figure 5.8: (a) Si2p and (b) C1s XPS spectra obtained with 32% porous NPS films after either 1 minute exposure to remote O_2 or H_2 plasmas. The substrate temperature was maintained at 260^0C. For comparison, XPS data obtained with an untreated NPS film are also shown. Discharges were generated using 1000 W source power, a pressure of 100 mTorr, and a total gas flow rate of 50 sccm. 160

Figure 5.9: Dynamic SIMS depth profiles of 32 % NPS materials after 30 s exposure to remote(a) O_2 or (b) H_2 plasmas at a substrate temperature of 260 ^{0}C. For comparison, dynamic SIMS data obtained with an untreated NPS film are also shown. Discharges were generated using 1000 W source power, a pressure of 100 mTorr, and a total gas flow rate of 50 sccm. 162

Figure 5.10: Cross-sectional images of NPS films obtained by TEM. (a) untreated; (b) after 1 minute exposure to a remote H_2 plasma at a substrate temperature of 260^0C; (c) after 1 minute exposure to a remote O_2 plasma at a substrate temperature of 260^0C. Discharges were generated using 1000W source power, a pressure of 100mTorr, and a total gas flow rate of 50sccm. 164

Figure 5.11: RMS roughness results obtained by AFM measurements employing NPS films exposed to H_2 and O_2 remote plasma ashing processes. An untreated control is shown for comparison. Discharges were generated using 1000 W source power, a pressure of 100 mTorr, and a total gas flow rate of 50 sccm. 166

Figure 5.12: Cross-sectional scanning electron microscopy images of NPS trench structures after: (a) directional etching using C4F8/90% Ar and employing a selfbias voltage of –125V; (b)1 minute remote O_2 discharge ashing;(c)3.5 minute remote H_2 discharge ashing. Discharges were generated using 1000W source power, a pressure of 100mTorr, and a total gas flow rate of 50sccm. 168

Figure 6.1: Molecular structures of (a) 193nm and (b) 248nm photoresists. 173

Figure 6.2: OSG Etching/FC Deposition results: (a) conventional exposure; (b) shutter approach. Discharges were generated with 1000 W source power, a pressure of 10 mTorr, and total gas flow rate 50 sccm with a fixed bias voltage –125 V. 177

Figure 6.3: Concept of moving shutter: (a) Shutter containing a 18 mm wide slit to control the interaction of a substrate with a plasma. (c) Solid shutter that is used to generate gradients of exposure time across a sample 179

Figure 6.4: Photoresist mask evolution during C_4F_8/90% Ar etching: (a) 0s, (b) 1.6s, (c)7s, and (d) 60s for 193 nm photoresist etching; (e) 0s, (f) 1.6s, (g)7s, and (h) 60s for 248 nm photoresist. Discharges were generated using 1000 W source power, a pressure of 10mTorr, and 50sccm as total gas flow rate with a fixed bias voltage –125V. 181

Figure 6.5: (a)193 and 248 nm photoresist etch rates, (b) Trench/Line width evolution of 193 nm photoresist feature and (c) Trench/Line width evolution of 248 nm photoresist feature during pattern transfer. Discharges were generated using 1000 W source power, a pressure of 10mTorr, and 50sccm as total gas flow rate with a fixed bias voltage –125V. 183

Figure 6.6: Striation evolution on the sidewall of 193 nm photoresist mask during pattern transfer with C_4F_8/90% Ardischarges: (a) as received, (b) 1.6s, (c) 7s, (d) 15s, (e) 29s and (f) 60s. Discharges were generated using 1000 W source power, a pressure of 10mTorr, and 50sccm as total gas flow rate with a fixed bias voltage –125V. 185

Figure 6.7: Striation evolution on the sidewall of 248 nm photoresist mask during pattern transfer with C_4F_8/90% Ardischarges: (a) as received, (b) 1.6s, (c) 7s, (d) 15s, (e) 29s and (f) 60s. Discharges were generated using 1000 W source power, a pressure of 10mTorr, and 50sccm as total gas flow rate 186

with a fixed bias voltage –125V.

Figure 6.8: Quantitative results of striation evolution during 193 nm and 248 nm photoresists etching with C_4F_8/90% Ar plasma shown in Figs. 6.6 and 6.7. 189

Figure 6.9: Comparisons of SEM cross-section images of 193 and 248 nm photoresists between short time etching (1.6s) and untreated samples: (a) as received 193 nm photoresist, (b) 193 nm photoresist feature after 1.6s etching, (c) as received 248 nm photoresist, (d) 248 nm photoresist feature after 1.6s etching. Discharges were generated using 1000 W source power, a pressure of 10mTorr, and 50sccm as total gas flow rate with a fixed bias voltage –125V. 191

Figure 6.10: XPS C1s spectra of 193 nm and 248 nm photoresists after short time argon sputtering. Discharges were generated using 600 W source power, a pressure of 10mTorr, and 50sccm as total gas flow rate with a fixed bias voltage –125V. 193

Figure 6.11: (a) Thickness removal and (b) etch rate of blanket 193 nm or 248 nm photoresist films during fluorocarbon plasma etching with combinatorial approach shown in Fig.3 (b). Discharges were generated using 1000 W source power, a pressure of 10mTorr, and 50sccm as total gas flow rate with a fixed bias voltage –125V. 195

Figure 6.12: Effective refractive index evolution of 193 nm or 248 nm photoresists during C_4F_8/90% Ar plasma etching. Discharges were generated using 1000 W source power, a pressure of 10mTorr, and 50sccm as total gas flow rate with a fixed bias voltage –125V. 197

Figure 6.13: Time evolution of RMS roughness of 193 nm or 248 nm photoresists during C_4F_8/90% Ar plasma etching. Discharges were generated using 1000 W source power, a pressure of 10mTorr, and 50sccm as total gas flow rate with a fixed bias voltage –125V. 198

Figure 6.14: RMS roughness evolution as a function of etch depth during the etching of193 and 248 nm photoresists with C_4F_8/90% Ar discharges. Discharges were generated using 1000 W source power, a pressure of 10mTorr, and 50sccm as total gas flow rate with a fixed bias voltage –125V. 199

Figure 6.15: Chemical signature evolutions during plasma etching of (a) 193nm and (b) 248nm photoresists. C_2F_5O and $C_6F_{13}O$ represent the FC coverage on the surface, GBLMA and MAMA is copolymer for 193nm photo resist while C_4H_9O indicates the information for 248nm photoresist. (c) PAG information can be found as PFBS and SO_3 for 193nm and 248nm photoresist respectively. C_4F_8/90% Ar discharges were generated using 1000 W source power, a pressure of 10mTorr, and 50sccm as total gas flow rate with a fixed bias voltage –125V. 202

Chapter 1 Introduction

1.1 Basics of Plasma Processing of Thin Films

Plasma, an electrified gas consisting of electrons, ions, and neutral atoms, is by far the most abundant state of matter in the universe, comprising more than 99% of the mass of the visible universe. It is produced by adding energy to a gas, which strips electrons from atoms and molecules. In neutral plasmas, free atoms or molecules are partially or fully ionized while the whole body is electrically neutral on average. Charged particles in a plasma interact simultaneously with many others due to the long range nature of the electric force. Because of this plasmas exhibit collective behavior. Plasma can be accelerated or steered by electric and magnetic fields. The object of this section is to introduce the main concepts of plasma science, and explain how these concepts relate to materials processing applications.

The plasma state can exist over a broad temperature range (10^2~10^9K) and plasma density(10^3~$10^{33}$$m^{-3}$).[1.1,1.2] It can be cool and tenuous like aurora, or very hot and dense like the central core of a star. Partially ionized low temperature plasmas are used extensively for thin-film materials processing applications such as etching and deposition.[1-4] In this type of plasma, the degree of ionization is typically only 10^{-4}, so the gas consists mostly of neutrals. The positive charge is mostly in the form of singly ionized atoms or molecules formed by removal of a single electron from neutral species. The majority of negatively charged particles are usually free electrons, but in very electronegative gases such as chlorine, negative ions can be more abundant. For typical process plasmas, the electron and ion densities are in the range of 10^9 –10^{12} cm^{-3} and the neutral species density is in range of 10^{13}-10^{16} cm^{-3}.[1.3,1.4] Electrons are

the main current-carriers because they are light and mobile. The energy transfer from electrons to gas molecules is inefficient due to the mass of an electron being much smaller than that of neutral gas species, generally by a factor of ~5×10^{-6} to 5×10^{-4}. Therefore, electrons are not in thermal equilibrium with ions and neutral species and can attain a high average energy, often many electron volts (equivalent to tens of thousands of degrees above the gas temperature). The high electron temperature in plasmas enables high-temperature type reactions to take place. These occur as a result of inelastic electron-molecule collisions. Reactive free radicals and ionized species are formed in this way in a low-temperature neutral gas. The fact that high-temperature active species (electrons) and a warm gas coexist in plasma distinguishes the plasma reactor from conventional thermal processing.

The second unique property of plasma is that ions can be drawn from the plasma at energies ranging from tens to hundreds of eV. The ions are incident on substrates normal to the surface, thus enabling anisotropic etching and deposition processes. Both ions and electrons diffuse to the walls and recombine on the boundary surfaces. This tends to deplete charge in the adjacent gas phase and forms a thin boundary layer called a “sheath”.[1.1,1.2] The average velocity of electrons is enormous relative to those of the ions and neutrals because of both the high temperature and low mass of the electrons. Since the number density is the same for positively and negatively charged particles in plasma, the initial electron flux that strikes a surface in contact with the plasma is much greater than initial flux of positive charges. Hence, the boundary surface builds up a negative charge and a negative potential with respect to the plasma is generated. The voltage across the

sheath ranges from a few volts to thousands of volts, depending on discharge properties and whether the substrate is biased or not. The positive ions that diffuse into the sheath region are accelerated by the sheath electric field and strike the substrate at near normal incidence and at high energy.

Although the ions strike the surface with high energy, the current is low when the plasma density is in the range of 10^{-9}-10^{-12}cm^{-3}. Heating of the substrate is prevented by efficient thermal mounting of the substrates on a temperature controlled electrode.

Because of these unique properties, plasmas have become indispensable for advanced materials processing in many high-tech industries. Pattern transfer by dry etching and plasma-enhanced chemical vapor deposition are two of the cornerstone techniques for modern integrated circuit fabrication. The microelectronics industry employs plasma-based etching to produce submicron device features in thin films with precisely controlled dimensions, and uses plasma-enhanced chemical vapor deposition methods to synthesize insulators, conductors, diamond thin films, and high-temperature superconductors. Plasmas are also used to harden the surfaces of cutting tools and to modify surfaces of plastics so paint will stick to them. The success of these methods have also sparked interest in their application to other techniques, such as surface-mircomachined sensors, read/write heads for data storage and magnetic random access memory (MRAM).

The development of plasma processing of materials has been especially stimulated by its application to the manufacture of microelectronic devices. Photolithography and plasma etching have enabled the enormous shrinkage of

transistors, one of the basic building blocks of the integrated circuit (IC). In an IC, individual transistors are connected by metallic interconnects. An example of a multilevel metalization scheme of an interconnect structure is shown in Fig. 1.1 (from JSR Microelectronic Inc.): M1, M2, M3 refer to the multi metal layers which are separated by insulating layers that are formed of SiO_2 and JSR dielectric materials. The JSR dielectric is a nanoporous silica, essentially SiO_2 with nanoscale pores, and its plasma processing characteristics will be described in this Thesis (chapters 4 and 5). The width of interconnects nowadays is of the order of 100 nm, 200 times narrower than a human hair!

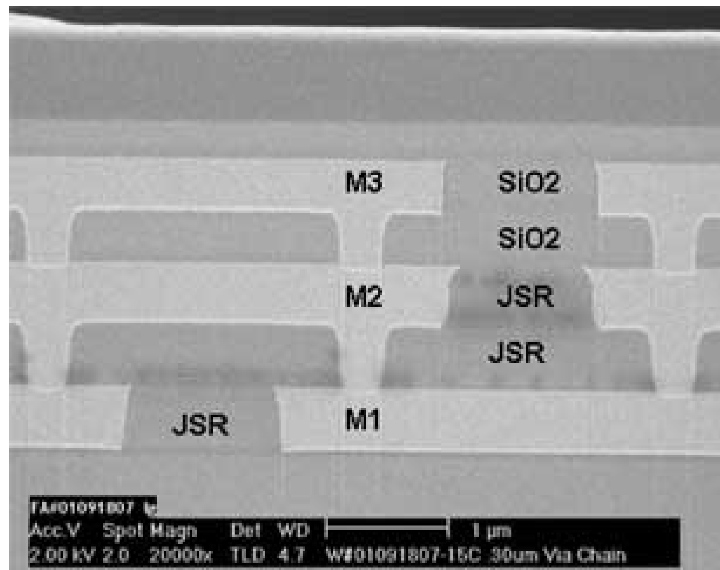

Figure 1.1: *An example of a multilevel interconnect structure* (From JSR Microelectronics Inc.).

The patterning scheme of these dielectrics is redundantly outlined in Fig. 1.2. Panel a) shows a portion of a partially completed integrated circuit. In the next step (b), a dielectric film is deposited. The dielectric film is then patterned by photolithohraphy. A light-sensitive polymer, referred to as photoresist, is spun onto the dielectric. The interconnect routing is mirrored in the photoresist film using light

and imaging techniques (step c). The light alters the chemical composition of the photoresist in the exposed areas, which can then be dissolved using wet chemicals (step d). The pattern in the photoresist is subsequently transferred into the dielectric using plasma etching (step

e). When SiO_2 is applied as a dielectric, it is common to use fluorocarbon gases (C_xF_y) to produce a plasma, since the ions and radicals that are formed are highly effective for directional etching of SiO_2. Fluorocarbon gases allow for a highly anisotropic etch of SiO_2 and straight sidewalls can be obtained (step f).[1.5-1.9] Using optimized processing conditions, it is possible to etch the SiO_2 much faster than the photoresist mask and the material below the dielectric layer. Once the etching of the trench or hole in the SiO_2 is completed upon reaching the underlying film, the remaining photoresist can be stripped by using an O_2 plasma. The intermediate pattern that is obtained can be filled with a metal to make a connection with the underlying circuitry. At this point, steps a) through f) can be repeated to build a 3-dimensional structure.

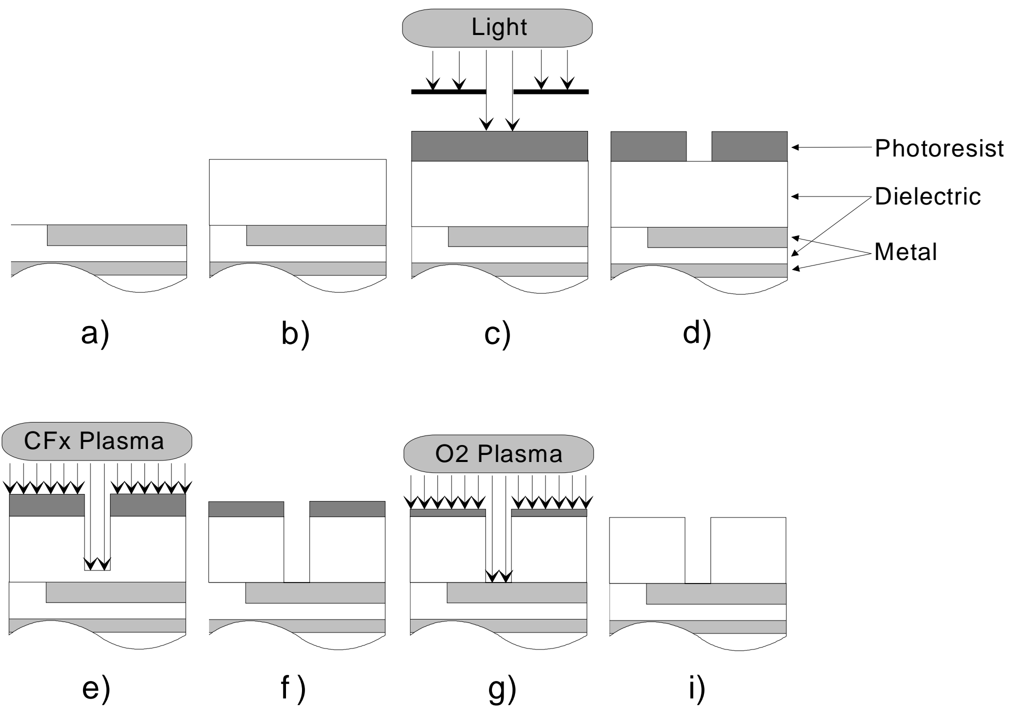

Figure 1.2: *Patterning scheme for forming trenches and holes in dielectric materials that will be filled with metal to form the interconnecing wiring of an IC (called damascene process[10]).*

1.1.1 Plasma Sources for Plasma Processing of Thin Films

Direct current plasma sources are not commonly used in processing applications because DC power cannot be coupled through insulating substrates, the pressure required is relatively high, the discharge is not efficient and the cathode voltage is not controllable. Radio frequency (rf) or microwave powers are generally used to produce and sustain the plasma in plasma processing tools. Many types of rf plasma sources are available for plasma processing and they normally classified into capacitive, inductive, and wave sources. [1.2,1.4] In this work, an inductively coupled plasma is used and will be discussed in detail. A brief description of capacitive

coupled plasma is also present since it is widely used and important for dielectric etching.

A. Capacitively Coupled Plasma

Capacitive sources are often referred to as parallel plate, or reactive ion etch (RIE) sources.[1.3,1.4] The energy is coupled from the rf to the electrons by several mechanisms: Free electrons in the plasma bulk gain energy from the rf electric field and release the energy gained once their oscillatory motion is interrupted by collisions with other particles. Energetic electrons are also created at the cathode because of secondary emission from ion bombardment. These electrons are accelerated by the sheath into the body of the plasma. Stochastic heating due to the moving sheath boundary is another mechanism for rf power coupling in capacitive sources. The plasma density of capacitive source is typically limited to $10^{10}cm^{-3}$. To increase the density, more rf power is required. This results in many issues, including low efficiency of plasma heating, and a wider sheath leading to more ion-neutral collisions in the sheath. Another shortcoming of this source is that no independent control of plasma density and the substrate bias voltage is possible. To solve this problem, CCP reactors employ two different RF frequencies. The high frequency RF supply is used to produce the plasma (source) and the low frequency RF supply is used to bias the substrate. This design is based on the fact the electrons can respond to high frequency rf power because they are light. Ions are heavy, but can gain energy from low frequency rf electric fields. The dual frequency capacitive plasma reactor is currently used in the semiconductor industry for dielectric etching.

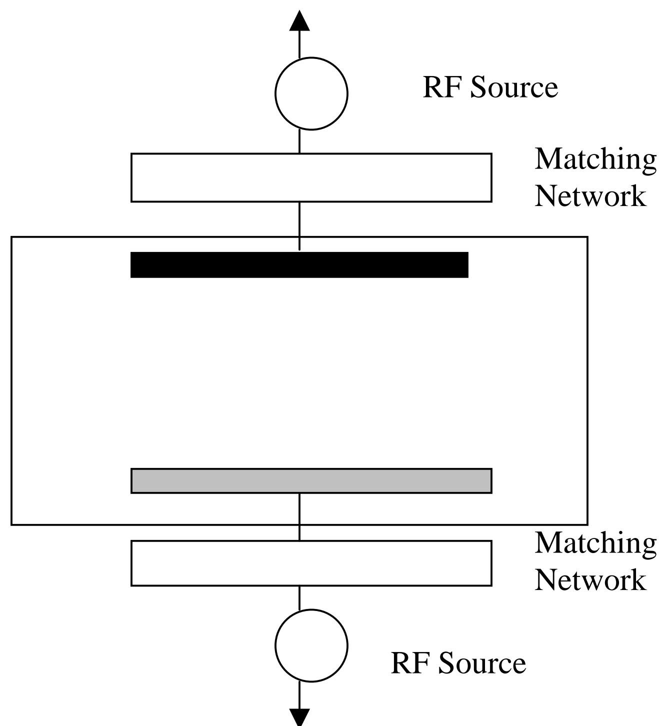

Figure 1.3: Schematic of a c*apacitive plasma source.*

B. High Density Plasma---Inductively Coupled Plasma

This section reviews the basic principles of a high-density plasma. These principles will be illustrated using a planar-coil inductively coupled plasma (ICP) reactor employed for this work. The ICP reactor used in this work is shown in Fig. 1.4. A planar, stovetop-like coil is placed on top of a quartz coupling window. The region below the quartz window is evacuated to a pressure of the order of 10 mTorr (10^{-5} bar). When a RF current is driven through the coil, an electromagnetic field is

coupled into the vacuum below the window. Due to their low mass, electrons have high mobility and are able to respond to the applied electromagnetic fields varying at 13.56 MHz. Ions, on the other hand, have a much lower mobility and respond only to a time-averaged electromagnetic field. An electron current runs below the quartz window in the opposite direction of the coil current and shields the electromagnetic fields. Low energy electrons in this current cannot efficiently transfer their kinetic energy to the much heavier neutrals. Hence, electrons are heated by the electromagnetic fields while their direction is randomized by neutral collisions. The electron temperature is 3 to 5 eV for typical processing conditions and is much higher than the ion-neutral temperature which is of the order of 0.05 eV. Energetic electrons can transfer their energy to neutrals and ions through inelastic collisions which leads to ionization, attachment, recombination, dissociation, excitation, or a combination of these. The electron energy required for these processes ranges typically from 1 to 20 eV.

The electron temperature is adjusted such that the electron generation through ionization balances the electron loss in the plasma. In addition to recombination and attachment, electrons are lost due to ambipolar diffusion. Since the plasma is generated just below the window, electrons diffuse towards the quartz window, chamber wall, and substrate. As electrons diffuse from the plasma generation area, an electric field builds up between the electrons and ions that accelerates the ions but slows down the electrons. This electric field rises the potential of the plasma generation area and assures that the flux of electrons balances the flux of ions. The diffusion of electrons is thus enhanced by the relatively high electron temperature, but

is impeded by the relatively slow ions. Additionally, all floating surfaces in contact with the plasma charge up negatively while a positive space charge builds up near the surface. This space charge is referred to as a sheath. The sheath thickness is on the order of 1 mm and is the only region where charge separation exists. All other areas can be considered quasi-neutral over a length scale larger than ~15 μm. The potential across the sheath (the floating potential) is typically 10-30 V and accelerates the ions that enter the sheath towards the floating surfaces. It is important to realize that the flux of ions and electrons is governed by ambipolar diffusion, not by the floating potential (which is a result of the electron loss to the surface).

The energy of the ions bombarding the substrate can be increased by applying an rf bias to the substrate. The flux of electrons and ions to the substrate is not affected by the rf bias. However, during the first rf cycles electrons are collected faster at the electrode which charges up more negatively while the positive sheath near the substrate expands. This increases the sheath voltage and, consequently, the average energy of impacting ions. The ability to control ion energies independent of plasma density is an important feature of high-density plasma systems and is absent in medium-density plasma systems such as reactive ion etching (RIE) tools, where the substrate electrode is used for plasma generation.[1,2]

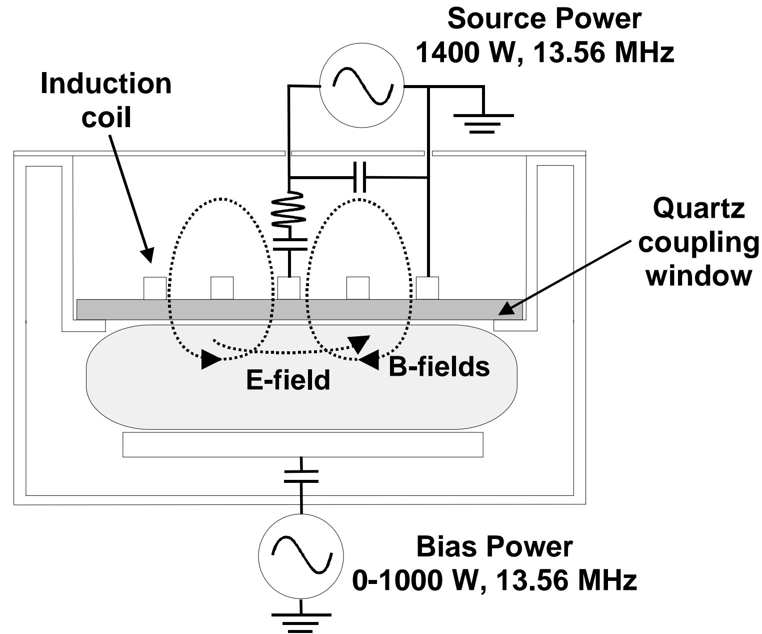

Figure 1.4: *Schematic of inductive coupled plasma reactor used in this work*

1.1.2 Facility of the Laboratory for Plasma Processing of Materials

The inductively coupled plasma reactor described above is housed in the laboratory for plasma processing of materials, University of Maryland. The major scientific theme of this laboratory is the characterization and understanding of the processes at the plasma-material interface that control the properties of the material or structure that is ultimately produced. This research requires a variety of equipment, including reactors that can generate the plasmas, instruments that characterize the plasma and the plasma-treated materials, and measurement tools that evaluate the crucial variables that determine the ultimate usefulness of the materials and structures thus produced. Main equipments are shown in Fig. 1.5. Various reactors, such as inductively coupled plasma reactor, capacitively coulpled plasma reactor/microwave-based remote plasma processing chamber, and magnetically enhanced plasma, and

surface analysis chamber (Vacuum Generator ESCA Mk II) are all connected in the cluster system. This enables the vacuum transfer of samples treated with plasma process, which eliminates the surface modification due to the air exposure. To understand the plasma properties, measurements are conducting to obtain information of radical or ion species using mass spectroscopy, ion sampling system, and optical emission spectroscopy. These tools provide real time information on plasma properties and enhance the process control. Furthermore, *in situ* ellipsometries are installed in each reactor to monitor the surface modification of the sample.

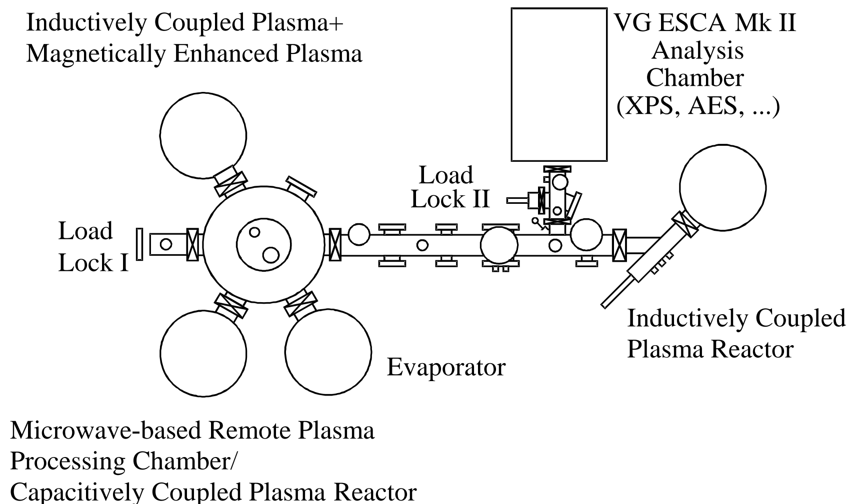

Figure 1.5: *University of Maryland cluster system for plasma processing of materials*

The studies in this thesis involve many collaborative efforts with industrial laboratories and universities throughout the world, in particular for the characterizations of the samples after plasma process done at University of Maryland (UMD). I am grateful to these collaborators. To emphasize their contributions, a summary of overall measurements involved in this thesis is shown below.

Measurement	Method	Location	Information
Ellipsometry	*In situ/ex situ*	UMD	Etch/deposition rates, optical properties
Langmuir probe	*In situ*	UMD	Ion current density, plasma potential
X-ray photoelectron spectroscopy	*Vacuum transfer*	UMD	Chemical information
Atomic force microscopy	*Ex situ*	ITC-irst (Paolo Lazzeri, Erica Iacob and Mariano Anderle)	Surface morphology
Time of flight secondary ion mass spectroscopy	*Ex situ*	ITC-irst (Paolo Lazzeri, Erica Iacob and Mariano Anderle)	Chemical information
Scanning electron microscopy	*Ex situ*	Texas Instruments (Ping Jiang)	Characterizations of structures
Transmission electron microscopy	*Ex situ*	University at Albany, SUNY (C. K. Inoki and T. S. Kuan)	Morphology characterizations
X-ray reflectivity porosimetry	*Ex situ*	NIST (Wen-li Wu)	Porosity of nanoporous silica

1.2 Patterning of Advanced Dielectrics Based on Plasma Processing

Fluorocarbon based plasmas are widely used for dielectric etching because they remove SiO_2 preferentially over silicon. In the past few decades, plasma etching of SiO_2 using fluorocarbon discharges has been a widely studied topic. This is explained by both its practical importance, and its scientific complexity. Fluorocarbon

plasmas are very complex, with an enormous number of possible reactions that can take place in the plasma gas phase and at the plasma-substrate boundary. In order to understand plasma processing mechanisms, the information of species incident on the surface is required. Extensive efforts have been devoted to the characterization of the properties of fluorocarbon based plasmas both experimentally and numerically.[1.11-1.16] In that work, absolute densities of important neutral or ion species were determined for fluorocarbon based discharges. It was found that adding argon to a fluorocarbon gas results in dramatic change in radical to ion ratio. For instance, neutral species dominate the gas phase of pure C_4F_8 discharges. Upon changing the composition of the feedgas to C_4F_8/ 90% Ar, ions become abundant in the discharges and more than 70% of ions are Ar^+. C_4F_8/Ar discharges are useful for understanding important processes in fluorocarbon etching for the conditions where fluorocarbon radical fluxes are higher or comparable to the total ion flux. With this knowledge, this thesis is focused on the plasma surface interactions during nanoscale pattern transfer of advanced electronic materials using fluorocarbon/Ar discharges.

It is well known that in fluorocarbon plasma processing, RF biasing of the substrate is required to increase ion energies sufficiently to enable SiO_2 etching. If the ion energy is below a certain threshold, only fluorocarbon deposition on the substrate occurs.[1.17-1.21] In the plasma etching process, the SiO_2 or Si film is covered by a steady state thin fluorocarbon. Although significant research efforts have studied this topic, the physics and chemistry of the transition from deposition to etching is still poorly understood. For plasma processing at nanometer dimension, fundamental understanding of plasma surface interactions at the atomic and molecular level is

required for a precise control of the removal or addion of materials at nanometer scales. Studies of plasma surface interactions using C_4F_8/Ar is expected to provide important insights, since a broad range of ion to neutral ratios is available and this enables to determine specific roles that ions or neutrals play for the plasma process.

As integrated circuit dimensions continue to shrink, RC delay, crosstalk noise and power dissipation of the interconnect structure become the limiting factors for circuit performance.[1.22] To solve these problems, new materials with lower resistance and dielectric constant have to be developed for metal lines and interconnects to replace the conventional Al/SiO_2 interconnect structure. Cu interconnects have successfully replaced Al in ICs in 1997. However, the implementation of low dielectric constant insulators has been delayed due to the challenges associated with the thermal, mechanical and processing properties of low dielectric constant k materials.

Low k materials can be generated based on the SiO_2 structure by replacing an O atom in the Si-O bond with methyl carbon group -CH_3. The resulting organosilicate glass (OSG) is one candidate low k material and typically, the resulting k value is in the range 2.6 to 2.9. A comparison of OSG etching with SiO_2 is discussed in chapter 3. For future ICs, materials with k values below 2.6 are required. This can be achieved by introducing porosity in the dielectric. Nanoporous silica (NPS), a silica matrix containing nano cavities, can be created by removing organic carbon groups, a sacrificial phase, through thermal processes from the silica matrix. Porosity degrades the thermal and mechanical properties of NPS relative to those of SiO_2. Investigations of the influence of the presence of the nanopores on plasma-surface interaction

mechanisms, and overall plasma processing of nanoporous silica, are crucial to develop satisfactory integration of these materials in future devices and circuits.

For manufacturing of integrated circuits featuring devices with sub-0.13 μm critical dimensions, 193 nm photolithography is being introduced to produce the polymer mask for the pattern transfer to the dielectrics. However, conventional polymer masks containing aromatic rings are not suitable due to the high absorption of C=C bonds at 193 nm.[1.23,1.24] New polymer designs are required for 193 nm photolithography. Unfortunately, plasma-based pattern transfer of lithographically produced nanoscale patterns in 193 nm photoresist materials is often accompanied by photoresist surface roughening and line edge roughening due to factors which are not well understood. Scientific understanding of these issues is required to design reliable polymer mask for successful fabrication of integrated circuits with sub-100 nm critical dimensions.

1.3 Challenges of Plasma Processing at Nanoscale Dimension

Nanometer control of plasma etching and deposition processes of materials is required for devices with critical dimensions approaching 50 nm. For nanometer scale modifications of a substrate using plasmas, the plasma- substrate interaction time should be of the order of seconds. This is based on typical process plasmas, for which etching and deposition rates range from a fraction of a nm/s to many nm/s, and the requirement to add or remove nm thick layers. Simultaneously, a fully established plasma needs to interact with the work piece, rather than a plasma with discharge properties that are still evolving as a function of time. Slow evolution of plasma

properties is especially important for chemical reactive discharges, for which it may take up to 20s to establish a stable plasma [1.25,1.26].

Current technology suffers from several disadvantages when applied to plasma processing of nanoscale layers. The default of conventional technology is that the substrate is in contact with the plasma during all phases of the plasma process such as initialization of the discharge, biasing of the substrate, desired plasma processing by plasma/substrate interaction and plasma extinction. This sequence is schematically depicted in Fig. 1.6. The relative importance of the exposure of a substrate to a transient plasma increases as the total plasma exposure time decreases. This initial exposure of the substrate to a rapidly changing discharge rather than a stabilized discharge may dominate the consequences of plasma-surface interactions for the short-time plasma processing of layers with nanoscale dimensions leading to a loss of control which may be unacceptable. Any changes of the substrate introduced by the inadvertent interaction of the substrate with the plasma during one of the undesirable periods, such as initiation of the plasma, biasing the substrate, stabilizing the plasma, plasma extinction, and decay of long lived neutrals, may reduce the efficacy of the plasma process. For instance, for fluorocarbon (FC) based plasma etching processes used to transfer lithography defined features into dielectric films, fluorocarbon film deposition takes place after the plasma has been ignited and before RF biasing has been applied to the substrate electrodes. This deposition process can have unacceptable consequences for profile control of ultra-fine features (~20nm).[1.27,1.28]

In order to add or remove materials with a thickness of one to several nanometers, the plasma/surface interaction process must be tightly controlled. A shutter approach was developed to achieve this goal. A moving shutter containing slits in close contact with the substrate is used to control the interaction time of stabilized gas discharges with the substrate for nanoscale layer/nanostructure processing. Both substrate and shutter can be biased relative to the plasma. The choice of slit width and shutter velocity determines the exposure time of the initially covered substrate to the plasma. This technique enables precise nanoscale layer etching or deposition on both blanket and patterned substrates employing gas discharges. The shutter method enables nanoscale surface modifications of a substrate with a degree of control that cannot be achieved using conventional technology, as shown in our previous publication.[1.29] The shutter made of silicon contacts a substrate to eliminate the volume between shutter and substrate, and the bulk plasma properties remain essentially unchanged during the movement of shutter. In this thesis, shutter approach is employed in the study of 193 and 248 photoresist materials for understanding the mechanisms of surface roughness formation during fluorocarbon based plasma etching.

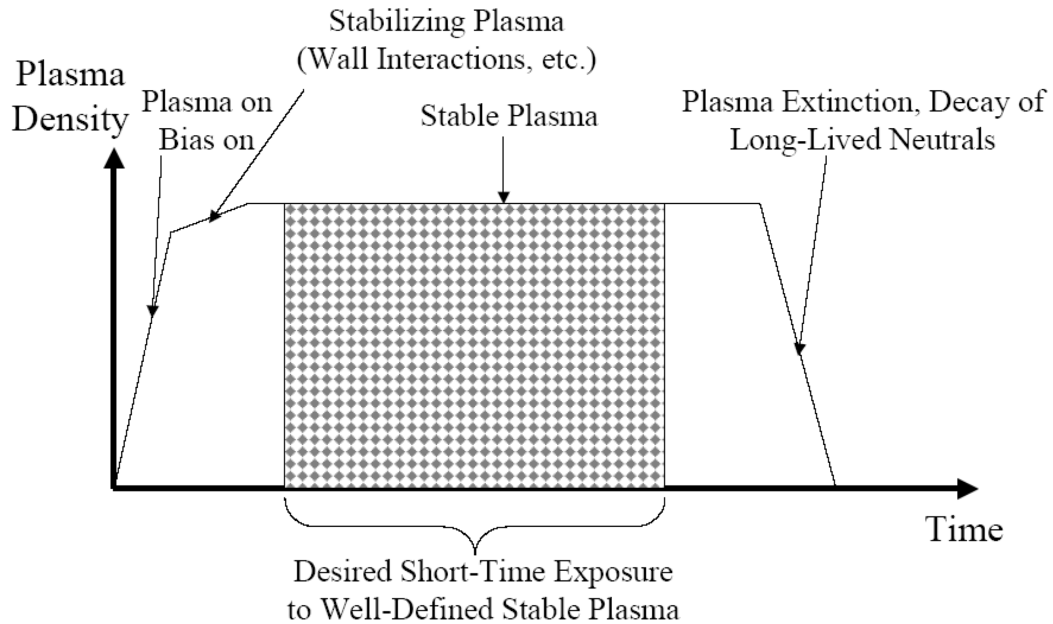

Figure 1.6: *Schematic of time evolution of plasma properties as a function of time during conventional schedule of plasma processing of a substrate. For clarity, the durations of the various regimes have been exaggerated or diminished and are not to scale(see reference 30).*

1.4 Thesis Outline

Important themes that will be addressed in the current PhD thesis are 1) the formation of vias and trenches in nanomaterials, i.e. nanoporous silica, which may ultimately replace SiO_2 as the dielectric material in the interconnect structure; 2) the precise formation of vias and trenches at nanometer dimension; 3) fundamental understanding of plasma processing at molecular level.

In chapter 2, a mechanistic study of fluorocarbon plasma etching of silicon and silicon dioxide is presented. This work clarifies the relative roles of neutrals and ions in the etching process and the main mechanistic factors controlling the etching process. We show that substrate etching requires that mobile carbon and fluorine atoms are produced by ion bombardment of the fluorocarbon (FC) films deposited on

a substrate due to fluorocarbon radical adsorption on the substrate from the plasma. Mobile fluorine atoms diffuse through the FC layer to the dielectric surface and etching reactions then take place. This work is a preparation for the study of plasma etching of advanced dielectric materials using fluorocarbon based plasmas.

The general effect of the substrate chemical composition on the plasma etching process has been investigated in chapter 3. A comparison of etching behaviors of OSG, SiO_2, Si_3N_4, SiC and Si will be discussed there. Additionally, the contribution of Ar additives on the ionization of molecular gases such as O_2 and N_2, is studied.

Novel phenomena that take place during plasma processing of nanoporous silica will be described in chapter 4 and 5. The materials modification caused by the plasma process is dramatically enhanced by the presence of pores. In chapter 4, fluorocarbon discharges are used for transfer of photoresist patterns into nanoporous silica. We observe severe surface roughening, deep fluorine permeation and fluorocarbon accumulation in the sub-surface region. The nature of the surface modifications varies strongly with the plasma properties. We also describe the results of the interactions of non-polymerizing discharges, i.e. O_2, H_2 and N_2 discharges, with NPS materials. Such discharges are of interest for the removal of photoresist masks from the nanoporous silica after completion of the pattern transfer step. The NPS surface and bulk modifications that result from these discharges include material densification and pore size reduction and are discussed in chapter 5.

Photoresist is used as the etching mask for pattern transfer of dielectrics. 193 nm photoresist requires significant modification in molecular structure with the

respect of 248 nm photoresist. In chapter 6, an evaluation of this modification on etching behavior and plasma-polymer surface interactions with fluorocarbon discharges will be present.

Finally, chapter 7 will summarize the main conclusions of these studies.

Chapter 2: Role of Fluorocarbon Radicals and Ions in SiO_2 or Si Surface Etching Mechanism with Fluorocarbon-Based Discharges

To be submitted to J. Vac. Sci. Technol. A., 2005

Xuefeng Hua and G.S.Oehrlein

ABSTRACT

To provide information on the synergistic and respective roles of fluorocarbon (FC) radical and ion fluxes in SiO_2 and Si surface etching mechanisms, we measured the surface chemical changes of deposited/steady-state FC films, and etching rates of SiO_2 and Si in C_4F_8/Ar inductively coupled discharges. Argon addition to C_4F_8 strongly increases the plasma density relative to pure C_4F_8 and results in a dramatic increase of the ion/neutral flux ratio for C_4F_8/90%Ar discharges relative to C_4F_8. Nevertheless, the x-ray photoelectron spectra of FC films formed on SiO_2 and Si surfaces without RF bias remain remarkably similar to those of films produced in pure C_4F_8 discharges, which is characterized by a much lower ion/neutral ratio. Upon applying an RF bias, etching of FC, SiO_2 or Si films commences. At a dc self bias voltage of –125V the C (1s) spectra of FC surface films for C_4F_8/90%Ar discharges become strongly fluorine-deficient relative to conditions without RF bias, whereas the C (1s) spectra of FC films in C_4F_8 discharges change little. The surface chemical characteristics of FC films remain similar as to those of FC films deposited at floating voltage as the ion bombardment energy increases up to the Si or SiO_2 etching threshold energy. This indicates that the loss of the fluorine content in the FC layers during substrate steady-state etching is mainly caused by interaction with the substrate. Ion bombardment defluorinates the FC layer, the fluorine diffuses through

the FC layer, interacts with the substrate and substrate etching occurs. An etching model based on the carbon and fluorine mass balance between fluorocarbon deposition, fluorocarbon etching, and substrate etching is presented that describes the relationship of substrate etching rate, fluorocarbon deposition rate (DR), FC layer defluorination, and FC layer thickness.

2.1 INTRODUCTION

Fluorocarbon gas plasmas are extensively used for dielectric etch etching due to the ability to selectively etch SiO_2 and related materials with respect to photoresist masking layers, Si and Si_3N_4. As semiconductor devices continue to shrink to below 100nm critical dimension, precise control of etching processes becomes necessary and high selectivity of SiO_2 relative to photoresist, Si or Si_3N_4 is desirable. To achieve this, it is required to understand the fundamental mechanisms during the etching process of different films. Recently, significant efforts in both experiments and simulations have been focused on exploring the mechanism of silicon dioxide etching using fluorocarbon plasmas (see references 2.1-2.13).

Studying all species to model the interactions in the fluorocarbon plasma is not practical because of the multitude of different species and the complexity of the interactions in both gas phase and at the substrate surface. However, measuring important plasma-surface interaction parameters, e.g. ion current density and composition, ion energy, fluorocarbon deposition and surface chemical information can provide key insights on the most important elements of the etching mechanism. It is well known that the self-bias voltage on the substrate is required to exceed the etching threshold to achieve the steady state etching in fluorocarbon discharges. Below the energy threshold, a net growth of fluorocarbon film on the substrate occurs. During steady state etching, the surfaces of SiO_2 or Si are covered by a dynamic fluorocarbon (CF_x) layer [2.5-2.9], which blocks the direct interaction of the plasma with the substrate. Since this layer limits the arrival rate of etchant species at the substrate by diffusion, it is often considered as an inhibitor for substrate etching. More recent

work[1] has shown that the fluorine content of this fluorocarbon layer can be transferred to the substrate by ion bombardment. It was found that the substrate etching rate is linearly proportional to the ion-induced defluorination of the steady-state fluorocarbon film and the fluorocarbon film was suggested to be the dominant etchant source for the conditions studied. These studies shed some light on the mechanisms of the plasma surface interaction with fluorocarbon discharges. But it is still unclear how the ion energy contributes to the transition from deposition to etching, how ion energy affects on the chemistry of the fluorocarbon films during this transition. Respective roles that ions and neutrals play in the interaction between substrate and plasma are still to be identified. To improve our understanding, a system enabling the study of a large range of ion-to-neutral ratios is preferred, which will enable us to evaluate the relative importance of ions and neutrals during the etching process more clearly.

Argon addition to fluorocarbon discharges is widely used since it enables achievement of dense and highly dissociated plasmas. This is explained by the fairly high electron temperature of these discharges, which is explained by the high electron impact energy thresholds of Ar. Furthermore, the presence of argon metastables that carry a relatively high energy (11.6 eV) can enhance fluorocarbon dissociation and ionization[2.14]. The relative importance of ions and neutrals can be easily changed by varying the percentage of argon in the Ar/C_4F_8 gas mixture. The ions become the dominant species in highly diluted fluorocarbon discharges, for >90% Ar addition, which are characterized by low polymerization rates. Thus the picture of plasma surface interaction during steady state etching is significantly different from high

polymerization conditions since in the latter case the extent of ion bombardment is typically low and most energy released from ion bombardment is consumed by the relatively thick fluorocarbon overlayer while significant ion induced reaction between plasma and surface is expect in the case of ion-rich plasmas.

In this work, we investigated the mechanism of silicon and silicon dioxide etching in C_4F_8/Ar plasmas using this approach. Their substrate specific abilities to consume carbon are different, leading to different steady-state fluorocarbon layer thicknesses and different surface chemistry. Ar was introduced into the gas mixture to enhance the plasma density and ion current density incident on the substrate. Simultaneously, the fluorocarbon deposition rates changed significantly owing to the reduced fluorocarbon flow for C_4F_8/Ar. The composite of etching behavior and surface studies provides a fairly detailed view of the dominant surface etching mechanism and ion/neutral synergy.

2.2 EXPERIMENTAL SETUP AND PROCEDURES

Plasma processing of SiO_2 or Si in C_4F_8/Ar was performed in an inductively coupled plasma reactor described in Reference 2.14. The discharge was maintained at 10 mTorr, 50 sccm gas flow and 1000 W source power (13.56 MHz). The self-bias voltage of the substrate varied from no bias to –200 V and was produced using an additional RF bias power supply (13.56 MHz). A Langmuir probe was used to measure the ion current density with the probe tip biased at –100 V to avoid surface polymerization by fluorocarbon radicals. Etch rates were measured by *in situ* real-time single wavelength (632.8 nm) ellipsometry. X-ray photoelectron spectroscopy (XPS) analysis of partially processed SiO_2 or Si specimens was performed after

transfer in vacuum to an ultra-high vacuum chamber at 90^0 take-off angle using a nonmonochromatized Mg K-alpha X-ray source (1253.6 eV) to obtain the surface information of partially etched samples. The pass energy of the hemispherical analyzer was fixed at 20 eV. We have previously presented results of absolute density measurements of CF, CF_2 and COF_2 for these discharges by IR laser diode absorption measurement[2.15]. Ion compositional analysis of these discharges has also been performed[2.16].

2.3 RESULTS:

2.3.1 Ar addition effect on fluorocarbon plasma characteristics: Ion current density and surface polymerization rate

Figure 2.1 a) shows the effect of argon addition on the ion current density measured with a Langmuir probe. At low Ar concentration (<60%), the ion current density is nearly unaffected by the argon addition. It rises dramatically as a function of the percentage of argon at high Ar flow (>80%). Ion compositional measurements performed for these conditions revealed that in inductively coupled fluorocarbon/argon discharges, the flux of fluorocarbon ionic species decreases with argon addition especially for the heavier ions like $C_2F_4^+$. More than 70% of the total ion flux is Ar^+ for a C_4F_8/90%Ar gas mixture[2.16].

In infrared laser absorption spectroscopy (IRLAS) measurements[2.15], an increased dissociation of C_4F_8 was observed when a low Ar percentage was added to C_4F_8 ($\leq$ 20%). The fluorocarbon radical densities decreased as the percentage of Ar is increased in C_4F_8/Ar discharges above 20%. The fluorocarbon deposition rate vs. % Ar (Fig. 2.1 b)) shows a qualitatively similar behavior as the fluorocarbon radical

densities. At high C_4F_8 concentration, a saturation of fluorocarbon deposition rate was observed, which is plausible since the neutral radicals are abundant for these conditions, especially the dominant radical species CF_2[2.15]. The fluorocarbon deposition rate drops steeply when the Ar percentage was increased to above 80%, providing evidence of a neutral limited regime. This behavior qualitatively mirrors the increase of the total ion current density, indicating that ions may play an important role in the surface polymerization.

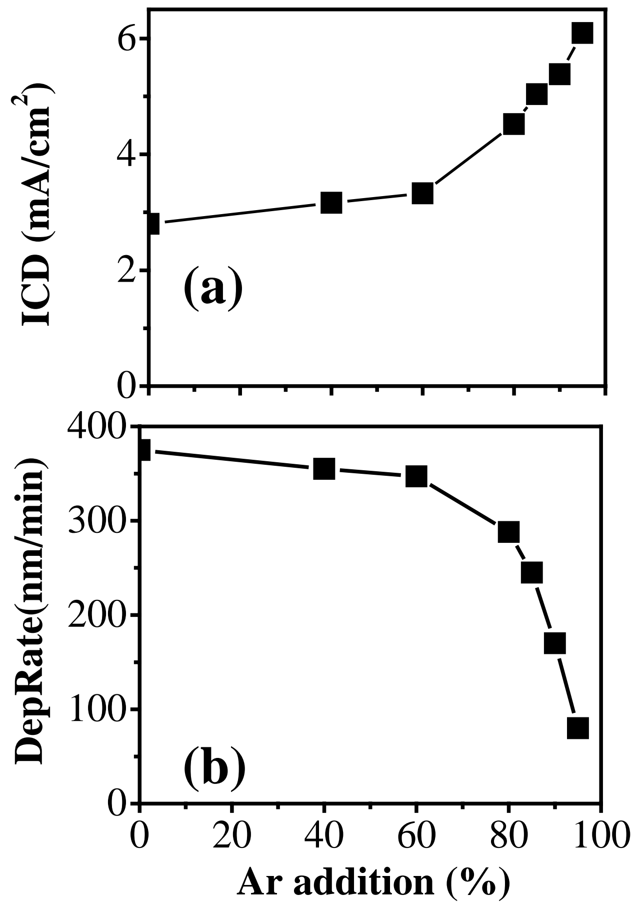

Figure 2.1: *Ion current density (a) and fluorocarbon deposition rate (b) as a function of Ar addition in C_4F_8 discharge. Pressure, source power and total gas flow rate were fixed at 10mTorr, 1000w, 50sccm, respectively.*

2.3.2 SiO_2 or Si etching in C_4F_8/Ar discharges with fixed bias voltage

a. Etch rate, etching selectivity and etch yield versus argon proportion

Blanket samples of SiO_2 and Si were etched in C_4F_8/Ar discharges at two different self-bias voltages: -125V or –200V. The argon addition effect is shown in Fig. 2.2. An increase in the absolute SiO_2 etching rate was achieved by adding up to 80% Ar to C_4F_8 (Fig.2.2 a)) at both bias voltages. Because the fluorocarbon ion fluxes decrease with argon addition, this observation is not consistent with the direct reactive ion etching model suggested by Steinbruchel[2.17] where reactive ions provide the constituents required for producing SiO_2 etch products. A different etching mechanism is required to explain the present data. Since the etching rate of Si does not change much when the Ar percentage is increased to 80%, a maximum of the SiO_2 /Si etching selectivity exists at about 80% argon addition. When the argon proportion is above 90%, the SiO_2 etching rates drop quickly while the Si etching rates increase for both –125V or –200V. This leads to a reduction of the SiO_2/Si etching selectivity. The SiO_2/Si etching selectivity decreases when the RF bias voltage is increased. To explain this, surface analysis is necessary which will be discussed in the next section.

Beam experiments [2.18,2.19] have shown that the etching yield strongly depends on the neutral to ion ratio of the incident species fluxes. We can change the neutral to ion ratio by changing the argon fractions of the gas mixture. The etching yields of SiO_2 or Si are shown in the Fig.2.2 (c). The trend of the Si etching yield using different Ar percentages (below 80%) is qualitatively more similar to the behavior observed in beam experiments using Ar^+ with F rather than Ar^+ with CF_2[2.14].

However, quantitatively the data is much closer to the CF_2/Ar^+ case. This implies that CF_2 is probably responsible for the surface polymerization and fluorine is the major etchant for Si etching. The increase of the etching yield for Ar percentage greater than 80% is plausible keeping the reduction of the fluorocarbon coverage in mind (see below). In terms of SiO_2 etching, the yields measured here are similar to the F/Ar^+ yields, with the values of CF_2/Ar^+ a little lower[2.15]. This indicates that fluorine is also a possible etchant source for SiO_2. The saturation of the SiO_2 etching yield in the case of a selfbias voltage of –125V (for Ar percentage greater than 80%), but lack of saturation for–200V, indicates that etching is limited in the –125V case by energy deposition.

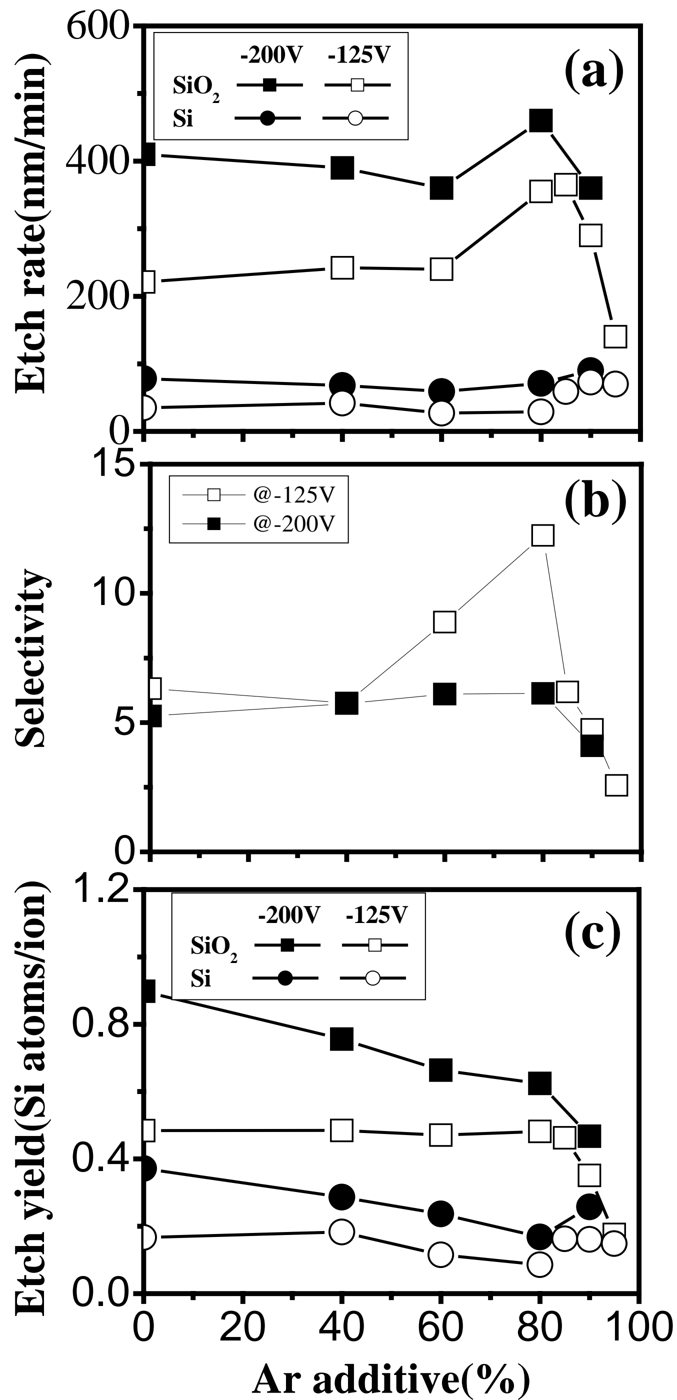

Figure 2.2: *Etch rate a), selectivity b) and etch yield versus Ar addition into C_4F_8. Pressure, source power and total gas flow rate were fixed at 10mTorr, 1000w, 50sccm, respectively. RF bias voltage was –125V or –200V.*

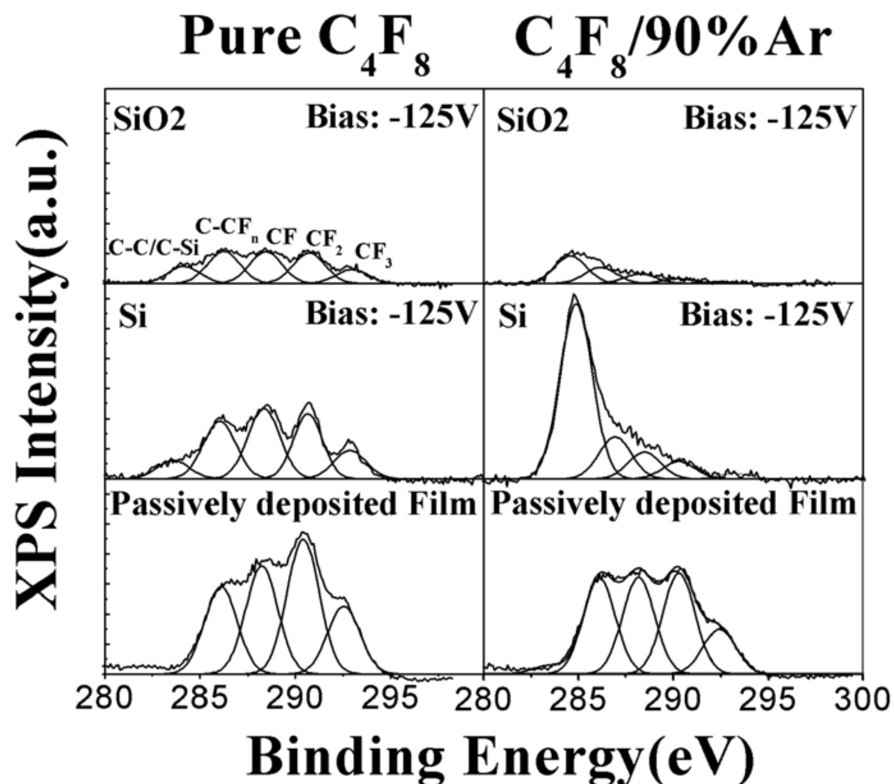

Figure 2.3: *C (1s) photoemission spectra of steady-state fluorocarbon films on Si or SiO_2thin films and passively deposited films produced in C_4F_8 or C_4F_8/90%Ar discharge. The spectra were obtained at a collection angle of 90^0.*

b. Surface Analysis

Since argon addition to C_4F_8 changes the fluorocarbon plasma characteristics, and therefore the plasma-surface interactions, surface chemical information is essential for the interpretation of the results. Blanket SiO_2 or Si samples were characterized by XPS after processing using C_4F_8/Ar plasmas. We examined both samples without RF bias (passive FC film deposition) and with RF bias (partially etched). Figure 2.3 shows the C (1s) photoemission spectra (electron take-off angle 90^0) for SiO_2 or Si samples and two extreme conditions: ion-limited (pure C_4F_8) and neutral-limited (C_4F_8/90% Ar) processing. For the passively deposited samples, the C (1s) spectra are remarkably similar. The intensities of CF_2 and CF_3 bonds are a little

lower in the C_4F_8/90% Ar case than for pure C_4F_8, consistent with the limitation of the fluorocarbon content of the gas mixture. Upon applying an RF bias (-125V), substrate etching commences and the stoichiometry of partially etched samples changes from those measured for deposited samples: an additional bond (C-Si/C-C) contribution is evident in the spectra and it suggests the presence of silicon at the fluorocarbon film/substrate interface when etching occurs. The C-Si /C-C bond component contribution is similar between SiO_2 and Si in pure C_4F_8 plasma while it is enhanced dramatically on Si etched in C_4F_8/90% Ar discharge The C-Si intensity does not vary significantly for SiO_2 samples partially etched in pure C_4F_8 or C_4F_8/90% Ar plasmas. The structures of the various C-F bonds for C_4F_8 etched samples remain similar to those observed for deposited films produced in pure C_4F_8. This means that for pure C_4F_8 discharges, energetic ion bombardment (fluorocarbon ions) cannot change dramatically the fluorine content of the surface fluorocarbon film. The fluorocarbon radical flux at the surface is high enough to maintain the F/C ratio even with energetic ion bombardment. For C_4F_8/90% Ar, the fluorocarbon layer is strongly fluorine-deficient when an RF bias is applied as compared with FC films deposited without RF bias, indicative of neutral-limited surface chemistry. Overall, the C (1s) photoemission spectrum intensity on Si is higher than for SiO_2 implying there is a thicker fluorocarbon layer on the Si surface during steady-state etching. This is the basis of the observed SiO_2/Si etching selectivity.

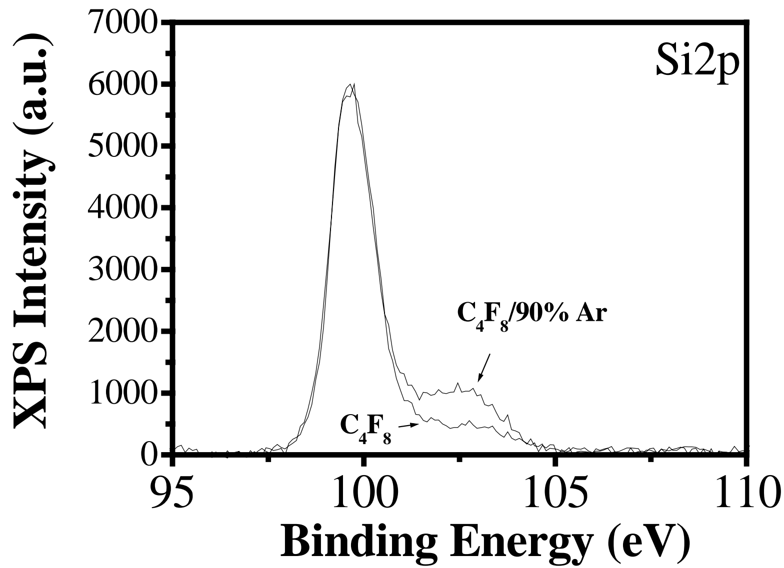

Figure 2.4: *Normalized Si (2p) photoemission spectra of partially etched Si samples in C_4F_8 or C_4F_8/90%Ar discharge. The spectra were obtained at a collection angle of 90^0.*

It is well known that an amorphous fluorocarbonsilyl mixing layer ($Si_xF_yC_z$) exists on the SiO_2 or Si during the steady-state etching [2.1]. Since it is difficult to differentiate Si-F_y bonds from SiO-bonding due to their similar binding energy, we only focus on Si(2p) spectra of Si samples. To eliminate the effect of overlayer (FC) on Si (2p) intensity, the intensity of Si (2p) spectra was normalized to 6000 counts per second at the main elemental Si contribution (99.7eV). In Fig.2.4, a significant increase of Si-F_y contribution was observed when adding 90% Ar to the gas mixture. This indicates that the fluorination of Si strongly depends on the ion to neutral ratio. For a higher ion bombardment flux (in the C_4F_8/90% Ar case), more fluorine can be driven to the substrate even though in this case the fluorine is much less in the gas

phase than for the C_4F_8 case due to the dilution effect. The effect of ion bombardment on the interface mixing will be discussed further in the next section.

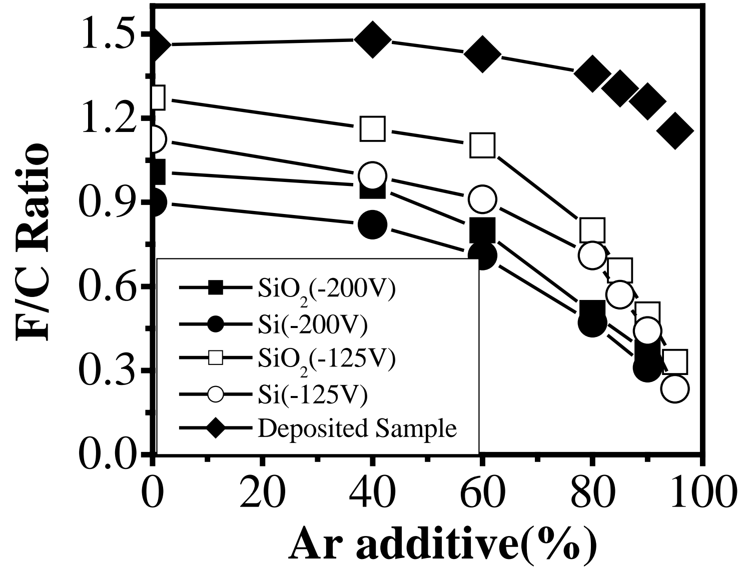

Figure 2.5: *F/C ratios in the steady-state fluorocarbon film on Si or SiO_2 samples at RF bias voltage –125V or –200V and passively deposited films at floating voltage processed by C_4F_8 with different argon addition discharges.*

Figure 2.5 shows the change in F/C ratio of FC films by ion bombardment at dc self bias voltages of –125V or –200V as a function of argon addition. The F/C ratio of the fluorocarbon films formed on SiO_2 or Si during steady-state etching or deposition is calculated from the C1s spectra using the method describing the reference 2.14. Deposited fluorocarbon films have similar F/C ratio for different argon percentage up to 90% Ar. When etching is induced by RF biasing, defluorination occurs. For higher argon percentages more fluorine-deficient fluorocarbon layers are formed. The defluorination of the fluorocarbon layer also reflects the change in total ion energy as the bias voltage is increased from –125V to -200V, and also the substrate type (SiO_2 or Si). This partially explains the increase of SiO_2 etching rate as a result of argon addition (for Ar percentage less than 85%).

The fluorocarbon layer on SiO_2 has a higher F/C ratio than on Si suggesting the abilities to consume fluorocarbon are different for SiO_2 and Si. Angle resolved x-ray photoelectron spectroscopy provides more insight into the surface chemistry. The results for SiO_2 and Si films etched in pure C_4F_8 or C_4F_8/90% Ar are shown in Fig.2.6. In the case of silicon, the F/C ratio with take-off angle 20^0 is higher than at 90^0, suggesting that the surface of the fluorocarbon film is more fluorinated and a fluorine gradient exists towards the silicon interface. It is opposite in the case of SiO_2 etching. A possible mechanism is the removal of carbon in the fluorocarbon layer by the oxygen release from SiO_2, leading to a higher F/C ratio relative to the F/C ratio at the FC- film surface (take-off angle 20^0). A more detailed discussion of this will be provided below.

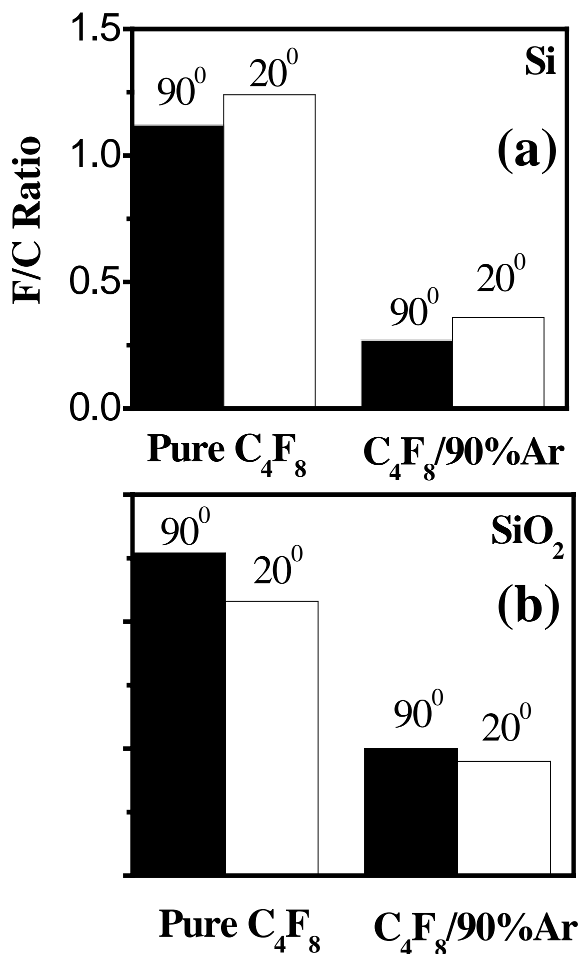

Figure 2.6: *Angle resolved XPS analysis on the steady-state fluorocarbon film formed on Si (a) or SiO_2 (b). The electron emission angles were 90^0 or 20^0.*

During steady-state substrate etching, the competition between fluorocarbon deposition and etching along with substrate consumption results in the formation of a steady-state fluorocarbon layer on the substrate surface. The thickness of this layer is thought to strongly depend on the polymerization rate of the plasma, which in turn is determined by the FC mass flow and the fluorine-deficiency of the feed gas, along with the composition of the substrate. Figure 2.7 shows the FC steady-state film

thickness versus percent argon added. In the case of Si etching, argon addition enhances the FC film thickness, despite the decrease of the deposition rate as a result of reduced fluorocarbon gas flow [2.20]. Argon ion bombardment of the surface [2.21-2.23] produces a fluorine-deficient carbonaceous film (see Fig. 2.3), which is hard to etch because of the lack of fluorine. The FC film thickness on Si strongly supports the conclusion that the etching rate decreases as a function of the FC film thickness. Oxygen from the SiO_2 substrate etching is considered to be an effective reactant to remove the carbonaceous film[24]. The FC film thickness decreases for SiO_2 with argon addition and behaves qualitatively similar as the deposition rate.

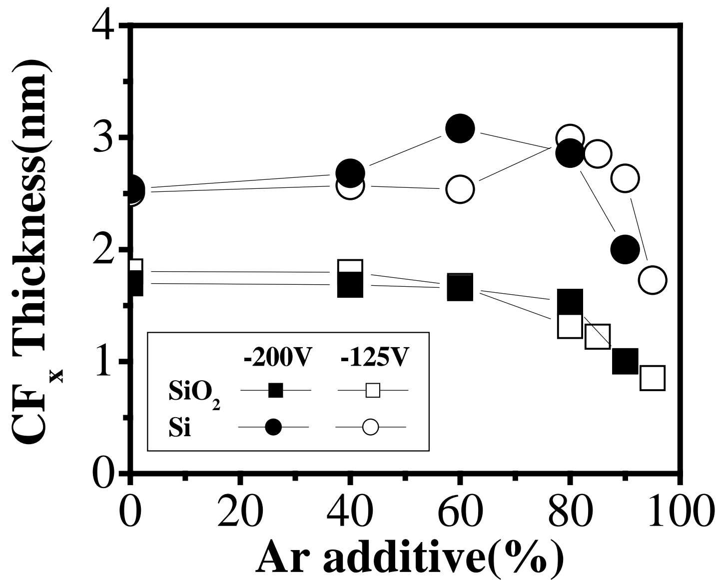

Figure 2.7: *The steady-state FC film thickness formed on SiO_2 or Si etched by C_4F_8 with different argon addition discharges at RF bias voltage –125V or –200V.*

2.3.3 SiO_2 or Si etching in C_4F_8/Ar discharges with various bias voltages:

In the process regime investigated, no significant influence of RF biasing of the substrate on the bulk plasma is observed. The ion energy dependence of the fluorocarbon etching mechanism can therefore be explored in detail by varying the bias voltage. In order to understand specific roles of different ion species like CF_x^+(x=1,2,3) and Ar^+, two gas chemistries are used: pure C_4F_8 and C_4F_8/80%Ar. Ar^+ is by far the dominant ion species in the latter case (our plasma sampling measurements show that around 60-70% of the total ion flux is Ar^+ in this case and CF^+ is dominant for pure C_4F_8). Etching rates measured for these conditions are plotted in Fig.2.8. Steady-state fluorocarbon film thicknesses are shown in Fig.2.9. It is clear that the ion energy is an important parameter in the etching process. Initially, at low bias voltage fluorocarbon deposition occurs (negative values). As the bias voltage exceeds a threshold, net substrate etching starts. No significant threshold shift between SiO_2 and Si was observed, implying the etching energy threshold mainly depends on the fluorocarbon removal, which in turn depends on fluorocarbon deposition and ion energy. A lower etching energy threshold exists in C_4F_8/80%Ar, consistent with the lower surface polymerization (see Fig.2.1 (b)). The etching rate of SiO_2 in C_4F_8/80%Ar saturates more quickly as a function of bias voltage than in a pure C_4F_8 discharge, indicative of the different characteristics of these two discharges. It is interesting that the FC steady-state film thickness is very sensitive to the voltage near the threshold and varies only weakly if the bias voltage is high. In the saturation regime of the etching rate, the FC steady-state film thickness is almost a

constant. We now show that the role of ion energy is to enhance the etching rate of the substrate by ion-induced defluorination of the fluorocarbon film.

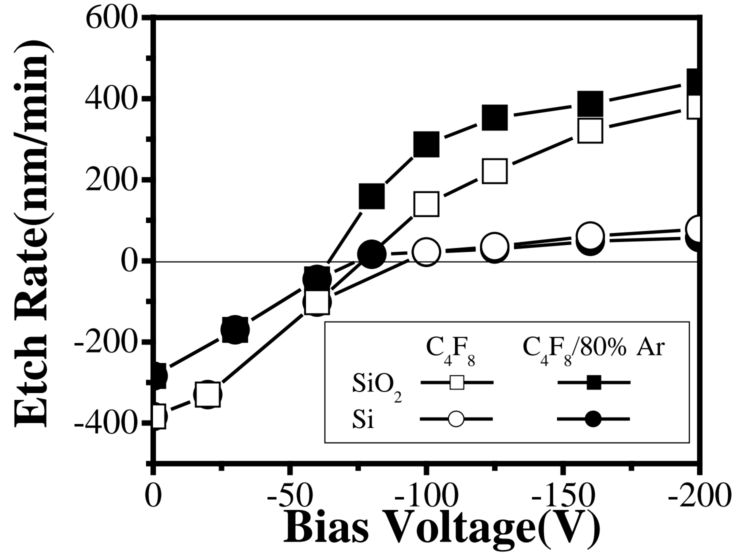

Figure 2.8: *SiO_2 or Si etch rate (positive values) and fluorocarbon deposition rate (negative values) processed in C_4F_8 or C_4F_8/80%Ar discharge with different RF bias voltages.*

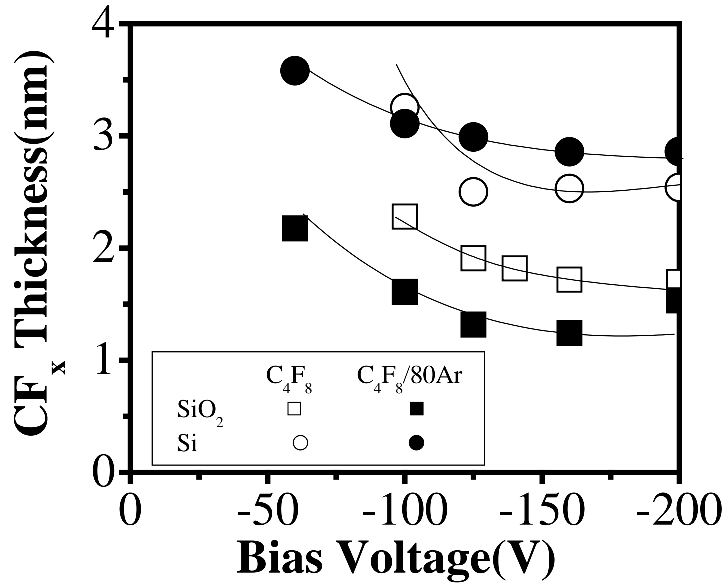

Figure 2.9: *The thickness of the fluorocarbon film formed on SiO_2 or Si during steady-state etching with different RF bias voltages in C_4F_8 or C_4F_8/80%Ar discharge.*

Figure 2.10 shows F/C ratios of the FC steady-state film for various bias voltages and substrates. Low energy ion bombardment (above plasma potential) does not appear to have a significant effect on the fluorocarbon surface composition in both pure C_4F_8 and C_4F_8/80% Ar. This implies that for low energy ion bombardment, the fluorocarbon stoichiometry is primarily determined by the fluorocarbon radical fluxes, rather than the high Ar^+ flux in C_4F_8/80% Ar plasma. The coincidence of substrate etching with ion-induced defluorination of the fluorocarbon layer suggests that this process dominates the etching process. The fluorocarbon layer becomes more fluorine-deficient as the ion energy increases leading to an enhancement in the etching rate of the substrate. The F/C ratio drops more quickly in C_4F_8/80% Ar than for pure C_4F_8, showing that at this high Ar^+/fluorocarbon radical flux ratio the radical flux (primarily CF_2) is insufficient to maintain the F/C ratio seen for low energy bombardment conditions. The leveling off of the F/C ratio of the FC film appears to coincide with the regime where the SiO_2 and Si etching rates vary only weakly with bias voltage for C_4F_8/80% Ar.

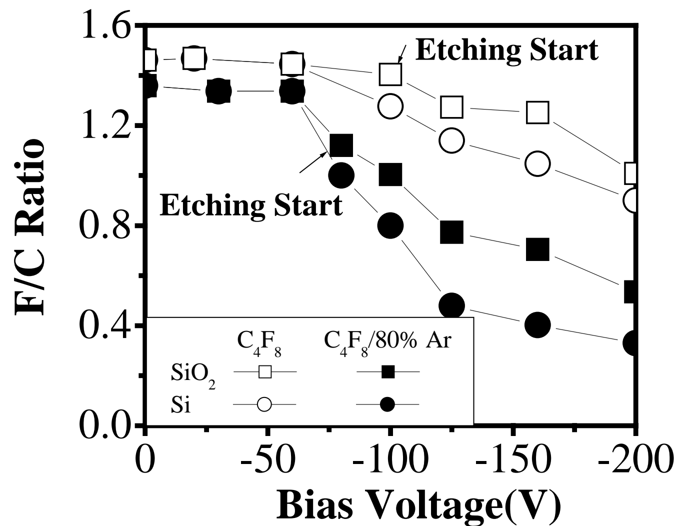

Figure 2.10: *F/C ratios in the fluorocarbon film formed on SiO_2 or Si processed with C_4F_8 or C_4F_8/80%Ar discharge as a function of RF bias voltage.*

As discussed above, the silicon-fluoride reaction layer on the Si surface observed for steady-state etching is related to the ion bombardment of the FC overlayer. The equivalent thickness of SiF_y layer is shown in Fig. 2.11 a) as a function of RF bias voltage for C_4F_8 or C_4F_8/80% Ar steady-state etching. An increase in the SiF_y thickness was observed as the RF bias voltage increases in both cases. In the ion-limited regime, this layer is weakly dependent on the ion bombardment energy (pure C_4F_8 case). When the ion to neutral ratio increases, ion bombardment can efficiently drive the fluorine to the substrate and the SiF_y layer thickness increases much more quickly with RF bias voltage (the C_4F_8/80% Ar case). This is consistent with the defluorination of FC layer (see Fig. 2.10). The thicker SiF_y layer does not result in a higher etching rate in the C_4F_8/80% Ar case (see Fig.2.8). In addition, the increase of the etching rate in the C_4F_8 case with RF bias voltage does not seem strongly correlated with this layer. All of these imply that the SiF_y layer mirrors the ion-induced defluorination of FC layer, but does not show a perfect correlation with the substrate etching rate. The intensity of C-Si/C-C bonds, which is plotted in Fig. 2.11 b), also reflects the defluorination of the FC layer. The dramatic increase of the C-Si/C-C intensity with bias voltage coincides with the quick drop of the F/C ratio in the C_4F_8/80% Ar case (see Fig. 2.10). For C_4F_8, the RF bias voltage increase changes the F/C ratio of the steady-state FC layer only weakly and the intensity of the C-Si/C-C bonds also increases slowly with bias voltage. The process of driving the fluorine to the interface between the FC layer and the substrate and the formation of the mixing layer has been treated by a molecular dynamics simulation [2].

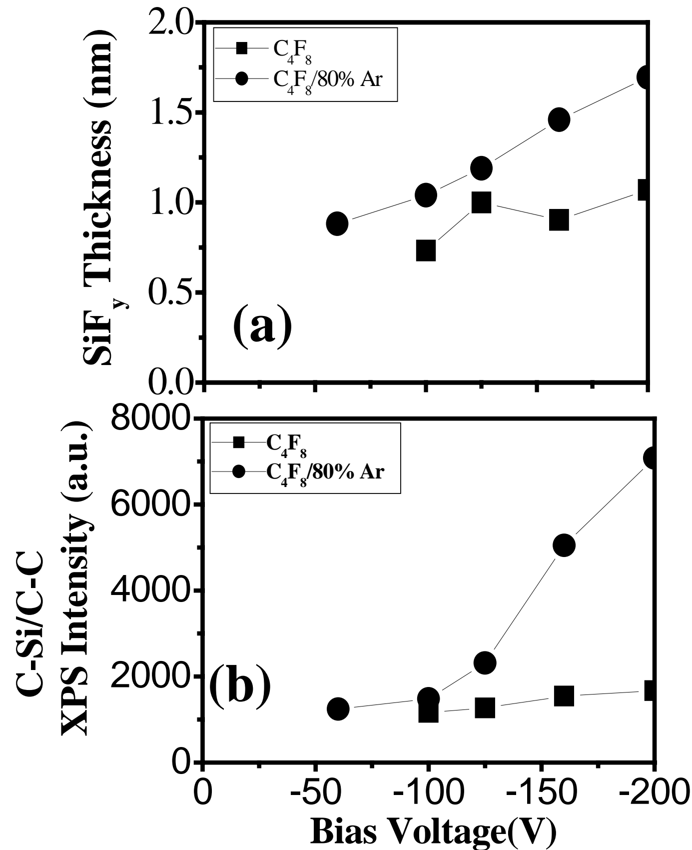

Figure 2.11: *a) The thickness of the SiFy layer formed on Si (a) and C-Si/C-C intensity from C(1s) spectra of the CFx film (b) during steady-state etching with different RF bias voltages in C_4F_8 or C_4F_8/80%Ar discharge.*

2.3.4 FC film etching

To maintain the steady state, the adsorbing fluorocarbon species fluxes must be balanced by desorbing fluorocarbon fluxes. Therefore fluorocarbon film etching is also very important in the etching mechanism. We studied the argon addition effect on the etching rate of the deposited fluorocarbon films, which is shown in Fig. 2.14. The fluorocarbon film was deposited at a floating substrate (>600nm) before an RF bias voltage (-125V) was applied using the same gas mixture discharges and etching started. The etching rate of the thick fluorocarbon film exhibits a similar behavior as the fluorocarbon deposition rate as a function of argon concentration in the gas

mixture and also is of similar magnitude. For C_4F_8/Ar discharges, fluorocarbon film etching my also be CF_x-based, e.g. through the reaction of gas phase CF_x with surface CF_y to form volatile species. Other possibilities exist as well. The surface analysis shows that the stoichiometry of the partially etched semi-infinite FC film is similar to that of passively deposited FC film (Fig. 2.15), and the change with increasing Ar content is small, but definite. In extremely fluorine deficient case (95% Ar added), the fluorine content drop is obvious. This indicates that fluorine can be preferentially released from C-F network upon ion bombardment and enhance the etching of the FC film. The stoichiometry of the film measured by XPS is primarily determined by the first 2~3nm layer[2.9]. A comparison with the data presented in Fig.2.5 shows that ion-induced defluorination of the FC film during steady-state etching is greatly increased by Si or SiO_2 substrate etching. The fluorine released from fluorocarbon ion species or fluorocarbon radicals, either by ion impact fragmentation or film dissociation can be transported to the substrate and converted into a stable product by reaction with the substrate.

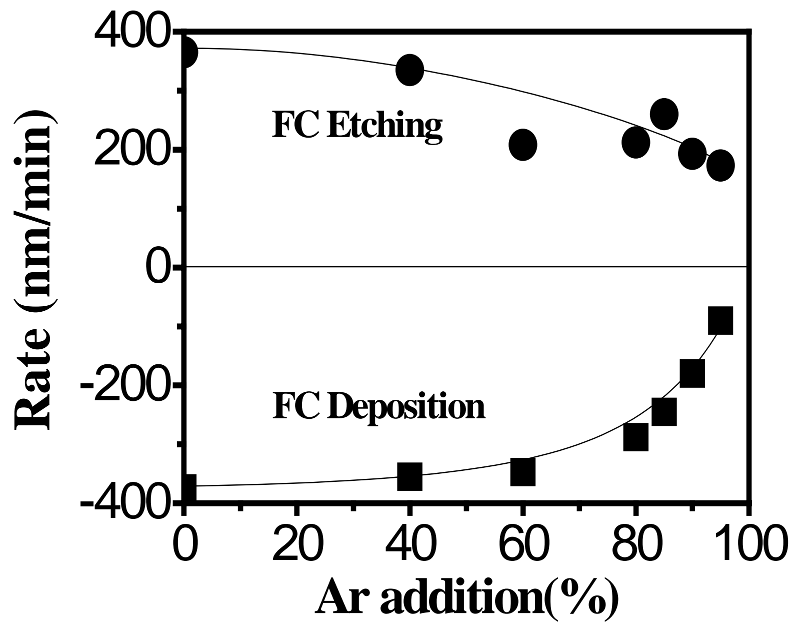

Figure 2.12:*A comparison of semi-infinite FC film etching rate with RF bias voltage:-125V and deposition rate on a floating sample.*

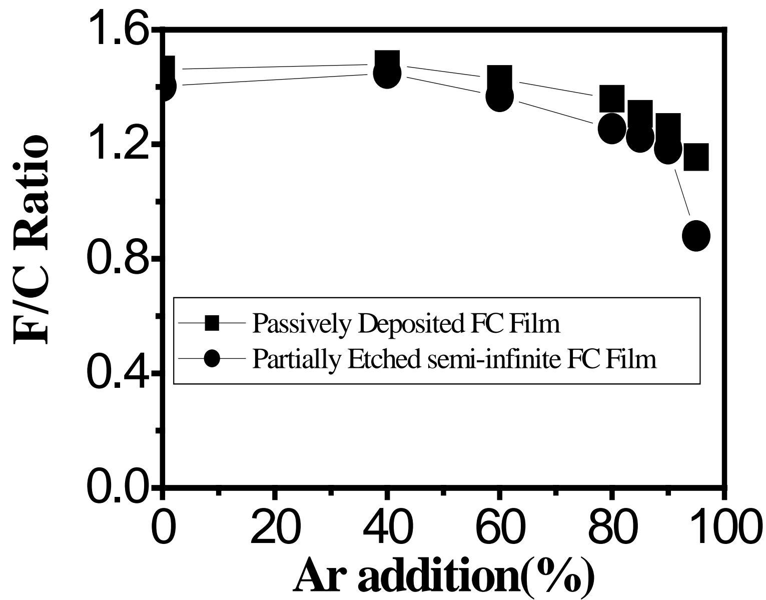

Figure 2.13:*A comparison of the F/C ratio of a partially etched semi-infinite FC film using an RF bias voltage of –125V with that of a passively deposited FC film (substrate at floating voltage relative to plasma).*

2.3.5 Physical sputtering of FC film with argon discharges

It has been shown that defluorination of C-F network enhances the etching. The fluorine is driven to underlying substrate and fluorination occurs. The bond energy of C-F is 5.18eV. Since the plasma potential for our experimental conditions is in the range of 20~30eV, the energy of incident ions is sufficient to break the C-F bond even without applying RF bias power. However, no etching takes place at the floating potential. This implies that defluorinatin of the FC film is not sufficient to initiate the etching process. To evaluate this, we studied physical sputtering of FC film initially passively deposited on Si wafer using pure C_4F_8 discharges. Various bias power were applied to argon discharges produced using 400W source power at a pressure of 10mTorr. The etching rates of the FC film are plotted in Fig. 2.14 (a). At floating potential, no significant etching of the FC film was observed. According to the trend shown in the plot, a bias voltage of ~-10V is required to initiate the FC film removal. Thus the energy threshold is the range of 30~40eV, consistent with the carbon atom displacement energy in graphite obtained in ion beam studies [2.25]. This suggests that carbon atoms need to be liberated from the C-F network for etching. No etching occurs at the floating potential since the ion energy is only 10eV to 20 eV, sufficient for releasing fluorine from the FC network. Surface analysis of the samples treated with argon discharge at floating potential confirms this picture. The data are shown in Fig. 2.14 (b). The CF_2 and CF_3 intensities drop significantly after the Ar etching process. On the other hand, the C-C bond is created and the intensity of C-CFx bonds increases. Argon ion bombardment knocks off fluorine atom from the FC network, and generates dangling C-C bonds. Some C-C dangling bonds can be cross-

linked. This indicates that both mobile carbon and fluorine atoms are required to achieve FC film etching in pure argon discharges. In fluorocarbon discharges, lots of fluorocarbon radicals are absorbed at surface along with ion bombardment and the process is more complicate. The threshold of etching is expected to be higher since more fluorocarbon species need to be broken, consistent with the results shown in Fig. 2.8.

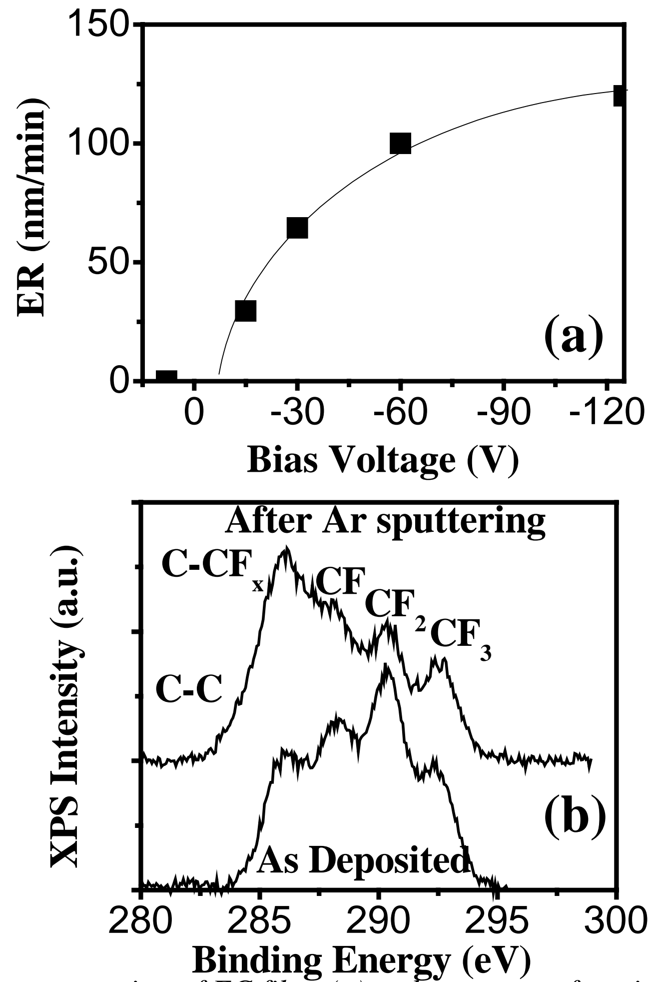

Figure 2.14: *Argon sputtering of FC film: (a) etch rates as a function of bias voltage; (b) XPS C1s spectra of FC film after argon plasma sputtering at floating potential.*

2.4 MODELING OF THE DATA

In order to provide a framework of C_4F_8/Ar plasma processing, we summarize some important data of our IRLAS and ion sampling measurements, the corresponding ion or neutral surface fluxes, and the measured surface chemistry data in Table 2.1 for two extreme conditions: C_4F_8 and C_4F_8/90%Ar.The ion to neutral ratio is enhanced dramatically in the 90% Ar case and as we saw above this high ion/neutral ratio leads to a very different surface chemistry for high (corresponding to plasma potential) ion bombardment energies. For ion bombardment at low ion energies the surface remains similar for the two gas mixture. In the table, we only list CF_2, which is the dominant neutral radical species[2.15]. We assume a CF_2-based deposition process in C_4F_8/Ar discharges.

	D. F/C Ratio		CF_2 Flux (mL/s)		Total Ion Flux (mL/s)		Ion Composition	
	C_4F_8	C_4F_8/ 90%Ar	C_4F_8	C_4F_8/ 90%Ar	C_4F_8	C_4F_8/ 90%Ar	C_4F_8	C_4F_8/ 90%Ar
Floating Voltage	~1.4	~1.25	>4000	<500	~50	~120	100% $C_xF_y^+$	>70% Ar^+
RF Bias -125V	~1.2	~0.6	>4000	<500	~50	~120	100% $C_xF_y^+$	>70% Ar^+

Table 2.1: *Summary of ionic or dominant neutral fluxes and surface chemistry information during processing conditions: C_4F_8 (ion-limited) or C_4F_8/90%Ar (neutral-limited) with a floating substrate or with a substrate biased –125V.*

Based on the result that an inversely proportionalities exist between the etching rate and the FC layer thickness, Oehrlein *et al.*[2.26,2.27] proposed an etchant transport limitations, e.g. due to a diffusion process, for low ion density etching. However, in high ion density discharges the role of ions contributing to the etching becomes very important. Figure 2.9 shows that ion-induced defluorination of the FC

overlayer accompanies substrate etching. The etching rates correlate to the defluorination of the FC layer[2.1]. During steady-state etching, the F/C ratio at the interference between the FC layer and bulk plasma is determined by the plasma characteristics, e.g. for our conditions by the CF_2 that is incorporated into the FC film. The defluorination of the FC layer therefore reflects the gradient of the fluorine concentration towards the substrate. According to Fick's law, the atomic fluorine flux that migrates through the FC layer is proportional to this gradient. In order to specify the role of the defluorination of the FC layer in the etching mechanism, it is necessary to clarify how the carbon content is consumed. In steady state, the adsorbing and desorbing (through fluorine etching) carbon fluxes are balanced with substrate consumption. The question arises how the substrate etching contributes to the removal of the fluorocarbon film. Clearly for Si etching, the etching substrate has no ability to remove the carbon formed by defluorination of the fluorocarbon. In oxide etching, the substrate can be etched through various reaction channels, for example through the formation of SiF_4, COF_2, CO and CO_2, contributing to the removal of both constituents of the FC overlayer.

The etching of the FC layer by fluorine results in the formation of volatile products, e.g. C_2F_4, CF_4 and so forth. Surface analysis shows that for SiO_2 etching, the F/C ratio of the FC layer is lower at the top than at the interface with the SiO_2. Therefore, during SiO2 etching the following or equivalent reactions should occur:

$$SiO_2 + 2C + 4F -> SiF_4 \uparrow + 2CO \uparrow \qquad (1)$$

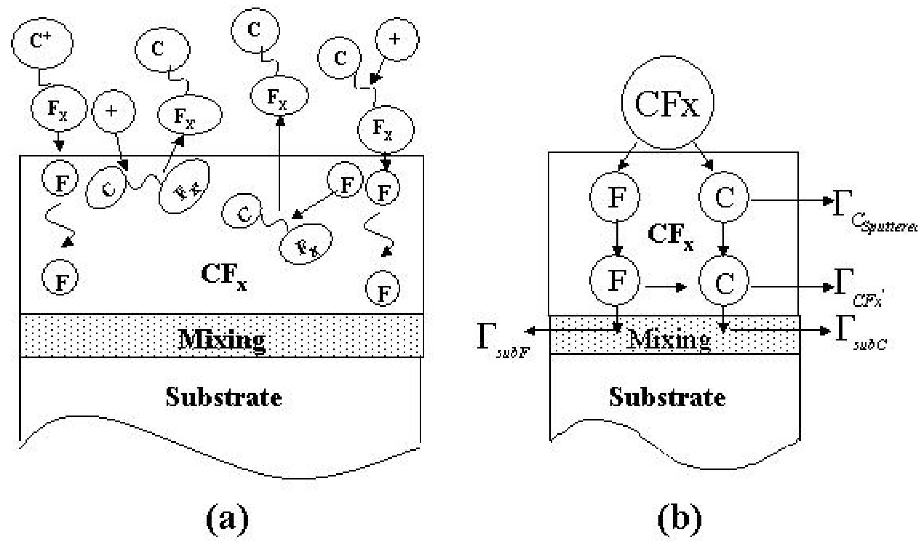

Figure 2.15: *Schematic of the model presented. The left-hand portion shows the basic processes in the FC layer and on the substrate. The right-hand portion indicates carbon or fluorine mass flux balance during the steady-state etching.*

A schematic picture of the model is presented in Fig. 2.15 based on the above discussion. During steady state, the FC film interacts with fluorocarbon ions and fluorocarbon radicals. The arrival of energetic ions at the FC film surface is accompanied by fragmentation of the molecular ions and surface molecules, providing atomic fluorine for the substrate etching by diffusion. Fluorocarbon fragment with relatively high energy can also produce volatile species in the FC overlayer. If the substrate is able to react with carbon to form volatile species, e.g. SiO_2, a different gradient of carbon density will exist than for a substrate where a reaction of the substrate with C cannot produce volatile species. The former is likely achieved by the ion-induced interaction of O from the SiO_2 with the FC overlayer,

and oxidation of the FC film. In this case, the steady-state FC film becomes much thinner than for the substrate without oxygen and etching selectivity is achieved. Due to the ion bombardment, the FC film is in an energetic state. There should be a gradient in the energy density, which is important for the diffusivity of the species. Because of the energetic state, it may not be necessary to distinguish between free F (no bonds with carbon atoms) and bound F (F bound to C in the FC layer). Therefore in this work, we only consider the mass flow balance for both carbon and fluorine during the steady-state substrate etching.

2.4.1 Mathematical Description

The above discussion suggests that during the steady state etching, the balance between FC deposition, FC etching and substrate etching controls the steady state FC film thickness. This balance can be written as

$$\frac{d}{dt}d(t) = DR_{CF_X} - ER_{CF_X} - CR_{CF_X} \quad (2)$$

where d(t) is the FC film thickness, DR_{CFx} is the FC deposition rate during etching, ER_{CFx} is the total FC etch rate due to the plasma, and CR_{CFx} is the FC consumption rate due to the substrate etching. During the steady state etching, the FC film thickness is constant, and the mass flow (fluorine or carbon) balance is given by

$$\Gamma_{i0} = \Gamma_{iCFx} + \Gamma_{iSub} \quad (3)$$

here i represents fluorine or carbon component, Γ_0 is the mass flux adsorbed by the surface, Γ_{CFx} is the desorbing mass flux through the FC etching and Γ_{Sub} is the consumption by the substrate etching. Here we follow the approach presented by

Standaert *et al*[9]. Fluorine flux diffuses through the FC film down to the substrate, meanwhile reacts with the FC film and substrate and forms volatile species, e.g. fluorocarbon, SiF_4 or CO in the case of SiO_2 etching. Detailed mathematical description is available in Reference 2.5.

During a small length dx in the FC film, the consumption of fluorine is proportional to the fluorine density $n(x)$ and a reaction rate constant k. The fluorine flux change $d\Gamma$ is given by

$$d\Gamma = -kn(x)dx \qquad (4)$$

According to Fick's law,

$$\Gamma = -D\frac{d}{dx}n(x) \qquad (5)$$

where D is a diffusion constant, and Eq.(4) can be rewritten as

$$D\frac{d^2}{dx^2}n(x) - kn(x) = 0 \qquad (6)$$

Using the following boundary conditions:

$$n(0)=n_0,$$

$$-D\frac{d}{dx}n(x)|_{x=d} = \Gamma_{Sub} = Kn_d \qquad (7)$$

the expression for the fluorine flux Γ_0 into the FC film is derived as

$$\Gamma_0 = \frac{2n_0\sqrt{kD}\sinh(\sqrt{\frac{k}{D}}d) + \Gamma_{Sub}}{2\cosh(\sqrt{\frac{k}{D}}d)} \qquad (8)$$

For rather thick steady state FC film, i.e. $d \geq 3\sqrt{D/k}$, the fluorine flux Γ_0 into FC layer is nearly independent of the layer thickness d:

$$\Gamma_0 \approx n_0 \sqrt{kD} \qquad (9)$$

The substrate etch rate can be expressed in terms of FC layer thickness *d*:

$$\Gamma_{Sub} = \frac{n_0 \sqrt{kD}}{2[\sqrt{kD}/K + \tanh(\sqrt{\frac{k}{D}}d)]\cosh(\sqrt{\frac{k}{D}}d)} \qquad (10)$$

2.4.2 The role of FC film thickness in SiO_2 and Si etching with fluorocarbon based plasmas

The fluorocarbon layer formed during the steady-state etching process has a thickness of more than ~1nm for almost all conditions examined here. The FC layer likely inhibits direct reactions of the reactive radicals with the substrate and probably blocks most direct substrate interactions since most of the energy of impacting ions (~150eV) is dissipated by the first few monolayers (~1nm)[2.28]. Thus the CFx thickness strongly correlates with the etch rate of the substrate materials. A general trend is that the substrate etch rate is inversely proportional to the thickness of this fluorocarbon film. It also has been found that the etch yield rather than etch rate is controlled by the FC film thickness when the ion density varies[2.29]. Figure 2.16 a) shows the relationship between etching rate and FC film thickness measured in all of the above experiments (see section III B and C). The general trend mentioned above was observed but a great deal of scatter was also seen. Furthermore, the etching yield shows a much weaker correlation with the FC film thickness in the presence of C_4F_8/Ar discharges (Fig. 2.16 (b)). The FC steady-state film thickness also reflects the surface polymerization rate.

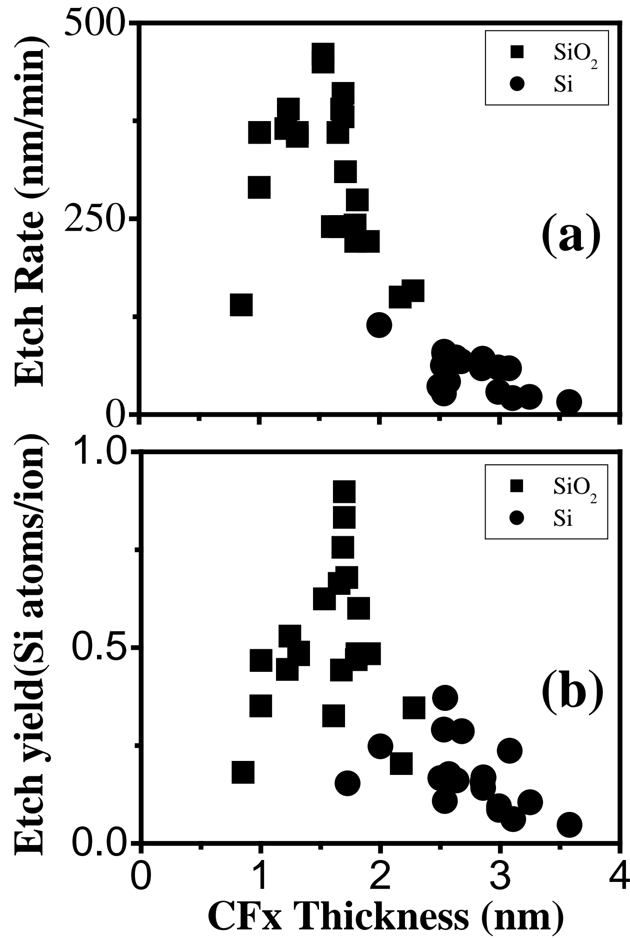

Figure 2.16: *(a) Etch rate and (b) etch yield as a function of CFx film thickness.*

From Eq. (8), the etching rate is not only controlled by the FC layer thickness, but also fluorine flux Γ_0. This probably results in the scatter seen in Fig. 2.16 (a). It is not practically to measure the latter parameter, since this flux is partially from the gas phase and ion induced dissociation and fragmentation of FC species also provide the etchant source for the substrate or FC layer etching. FC layer. Recent work revealed that the latter process may dominate in the etching mechanism for fluorine deficient gas discharge, e.g. CHF_3 or C_4F_8.[2.1] In our experiments, the atomic fluorine or

fluorine ion density are believed to be very low and major fluorine content exists in fluorocarbon radicals or ions especially for high Ar addition conditions. To provide a transparent picture how the substrate ER is influenced by the plasma gas phase properties, which can be mirrored by measurable parameter, e.g. DR, it is assumed that there is no significant fluorine flux directly from the gas phase. Ion induced defluorination of the FC layer provides major etchant source for both FC and substrate etching. We assume that CF_2-based deposition dominates (consistent with the flux data shown in Table 1), but validity of the model does not really depend on this. From Eq. (9), the substrate covered with a very thick FC layer has no significant effect on the fluorine flux Γ_0. Based on these assumptions, the mass fluorine flux Γ_0 into a very thick FC layer (i.e. $d \geq 3\sqrt{D/k}$) is given by

$$\Gamma_0 = s \bullet D_{F/C} \bullet \Gamma_{CF_2} \qquad (11)$$

where s is the sticking coefficient of CF_2 radicals, $D_{F/C}$ is the fluorine to carbon ratio of the passively deposited FC film shown in Fig. 2.5. The reason to introduce $D_{F/C}$ in Eq. (10) is that it is noted that the F/C ratio of the passively deposited FC film is not equal to 2 (see Fig. 2.5). However, XPS results showed that the C1s intensities of these passively deposited films are all similar but the F1s intensities change with conditions. The fluorine density at the interface between plasma and FC layer is determined by the plasma characterization and $n(0)$ is similar for different substrates. From Eq. (8), (9)&(10) and assuming $K \to \infty$, we have

$$\Gamma_{Sub} = \frac{n_0\sqrt{kD}}{2\sinh(\sqrt{\frac{k}{D}}d)} \approx s \bullet D_{F/C} \bullet \Gamma_{CF_2} / 2\sinh(\sqrt{\frac{k}{D}}d) \qquad (11)$$

At the floating voltage, a FC layer grows and the growth rate *DR* is given by

$$DR = s' \bullet \Gamma_{CF_2} / \rho_{FC} \tag{13}$$

here *s'* is the sticking coefficient at the floating voltage and ρ_{FC} is the carbon atomic density of FC layer. On the other hand, the consumption of fluorine flux by the substrate is related to the measured substrate *ER*

$$ER = \frac{\Gamma_{Sub}}{4\rho_{Sub}} \tag{14}$$

where ρ_{Sub} is the silicon atomic density of the substrate, i.e. ~2.3×10^{23} cm^{-3} for SiO_2 and 5.0×10^{22} cm^{-3} for Si. The factor "4" was introduced because of the fact that one silicon atom requires 4 fluorine atoms to form volatile specie SiF_4. A general relationship between *ER* and *DR* (for corresponding conditions) correlated with the steady state FC film thickness *d* is as following

$$ER / DR \approx \frac{s}{8s'} \bullet \frac{\rho_{FC}}{\rho_{Sub}} D_{F/C} / \sinh(-\sqrt{\frac{k}{D}} d) \tag{15}$$

The value of $ER \bullet \rho_{Sub} / (DR \bullet D_{F/C})$ is plotted as a function of $1/\sinh(\sqrt{\frac{k}{D}} d)$ in Fig. 2.17. with $\sqrt{\frac{k}{D}} \sim 1$. The data points in the ellipse are obtained at high Ar addition conditions ($\gtrsim$90%). The deviation of these points implies that direct ion reaction with the substrate becomes important at those conditions since the FC layer thickness is low. A linear regression (excluding the deviated points) shows that the slope is ~2, which means $\frac{s}{8s'} \rho_{FC} \sim 2$. This suggests that the sticking coefficients are similar at the biasing cases, consistent with the fact that most of our biasing conditions were

operated within the suppression regime due to the energetic ion bombardment and the sticking coefficient may be saturated at this regime. With energetic ion bombardment, the sticking coefficient is about several times greater than the value at the floating voltage.

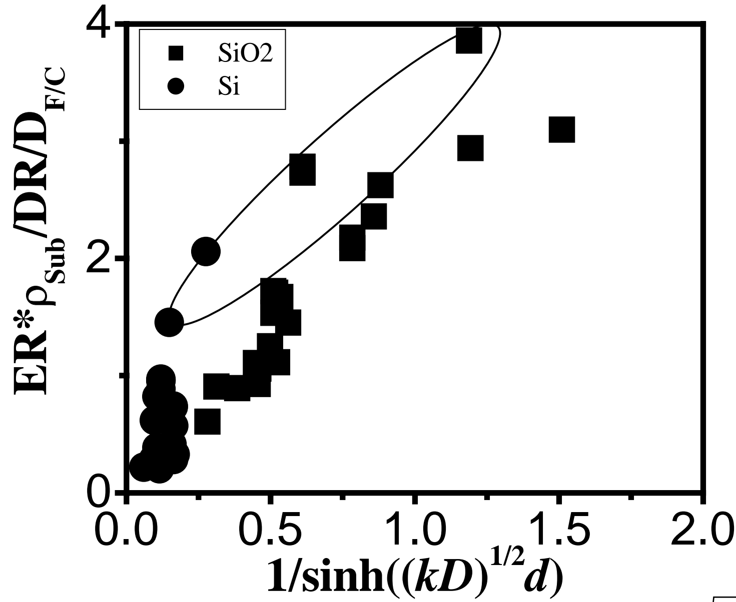

Figure 2.17: *Modeling result of* $ER \bullet \rho_{Sub} / (DR \bullet D_{F/C}) \sim 1/\sinh(\sqrt{\frac{k}{D}}d)$, *data in ellipse are obtained at high Ar addition conditions (≥90%).*

2.4.3. Ion-induced Defluorination of FC film

Above discussion reveals how the steady state FC film controls the substrate etching. But it is not clear how the adsorbed fluorine converts into etchant source. Recent work shows that the substrate etching rate scales linearly with the fluorine depletion of the fluorocarbon film[2.10]. It is important to note that that work was performed with pure fluorocarbon gas discharges. Some important parameters such as deposition rate did not vary significantly in that work. We have determined the change in fluorine content of steady state FC layers. The defluorination is defined as

the difference between the F/C ratio $D_{F/C}$ of a thick fluorocarbon film (~300nm) deposited at floating potential and the F/C ratio $E_{F/C}$ of the steady-state fluorocarbon film:

$$DF = D_{F/C} - E_{F/C} \qquad (16)$$

The present work shows that the fluorine liberation in the fluorocarbon film does not enhance the substrate etch rate linearly (Fig.2.18a)). In order to account for changes in deposition rate, the ratio of substrate etching rate to deposition rate is plotted as a function of defluorination. The ratio of etching rate (ER) to deposition rate (DR) scales linearly with DF (see Fig. 2.18b)), which indicates that the fluorine depletion of the fluorocarbon film is an important process in SiO_2 and Si etching. With linear regression, the slope is 1.607 for SiO_2 etching and 0.362 for Si. The ratio between the slopes (1.607: 0.362) is much greater than the ratio of the silicon atomic density to the SiO_2 density (5:2.3). One may conclude from this that ion-induced defluorination process does not directly contribute to the substrate etching. The fluorine released by the ion induced defluorination needs to be driven down to the substrate, e.g. by diffusion process.

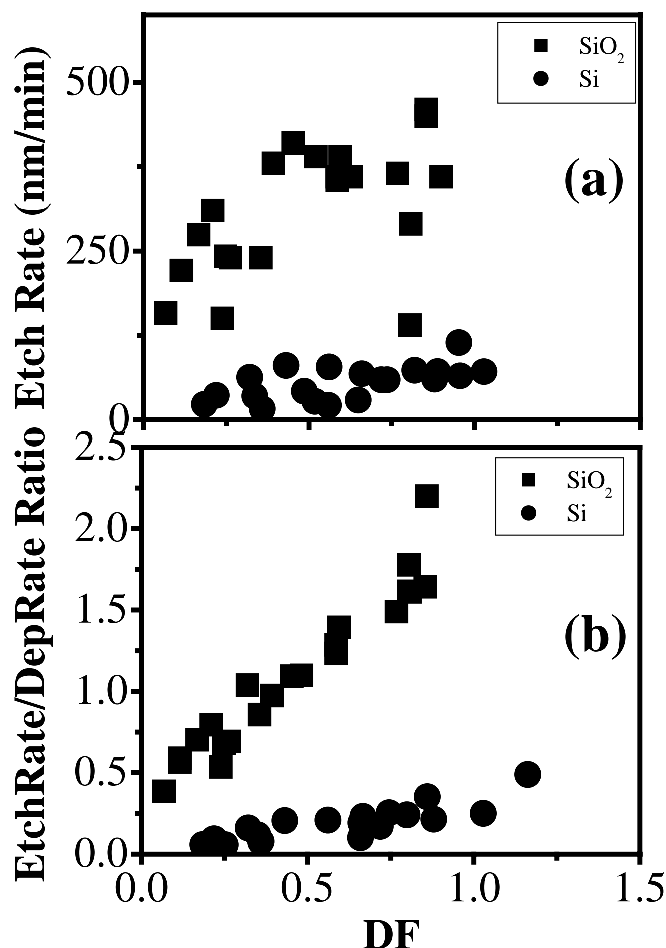

Figure 2.18: *Etch rate (a) or the ratio of etch rate to deposition rate (b) versus the defluorination in the CFx film.*

During the steady state etching, the ratio of desorbing fluorine flux to carbon flux may change for different conditions, for instance, carbonaceous specie can be removed upon high ion energy sputtering. We assume that this ratio is equal to the F/C ratio of the steady-state FC film measured with XPS. This is consistent with the etching results of semi-infinite FC films (see section III-D). In those cases, the F/C ratios of removed species are similar as the F/C ratios of etched films. Thus remained

films have similar F/C ratios during the etching (see Fig. 2.13). According to Eq. 2, we have

$$E_{F/C} = \frac{\Gamma_{0F} - \Gamma_{SubF}}{\Gamma_{0C} - \Gamma_{SubC}} \tag{17}$$

For Si etching, $\Gamma_{SubC} = 0$, since silicon does not contribute in carbon removal. In the case SiO_2 etching,

$$\Gamma_{SubC} = 2ER \bullet \rho_{Sub} \tag{19}$$

Based on Eq. (8), (9), (11), (13), (14),(18)&(19), it is possible to obtain an express of *ER/DR* in term of $D_{F/C}$, $E_{F/C}$, and FC layer thickness d:

$$ER/DR \approx \begin{cases} \frac{s}{s'} \bullet \frac{\rho_{FC}}{\rho_{SuB}} \bullet \underbrace{\frac{D_{F/C}\tanh(\sqrt{\frac{k}{D}}d) - E_{F/C}}{4(1 - \frac{1}{2\cosh(\sqrt{\frac{k}{D}}d)}) - 2E_{F/C}}}_{X_{SiO_2}} & \text{for } SiO_2 \text{ etching} \\ \frac{s}{s'} \bullet \frac{\rho_{FC}}{\rho_{SuB}} \bullet \frac{\overbrace{D_{F/C}\tanh(\sqrt{\frac{k}{D}}d) - E_{F/C}}^{X_{Si}}}{4(1 - \frac{1}{2\cosh(\sqrt{\frac{k}{D}}d)})} & \text{for Si etching} \end{cases} \tag{20}$$

$ER \bullet \rho_{Sub} / DR \sim X_{SiO_2}$ or X_{Si} is plotted in Fig. 2.19. Again, a deviation was seen for high Ar addition conditions. In this case, linear regression indicates $\frac{s}{s'}\rho_{FC} \sim 12$. The discrepancy of $\frac{s}{s'}\rho_{FC}$ value obtained by these two fittings may be explained by the overestimation of fluorine flux Γ_{0F} shown in Eq. (11). Since ion induced dissociation or fragmentation of fluorocarbon species cannot completely deplete the fluorine from those species, one part of Γ_{0F} can participate in the diffusion process. But in Eq. (17) the mass flows of fluorine or carbon are considered.

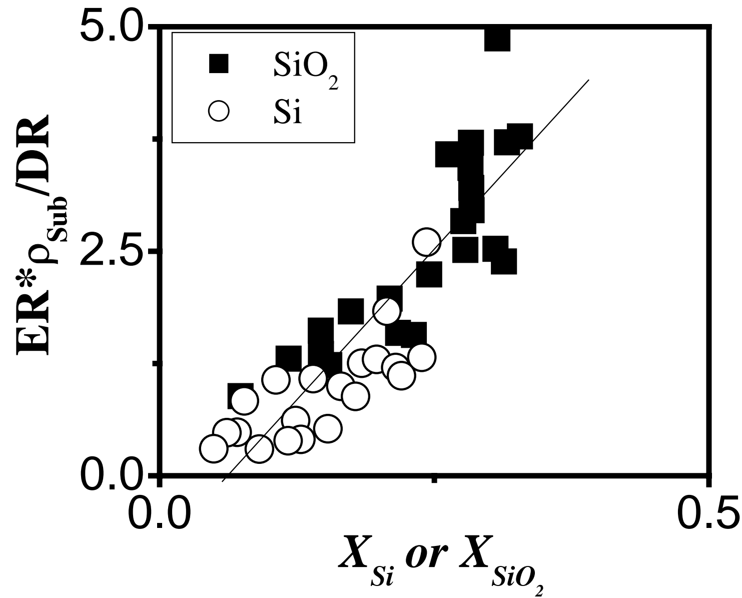

Figure 2.19: *SiO_2 or Si etching rate versus the parameter presented in the model*

2.5 CONCLUSIONS

All data presented in this work are consistent with a picture where ion-induced defluorination of a thin FC layer formed on the substrate surface is the main source of substrate etchant in fluorine deficient fluorocarbon discharges. The fluorine released by ion fragmentation, and dissociation of the FC film network as a result of energetic ion bombardment is transported to the substrate by a diffusion-like process, where it will react and form volatile etching product. Through this indirect process, the substrate etching rate becomes strongly dependent on substrate stoichiometry and bond strength, and the relative magnitudes of the species fluxes incident from the plasma on the substrate overlayer surface, and the amount of energy deposited per gas phase species incorporated in the substrate overlayer. The difference in fluorine and carbon gradients seen for SiO_2 and Si seen in this work are consistent with the well-known model that during SiO_2 etching, oxygen from the substrate leads to more efficient volatilization of deposited fluorocarbon material than for Si, resulting in a thinner steady-state fluorocarbon film for SiO_2 than for Si, and enabling the achievement of SiO_2/Si etching selectivity.

ACKNOWLEDGEMENTS

This work was financially supported by the Department of Energy under Contract No. DE-FG0200ER54608. The authors would like to thank X. Wang, X.Li, and L.Ling for assistance and helpful discussions.

Chapter 3: Study of C_4F_8/N_2 and $C_4F_8/Ar/N_2$ plasmas for highly selective Organosilicate Glass (OSG) etching over Si_3N_4 and SiC

J. Vac. Sci. Technol. A., 21,1708 (2003)

Xuefeng Hua, X.Wang, D.Fuentevilla, G.S.Oehrlein, F. G. Celii and

K. H. R. Kirmse

Abstract:

We report the effect of N_2 addition to C_4F_8 and C_4F_8/Ar discharges on plasma etching rates of Organosilicate Glass (OSG) and etch stop layer materials (Si_3N_4 and SiC), and results of surface chemistry studies performed in parallel. N_2 addition exhibits different effects in C_4F_8 and C_4F_8/Ar plasmas, which may be explained by a higher plasma density, electron temperature and possibly the presence of argon metastable species in the C_4F_8/Ar plasma, all of which serve to dissociate N_2 more effectively. When N_2 is added to a C_4F_8/Ar plasma, a reduction of the steady-state fluorocarbon surface layer thickness, one of the key parameters that controlls the etching rate and etching selectivity, on partially etched samples is observed. This effect leads to a loss of etching selectivity for $C_4F_8/Ar/N_2$ discharges. Adding N_2 to C_4F_8 plasmas without Ar enhances the steady-state fluorocarbon layer thickness. X-ray photoelectron spectroscopy analysis shows in this case that there is an important change in the stoichiometry of either passively deposited films or the fluorination reaction layers formed on etching samples: a significant amount of nitrogen is incorporated in the fluorocarbon film for deposited films, which implies that C_xN_y needs to be removed to achieve an etching condition. The incorporation of nitrogen in fluorocarbon films could reduce the etchant supply for Si_3N_4 or OSG from the gas

phase, especially for $C_4F_8/Ar/N_2$ plasmas, but not for SiC owing to the differences of the chemical compositions. SiO_2 and Si are also studied for comparison materials: SiO_2 has similar etching behavior as OSG and Si_3N_4, while Si behaves more similar to SiC during fluorocarbon etching. In addition, a comparison of N_2 and O_2 addition to C_4F_8 or C_4F_8/Ar plasma in terms of consequences on etching behavior of the above materials is presented.

3.1 Introduction:

The signal delay caused by the resistance of the metal lines and parasitic capacitance between adjacent interconnect lines is expected to be greater than the gate related signal delay and dominate device performance as the device feature size of ULSI circuits shrink to less than 250 nm. Integrating low-*k* or ultralow-*k* dielectric materials into the backend of the line (BEOL) processing is required to reduce the RC delays. A variety of novel low dielectric constant (low-*k*) materials having dielectric constants below 3.0, including organic and inorganic films, have been investigated to replace conventional SiO_2 for advanced devices[3.1]. Organosilicate glass (OSG) with a dielectric constant (*k*) ranging from 2.6 to 3.1 is a promising low-*k* material for next generation devices, since OSG is thermally stable and mechanically strong. SiC is a potential candidate to replace Si_3N_4 as an etch stop layer (ESL), since it has a lower dielectric constant than Si_3N_4.

Fluorocarbon plasmas are widely used for etching silicon dioxide layers, but to effectively determine the best composition of fluorocarbon plasmas to etch these new low-*k* materials with high selectivity relative to the etch stop layers, basic understanding of the gas-phase reaction and plasma-surface interaction mechanisms is necessary. As a result of the interaction of the fluorocarbon plasma and a biased surface, a thin steady-state fluorocarbon layer is formed[3.2-3.4] on the surface of the etching material and has been identified as one of the key parameters in the etching of various substrate materials. This layer inhibits the ions or neutrals from directly reacting with the substrate. Normally, etch rates are thought to decrease with the fluorocarbon thickness[3.5]. On the other hand, ion-induced defluorination of the

fluorocarbon layer enhances the etch rate, by providing additional etchant for the substrate[3.6]. In this work, we introduced nitrogen into the discharge in an effort to increase OSG/ESL etching selectivity. N_2 addition to C_4F_8 or C_4F_8/Ar makes the gas-phase and surface reactions more complex, especially when argon is additionally present.

3.2 Experimental setup and procedures

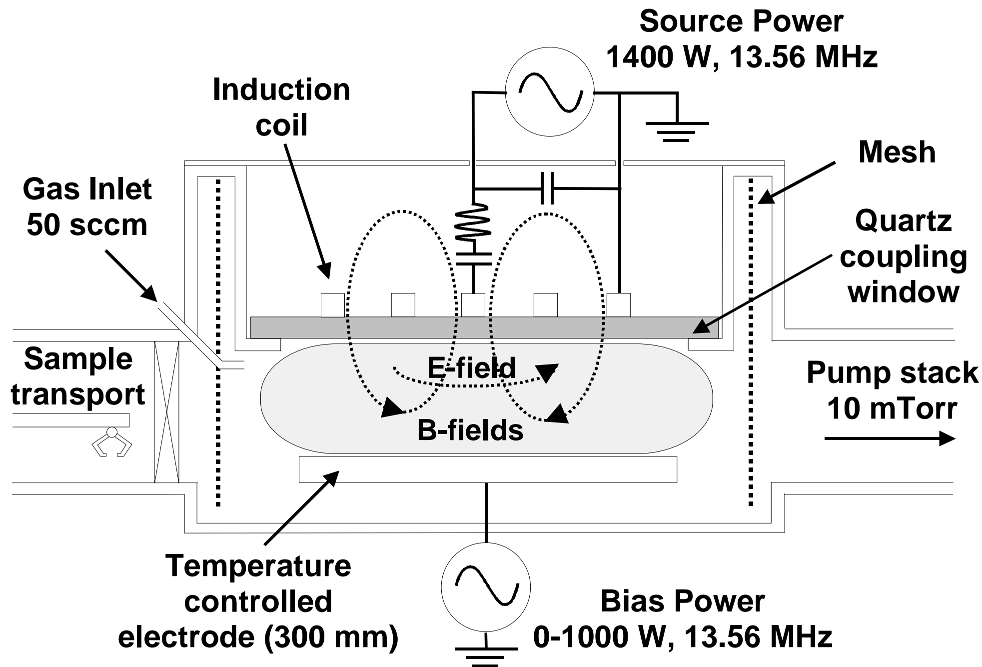

Figure 3.1: *Schematic outline of the planar coil ICP*

The inductively coupled high-density plasma-etching reactor used for this study is schematically shown in Fig. 3.1. A planar coil is placed on top of a quartz window and powered through an L-type matching network by a 13.56 MHz, 0-2000 W power supply to generate plasma which is confined to a narrow region 2-

3cm below the window by induced electromagnetic fields. The ion bombardment energy at the substrate electrode (300mm diameter) is controlled by applying a RF bias voltage using another 13.56 MHz power supply (0-1000 W). The wafers are located at the center of the electrode that is cooled by circulation of a cooling liquid to 15 ^{0}C. Total gas flow into the reactor was set at 50 sccm. An operating pressure of 10 mTorr was maintained by using an automatic throttle valve in the exhaust line. Before each experiment, the chamber was cleaned using an O_2 plasma, followed by a 3 minute chamber seasoning using the conditions for the next experiment. After that, the sample is loaded and the experiment of interest is conducted. A thin metal mesh is installed around the discharge region to ensure stable processing conditions and reproducibility. The temperature of the vessel wall was kept constant at 50 ^{o}C using heating straps.

A Langmuir probe was used to measure the ion current density. The probe tip was biased at –100V to avoid surface polymerization by fluorocarbon radicals. In the process regime investigated, no significant influence of rf biasing of the substrate on the ion current density in the bulk plasma is observed, consistent with the observation that the rf power coupled to the substrate electrode is linearly proportional to the self-bias voltage developed at that electrode. The ion current density can also be calculated by the slope of this linear relationship[3.6].

Blanket film etching of OSG, Si_3N_4, SiO_2, SiC, and Si were studied in discharges fed with C_4F_8/N_2 and $C_4F_8/Ar/N_2$ gas mixtures discharge using a total flow rate of 50 sccm (in the latter case, the ratio of C_4F_8 to Ar was fixed at 1:9). The source power and RF bias voltage were fixed at 1000 W and –125 V, respectively. *In situ*

real-time single wavelength (632.8 nm) ellipsometry was employed to measure the etch rates and the surface modification during etching. X-ray photoelectron spectroscopy (XPS) analysis was performed at 90^0 take-off angle using a nonmonochromatized Mg K-alpha X-ray source (1253.6 eV) to obtain the photoemission spectra of partially etched samples. The pass energy of the hemispherical analyzer was fixed at 20 eV.

3.3 Experimental Results:

3.3.1 C4F8/N2 plasmas:

1. Effect of N_2 addition on etch rates, deposition rates and steady-state fluorocarbon film thickness:

Blanket OSG, Si_3N_4, SiO_2, SiC and Si films were etched in C_4F_8/N_2 discharges which are maintained at 10 mTorr, using 1000 W source power and –125 V self-bias voltage with respect to ground. The etch rates were determined by *in-situ* ellipsometry (632.8 nm) and are plotted in Fig.3.2. Negative etch rates correspond to flurocarbon film deposition, which is observed with the substrate at floating voltage. The etch rates remain almost the same for different proportions of N_2 in the feed gas, implying that the etchant density was not changed strongly by nitrogen addition. This is also confirmed by the fact that the ion current density changed only little as a function of the percentage N_2 added to C_4F_8 (see discussion section). When N_2 is added to C_4F_8, higher fluorocarbon deposition rates were observed, indicative of a reaction of nitrogen and fluorocarbon radicals, and further characterized by XPS (see below). The deposition rate

reaches a saturation level when the concentration of N_2 increases above 20%, and may be explained by the simultaneous reduction of the fluorocarbon gas flow rate. In this work the nitrogen concentration was limited to 40% or lower. Although the etching rates of all above materials dropped slightly as nitrogen was added, the selectivities of OSG/Si_3N_4 and OSG/SiC are increased to around 4 when 40% N_2 is added.

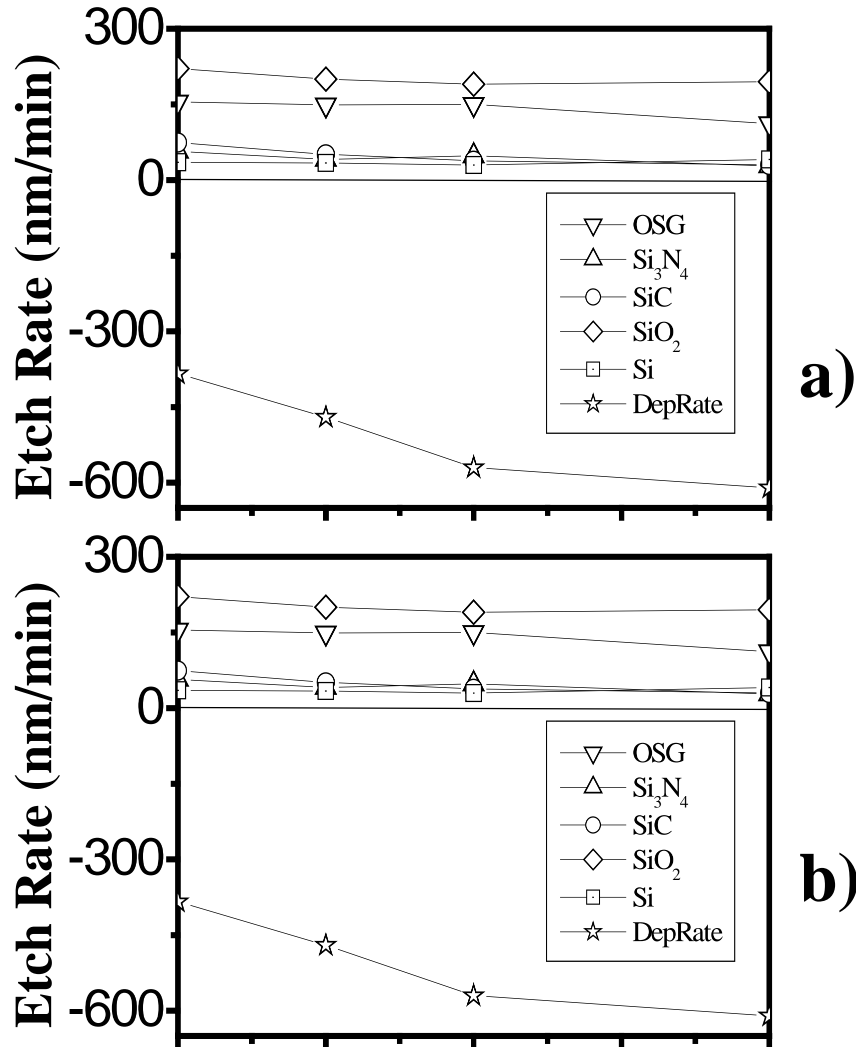

Figure 3.2: *Etch rate a) and selectivity b) as a function of N_2 addition into C_4F_8. Pressure, source power and total gas flow rate were fixed at 10mTorr, 1000w, 50sccm, respectively.*

In order to explore the mechanism of N_2 addition effect on the etching behavior, the key parameter of the fluorocarbon etching—the steady-state fluorocarbon layer thickness on a Si stop layer was studied carefully with ellipsometry: First a pure C_4F_8 plasma was ignited in the reactor, and the substrate was RF biased at –125 V. This formed a steady-state fluorocarbon layer. Subsequently, nitrogen is added into the reactor. Fig.3.3 shows that a slight increase of the steady-state film thickness was observed as a result of N_2 injection, leading to a drop of the Si etch rate.

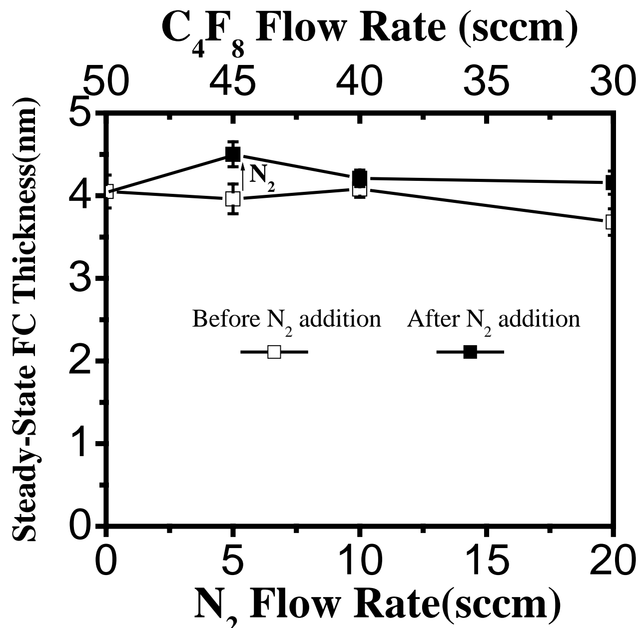

Figure 3.3: *N_2 effect on the steady-state fluorocarbon film thickness on Si sample when added into C_4F_8. Pressure, source power and total gas flow rate were fixed at 10mTorr, 1000w, 50sccm, respectively.*

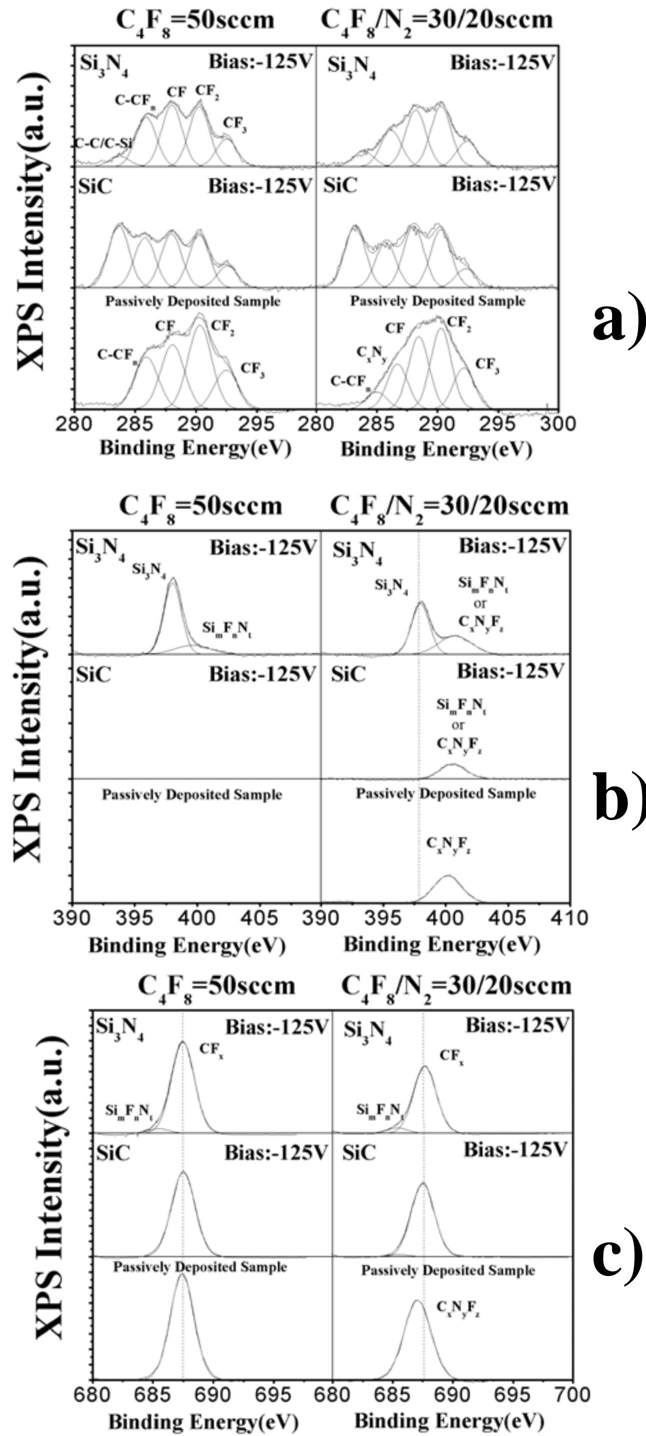

Figure 3.4: *a) C (1s), b) N (1s) and c) F (1s) photoemission spectra of steady-state fluorocarbon films on SiC or Si_3N_4 thin films and passively deposited films produced in C_4F_8 or C_4F_8/N_2 discharge. The spectra were obtained at a collection angle of 90^0.*

2. Surface Analysis: XPS

The stoichiometry of the films formed during passive deposition was significantly changed by nitrogen addition. In Fig. 3.4 a), a comparison of C (1s) photoemission spectra of deposited films in either C_4F_8 or C_4F_8/40%N_2 is shown. Nitrogen was strongly incorporated into the film, identified as C_xN_y, which is responsible for the enhancement of the deposition rate. The fluorocarbon film stoichiometry of etching samples of SiC or Si_3N_4 did not show a significant difference when etched in either C_4F_8 or C_4F_8/N_2. This indicates that C_xN_y is effectively removed from the surface when an RF bias is turned on. Without C_xN_y, in steady state, the fluorocarbon layer thickness does not change as a function of time and the fluorocarbon etching and substrate etching balance fluorocarbon deposition. But if C_xN_y is present in the process, a thicker film may be expected because of a higher deposition rate and the fact that the ion energy flux and the fluorine flux are partly consumed by etching C_xN_y, explaining the drop of the substrate etching rate.

Figure 3.4 b) c) show N (1s) and F (1s) respectively. These data demonstrate that nitrogen also remains on the surface of a partially etched sample in the case of C_4F_8/N_2 discharges. As mentioned above, the amount of nitrogen incorporated into the fluorocarbon film in the etching case is small. It is important to determine where nitrogen exists on the sample surface. In Fig.3.5, N (1s) photoemission spectra of partially etched Si_3N_4 using a C_4F_8/N_2 plasma show low nitrogen incorporation on the surface next to Si-N. Both Si (2p) and F (1s) show additional peak components. The C (1s) spectrum clearly shows the various bonds between carbon and fluorine atoms (C-C/C-Si and C-F_i, i=1,2,3) dominate the spectrum. Carbon may also be bonded to a

small amount of nitrogen. In addition, the smaller peaks could be due to $Si_mF_nN_t$, which exists as an interaction layer between the steady-state fluorocarbon layer and the substrate. XPS analysis performed on other etched materials such as SiC, Si, SiO_2 and OSG also showed that the contribution from carbon atoms bonded to nitrogen was small for in the C (1s) spectra of partially etched samples.

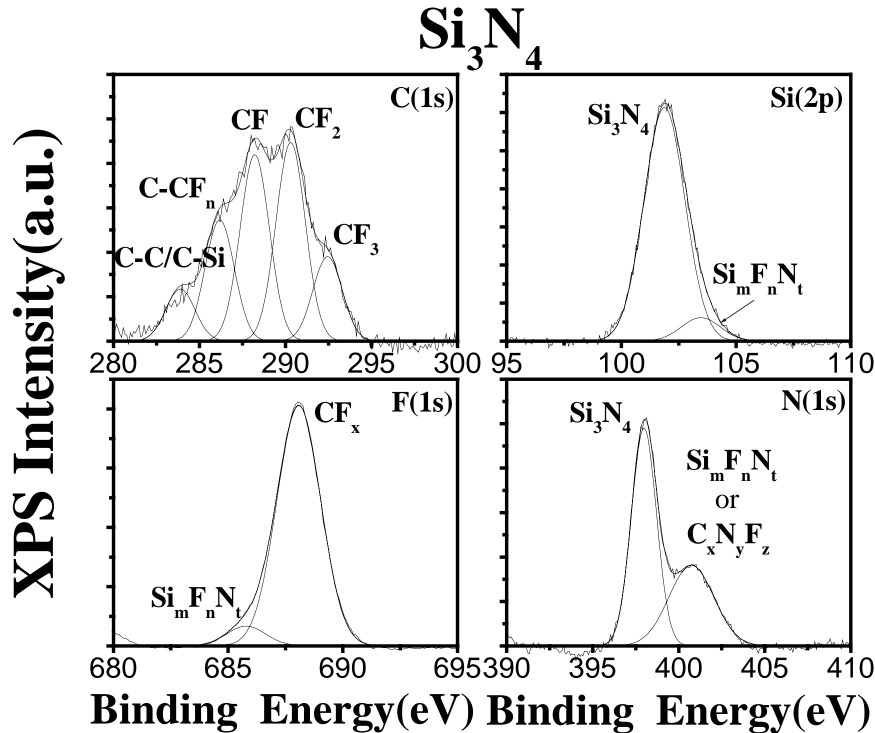

Figure 3.5: *C(1s), Si(2p), F(1s) and N(1s) photoemission spectra of steady state fluorocarbon film on* Si_3N_4 *processed by* C_4F_8/N_2 *plasma.*

Normally, the steady-state fluorocarbon layer thickness is estimated by using Si (2p) or C (1s) spectra, as described in references 3.8, 3.9. Since materials like OSG and SiC contain carbon, it is more accurate to estimate the fluorocarbon layer thickness from Si (2p) spectra instead of C (1s). Furthermore, typical hydrocarbon contamination of the materials and significant stoichiometric differences between

passively deposited samples and etched samples also make it difficult to calculate the fluorocarbon layer thickness using C (1s) spectra. In this work, the fluorocarbon layer thickness was measured from the decrease in Si (2p) intensity by comparison with that of untreated material as follows[3.8]:

$$d_{CF} = -\lambda_{Si(2p)} \ln(I_{si(2p)} / I_o) \sin\theta \qquad (1)$$

Here the escape depth $\lambda_{Si(2p)}$ of Si (2p) photoelectrons in the CF_x layer is assumed to be 3.0 nm, and θ is the photoelectron take-off angle, which is 90^0 in this work; $I_{si(2p)}$ and I_o are the Si(2p) photoemission spectrum intensities of partially etched or untreated samples respectively. Fig.3.6 shows the relationships between steady-state etch rates and the steady-state fluorocarbon film thickness for different materials processed using C_4F_8 or C_4F_8/40%N_2 plasmas. N_2 addition results in a slight increase of the fluorocarbon film thickness, leading to a reduction of etch rate.

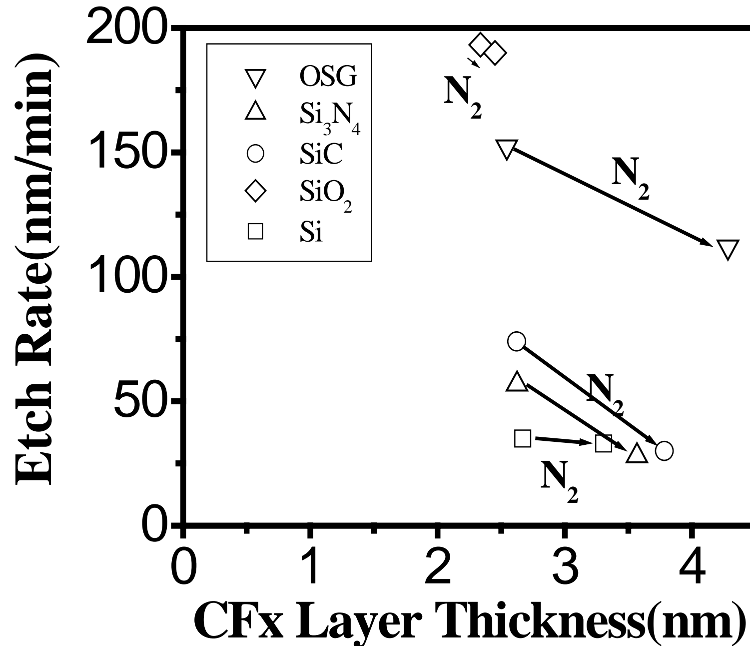

Figure 3.6: *Etch rate as a function of the steady-state FC film thickness of OSG, Si_3N_4, SiC, SiO_2 and Si etched by C_4F_8 or C_4F_8/N_2*

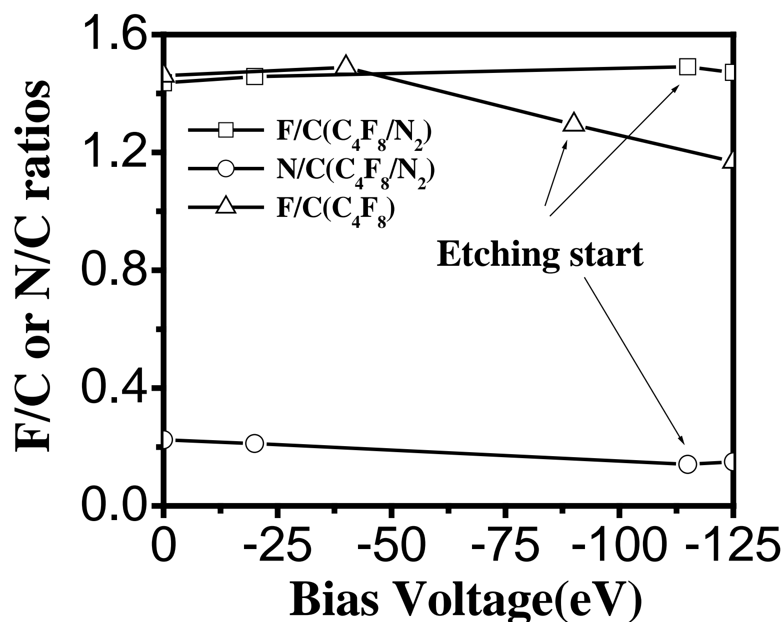

Figure 3.7: *F/C and N/C ratios in the fluorocarbon film on Si sample processed by C_4F_8/N_2 or C_4F_8 discharge as a function of bias voltage.*

Studies performed using different self-bias voltages helped develop the picture of the influence of ion bombardment on surface etching and chemistry further. Fig.3.7 shows the changes in Si surface stoichiometry as a function of the

self-bias voltage. The Si samples were analyzed by XPS after processing in the plasma. N/C and F/C ratios were calculated from XPS data for the $C_4F_8/40\%N_2$ discharge, while for pure C_4F_8 only the F/C ratio was obtained. It is important to note that the F/C ratio presented here is the ratio of the fluorine in the fluorocarbon film to the intensity of C (1s), and fluorine may also exist in the interaction layer for partially etched samples. The fluorine in the fluorocarbon layer can be expressed by the atomic fluorine to carbon ratio (F/C) and is defined as[3.5]

$$F/C = \frac{\sum_{i=1}^{3} iI(C-F_i)}{I(C-Si) + I(C-C) + \sum_{i=1}^{3} iI(C-F_i)} \quad (2)$$

where *I(…)* is the area of the fitted Gaussian function for the chemically shifted contribution indicated between the parentheses. A higher energy threshold is required to change the film stoichiometry for a C_4F_8/40%N_2 discharge than for a pure C_4F_8 discharge. This may indicate that the ion energy is dissipated not only by the etching of the fluorocarbon film but also of C_xN_y species when N_2 is added to C_4F_8. In C_4F_8/40%N_2 discharge, the F/C ratio is enhanced when more C_xN_y is removed as the bias voltage is increased, but drops slightly when substrate etching starts since the fluorine is consumed by the substrate after fluorine has diffused through the fluorocarbon layer[3.8]. For a pure C_4F_8 discharge, ion bombardment does not change the film stoichiometry in the deposition region and F/C decreases quickly when substrate etching occurs, resulting from ion-induced defluorination. The ion energy consumption by C_xN_y removal could be comparable to CF_x etching in the case of C_4F_8/40%N_2 plasma due to the fact that the deposition rate increases nearly twice, therefore the ion-induced defluorination is less and the fluorocarbon film is more fluorine-rich in C_4F_8/40%N_2 than in pure C_4F_8. It is interesting that the N/C ratio remains constant once etching has started, suggesting that nitrogen incorporation in the interaction layer is not a dominant factor of the etching mechanism[3.9].

3.3.2 C_4F_8/Ar/N_2 plasmas:

1. Effect of N_2 addition on etch rates, deposition rates and steady-state fluorocarbon films:

Although C_4F_8/N_2 plasmas exhibit several interesting phenomena, the effects on etching behavior are weak because of the stability of the N_2 molecule. Argon is commonly used for the plasma processing, and can enhance the dissociation and ionization of molecular gases[3.10, 3.11]. A $C_4F_8/Ar/N_2$ mixture was used in the etching of blanket films of OSG, Si_3N_4, SiO_2, SiC and Si, in which the ratio of C_4F_8 to Ar was fixed at 1:9. In our previous studies of Ar addition to C_4F_8 and C_4F_6 we found that for this C_4F_8/Ar ratio the SiO_2/Si etching selectivity and SiO_2 etching rates are optimized[12].

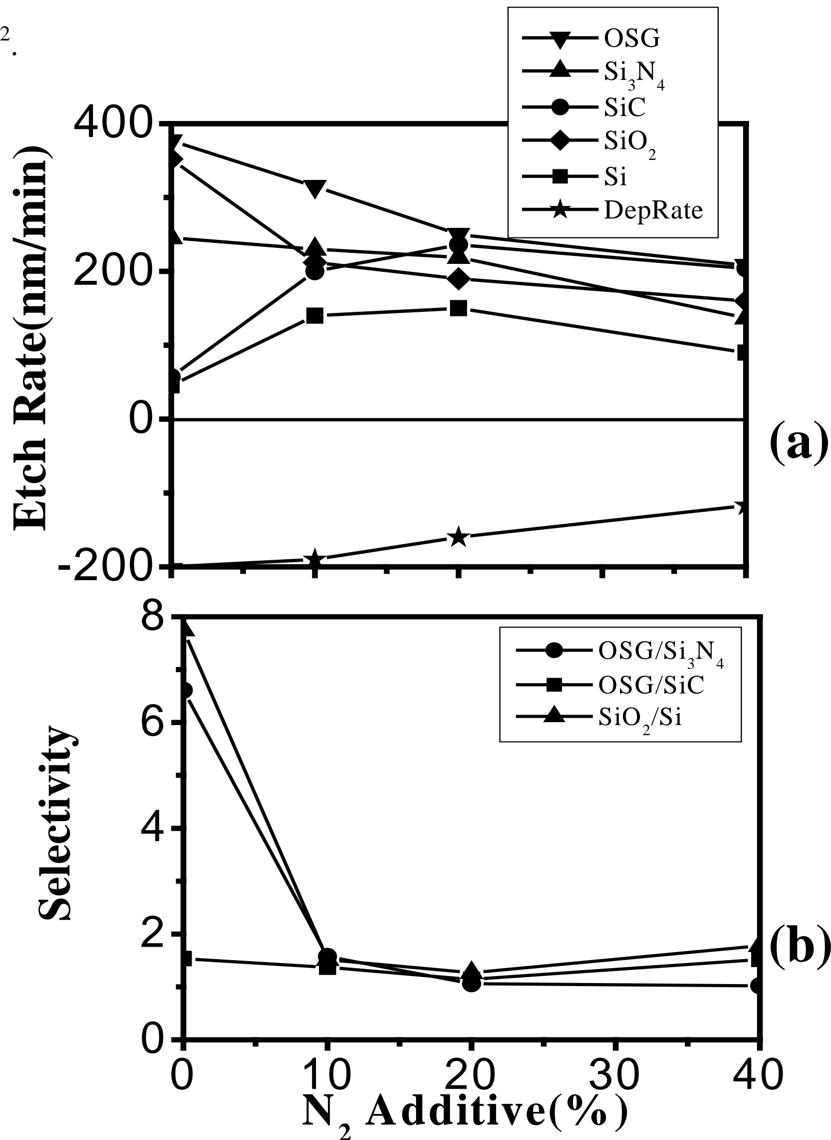

Figure 3.8: *Etch rate & deposition rate a) and selectivity b) as a function of N_2 addition into C_4F_8/90%Ar. Pressure, source power and total gas flow rate were fixed at 10mTorr, 1000w, 50sccm, respectively.*

The measured etch rates and the film deposition rate are plotted in Fig.3.8 as a function of percentage N_2 added. SiC and Si exhibit similar dependence on the percentage N_2 added: the etching rates increase initially, and then saturate at a high concentration of N_2. For OSG, Si_3N_4, and SiO_2 the etching rate always decrease as N_2 is added. A different mechanism is indicated for these materials, and the reduced etching rates may in part be explained by the reduced C_4F_8/Ar flow as the percentage of N_2 increases. The fluorocarbon film deposition rate was reduced when N_2 was added to C_4F_8/Ar owing to the reduced flow of the fluorocarbon gas. Thus a reduced steady-state fluorocarbon film thickness may be expected, especially for Si and SiC.

In order to verify this expectation, a similar experiment as described in the C_4F_8/N_2 plasma section was also performed with spectroscopic ellipsometry: First C_4F_8 /Ar gas mixture was injected to the reactor to form a steady-state fluorocarbon layer. Subsequently nitrogen is added into the reactor. In Fig.3.9, a significant steady-state film reduction was observed after nitrogen had been added, which is opposite to the behavior seen for C_4F_8/N_2. An enhancement of the Si etch rate may be expected from the reduction of the fluorocarbon film thickness, consistent with the observation that the Si and SiC etching rates were increased in C_4F_8/Ar/N_2 plasmas. Since this is not the case for OSG, Si_3N_4, and SiO_2, the steady-state fluorocarbon film thickness is not the dominant factor that controls the etch rate of these material when the etchant flow (C_4F_8/Ar) is very low.

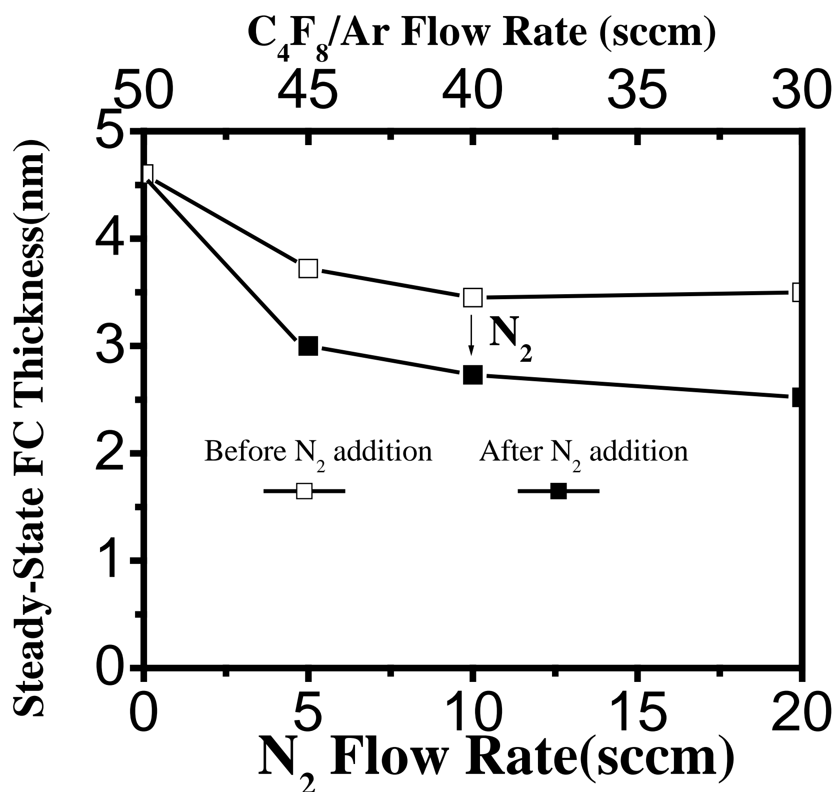

Figure 3.9: *N_2 effect on the steady-state fluorocarbon film thickness on Si sample when added into C_4F_8/Ar. Pressure, source power and total gas flow rate were fixed at 10mTorr, 1000w, 50sccm, respectively.*

2. Surface analysis: XPS

A comparison of surface stoichiometry between C_4F_8/Ar and C_4F_8/Ar/N_2 is shown in Fig.3.10. Nitrogen addition to C_4F_8/Ar exhibits several similar characteristics as adding N_2 to C_4F_8, such as high nitrogen incorporation in the fluorocarbon layer for passively deposited samples and shown in Fig.3.10 a), and nitrogen incorporation beneath the steady-state fluorocarbon layer on etched samples (see Fig.3.10b)). But in the case of nitrogen addition to C_4F_8/Ar the fluorocarbon

layer on partially etched sample is much fluorine-deficient relative to adding nitrogen to C_4F_8 even though the passively deposited fluorocarbon layers are quite similar.

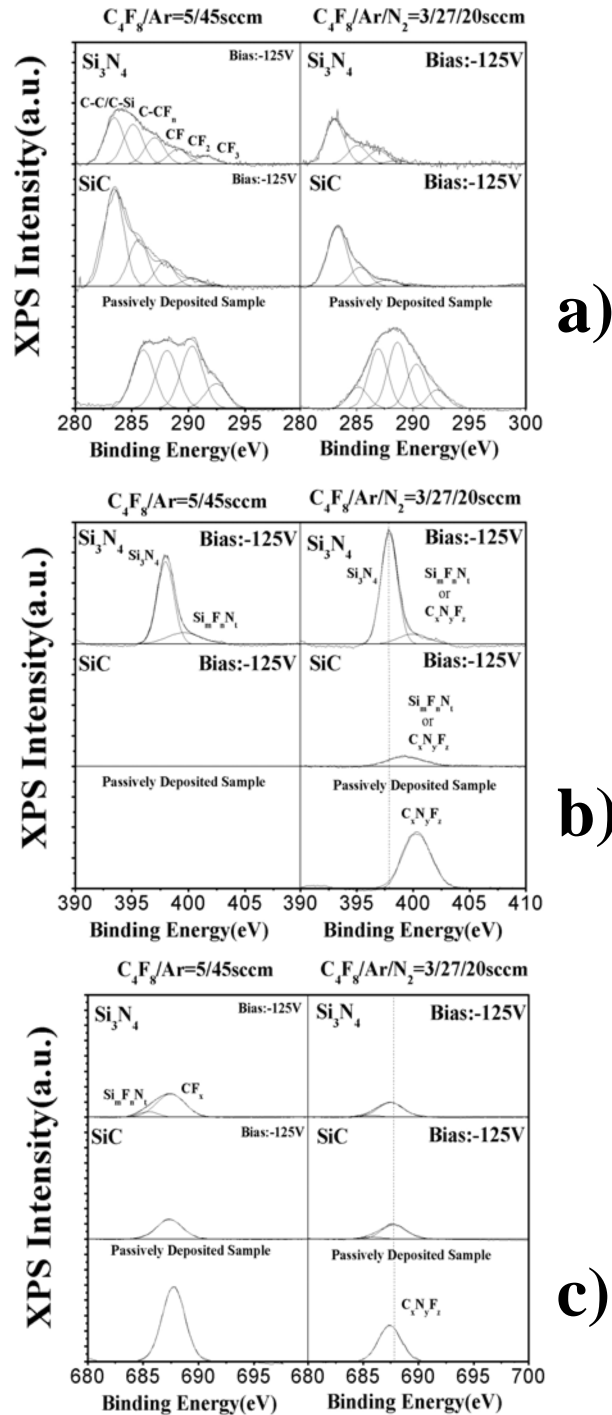

Figure 3.10: *a) C (1s), b) N (1s) and c) F (1s) photoemission spectra of steady-state fluorocarbon films on SiC, Si_3N_4 and passively deposited samples in C_4F_8/Ar or C_4F_8/Ar/N_2 discharge. The spectra were obtained at a collection angle of 90^0.*

The fluorocarbon film thicknesses on different materials were calculated using the method described in the C_4F_8/N_2 section, and are plotted along with the etching rates in Fig.3.11. In this plot, only C_4F_8/Ar and C_4F_8/Ar/40%N_2 data are shown. Adding N_2 resulted in a reduction of the fluorocarbon film thickness, which is different from adding N_2 to pure C_4F_8. This reduction leads to a strong enhancement of etching rates of SiC or Si, as expected. For OSG, SiO_2 and Si_3N_4 etched in the C_4F_8/90%Ar plasmas, the fluorocarbon film thickness is much smaller than for Si and SiC. When adding 40% N_2 to C_4F_8/Ar, a reduction of the film thickness is seen, but this does not have a dominant effect on the SiO_2, OSG or Si_3N_4 etching rates. In C_4F_8/Ar/N_2, C_xN_y was also completely removed from the fluorocarbon film when etching occurred. The reduction of the fluorocarbon film may be caused by the additional interaction with N atoms, and possibly an enhancement of this interaction by Ar^+ bombardment. A more detailed discussion of this will be provided in the Discussion section.

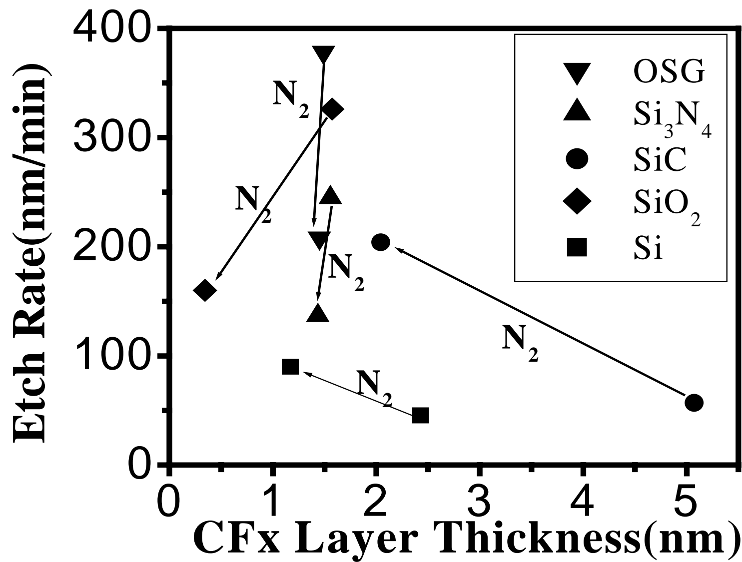

Figure 3.11: *Etch rate as a function of the steady-state FC film thickness of OSG, Si_3N_4, SiC, SiO_2 and Si etched by C_4F_8/Ar or C_4F_8/Ar/N_2*

Figure 3.12 show the RF bias effect on the fluorocarbon layer stoichiometry. For C_4F_8/Ar/N_2, within the deposition region, the F/C ratio was increased significantly due to the carbon removal, and dropped quickly after etching occurred. The N/C ratio remained constant when etching took place, implying that the N/C ratio is not dramatically different for etching or deposition conditions. The F/C ratio is slightly lower in the case of C_4F_8/Ar/N_2 than for C_4F_8/Ar, different from C_4F_8/N_2, indicating nitrogen could also remove fluorine in the fluorocarbon layer.

The comparison of the etch rates of different materials in C_4F_8/Ar/N_2 plasma clearly shows that the chemical composition of the substrate plays an important role during the etching and ultimately results in different steady-state fluorocarbon film thicknesses. For selective etching, SiC is preferred as an etch stop layer material because of the qualitative difference in its etching behavior relative to OSG; OSG and Si_3N_4 behave chemically more similar, which limits the etching selectivity that can be achieved.

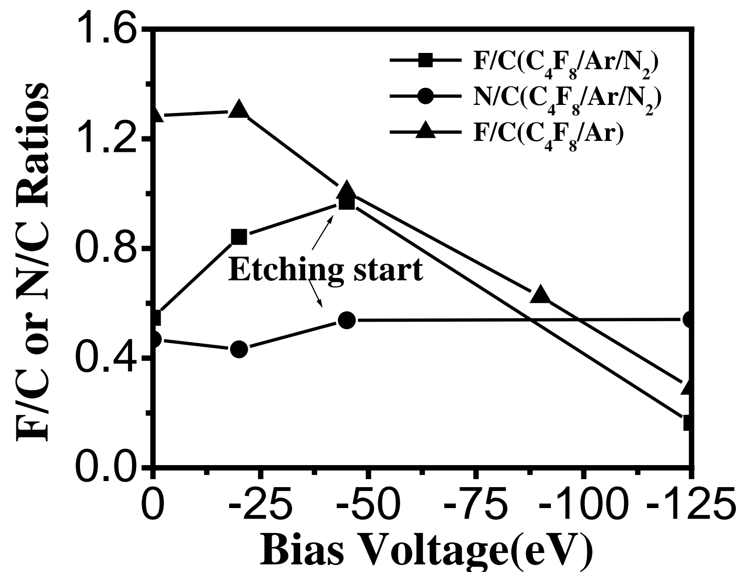

Figure 3.12: *F/C and N/C ratios in the fluorocarbon film on Si sample processed by C_4F_8/Ar/N_2 or C_4F_8/Ar discharge as a function of bias voltage***.**

3.3.3 A comparison of O_2 addition and N_2 addition into C_4F_8 or C_4F_8/Ar plasma:

In order to clarify the mechanism of the effect of N_2 addition, O_2 addition was also investigated since both of them are molecular gases. The difference between nitrogen and oxygen is that N_2 gas is much more stable than O_2. Fig.3.13 shows a comparison of the effects of N_2 and O_2 addition on etching rates. From this figure, it is clear that adding N_2 or O_2 into C_4F_8/Ar (closed symbols) caused similar changes, but for pure C_4F_8 (open symbols), the etch rate was enhanced if O_2 was added, which is different from N_2 addition.

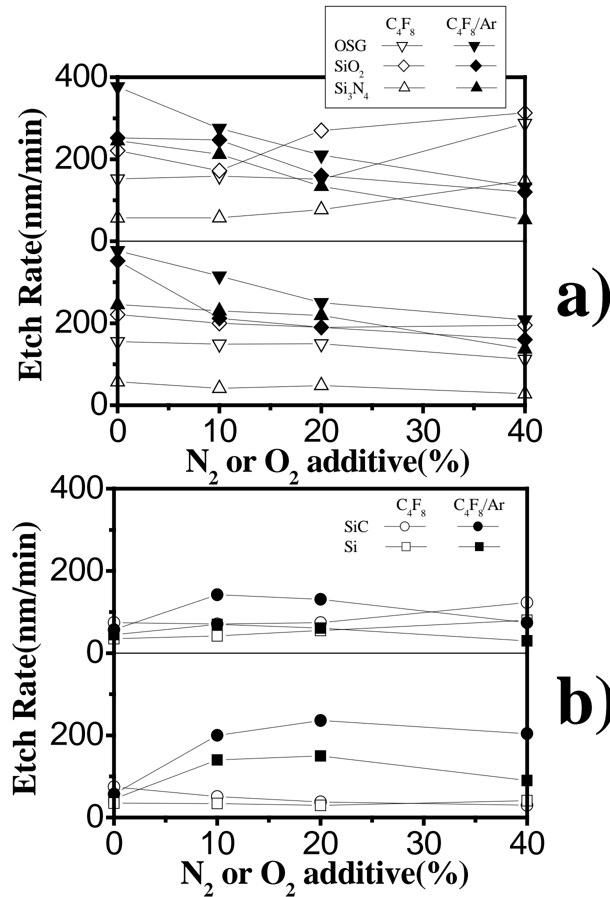

Figure 3.13: *Etch rates of (a) OSG, Si_3N_4& SiO_2 and (b) SiC&Si for O_2 (the up row) and N_2 addition (the down row) into C_4F_8 or C_4F_8/Ar. Pressure, source power self-bias voltage and total gas flow rate were fixed at 10mTorr, 1000w, -125V and 50sccm, respectively.*

The effect on the steady-state fluorocarbon film thickness when adding O_2 is plotted in Fig.3.14. Adding O_2 into C_4F_8 or C_4F_8/Ar resulted in both cases in the reduction of the steady-state fluorocarbon film thickness. The reduction in case of C_4F_8/O_2 leads to the increase in etching rates of all materials, while with the presence of argon, OSG, SiO_2 and Si_3N_4 behave different from SiC or Si. The etching rates of SiC and Si were enhanced when O_2 was added.

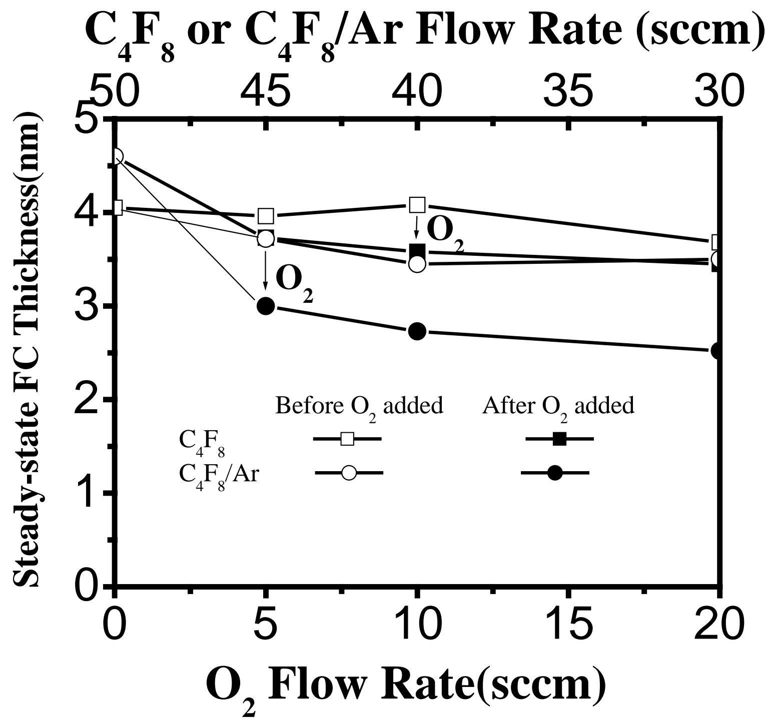

Figure 3.14: *O_2 effect on the steady-state fluorocarbon film thickness on Si sample when added into C_4F_8 or C_4F_8/Ar. Pressure, source power self-bias Voltage and total gas flow rate were fixed at 10mTorr, 1000w, -125V and 50sccm, respectively***.**

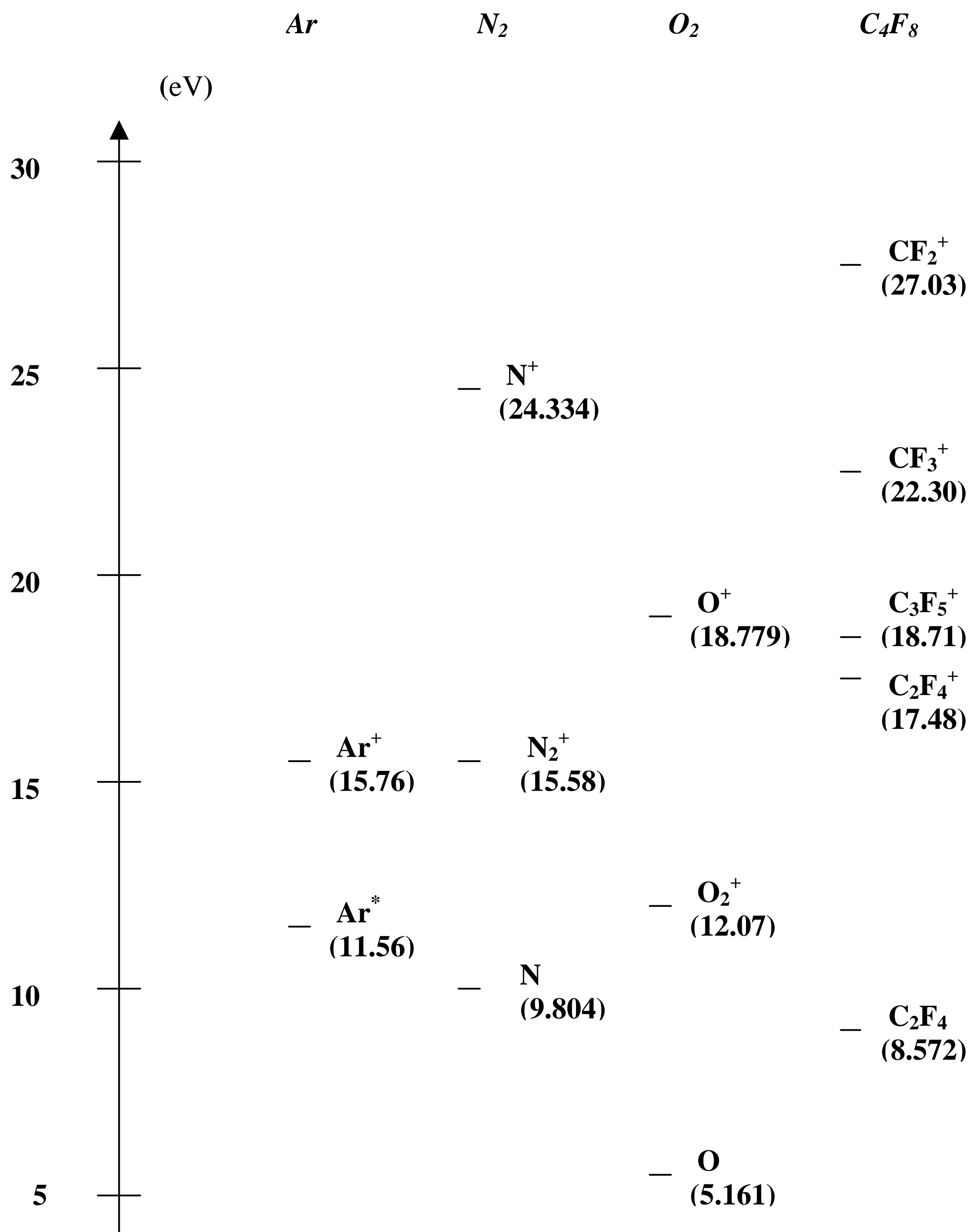

Figure 3.15: *Comparison of important electron impact dissociation or ionization energies (for C_4F_8) and thermal dissociation or ionization energies (for N_2 and O_2). Ar^*: argon metastable. According to measurements by Cosby (J. Chem. Phys., Vol. 98 , No.12, 15 June 1993), the cross section for electron induced dissociation of N2 becomes significant (within the uncertainty of the measurement) above 18eV electron energy.*

3.4 Discussions:

The electron impact or thermal dissociation and ionization energetics[3.13] for related species in N_2, O_2, Ar or C_4F_8 are presented in an energy level diagram in Fig. 3.15. To ionize N_2 or O_2 into atomic ions (N^+ or O^+) [3.9, 3.10], higher electron impact energies are required than for producing molecular ions (N_2^+, or O_2^+). Y.Wang, *et al,* investigated the ion energy distribution in N_2: Ar and O_2: Ar[3.9.]. The intensities of atomic ions are enhanced by Ar addition due to the formation of argon metastables (Ar*), which carry 11.6 eV of energy. For pure O_2 or N_2, O^+ contributes more to the total ion flux than N^+ because of the lower formation energy required for O^+. Ar* does not play a significant role in the dissociation of N_2, since the degree of N_2 dissociation is very small[3.10]. Fig.3.16 shows the effect on ion current densities for N_2 and O_2 addition into fluorocarbon discharge in our system. N_2 or O_2 addition does not change the total ion current density significantly, which basically stays constant when these gases are added to pure C_4F_8. When argon is introduced to C4F8, the ion current density is nearly doubled, but decreases when either O_2 or N_2 are also added.

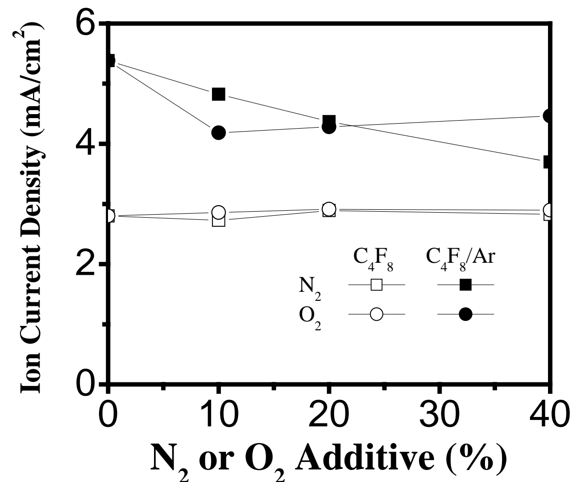

Figure 3.16: *Ion current densities for N_2 and O_2 addition into C_4F_8 or C_4F_8/Ar discharges. Pressure, source power self-bias voltage and total gas flow rate were fixed at 10mTorr, 1000w, -125V and 50sccm, respectively.*

When nitrogen is added into the gas mixture, the following reactions can occur in both the gas phase and the steady-state fluorocarbon layer:

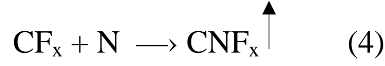

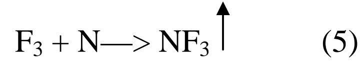

C_xN_y would deposit on the substrate without bias and can be etched if an RF bias is turned on. CNF_x is volatile, so if reaction (4) occurs in the steady-state layer, its thickness would be reduced. The reactions, (4) and (5), are expected to be much more important in $C_4F_8/Ar/N_2$, due to Ar^+ ion bombardment. In addition, the presence of argon metastables increases the intensity of N^+ and may in part be responsible for the fluorine and fluorocarbon radical removal and the reduction of the fluorocarbon thickness. Because of that, the CF_x film becomes carbon rich and thinner after N_2 is added to C_4F_8/Ar, while thicker if N_2 is added to C_4F_8; the F/N ratio (corrected with photoemission crossection) of the passively deposited film is reduced to 1.167 in $C_4F_8/Ar/40\%N_2$ plasma from 6.390 in the case of $C_4F_8/40\%N_2$. For O_2 addition, oxygen also reacts with fluorocarbon radicals to form species that are volatile, and thus reduces the thickness of the fluorocarbon film in both cases.

Based on the previous work done by this group[3.12], fluorocarbon radicals, especially CF_2 are believed to become major etchants for Si_3N_4, SiO_2 and OSG thin films after surface adsorption and subsequent ion-induced reaction with substrate atoms. For SiO_2, OSG, and Si_3N_4 the steady-state fluorocarbon film thickness is small in C_4F_8/Ar and likely not rate limiting. Reducing the film thickness, while at the same time reducing the supply of the etchant (lower C_4F_8/Ar flow) results in a lower

etching rate overall. For SiC and Si substrate the fluorocarbon film thickness is large and fluorine diffuses through the steady-state layer and reacts with the substrate[3.8]. In that case, fluorocarbon film thickness dominates the etching. The etching rates of SiC or Si increase due to the reduction of the fluorocarbon film thickness in $C_4F_8/Ar/N_2$ or $C_4F_8/Ar/O_2$. Fig.3.8 shows that the etch rate ratio of SiO_2 to Si dropped from 7.75 (C_4F_8/Ar) to 1.78 ($C_4F_8/Ar/40\%N_2$). Without N_2 addition for $C_4F_8/90\%Ar$, the SiO_2 and OSG etching rates are nearly 400 nm/min, whereas the Si and SiC etching rates are almost 50 nm/min. The SiO_2 and OSG etching rate are starved for etchant, but not the Si and SiC etching rate. As N_2 is added, the SiO_2 and OSG etching rate decrease, and the Si and SiC etching rate increase (fluorocarbon film reduction). The OSG etching rate always remains the highest and for 20% and 40% N_2 addition is approached by the SiC etching rate.

3.5 Conclusions:

Although argon has frequently been considered an inert gas in low pressure discharges, it can activate molecular gases like nitrogen and oxygen when added to gas mixtures containing a large proportion of Ar, e.g. fluorocarbon/argon containing discharges. The presence of argon metastables can affect the composition of ionic and neutral species in the gas phase of the plasma. A change in the discharge electron temperature due to the high electron impact energy thresholds of Ar relative to fluorocarbon gases can also produce this effect.

For OSG, SiO_2, Si_3N_4, SiC and Si, deposition of fluorocarbon films followed by ion-induced activation which defluorinates the fluorocarbon films and drives a

reaction with the substrate is important. The steady-state film thickness will reflect differences in substrate chemistry, e.g. Si, SiC exhibit no consumption rate of the fluorocarbon film and therefore the steady-state fluorocarbon film thickness is greater than for OSG, Si_3N_4 and SiO_2 for which the consumption rates of fluorocarbon film are fairly high. A change of the steady-state fluorocarbon film thickness caused by the addition of N_2 to C_4F_8/Ar gas mixture will have a small effect, for OSG, SiO_2, and Si_3N_4, which is more than over-compensated by the simultaneously lowered C_4F_8/Ar etchant flow rate. For SiC and Si, N_2 addition produces thinner fluorocarbon surface layers and increases the etching rate. For selective etching, SiC is preferred as an etch stop layer material over Si_3N_4 because of its different chemical behavior due to its composition relative to OSG.

ACKNOWLEDGEMENTS

Financial support of this work by the Semiconductor Research Corporation is gratefully acknowledged. The authors also would like to thank Texas Instruments, Inc., Dallas, TX, USA for support and supply of the thin film materials used in this work. We also thank W.L.Morgan, X.Li, M.Fukasawa, L.Ling for assistance and helpful discussions.

Chapter 4: Plasma-Surface Interactions of Nanoporous Silica During Plasma-based Pattern Transfer Using C_4F_8 and C_4F_8/Ar Gas Mixtures

J. Vac. Sci. Technol. A 23, 151 (2005)

Xuefeng Hua, Christian Stolz, G. S. Oehrlein, P. Lazzeri, N. Coghe and M. Anderle,

C. K. Inoki, T. S. Kuan and P. Jiang

ABSTRACT

We have investigated plasma surface interactions of nanoporous silica (NPS) films with porosities up to 50%, and SiO_2 with C_4F_8/Ar discharges used for plasma etching. The pore size was about 2~3nm for all films. In highly polymerizing plasmas (e.g., pure C_4F_8 discharges), the porous structure of NPS material favors surface polymerization over etching and porosity-corrected etching rates (*CER*) were suppressed and lower than SiO_2 etching rate for the same conditions. The etching rates of NPS were dramatically enhanced in ion rich discharges (e.g. C_4F_8/90% Ar) and the *CER* in this case is greater than the SiO_2 etching rate. Both X-ray Photoelectron Spectroscopy (XPS) and Static Secondary Ion Mass Spectroscopy (Static SIMS) show that fairly thick (~2-3 nm) fluorocarbon layers exist on the NPS surface during C_4F_8 etching. This layer blocks the direct interaction of ions with the NPS surface and results in a low etching rate. For C_4F_8/90% Ar discharges, little fluorocarbon coverage is observed for NPS surfaces and the direct ion surface interaction is significantly enhanced, explaining the enhancement of *CER*. We can deduce from analysis of angular resolved XPS data that the surface of NPS materials

and SiO_2 remain smooth during C_4F_8 etching. For C_4F_8/90% Ar etching, the NPS surfaces became rough. The surface roughening is due to angle-dependent ion etching effects. These surface models were directly verified by the transmission electron microscopy (TEM). Depth profiling study of NPS partially etched using C_4F_8 or C_4F_8/90% Ar discharges using Dynamic SIMS indicates that the plasma induced modification of NPS was enhanced significantly compared with SiO_2 due to the porous structure, which allows the plasma attack of the sub-surface region. The modified layer thickness is related to the overall porosity and dramatically increases for NPS with an overall porosity of 50%. The distinct etching behavior of high porosity NPS (~50%) in fluorocarbon-based discharges relative to NPS material with lower overall porosity is possibly due to interconnected pores, which allow plasma species to more easily penetrate into the subsurface region.

4.1 INTRODUCTION

As microelectronic device sizes shrinks, low dielectric constant (low *k*) or ultra-low dielectric constant material are being investigated for integration into the backend of the line (BEOL) processing to reduce the parasitic capacitance between adjacent interconnect lines. The next generation of interlayer dielectric materials for microelectronics must have an ultra-low dielectric constant of less than 2.0 to meet the National Technology Roadmap for Semiconductors.[4.1] The entire semiconductor industry is currently poised at an important junction as device performance dictates a transition from vapor-deposited silicon dioxide (having a dielectric constant, $k = 4.0$), and organosilicate glass ($k<3$), to a material with a dielectric constant less than 2.0. Unfortunately, there are few known materials with dielectric constants this low, and none are compatible with semiconductor manufacturing requirements. Nanoporous materials are compelling candidates for the future microelectronic and optoelectronic applications requiring ultra-low dielectric constant and /or refractive indices, respectively. The presence of the pores lowers the dielectric constant of the nanoporous film as the dielectric constant of air is 1.0. One of the nice features of a porous material is the ability to control porosity and hence tailor the performance of the material to meet the requirements of successive generations of future integrated circuits.

Recently there has been a great deal of activity focused on NPS characterization [4.2-4.6], and NPS processing [4.7-4.9]. There are still many unresolved issues related to plasma etching of NPS materials. Standaert and co-workers[4.7]investigated fluorocarbon plasma etching of NPS (xerogel) of varying

porosity using an inductively coupled plasma source, and compared their results with SiO_2. The etching rates of NPS materials were found to be strongly dependent on plasma polymerization. The simulation[4.8] of their data based on the integration of a Monte-Carlo Feature Profile Model and the Hybrid Plasma Equipment Model revealed that the ratio between the steady state polymer thickness L and pore radius r is a critical parameter for the mass corrected etching rate comparison between NPS and SiO_2. The porous structure of the NPS material not only increases the plasma surface interaction area in the near surface region, but also enhances the transport in the bulk material and thus increases the importance of subsurface reactions.

In the present work, we have studied etching characteristics of MSQ based NPS material in fluorocarbon plasmas. In addition, we employed various techniques to characterize the properties of NPS material before/after plasma etching in an effort to improve our knowledge of plasma-surface processes for fluorocarbon plasmas interacting with NPS surfaces.

4.2 EXPERIMENTAL SETUP AND PROCEDURES

The nanoporous materials used in this work are porous methyl silsesquioxane (MSQ) thin films with a dielectric constant in the range 1.90~2.6, pore size on the order of 2~3 nm, and overall porosity of up to ~50%. The porosity is estimated using Looyenga's effective medium approximation using the dielectric constant. In this work, we assume that the porosity of conventional solid material SiO_2 is 0%. In most of the experiments the thickness of untreated NPS films is 400 nm, except for samples used for depth profiling work. The pores (nano-cavities) of NPS material are

created by the removal of the organic carbon groups, a sacrificial phase, from the matrix. The location of the residual content of carbon groups is important in terms of compatibilities with plasma processes. For instance, O_2 plasmas used for resist mask stripping strongly modify the properties of Organosilicate Glass (OSG) by the depletion of carbon groups[4.10]. The untreated NPS films were analyzed by XPS. The intensities corrected for the photoelectron emission cross sections are shown in Fig. 4.1. The C 1s background is independent of the porosity of NPS (except 0% porosity that is SiO_2), implying that the methyl carbon groups are related to the matrix instead of the pores. The lower O 1s intensity of NPS also confirms this fact. These measurements indicate that the present NPS materials are SiO_2 containing methyl groups and pores, rather than SiO_2 with pores.

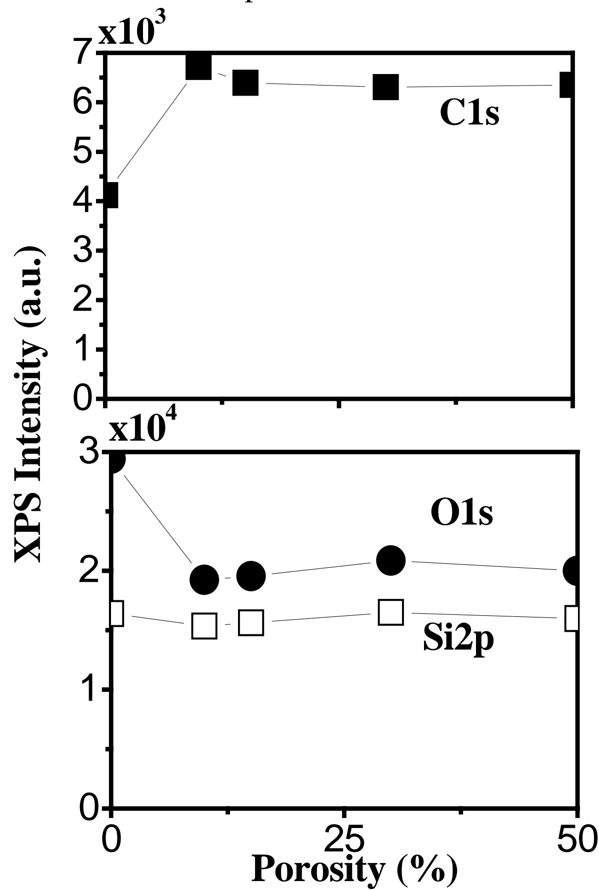

Figure 4.1: *Integrated photoemission intensity C1s (a), Si2p and O1s (b) from untreated NPS films.*

Huang *et al* [4.7] studied pore size distribution of nanoporous methyl silsesquioxane films over a porosity range of 5~50% with small angle x-ray scattering (SAXS) measurements. They found that the average pore size increased with porosity. The sacrificial organic component (porogen) in those porous MSQ films is removed by thermolysis. The pore formation process in the films used for the present work is different and the deposition technique of these films is still proprietary. Both nitrogen adsorption-desorption method and TEM results (see TEM section) indicate that the average pore size of 30% NPS used in this work is of order of 2~3nm, which is consistent with the measurement done by Das *et al*[4.11] with ellipsometry porosimetry method but much smaller than the one in Huang's work for NPS materials with the same porosity. The pore size distribution of the present NPS material is narrow as compared with distributions reported by Huang[4.7]. We assume that the average pore size of the films used in this work is similar over the whole porosity range. In high porosity (~50%) NPS, a great number of pores are likely to be connected. For instance, Wu *et al*[4.3] determined that (22.1$\pm$0.5%) of the pores have connective paths to the surface in (53%$\pm$1)% porosity NPS. Pore interconnectivity may be a very important parameter governing the NPS etching mechanism in fluorocarbon plasma, since sub-surface reaction can occur through the connective paths and the modification induced by the plasma may penetrate much deeper than the plasma-substrate interface. However, the pore morphology of NPS could be modified as a result of fluorocarbon plasma exposure, i.e. the pore size, porosity, and pore shape may be different from those of untreated NPS after the interaction with the plasma.

Plasma processing of NPS was performed in an inductively coupled plasma reactor described previously[4.7]. The discharges were maintained at 10 mTorr, 50 sccm gas flow and 1000 W source power (13.56 MHz) for C_4F_8/Ar discharges. The self-bias voltage of the substrate was fixed at –125 V and was produced using an additional RF bias power supply (13.56 MHz). The temperature of the substrate was maintained at 10^0C during the processing. Samples of approximately 2cm$\times$ 2cm in size were positioned at the center of the electrode. Etch rates were measured using *in situ* single wavelength (632.8 nm) ellipsometry. The etch time varied with conditions and in most cases was much greater than the time required to achieve a constant etching rate. This was determined by *in situ* ellipsometry and is used as the criterion for steady-state in this work. X-ray photoelectron spectroscopy (XPS) analysis of partially processed specimens was performed after transfer under vacuum to a ultra-high vacuum chamber at 90°, 30° and 20° electron take-off angles using a nonmonochromatized Mg K-alpha X-ray source (1253.6 eV). The pass energy of the hemispherical analyzer was fixed at 20 eV.

Fluorocarbon based plasmas have been used in the semiconductor industry for high fidelity pattern transfer in integrated circuit fabrication processes, and have been widely studied. A recent review with numerous references has been provided by Schaepkens *et al*[4.12].

For the present work we employed both C_4F_8 and C_4F_8/90% Ar discharges. We summarize key data of our previous studies[4.13-4.15] of C_4F_8 or C_4F_8/90% Ar plasmas in Table 4.1, which provides an understanding of the change of plasma properties when a high percentage of Ar is added to C_4F_8. The absolute density of the dominant

neutral species, CF_2, was measured using a infrared laser absorption spectroscopy (IRLAS). A Langmuir probe was used to obtain the ion current data and the probe tip was biased at –100V to prevent FC deposition on the metal surface and collect the ions in the ion saturation regime. Ion compositional analysis was performed using a combined ion energy analyzer-mass spectrometer. The results of these characterization studies clearly show that C_4F_8 and C_4F_8/90%Ar represent neutral-rich or ion rich plasma processing regimes. These measurements[4.13-4.15] were performed in an ICP reactor that was very similar to the one used for the present study, except for the size of the process chamber. It was impractical to reproduce these extensive experiments in the present processing chamber. However, etching experiments performed in both reactors showed identical trends as a function of operating parameters. In addition, we measured certain key parameters of C_4F_8/Ar plasma surface interactions, e.g. FC deposition rates, the ion current density, thin film etching rates, and selfbias voltage as a function of %Ar added to C_4F_8[4.16]. We observed nearly identical behavior in these experiments when argon was added to C_4F_8 as measured in the more completely characterized ICP reactor. Our data for the present reactor also showed directly that C_4F_8/90%Ar and C_4F_8 discharges represent neutral-rich and ion-rich processing conditions. Our previous ion energy distribution studies revealed that the plasma potential in these FC based discharges varies from 10V to 20V. The energy of the ions bombarding the substrate is determined by the difference between plasma potential and self-bias voltage forming at the wafer. The latter was controlled to be –125V for all of our experiments, and basically controls the ion energy for the conditions used in this work.

CF_2 Flux (mL/s)		**Total Ion Flux (mL/s)**		**Ion Composition**	
C_4F_8	C_4F_8/ 90% Ar	C_4F_8	C_4F_8/ 90% Ar	C_4F_8	C_4F_8/ 90% Ar
>4000	<500	~130	~700	100% $C_xF_y^+$	>70% Ar^+

Table 4.1: *Summary of ionic or dominant neutral fluxes and surface chemistry information during processing conditions: C_4F_8 (ion-limited) or C_4F_8/90%Ar (neutral-limited) with a floating substrate or with a substrate biased –125V.*

Time of Flight Secondary Ion Mass Spectroscopy (ToF-SIMS) was used to study the modifications of the NPS films induced by FC plasma processes. To this end, static SIMS (SSIMS) and dynamic SIMS (DSIMS) investigations were performed to characterize the samples surface and the film bulk. In particular, three SSIMS spectra per sample were collected for both detection polarities, using a bunched 11 keV Ga^+ as primary beam and probing an area of 150 µm x 150 µm in size. The mass resolution in these conditions was higher than 5500 at $^{28}Si^+$ and $^{16}O^-$. For evaluation of surface features, Principal Component Analysis (PCA)[4.17] of SSIMS spectra was performed. In addition, DSIMS depth profiles were acquired by using a 2 keV Cs^+ as sputtering beam and detecting negative SI. The mass resolution was about 5000 at $^{16}O^-$. The sputtered/analyzed area ratio was set to 10 to minimize crater edge effects. The sputtering crater depth was measured using a stylus profilometer. Both SSIMS and DSIMS measurements required to compensate for charge effects by means of an electron gun.

4.3 RESULTS AND DISCUSSIONS:

4.3.1 ETCHING RESULTS IN DIFFERENT DISCHARGES

Pure Ar Discharges: Figure 4.2 (a) shows etch rates of blanket NPS films in pure Ar plasmas maintained at 10mTorr, 600W source power and –125V self bias voltage. The sputtering rates of NPS increase with the porosity, which is expected because less material per unit thickness needs to be removed as the porosity increases. To account for this, a porosity-corrected etch rate (*CER*) is defined

$$CER = (1 - \Pi) ER , \quad (1)$$

where *ER* is the etch rate and Π is the porosity of the NPS film (e.g. $\Pi = 0.5$ for 50% porosity). The slight enhancement of the *CER* indicates differences in plasma/surface interaction mechanisms during physical sputtering of NPS in Ar plasmas relative to SiO_2.

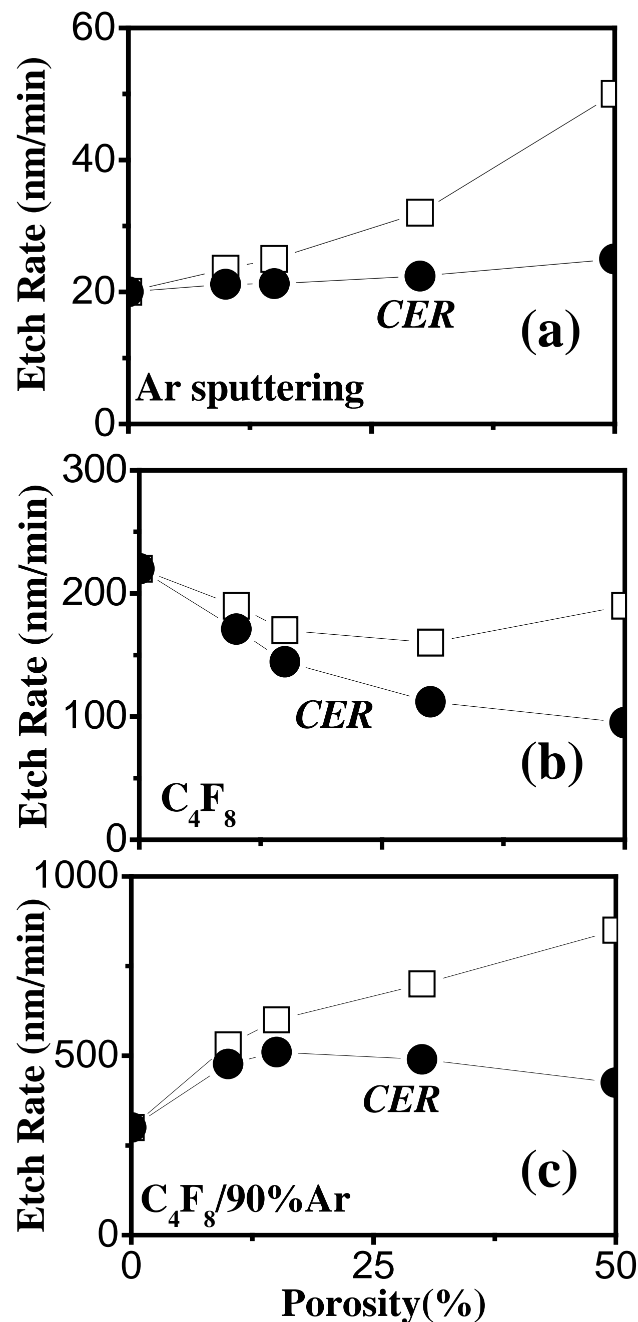

Figure 4.2: *NPS materials processed in different discharges: (a) Ar sputtering (600 W); (b) C_4F_8 (1000 W); (c) C_4F_8/90%Ar (1000 W). Pressure and total gas flow rate were fixed at 10 mTorr, 50 sccm, respectively. Self-bias voltage was set at –125 V.*

For pure argon plasmas, the films are removed by Ar^+ physical sputtering processes. Ions gain energy from the acceleration in the sheath and the direction of

the acceleration is perpendicular to the substrate surface. Since the ion temperature in the gas phase is on the order of ~0.1 eV for the conditions investigated and the self-bias voltage is set at –125 V, after the acceleration in the sheath the deviation of ion incidence angle from normal to the horizontal surface is negligible. For NPS, surface elements of nanoscale pores are inclined locally, and both the ion incidence angle and ion energy flux per unit surface area varies at the nano-meter scale for NPS. Due to the kinematics of momentum transfer to atoms in the surface layer, the etch yield in the physical sputtering processes depends on the ion incident angle and most materials exhibit a maximum at ~45°-60° [4.18]. Higher porosity NPS has more pores per unit surface area exposed to the plasma at the plasma/surface interface. Therefore, the average ion incidence angle increases with porosity, getting closer to the optimum angle. This mechanism can explain the slight enhancement of the *CER* observed in Fig. 4.2(a) as a function of overall porosity.

Pure C_4F_8 discharges: Blanket SiO_2 and NPS films were etched in C_4F_8 discharges produced at 10 mTorr, 1000 W source power and –125 V self bias voltage. The steady state etch rate initially decreases with porosity up to 30% and then increases because of lower mass density (Fig.4.2 (b)). It is surprising that the NPS etch rate drops below the SiO_2 (0% porosity) etch rate and that the *CER* decreases with porosity. This result implies that porosity and pore morphology can dominate the etching mechanism of NPS in fluorocarbon plasmas. The lower mass density of NPS does not necessarily result in a higher etch rate relative to SiO_2. Standaert *et al*[7] studied xerogel etching with C_4F_8 discharges produced at 1400 W and also found the

CER of high porosity xerogel (58%, 69%) to be lower than the SiO_2 etch rate while 30% NPS showed a similar *CER* as SiO_2. We explain this difference by the different ion/neutral ratio of these discharges, which is mirrored in the deposition rate measured for floating samples. At a source power of 1000 W, the FC film deposition rate is 380 nm/min in the present case and higher than the 1400 W case (330 nm/min) used by Standaert *et al*[4.7]. This implies that the polymerization characterization of the feed gas has a strong influence on the etching behavior of the NPS. The NPS etch rate drops off with respect to the SiO_2 etch rate in highly polymerizing discharges which are characterized by a high neutral/ion ratio.

In fluorocarbon plasma etching, it is well known that a steady state fluorocarbon film exists on the substrate surface, e.g. SiO_2, Si_3N_4 or Si[4.19]. If this film is thick (larger than ~1 nm, a typical ion penetration depth for ions with an energy of the order of ~100 eV), it prevents a large proportion of ions to directly impact the substrate, required for both physical sputtering and ion-enhanced substrate etching. Previous work in our group revealed that the steady-state fluorocarbon film thickness is about 1.7 nm for a SiO_2 surface during C_4F_8 plasma etching and the arrival of atomic fluorine through the fluorocarbon film may be of overriding importance for substrate etching[4.20-4.22]. For these conditions, ions impinge on the FC layer and the ion-induced defluorination can provide the dominant etchant source for the substrate rather than fluorine directly from the gas phase. The ion-induced defluorination is related to ion-induced molecular dissociation of the steady-state surface layer and ion fragmentation, which rely on the ion flux and ion energy. The average ion energy flux per unit area for NPS is lower than for SiO_2 because the pores of NPS increase

the effective surface area. Diffusion of FC material into pores/sub-surface pores of the NPS reduces the ion-induced defluorination, and the rate of FC conversion to the substrate is consequently reduced (see XPS section). Therefore, the *CER* is expected to decrease with porosity.

C_4F_8/90%Ar discharges: It is important to note that in pure C_4F_8 discharges the fluorocarbon polymerization rate is extremely high and the FC coverage on the NPS surface eliminates the enhancement of etching rate caused by the optimum ion incident angle. For low polymerization conditions, e.g. C_4F_8/90%Ar discharges, the surface FC coverage decreases and the likelihood of direct ion-surface interactions is enhanced. Fluorocarbon species can be dissociated and ion bombardment can drive species into the substrate by a diffusion-like process. For C_4F_8/90%Ar discharges the larger surface area of NPS can also lead to lower effective fluorocarbon coverage since in this discharge the FC species arrival rate is low (as compared with C_4F_8 discharges). The FC dissociation and ion-induced reaction with the substrate becomes easier. NPS is expected to have a higher *CER* in this discharge. The etch rate results shown in Fig. 4.2 (c) are consistent with this expectation: The *CER* of NPS is higher than the SiO_2 ER and the etching rates of NPS increase rapidly with porosity for high ion/neutral ratio C_4F_8/90%Ar discharges. For high porosity NPS (50%), the *CER* becomes lower than for low porosity materials. One possible explanation is that the pores are likely interconnected when the porosity is near 50%, which would strongly influence the etching mechanism, e.g. by enabling rapid sub-surface diffusion of FC species.

TIME TO REACH THE STEADY STATE: To evaluate the influence of overall porosity on the time required for the etching rate to reach a steady state value, NPS materials were etched in C_4F_8/90% Ar with a source power of 500 W. The FC polymerization rate in this discharge is relatively high as compared with C_4F_8/90% Ar with a source power 1000 W. The etching rate as a function of time is shown in Fig. 4.3. Figure 4.3 shows that it takes a longer time to establish steady-state etching conditions for NPS materials than for SiO_2. For 50% porosity NPS, it takes of the order of 1min to reach a steady state etch rate value and the etch rate at that time is lower than values measured initially. For SiO_2 or low porosity material, the etch rate increases with time. This difference may be explained by the fact that for 50% NPS, a large amount of pores are likely connected. This enables an interaction of the plasma with deeper lying pores. This process is slower, than the interaction of plasma with the surface only. For 15% NPS we expect the pores to be essentially isolated, restricting the plasma-NPS surface interaction to the surface region. It appears from Fig. 4.3 that the time to reach steady-state etching conditions is similar to that seen for SiO_2.

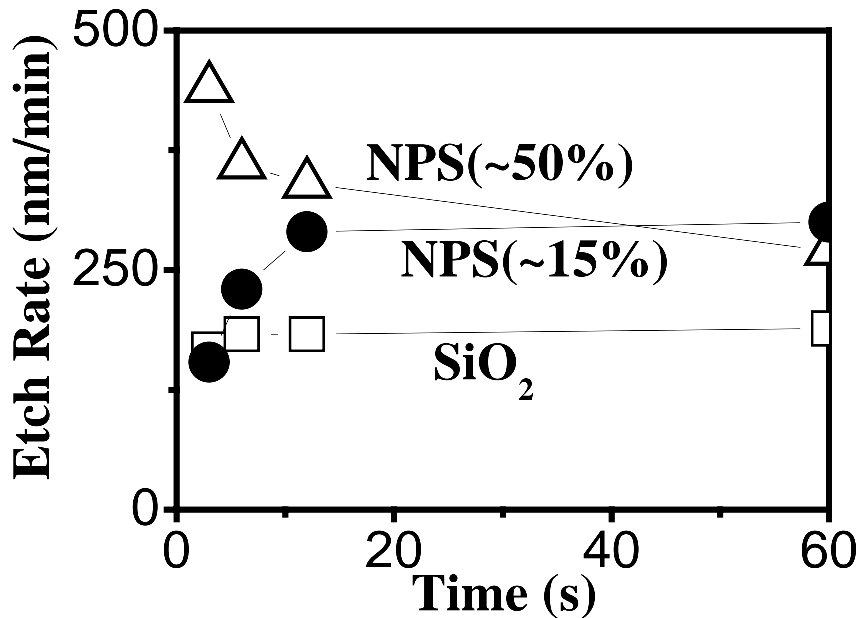

Figure 4.3: *Time resolved etching of NPS. The discharges are maintained at at 10 mTorr and 500 W source power. The self-bias voltage was set at –125 V.*

PROFILE ETCHING: The NPS films were patterned with 0.6 µm deep ultraviolet photoresist and 75 nm of organic antireflection coating (ARC) with Si_3N_4 as an etch stop layer (ESL). The pattern was transferred using a C_4F_8/90% Ar discharge maintained at 10 mTorr and 1000 W source power and the process time was 2 minutes. The self-bias voltage was set at –125 V. During the first 30 s of the process C_2F_6/90% Ar (10 mTorr, 600 W source power, –125 V self-bias voltage) was used to open the ARC layer. The NPS was 100% over etched. Figure 4.4(a) shows cross-sectional scanning electron micrographs (SEM) of etched trenches. To minimize the modification to the NPS caused by the electron beam exposure, 2kV electron beam was used. Even though the etch process is nonoptimized, it offers satisfactory profile control. Because of the long overetch, the Si_3N_4 etch stop layer was attacked. After

NPS etching, an O_2 plasma maintained at 100 mTorr and 400 W source power was used to remove the residual photoresist mask (for 2 min process time). As a result of the exposure to the O_2 plasma, the NPS film compressed both vertically and horizontally. The vertical shrinkage may be caused by the removal of residual carbon group from the SiO_2. During etching of the NPS, a fluorocarbon film exists on the sidewall and this is expected to enhance the horizontal shrinkage of NPS film. After O_2 plasma exposure, deep etching of the Si_3N_4 is also apparent, probably caused by the residual FC film formed during the fluorocarbon etching.

Figure 4.4 shows very clearly that the NPS/Si_3N_4 etching selectivity is not ideal for NPS profile etching, indicating that Si_3N_4 may not be a good candidate for ESL in NPS etching. It is known that the etching mechanism for SiC or SiCN etching in C_4F_8 based plasma is different from SiO_2-like materials due to the chemical composition, but that the Si_3N_4 etching behavior is similar to that of SiO_2-like materials[4.21]. A comparison of the NPS/SiCN and NPS/Si_3N_4 etching rate ratios is shown in Figure 4.5 for both C_4F_8 (a) and C_4F_8/90% Ar (b) discharges. The data strongly suggest that SiCN is a better candidate for an etch stop layer material and that low FC polymerization discharges are preferred for profile etching. NPS profile etching with SiCN as the ESL and improved conditions for post plasma clean will be discussed in a separate publication.

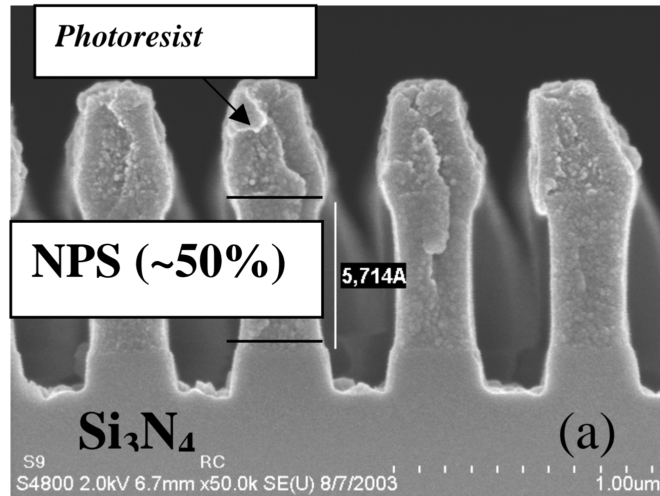

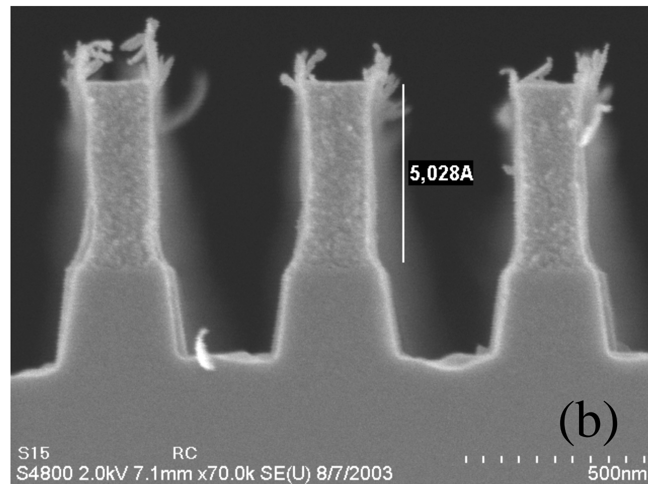

Figure 4.4: (a) Trenches in 50% NPS film using a C_4F_8/90% Ar discharge maintained at 10 mTorr and 1000 W source power. The self-bias voltage was set at –125 V. (b) SEM image for Patterned film (from a) after O_2 plasma cleaning.

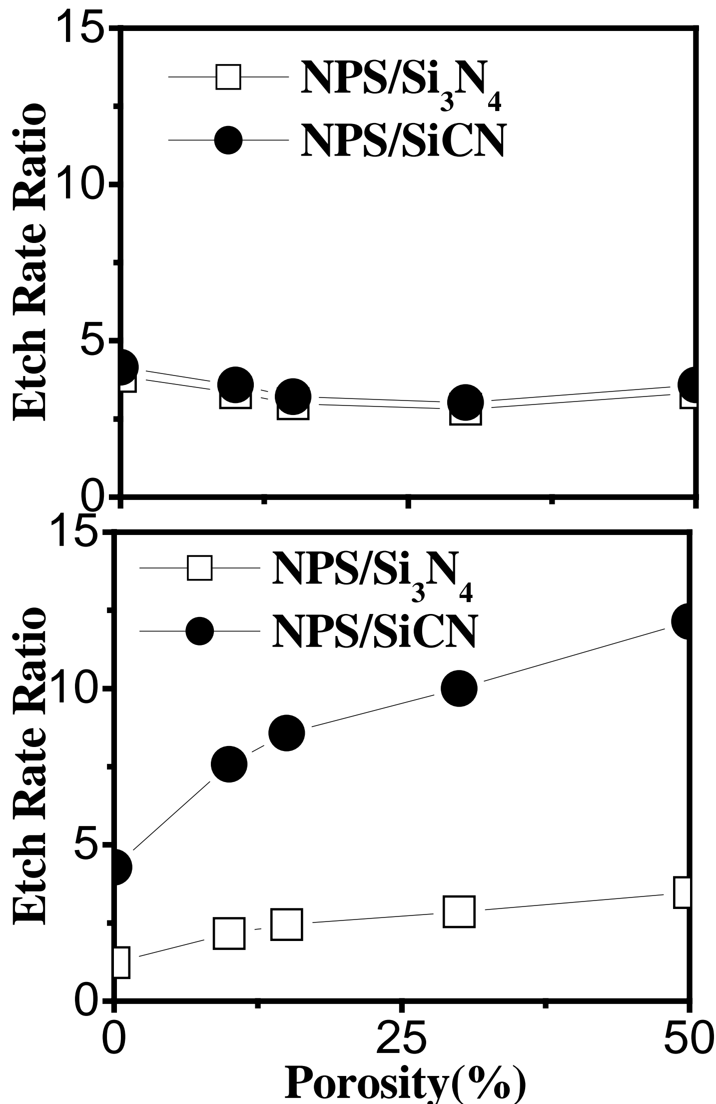

Figure 4.5: *Etch rate ratios for different NPS to SiCN or Si_3N_4 using a C_4F_8 (a) or C_4F_8/90%Ar (b) discharge maintained at 10mTorr and 1000W source power. The self-bias voltage was set at –125 V.*

4.3.2 NEAR SURFACE CHARACTERIZATION

ELLIPSOMETRY: Based on the etching behaviors of NPS in C_4F_8 and C_4F_8/90%Ar discharges, the plasma-induced modifications are expected to be different. The optical changes of the NPS bulk material can be easily monitored by *in situ* ellipsometry as a change of the refractive index. For C_4F_8 discharges (high FC

polymerization conditions) the near surface pores are expected to fill up with FC material, resulting in a change of the optical properties of the NPS material. The effective refractive indices of 30% porosity NPS material for different plasma etching conditions are shown in Fig.4.6. For C_4F_8 discharges the refractive index change indicates a significant modification of the properties of the NPS material. The modification is greatly reduced in C_4F_8/90% Ar, which shows a refractive index that is similar to untreated NPS material. The change of the refractive indices is believed to be a result of the fluorocarbon incorporation. The refractive index of fluorocarbon material depends on its chemical properties, e.g. its F/C ratio. Lower F/C ratio fluorocarbon material is characterized by a higher ellipsometric refractive index. Since the refractive index of fluorocarbon material for C_4F_8/90% Ar is higher than for C_4F_8, the increase of the NPS refractive index must be related to the amount of incorporated fluorocarbon material. The data shown in Fig. 4.6 indicate that for NPS etching in C_4F_8 discharges, a significant amount of FC material was incorporated into the NPS material, whereas only little FC material deposited into the NPS pores for C_4F_8/90% Ar.

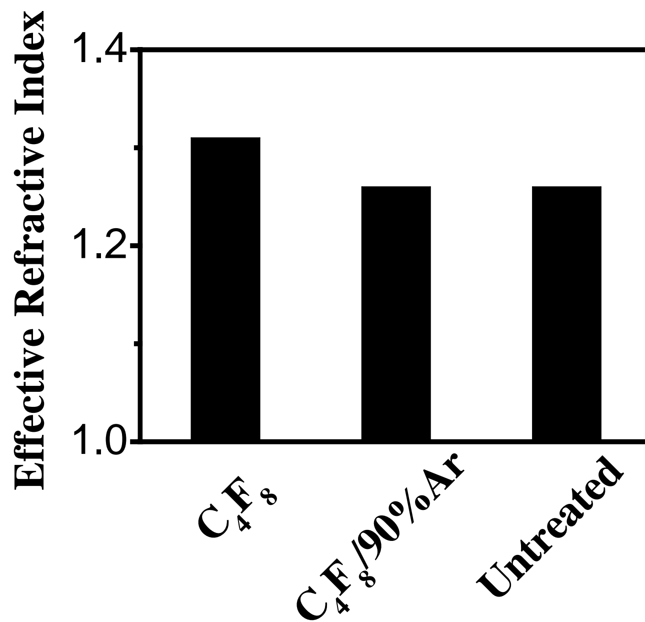

Figure 4.6: *Effective refractive index of NPS (30%) material upon different plasma treatment.*

TRANSMISSION ELECTRON MICROSCOPY: Partially etched NPS (30%) samples were also characterized by transmission electron microscopy (TEM). The TEM cross-sectional images are shown in Fig.4.7. The cross-sectional samples for TEM analysis were prepared using focused-ion-beam (FIB) techniques (30 kV Ga). The Ga ions during milling tend to fill in small cavities on the sample surface. Locally absorbed Ga gives rise to dark dots in the bright-field images, which reflect the size and distribution of pores in the NPS layer. After C_4F_8 plasma etching, the NPS surface is covered with a fluorocarbon layer, consistent with the XPS data. The etched surface is shown in the cross-sectional image in Fig. 4.7(a) and appears quite smooth in this case. One can also notice that the pores close to the surface (up to a depth of ~20nm) are enlarged, possibly caused by fluorocarbon filling. Figure 4.7(b)

shows a much rougher NPS surface after C_4F_8/90% Ar etching, with a roughness scale of about 30 nm. The pore size, however, remains uniform in the NPS bulk in this case, indicative of little fluorocarbon deposition in this discharge. This is also consistent with the ellipsometric results. The TEM results show that the modification of the underlayer is also reduced in this case. In the regime investigated, with the ion energy of the order of 100 eV, the ion penetration depth is about 1 nm[4.20]. Therefore, the under layer (SiCN) modification is a result of neutral species diffusion into the porous structure. The reduction in the under layer modification for the C_4F_8/90% Ar discharge is consistent with the small FC radical fluxes that is a characteristic of the C_4F_8/90% Ar discharge. The introduction of surface roughness for C_4F_8/90% Ar is consistent with the large ionic contribution to the overall etching reaction in this case, and the high etching rate.

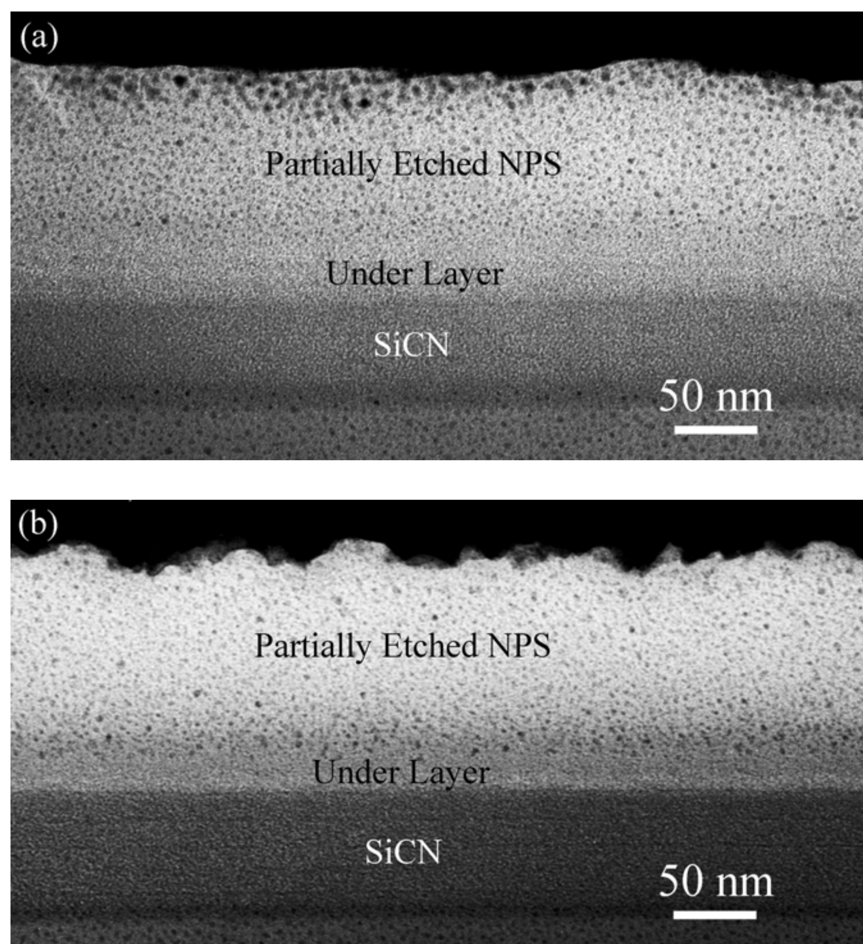

Figure 4.7: *TEM cross-section images for partially etched NPS (~30%) samples with (a) C_4F_8 or (b) C_4F_8/90%Ar plasmas maintained at 10 mTorr and 1000 W source power. The self-bias voltage was set at –125 V.*

STATIC SECONDARY ION MASS SPECTROSCOPY (SSIMS): SSIMS spectra were collected with SiO_2 and NPS samples (30% and 50% porosity) to characterize the chemistry of the surface before and after the plasma etching process. These data showed that the two untreated NPS samples were very similar from a chemical/compositional point of view. The spectrum of the 30% NPS sample is displayed in Fig. 4.8 (a). The fingerprint provided by the NPS samples is primarily related to Si-O-C-H compounds (highlighted in Fig. 4.8 (a)). The intensity of the various peaks is similar for both materials. The features of the NPS samples are

largely independent of materials porosity and the untreated SiO_2 has different characteristics.

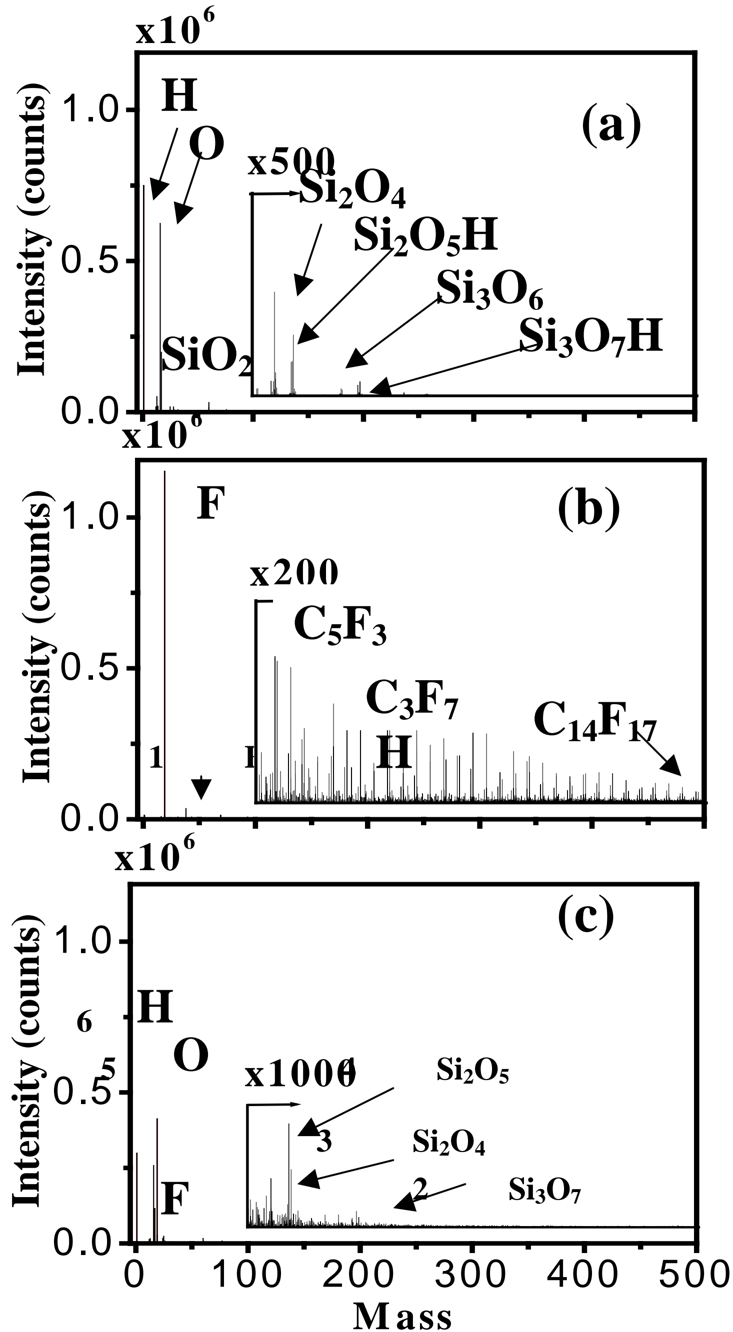

Figure 4.8*: Negative SSIMS spectrum of 30% NPS samples: (a) untreated; (b) partially etched with C_4F_8 discharges; (c) partially etched with C_4F_8/90%Ar discharges. The discharges are maintained at 10 mTorr and 1000 W source power. The self-bias voltage was set at –125 V.*

These conclusions are clearly summarized by the principle component analysis (PCA) results shown in Fig. 4.9. In fact, in the scores/scores plot the data related to both untreated NPS samples overlap, while the spectra from the untreated SiO_2 are completely different. For Principal Component Analysis, the logarithm of peak intensity was considered. Similar conclusions are obtained if both the negative and positive SSIMS spectra are considered.

The features of the SiO_2 and NPS surface appear to be very similar after processing in C_4F_8 discharges, regardless of the original stoichiometry and porosity of the materials. Five spectra out of six related with the NPS samples submitted to this plasma treatment have in fact practically the same scores in the PCA plot. The scores for the partially etched SiO_2 data are essentially alike, being slightly lower for PC #2. However, the variance represented by PC #2 is about 8%, whilst the variance captured by PC #1 is about 87%.

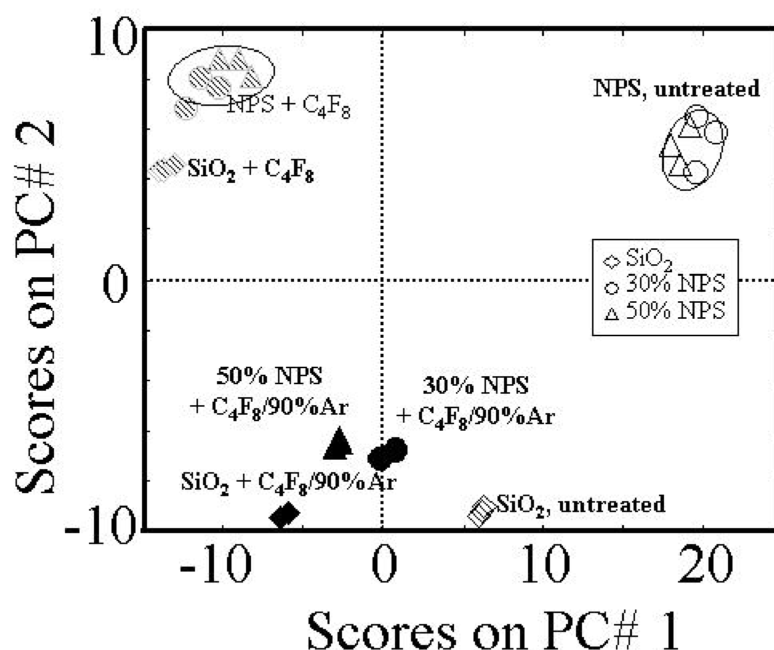

Figure 4.9: *Principal Component Analysis for untreated samples or partially etched samples with C_4F_8 or C_4F_8/90%Ar discharges.*

The analysis of the SSIMS data clearly shows the presence of a fluorocarbon layer on the surface of the samples treated in pure C_4F_8 discharge. By comparing the spectra of the untreated and etched 30% NPS samples for instance (shown in Fig. 4.8 (b)), it is seen that the signals related to both molecular Si-O-C-H compounds and elemental peaks disappear for the etched NPS material. Fluorine dominates the spectrum, and overall the occurrence of a sequence of regularly spaced peaks is seen in Fig.4.8 (b). These regularly spaced peaks evenly differ in mass by 12.000 or 18.998 amu with respect to each other, meaning that they are related to C_xF_y compounds. As the signals related to NPS can hardly be detected after plasma etching, it can be concluded that the surface coverage by the fluorocarbon layer is almost complete for all samples. Moreover, it can be noticed that the peaks related to C_xF_y

are detected at m/z larger than 500 amu. This implies that long chain fluorocarbon compounds are present on the surface (x and y can be as high as 14 and 17, respectively). Fluorocarbon deposition is the main transformation that takes place during C_4F_8 plasma processing and the fluorocarbon species block the direct ion impact with the silica material. In the spectra, little evidence was observed for ion-induced interaction with the silica matrix.

Figure 4.9 shows that samples treated in C_4F_8/90% Ar and in pure C_4F_8 plasma exhibit different PCA scores. These differences may be related to the polymerization characteristics of these discharges. Since the fluorocarbon deposition is extremely significant for C_4F_8 discharges, fluorocarbon deposition dominates the material transformation and "homogenizes" the surface chemistry for different pristine materials. Surface polymerization is much less important in C_4F_8/90% Ar, and the plasma-surface interaction process is unable to completely suppress the surface chemistry differences of the starting materials. Both the SSIMS results from the samples partially etched in C_4F_8/90% Ar plasma and the PCA results highlight unique characteristics for the C_4F_8/90% Ar treated SiO_2 and NPS samples.

SSIMS spectra obtained with samples partially etched in C_4F_8/90% Ar reveal the onset of several phenomena related to the characteristics of this discharge. Figure 4.8(c) displays the spectrum of a partially etched 30% NPS sample. The fluorine peak still dominates the mass spectrum, but no peaks related to fluorocarbon compounds can be observed (the intensity is multiplied by a factor of 1000 in this case). The matrix signals have lower intensities in comparison with the pristine material but can still be clearly recognized. One concludes that no deposition of a

thick fluorocarbon layer occurs in the low polymerization and high ion flux C_4F_8/90% Ar discharge and defluorination of deposited fluorocarbon compounds is almost complete. The absence of the FC layer on the surface allows the plasma ions to interact with the matrix. The high amount of available fluorine enhances the etching rate of the materials in this discharge. Novel species related to SiOF, SiO_2F and Si_2O_4F are present in the spectrum. The PCA shows clearly that the intensity variation of the peaks is unique for each sample. This suggests that ion-induced FC reaction with NPS and the NPS etching rates are related to thechemical/compositional characteristics and initial porosity of the NPS materials. Accordingly, SiO_2 and NPS exhibit different etching behavior, consistent with the previous section and as revealed by the XPS data to be discussed next.

X-RAY PHOTOELECTRON SPECTROSCOPY (XPS)-C_4F_8: In order to validate the suggested mechanism for NPS etching in C_4F_8 discharges, we examined the chemistry of NPS surfaces during steady state etching using angle resolved X-ray photoelectron spectroscopy (XPS). Photoemission intensities were acquired at 90°, 30°, and 20° take-off angles. The integrated C1s, F1s, O1s and Si2p photoemission intensities (90°) after blanket film etching in C_4F_8 discharges are shown as a function of porosity in Fig. 4.10(a). The increase of C1s as a function of porosity indicates that higher porosity NPS absorbs FC species more strongly. The O1s and Si2p intensities behaved similar after processing using C_4F_8 plasma, indicating that the substrate has been fluorinated and some oxygen was replaced by fluorine. The high fluorocarbon coverage on the high porosity NPS was found to be inconsistent with

the attenuation of Si2p intensity. This effect is possibly caused by interconnected pores, which allows fluorocarbon species to penetrate deeply and mix with the porous bulk material.

F/C ratios were calculated from the deconvolution of C1s spectra into the fluocarbon components (for a detailed discussion see reference 4.21) and the results are plotted in Fig. 4.10 (b). For a take-off angle of 90°, the F/C ratio of the steady-state fluorocarbon film formed on SiO_2 is higher than for FC films on NPS. The NPS films contain a significant density of methyl (CH_3) groups. The superposition of C1s intensity from CH_3 with FC film related signal may be responsible for the lower F/C ratios seen for partially etched NPS films when probed at 90° take-off angle. The enhancement of the F/C ratio for high porosity NPS indicates that ion-induced defluorination is low. It indicates that for high porosity NPS some of the FC is shielded from ion bombardment. Because of probing depth limitations of XPS, the methyl group contribution to the C1s intensities is expected to be very low for a 20° electron take-off angle. The signal is mainly related to the FC over-layer and possibly FC material penetrated into pores. At a take-off angle of 20°, a higher F/C ratio was observed for NPS as compared to SiO_2. The angular dependence of the F/C ratios for SiO_2 is consistent with the behavior of a substrate without carbon content. The behavior of the F/C ratios of NPS as a function of photoemission angle indicates that carbon from the substrate strongly affects the signal in this case.

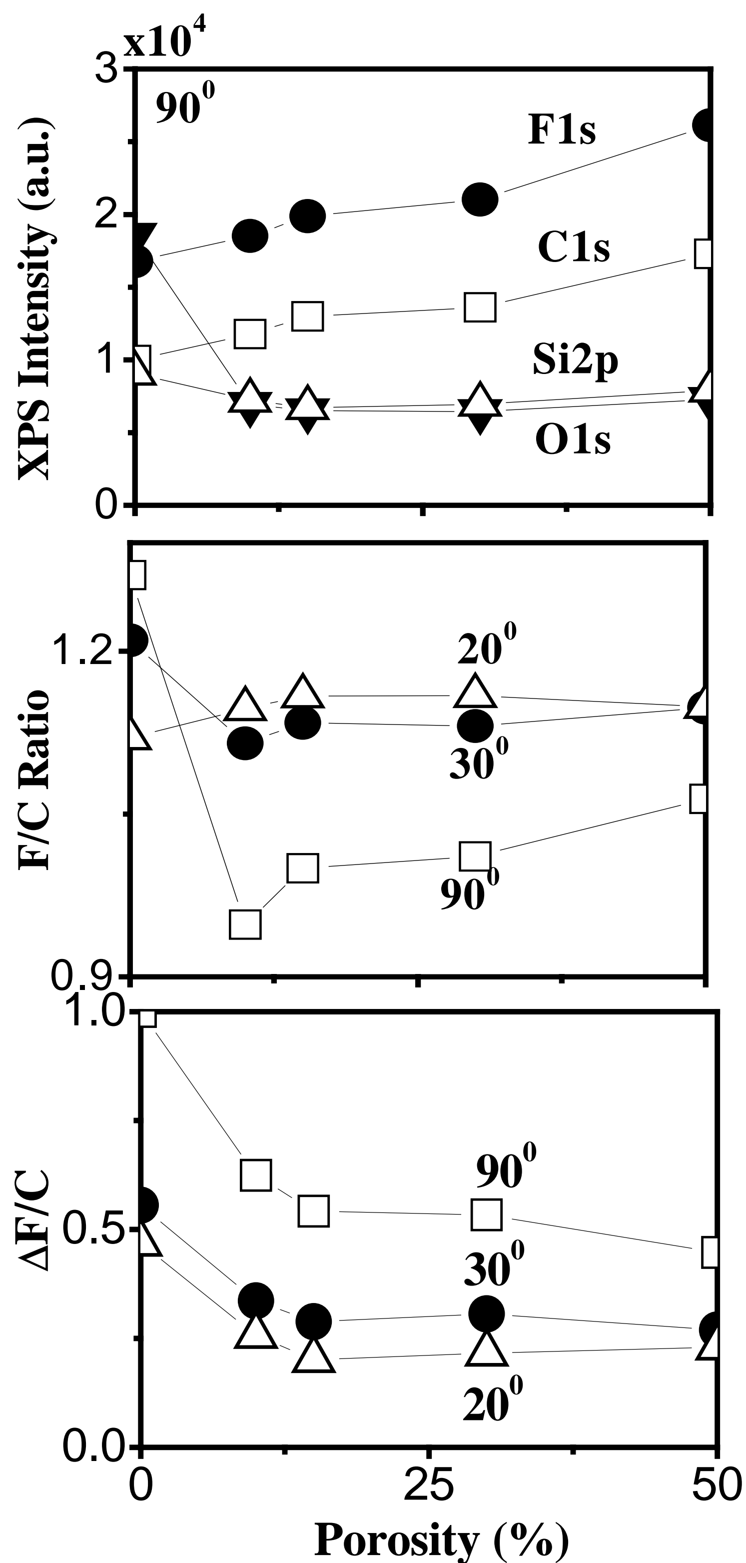

Figure 4.10: *Integrated photoemission intensity C1s, Si2p, O1s and F1s (a) (90° emission angle) from partially etched NPS film with C_4F_8 discharge. Angular dependent F/C or Δ F/C are shown in (b) or (c) respectively.*

The difference ΔF/C (shown in Fig. 4.10 (c)) between F/C ratio (from C1s) and F1s/C1s reflects the amount of fluorine that has been lost from FC films and reacted with to the substrate, e.g. to form SiO_xF_y for SiO_2. [A detailed discussion of this aspect is provided in reference 4.23]. For NPS material, the high fluorocarbon coverage of NPS shields the substrate and FC groups penetrated into the pores from ion bombardment. The data show that ΔF/C decreases with porosity. This implies that the rate of ion-induced conversion of fluorocarbon to intermediate etch product (SiOxFy) is lower for higher porosity NPS. This is consistent with the *CER* results (Fig. 4.1). The angular dependence of ΔF/C for NPS is similar as for SiO_2, implying a layer-like FC film structure on NPS during C_4F_8 plasma etching, with the near surface pores filled with FC material.

XPS-C_4F_8/90%Ar Plasma: Figure 4.11(a) shows the integrated C1s, F1s, O1s and Si2p photoemission intensities emitted at 90° for NPS films partially etched using C_4F_8/90%Ar. The FC coverage appears independent of porosity. This may indicate that the surface chemistry is limited by a low arrival rate of FC film precursors. The enhancement of the C1s intensity of NPS relative to SiO_2 is due to the residual carbon groups as seen for untreated NPS films. Although the C1s is nearly constant as a function of NPS porosity, a reduction in Si2p intensity was observed, which is not consistent with a simple layer structure. Due to the high ion bombardment flux at a surface in this discharge, ion-induced defluorination of fluorocarbon films is significant. Much lower F/C ratio (Fig. 4.11 (b)) fluorocarbon films were formed on the substrate during C_4F_8/90%Ar plasma etching. The angular dependence of the F/C ratio is totally different from that seen for NPS substrates after C_4F_8 plasma etching.

This suggests that the pores are not completely filled or that a rough surface exists for these etching conditions. For grazing photoelectron emission angles (30° or 20°), the sample area probed appears greater than at 90°.

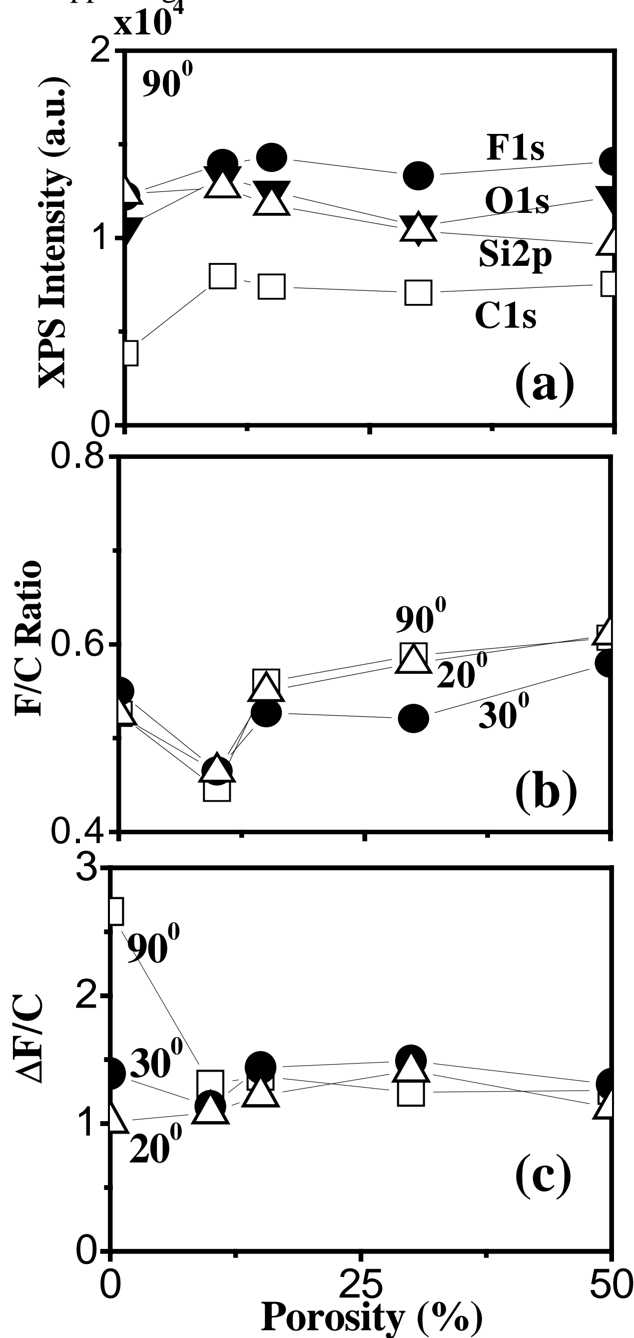

Figure 4.11: *Integrated photoemission intensity C1s, Si2p, O1s and F1s (a) (90^0 emission angle) from partially etched NPS film with C_4F_8 /90%Ar discharge. Angular dependent F/C or Δ F/C are shown in (b) or (c) respectively.*

This suggests the formation of a rough NPS surface. Ion-induced defluorination is more efficient in producing a lower F/C ratio in this case, as confirmed by the ΔF/C ratio results (Fig. 4.11(c)). For ions incident at large angles, the ion-induced reaction of fluorine with the NPS substrate is highly effective, as indicated by the high ΔF/C ratio observed in this case. Only for low porosity (~10%) NPS, the angular dependence of the ΔF/C ratio is qualitatively similar as for SiO_2, suggesting a layer-like structure in this case. As the porosity increases, the ΔF/C ratio of NPS material behaves very differently from that measured with SiO_2, indicative of a more complex surface structure. The behavior of the ΔF/C ratio is qualitatively consistent with the high *CER* as a function of porosity. The drop of the ΔF/C ratio at 50% porosity may be caused by increased pore interconnectivity, which would enable deep substrate penetration and reduce the importance of ion-induced mixing of FC material with the substrate.

Modeling of XPS data: NPS materials have non-ideal surface topographies and the surface is rough at the nanoscale. This non-ideal topography makes the interpretation and analysis of XPS data more difficult. The effect of surface roughness on XPS signals has been considered in many different models, with most efforts considering a conformal thickness of the overlayer on a rough surface [4.24-4.27]. The presence of nano cavities in NPS materials makes it difficult for a conformal overlayer to form inside pores since the layer thickness is normally comparable to the pore size. In addition, nano cavities in NPS materials may lead to novel XPS phenomena. For instance, since the wavelengths of photoelectrons (Si2p, C1s, O1s, and F1s) is much below the nanocavity size, scattering of photoelectrons at internal interfaces may be considered.

For simplicity, we assume in this work that there are no interactions between photoelectrons and nano pores in this work. Based on this assumption, the XPS intensity depends on the physical “depth”, i.e. mass depth, which only accounts for the volume for which matrix material is present and does not include the space occupied by pores. This physical depth is less than the geometric depth. All of NPS materials have the same depth profile of Si density as a function of the physical depth because of the same matrix material, which results in similar Si2p intensities. This is in agreement with the XPS characterization data of untreated NPS (see Fig. 4.1).

According to the interaction with plasma, we differentiate pores into 1) surface pores, which are open to the surface and will be filled with FC material during plasma treatment and 2) bulk pores, which are not connected with the surface and not filled with FC material. We assume that all surface pores are spherical, isolated and have the same pore sizes even though NPS materials show both a pore size distribution and pores may be interconnected.

If all pores are isolated, we have within a depth z

$$z < 2r \,, \tag{1}$$

all pores are surface pores and for a depth z

$$z \geq 2r \tag{2}$$

all bulk pores. Here r is the pore radius, and z is the geometric depth scale.

The pore volume is

$$V_P = \frac{4}{3}\pi r^3 \tag{3}$$

and the number of pores per unit volume is given by

$$n_P = \frac{\Pi}{V_P} \quad (4)$$

where Π is the porosity. If A is the surface area monitored by XPS, the number of surface pores detected by XPS is given by

$$N = A * 2r * n_P = 2Ar\frac{\Pi}{V_P}. \quad (5)$$

For our experimental conditions, A is of the order of mm^2, so the surface pore number N is of the order of 10^{11} for 10%NPS material. These pores are connected with the surface as spherical segments with various heights h ($0<h<2r$). The spherical segment volume is given by

$$V_{ss} = \frac{1}{3}\pi h^2(3r - h). \quad (6)$$

For simplicity, we assume a material for which the pores are arranged in a regular fashion (see Fig. 4.12). Thus, the segment height h has a uniform distribution over the range $0\sim 2r$ at the surface. At the depth z, only segments with heights above z contribute to the open volume of surface pores. The expectation of the volume of surface pores $V_S(z)$ can be easily calculated

$$V_S(z) = \int_z^{2r} \frac{1}{3}\pi(h-z)^2(3r-(h-z))dh * N / \int_0^{2r} dh$$

$$= \frac{\pi}{12}\frac{(2r-z)^3(2r+z)}{2r}N \qquad (0<z<2r) \qquad (7)$$

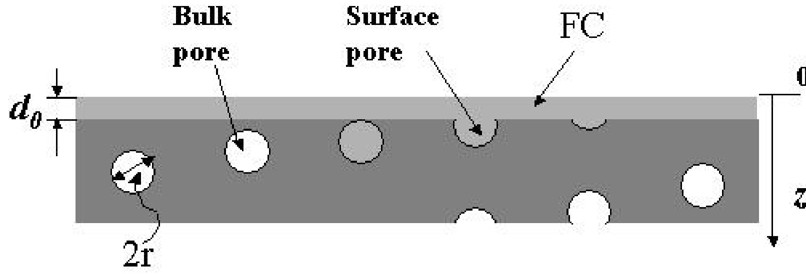

Figure 4.12: *Surface pores Vs bulk pores: surface pores will be filled with FC during fluorocarbon plasma etching.*

The fluorocarbon coverage resulting from fluorocarbon-based plasma etching exists mainly in the near surface region. The topography of the fluorocarbon film is determined by the surface structure of the substrate. Based on the results presented before, for neutral dominated discharges, i.e. C_4F_8, the fluorocarbon film thickness is high and comparable to the pore size. The surface pores of NPS are completely filled with the fluorocarbon material. In addition, a FC overlayer exists on the surface (see Fig. 4.12). For the FC inside the pores, the volume is the same as $V_S(z)$. The local effective concentration is given

$$C_{FC}^{'} = -C_{FC}\frac{d}{dz}V(z)/A$$

$$= C_{FC}\frac{(2r-z)^2(r+z)}{4r^3}\Pi \qquad (0<z<2r) \qquad (8)$$

Here C_{FC} is the concentration of a standard FC bulk. Accordingly, the Si concentration as a function of mass depth can be calculated as

$$C_{Si}^{'} = C_{Si}[1-\frac{(2r-z)^2(r+z)}{4r^3}\Pi] \qquad (0<z<2r) \qquad (9)$$

Considering the FC overlayer on the surface, the origin should be the interface between the FC layer and vacuum instead of the surface of NPS, i.e. $z \rightarrow z'-d_0$. Here d_0 denotes the thickness of the FC overlayer. Therefore, the FC concentration as a function of mass depth is

$$C'_{FC}(z') = \begin{cases} C_{FC} & (0<z'<d_0) \\ C_{FC}\dfrac{(2r-(z'-d_0))^2(r+(z'-d_0))}{4r^3}\Pi & (d_0<z'<2r+d_0) \\ 0 & (z'>2r+d_0) \end{cases} \tag{10}$$

For the Si component we have

$$C'_{Si}(z') = \begin{cases} 0 & (0<z'<d_0) \\ C_{Si}[1-\dfrac{(2r-(z'-d_0))^2(r+(z'-d_0))}{4r^3}\Pi] & (d_0<z'<2r+d_0) \\ C_{Si} & (z'>2r+d_0) \end{cases} \tag{11}$$

The XPS intensity can be described by[27]

$$I_i = \frac{I_i^0}{\lambda}\int_0^{\infty} C_i(z')\exp(\frac{-z'}{\lambda})dz' \tag{12}$$

where $C_i(z)$ is the local component i concentration at mass depth z, I_i^0 is the intensity for a bulk standard, and λ is the "effective" escape depth of photoelectrons. The

effective escape depth λ is determined by the inelastic mean free path or attenuation length of the electrons for a given energy and material and denoted as λ^0, and by the take off angle of the detector, according to

$$\lambda = \lambda^0 \sin\theta \,. \tag{13}$$

The Si2p intensity is given by

$$I_{Si2p} = I_{Si}^0 C_{Si} (e^{-d_0/\lambda} - \Pi e^{-d_0/\lambda} f(r/\lambda)) \tag{14}$$

and the C1s intensity is determined by

$$I_{C1s} = I_{FC}^0 C_{FC} (1 - e^{-d_0/\lambda} + \Pi e^{-d_0/\lambda} f(r/\lambda)) \tag{15}$$

with $f(r/\lambda) = 1 - \frac{3}{2}(\lambda/r)^2 (e^{-2r/\lambda} + 1) - \frac{3}{2}(\lambda/r)^3 (e^{-2r/\lambda} - 1)$ (16)

In the work, the total intensity $I^0 C_i$ is ~13000 and ~25000 for Si2p and C1s, respectively. These values were measured with a semi-infinite SiO_2 film and a passively deposited FC layer (>300nm), respectively. We also assume that λ = 3nm for both Si2p and C1s photoelectrons.

The model results (lines) are compared with the experimental data (dots) in Fig. 4.13 for C_4F_8. For C_4F_8 etching, the steady state fluorocarbon film thickness (d_0) on SiO_2 is chosen as d_0=1.8 nm, which is consistent with previous work.[20] The model qualitatively predicts both the observed C1s and Si2p intensities, especially for low porosity NPS material (10% or 15%), if a pore diameter in the range 4 to 8nm is assumed. The pore diameter is consistent with the TEM measurements, where the near surface pores are found to be enlarged after C_4F_8 plasma exposure. The pore sizes of the modified layer are similar when both Si2p and C1s data are modeled.

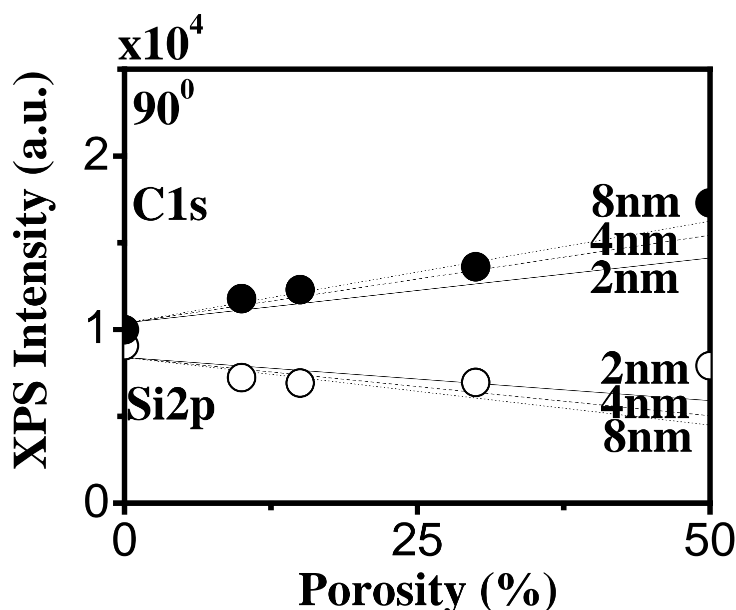

Figure 4.13: *Silicon 2p and C 1s model results as a function of pore size and experimental XPS data for etching of NPS using* C_4F_8 *discharges.*

As the porosity increases above 30%, the agreement of the model predictions and the observed C1s and Si2p intensities becomes worse (see Fig. 4.13). For higher porosities, interconnected pores become more likely, which changes the plasma-surface interactions. Once pores are interconnected, sub-surface pores can be filled with FC material. Pores are changed much beyond a distance of *2r* from the surface, as observed the TEM image. The fact that the model predictions cannot fit the Si2p or C1s data simultaneously is likely due to effects related to interconnected pores which have been ignored in the model. Consistent with this trend is the fact that fitting Si2p and C1s data requires completely different pore sizes for NPS material with 50% porosity, for which effects due to interconnected pores would be most important. These results are consistent with previous observations that siloxane-based materials

have closed cells and are microporous as long as the porosity is below 30% [4.29]. For ~30% porosity and greater, the material reaches the percolation threshold where films become mesoporous and pores become interconnected. The XPS modeling results of the 20^0 or 30^0 data is also consistent with this picture. While changes in pore size in the near-surface region is one possible mechanisms, and consistent with the TEM results, other possibilities for changes in the pore characteristics of the near-surface layer can be envisioned, e.g. a change in the overall porosity of this layer.

In the case of a C_4F_8/90% Ar plasma, a rough surface exists on the NPS film. The TEM work shows that the rough features are very large relative to the pore size. For the sake of simplicity we still assume that the pores are completely filled with fluorocarbon material but the FC overlayer thickness is reduced to 0.7 nm since the polymerization rate is very low in this discharge. With a similar approach as described for the C_4F_8 case, the XPS intensity $I(\theta_i)$ can be calculated as a function of take-off angles ($0 \sim 90^0$). If the frequency at which each angle occurs [$f(\theta_i)$] is known, the XPS intensity of this rough surface is given by

$$I = \sum_{\theta=0}^{90} I_0(\theta) f(\theta) d\tilde{A} \quad \text{and} \quad \sum_{\theta=0}^{90} f(\theta) = 1 \qquad (7)$$

$I_o(\theta)$ is the XPS intensity per unit area, with $d\tilde{A}$ the unit area, for a take-off angle θ for the XPS measurement. Figure 4.14 (a) shows the surface orientation (ϕ) with respect to the horizontal surface used in the model, which is equal to $90-\theta$. The inclined area is given by $d\tilde{A} = dA/\cos\phi$, where dA is the unit area on a horizontal surface. The C1s and Si2p spectra model results are shown in Figs. 4.14 (b) and (c), respectively. For a rough surface, the intensity of Si2p at 30° electron emission is

greater than at 20° or 90^0. which cannot be the case for a layer like structure. Also, a high fluorocarbon coverage on a rough surface does not necessarily result in the strong Si2p attenuation seen for a smooth surface.

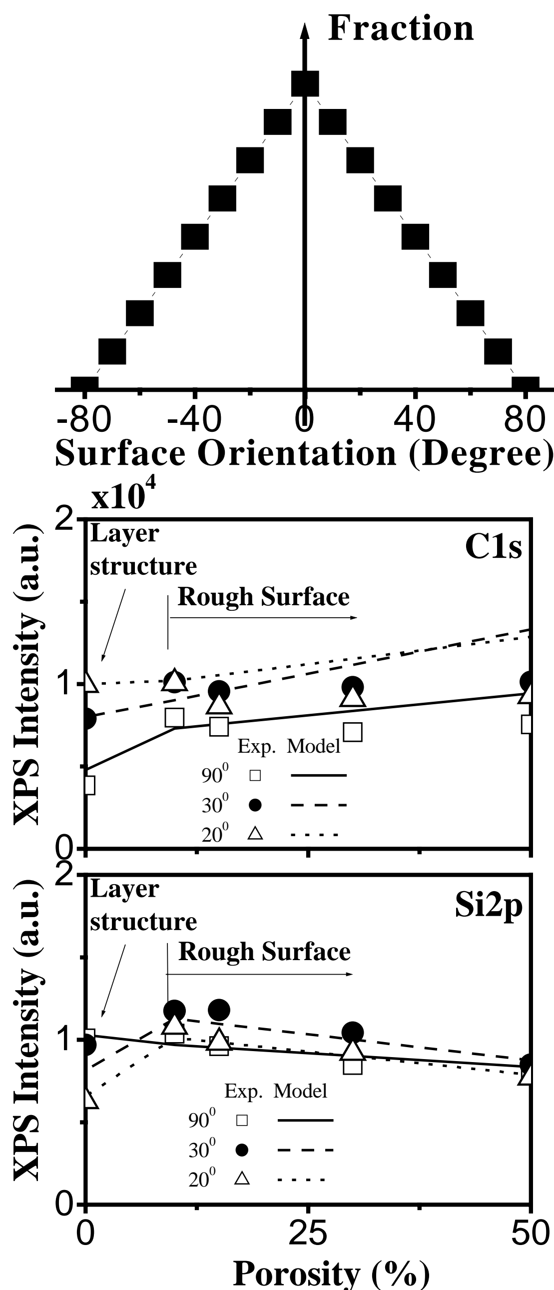

Figure 4.14: (a) Surface orientations (respected with horizontal surface) used in the model for C_4F_8/90% case; (b) Model results for C1s spectra; (c) Model results for Si2p spectra. Rough surface has been used for NPS materials, and for SiO_2 a smooth surface has been assumed.

4.3.3 SUB SURFACE MODIFICATION: After fluorocarbon plasma etching, a modified layer exists on the surface. This layer results from the combined effects of ion bombardment, and fluorocarbon species penetration of the bulk material. The extent of this modified layer is expected to depend on the overall porosity of the NPS material. A possible approach to determining the extent of the modified layer is by measuring its physical sputtering rate. The erosion rate of the near-surface region is expected to be enhanced by penetration of fluorocarbon species, and then decrease to the physical sputtering rate of the bulk material. A schematic picture is shown in Fig. 4.15. Using *in situ* real time ellipsometry, we measured an enhanced sputtering rate in a pure Ar discharge for the near-surface region. After the modified layer had been removed, the sputter rate became constant. From these data it is possible to determine the depth at which the sputtering rate became constant and equal to the sputtering rate of the bulk material. Figure 4.16(a) shows the removed thickness as a function of time in a pure Ar discharge for samples pretreated in C_4F_8 or C_4F_8/90% Ar plasmas. The removal rate is greater initially and after a certain time the removal rate becomes constant. The depth where the etch rate became constant was determined. This depth is shown in Fig. 4.16(b) for both pretreatments, C_4F_8 or C_4F_8/90% Ar, as a function of porosity.

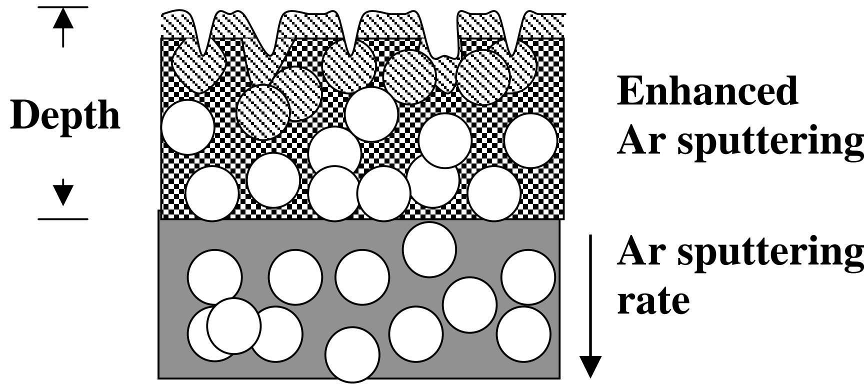

Figure 4.15: *A schematic picture for Ar sputtering of NPS films pretreated with fluorocarbon discharges.*

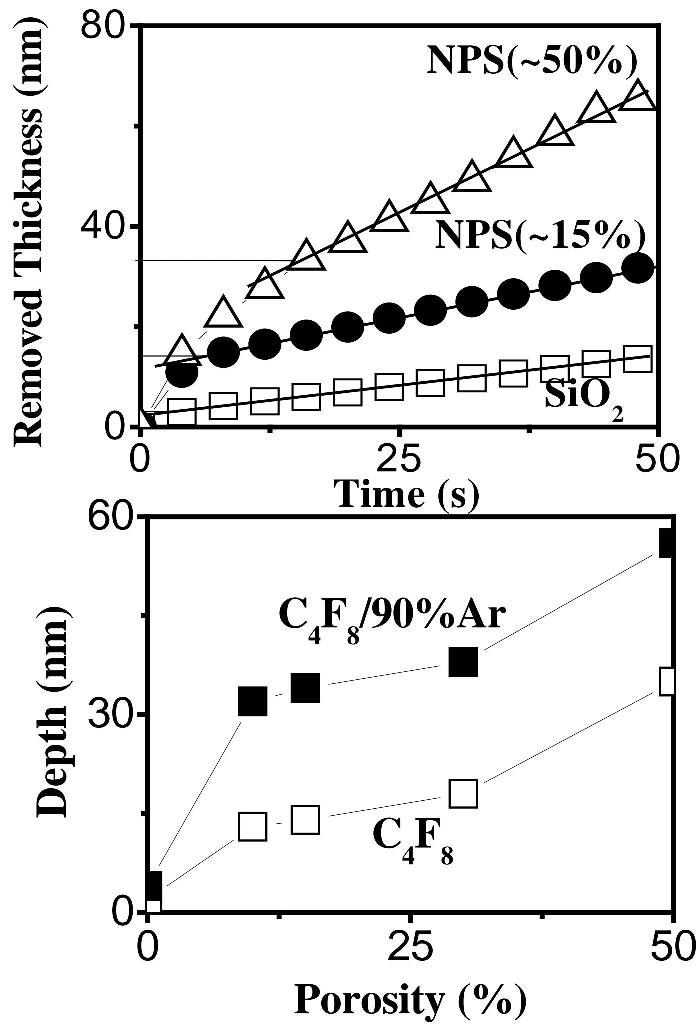

Figure 4.16: *(a) Removed thickness as a function of process time for NPS film (pretreated with C_4F_8 plasma) during argon plasma. (b) Depth (shown in Figure 4.5) Vs. NPS porosity.*

Fluorocarbon species likely diffuse deeply in a porous structure, and can react with the NPS material. A thick modified layer is observed because of penetration of FC material into the porous bulk after FC plasma etching. For a solid material like SiO_2, FC species can hardly penetrate into the sub-surface region and the modified layer is thin. The depth of the modification of the dielectric material also depends on the characteristics of the plasma. Because of a predominance of ion bombardment and lower fluorocarbon coverage for C_4F_8/90% Ar discharges, it is plausible that the modified layer thickness is greater in this case than for C_4F_8. For the lower porosity NPS, the extent of the FC related materials modification increases weakly with the porosity. The strongly increased extent of the modified layer thickness seen in the case of 50% NPS for both pretreatments is consistent with the expectation that a significant fraction of pores are likely connected for this overall porosity, which favors enhanced FC permeation of the interconnected pore network.

DEPTH PROFILING: Dynamic SIMS was used to examine the depth dependence of surface modification for SiO_2 and NPS materials after 1 min plasma etching (PE) in C_4F_8 and 30 s PE using C_4F_8/90% Ar. The initial thicknesses of the 30% and 50% porosity NPS materials were 330nm and 500nm, respectively. The in-depth distribution of selected species representing the overall changes in NPS and SiO_2 stoichiometry due to the plasma treatment in C_4F_8 discharge is displayed in Fig. 4.17(a). For SiO_2, only the near-surface region is modified by the plasma and the depth scale of interaction is below 10 nm. Conversely, F is present throughout the whole 30% NPS layer and reaches a nearly uniform concentration. The overall amount of F is lower in 50% NPS and a concentration gradient is apparent, but still a

significant amount of F is detected close to the interface. It is thus apparent that the porous structure of NPS permits long-range F diffusion and interaction with the matrix. The scale of interaction depends on the characteristics of the discharge and on NPS porosity, being prominent for 30% NPS. The fluorine intensity for 30% NPS and oxygen intensity for 50% NPS and SiO_2 exceed 10^5 counts, and are likely saturated. In spite of this, the amount of F is higher for 30% NPS in comparison to 50% NPS. The F distribution is almost constant as function of depth for 30% NPS (as confirmed by determining additionally the depth distribution of unsaturated signals like F_2), while the F intensity decreases with depth for 50% NPS. The reduction of O intensity (shown by other species related with the matrix as well) for the 30% NPS complements the F concentration in the way expected.

The depth profiles obtained with NPS and SiO_2 samples partially etched in C_4F_8/90% Ar discharge are shown in Fig. 4.17(b). Overall, a lower amount of F is present in both NPS samples in comparison with the treatment in pure C_4F_8 plasma (Fig. 4.17(a)). The 50% NPS material shows a higher amount of F than 30% NPS. For both NPS materials, F concentration gradients are observed.

These results agree with the XPS data which also indicate a higher efficiency of ion-induced defluorination of the FC films in this discharge for the NPS material. For low polymerization conditions, e.g. C_4F_8/90% Ar, a significant ion flux is able to directly react with the matrix. The etch rate is much higher for C_4F_8/90% Ar than for C_4F_8 plasma, which implies that etching will limit the build-up of a modified surface layer. The depth profiles clearly show that the modification of SiO_2 is located near the surface (below 10 nm) while the plasma-modified layer for NPS materials range

much beyond this depth scale. We also observe similar near-surface modification layers (I) for both 50% and 30% porosity materials. The thickness of layer I is about 30 nm, which roughly compares with the TEM cross-section results. Under this layer, an intermediate layer (II) appears for both NPS material. The scale of layer II strongly depends on the overall porosity. For 50% porosity NPS, the thickness of layer II is much greater than for 30% porosity material, and can be explained by increasing degree of pore interconnectivity. The thickness of layer I compare well with the results of the Ar sputtering experiments, but differ from the depths of the overall modified layer seen by DSIMS (see Fig. 4.17). The discrepancy may be due to the fact that we assume a constant sputtering rate for the depth calibration of the DSIMS measurements, whereas the time-resolved measurements showed that this is not the case.

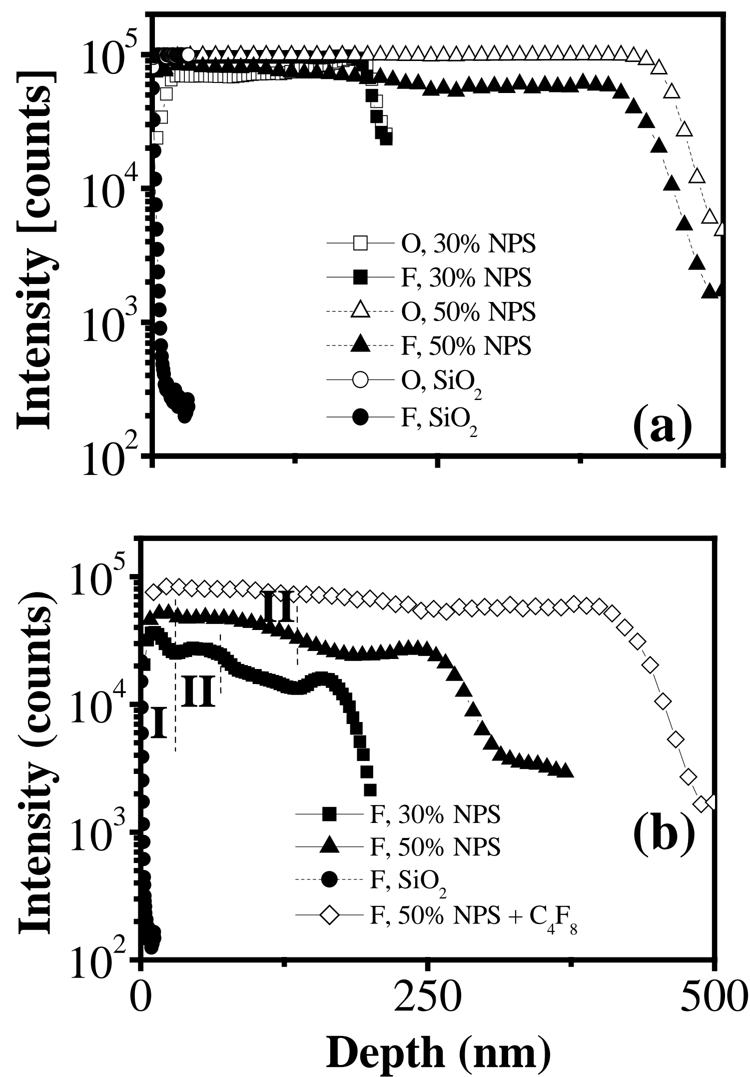

Figure 4.17: *DSIMS depth profiling results for NPS samples partially etched with (a) C_4F_8; (b) C_4F_8/90%Ar discharges.*

4.4 CONCLUSIONS

In this work important differences in the behavior of MSQ-based nanoporous silica were observed in neutral-rich and ion-rich fluorocarbon discharges used for plasma etching. We developed surface models that reproduce the experimental surface characterization data and strongly differ for neutral-rich and ion-rich discharge conditions. These models are based on results of complementary characterization methods, including XPS, secondary ion mass spectrometry, and transmission electron microscopy. The depths of the plasma-modified layers strongly differ for neutral-rich and ion-rich discharges, and depend on the overall porosity of the NPS material. Results of etching rate and surface characterization measurements, along with SIMS depth profiling of NPS after C_4F_8 or C_4F_8/Ar plasma etching reveal that high porosity (~50%) NPS exhibits a qualitatively different behavior compared with NPS materials of lower overall porosity. This suggests that increasing pore interconnectivity may play an important role in the etching mechanism and the plasma-induced near-surface modifications. This would be consistent with results of a pore percolation study based on Positronium Annihilation Lifetime Spectroscopy, which indicates a percolation threshold in the porosity range 20%~25%[4.30]. This work also has shown that important NPS material changes are introduced by O_2 post plasma removal of the resist mask. These modifications can be explained by the uncontrolled interaction of O_2 plasma-based species with residual carbon groups in the NPS material. The selective removal of the resist mask from NPS structures without attacking carbonaceous groups in the NPS material is an important current challenge.

ACKNOWLEDGEMENTS

Financial support of this work by the Semiconductor Research Corporation is gratefully acknowledged. We also would like to thank X. Li and L. Ling for assistance and discussions, and thank International SEMATECH and Texas Instruments for supply of NPS materials.

Chapter 5: Damage Of Ultra Low K Materials During Photoresist Stripping Process

To be submitted to J. Vac. Sci. Technol. A.,2005

Xuefeng Hua, G. S. Oehrlein, P. Lazzeri, E. Iacob, M. Anderle, C. K. Inoki, T. S. Kuan, Wen-li Wu, and P. Jiang

ABSTRACT

Plasma-based ashing of photoresist masks after pattern transfer is a common processing step in the fabrication of integrated circuits. In this work we investigated damage mechanisms of nanoporous ultra low k (ULK) materials with different overall porosities due to the ashing process. Oxygen-, nitrogen- and hydrogen-based photoresist-stripping using direct and remote plasma processes were examined. Ellipsometry, X-ray photoelectron spectroscopy (XPS), secondary ion mass spectroscopy (SIMS) and transmission electron microscopy (TEM) were utilized to study the damage layer thickness, physical (pore morphology) and chemical modifications of the nanoporous silica thin films after exposure to the O_2-, N_2- or H_2-based ashing processes. As a result of the plasma-exposure, carbon groups in nanoporous silica can be removed from the ULK layers which is also accompanied by material densification. We find severe ashing damage of ULK materials after O_2 -based ashing using both direct and remote discharges. N_2 and H_2 discharges also damage ultra low k materials for direct plasma ashing processes which are accompanied by low energy ion bombardment of the substrates. The introduction rate and degree of the ULK materials modifications correlates with the overall porosity. We show that pore interconnectivity is one of the key parameters that determine

ashing damage. ULK damage is greatly reduced for remote N_2 or H_2 discharges, but the resist removal rates are impractically low if the substrate is at room temperature. We show that both acceptable photoresist stripping rates and ULK damage levels can be achieved for remote H_2 plasma ashing processes if the substrate temperature is 250 ^{0}C and higher.

5.1 INTRODUCTION

Signal delays caused by interconnects have become more and more important relative to gate delays as the integration level of integrated circuits has increased to currently greater than a 100 million of transistors per integrated circuit.[5.1] Additionally, cross talk and power dissipation are problems for integrated circuits based on conventional Al/SiO_2 technology. Low k dielectric/Cu interconnects are required to solve these issues and achieve high speed and high IC performance. Low k materials can be produced based on conventional silicon dioxide by either inserting atomic groups with small polarizability, e.g. fluorinated silicate glasses (FSG), or by lowering electronic density. Incorporating terminating Si-H or Si-R (where R is organic group such as CH_3) in the Si-O-Si matrix results in lower electronic density compared with SiO_2 and enables achievement of a lower k value. Organosilicate Glass (OSG) is an example of this approach and can be produced using chemical vapor deposition yielding a k value of about 2.8~2.9. [5.1-5.5] Ultra low dielectric constant ($k<2.5$) materials are required for silicon integrated circuits of the 45 nm node and beyond (see the International Technology Roadmap for Semiconductors (ITRS)[5.6]). The introduction of nanopores into "dense" low k material is necessary when k values below 2.5 are desired.[5.6] Pores degrade the thermal and mechanical properties and enhance species permeation during processing.[5.7-5.9] These issues make the integration of nanoporous dielectrics into back-end-of-line device structures challenging.

Plasma etching and photoresist stripping are critical steps in the processing of ULK materials. The modifications of porous ULK materials due to these processes

can increase the effective k value through carbon depletion and densification, along with deep fluorine penetration and introduction of surface roughness. In our previous publications,[5.8,5.9] we discussed plasma-induced surface and bulk modifications of porous ultra low k materials during plasma etching using fluorocarbon-based discharges. The focus of the present work is the study of modifications of ultra low k materials caused by different photoresist removal (stripping) plasma chemistries.

It is well known that oxygen discharges conventionally used for the removal of photoresist masks causes carbon depletion even for dense materials like OSG because of the oxidation of carbon-containing groups and leads to a higher effective k value.[5.10] In addition, the carbon depletion makes the hydrophobic dielectric hydrophilic, which enhances moisture uptake. Alternative photoresist stripping chemistries based on N_2 or H_2 are promising for developing successful integration procedures for ULK materials.[5.11] In this work, we investigated ULK material modifications resulting from exposure to different photoresist ashing environments, specifically O_2, N_2, and H_2 discharges with the substrate either directly exposed to the discharge or placed remotely. In the first geometry low energy ion bombardment plays an important role in the ashing process, whereas in the second case only attack of neutrals causes the gasification of the photoresist.

5.2 EXPERIMENTAL SETUP AND PROCEDURES

A. Materials

The ultra low k materials used in this work are porous methyl silsesquioxane (MSQ) thin films coated on silicon substrate with a thickness around 330 nm. ULK

film properties, including composition, pore size, and porosity range were reported in our previous publication.[5.8] To distinguish the relative importance of residual methyl carbon group and nanopores in promoting ULK damage, we compared ULK damage results obtained for nanoporous ULK materials and OSG. Additionally, pore morphology, i.e. porosity and pore interconnectivity, was characterized using X-ray reflectivity porosimetry.[5.12,5.13] X-ray reflectivity can be employed to determine the film density profile. Porous low k films absorb vapors such as toluene, perfluorohexane, and the film densities change as a result. The change of density due to the presence of condensed vapors in the porous matrix is measured using X-ray reflectivity. The data can be directly converted to the amount of adsorbed vapor and sample porosity may be determined assuming that the density of the condensing fluid is known.[5.12, 5.13] The results of these measurements performed on the set of low k and ultra-low k materials used in the present work are summarized in table 1. Due to small size of the toluene molecule, it is assumed toluene that is able to access both isolated pores and interconnected pores. The porosity measured using toluene is believed to reflect the overall porosity of the material.[5.13] To evaluate the relative importance of interconnected pores, perfluorohexane is chosen as the feed vapor. Not all isolated pores are accessible to perfluorohexane molecules because of the large molecular size. Porosity data based on perfluorohexane X-ray reflectivity porosimetry provide a measure of pore interconnectivity. Significant pore interconnectivity of ULK materials can be caused by spin-on deposition followed by a baking process during sample preparation. The high pore interconnectivity values shown in Table 5.1 partially explain the deep modification of these ULK materials that we observed in

our previous work, i. e. deep fluorine permeation during fluorocarbon plasma etching.[5.8,5.9] The OSG material used here is deposited by chemical vapor deposition and is considered a non-porous material. Our measurements reveal a small amount of pores (7%) in OSG film with a very low proportion of interconnected pores (1%). The porosity result for the OSG material is in agreement with the low degree of fluorine permeation observed by dynamic SIMS measurements.[5.9] However, for OSG exposed to fluorocarbon plasmas the plasma surface reactions are mainly limited to the near surface regions. These findings suggest that plasma surface interaction mechanisms can be completely changed by both overall porosity and pore interconnectivity.[5.8,5.9]

	***k* Value**	**Porosity**	
		Toluene	**Perfluorohexane**
OSG	2.8~2.9	7%	1%
NPS I	2.2	32%	28%
NPS II	1.9	45%	40%

Table 5.1: *Dielectric constants and porosity of the materials used in this work. Toluene X-ray reflectivity porosimetry indicates overall porosity while the value revealed with perfluorohexane X-ray reflectivity porosimetry is believed to provide a measure of the proportion of interconnected pores.*

B. Plasma Processing and Diagnostics

The inductively coupled plasma reactor employed in this work has been described in detail in a previous publication.[5.14] The discharges were produced by a planar coil placed on top of a quartz coupling window and powered by a RF power supply at a frequency 13.56 MHz. The discharge pressure was maintained at 100 mTorr. This pressure emphasizes the attack of neutrals relative to that of ions and reduces ion energies by ion/neutral collisions in the sheath region for direct plasma

exposure conditions.[5.15] For remote plasma exposure conditions the radical flux is sufficient to enable high photoresist removal rates (>100 nm/min at certain conditions). The remote exposure conditions were achieved by using a small gap structure,[5.16] which prevents ion bombardment of the substrate located in the shadowed region. This gap structure approach enables the study of plasma surface interaction mechanisms in the neutral-dominated remote plasma region.[5.16] A schematic of the gap structure is shown in Fig. 5.1. The Si roof, 15 cm x 15cm, is supported by two spacers (8 mm high), which are laid on the electrode. The sample is shielded by the roof and ion bombardment is significantly reduced. Reactive species diffuse through the gap and react with the sample. Ions are effectively deionized by collisions with surfaces.[5.17] The remote location of the substrates necessitates multiple wall collisions of the diffusing species before the shielded substrates can be reached, reducing the overall importance of ions relative to neutrals in the remote plasma attack as long as the sample to be processed is placed far enough from the entry. Overall, we believe that the results obtained with this setup captures essential elements of the plasma-ULK surface interactions that would be seen for a commercial remote plasma reactor.

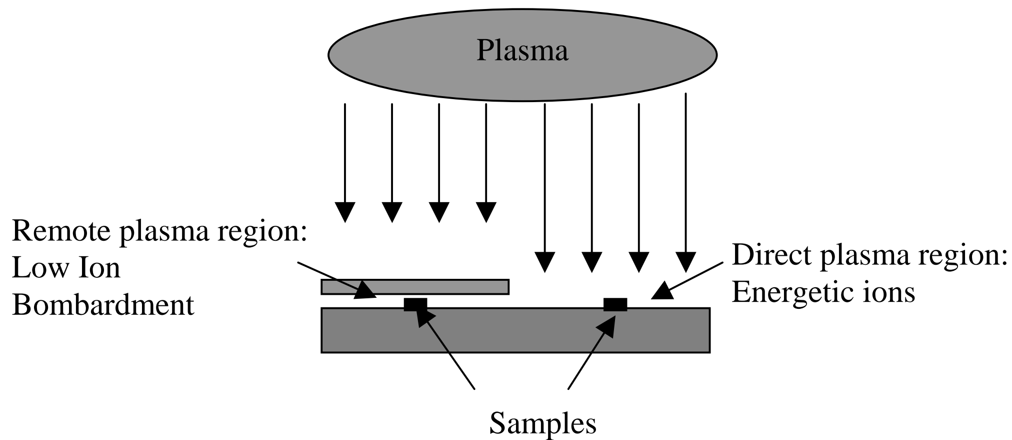

Figure 5.1: *A schematic of the gap structure: Samples placed in the region shielded by the roof primarily interact with neutrals, the remote plasma processing regime. For samples placed in the plasma exposed region, low energy ion bombardment assists in the plasma-surface interaction.*

A variety of complementary materials and surface characterization techniques were used to characterize film thickness, composition and bonding, pore morphology, and surface morphology of both blanket ULK films and plasma etched/ashed structures. The techniques included ellipsometry, x-ray photoelectron spectroscopy (XPS), secondary ion mass spectroscopy, x-ray reflectivity, transition electron microscopy (TEM), scanning electron microscopy (SEM), and atomic force microscopy (AFM). Experimental details on these measurements can be found in previous publications.[5.8,5.9]

A simple approach of establishing the carbon depletion depth of a carbon containing silica film is based on the following approach.[5.18] A 1% dilute HF solution cannot be used to dissolve as received OSG and ULK materials which contain carbon groups and Si-CH_3 bonds. Once the carbon has been removed to a significant extent

by the plasma exposure, the densified, carbon-deficient layer can be quickly etched using 1% diluted HF solution. This method, in conjunction with ellipsometry, has been shown to be a convenient method to study the modifications of ULK and low k materials induced by plasma ashing processes.[5.18]

5.3 RESULTS AND DISCUSSION

1. Direct Plasma Exposure

Direct plasma exposure is attractive for stripping of the photoresist mask after a plasma etching process, since it can be performed in the same process chamber. To avoid possible damage due to ion bombardment, the discharges used for photoresist stripping are normally generated at low power and high pressure without applying an RF bias voltage. Use of O_2 plasmas has been a standard approach for photoresist ashing.[5.19] Modifications of carbon containing dielectric materials induced by oxygen stripping processes can lead to unacceptable damage, in particular carbon loss, densification and an increase of the dielectric constant.[5.2] In this work, alternative ashing chemistries employing N_2 or H_2 were investigated and their performance was compared with that of O_2 discharges.

The photoresist removal rate has to be high enough so that complete mask removal is possible for different ashing processes. For our conditions, i. e. source power 500 W, pressure 100 mTorr, and total gas flow rate 50 sccm, the photoresist removal rates are 150 nm/min, 40 nm/min and 26 nm/min for direct O_2, N_2 and H_2 plasmas, respectively. O_2 discharges are certainly the most efficient for photoresist

ashing. However, the modification on ultra low k materials during these processes is another concern.

Damaged Layer Thickness: The damaged layer thickness is determined by the thickness difference between as received films, and the remaining film thickness for samples after plasma exposure and subsequent 1 % HF dissolution of the modified layer. The damaged layer thicknesses obtained with of OSG, 32 % porous NPS and 45 % porous NPS films due to direct exposure to O_2, N_2, or H_2 discharges are summarized in Fig. 5.2 (a). Discharge conditions were 500 W 13.56 MHz source power, a pressure of 100 mTorr and a total gas flow rate of 50 sccm. The figure shows that O_2 discharges introduce the most damage to the lowk/ULK materials investigated. For N_2 or H_2 discharges reduced damage levels are obtained. The net damage depth is similar for both types of discharges. For instance, within 1minute of plasma exposure, ULK materials can be modified to a depth of several hundred nanometer, comparable to the complete thickness of layers used in actual structures. The damage is linearly proportional to the process time for the nanoporous materials for these processes, showing that subsurface reaction is not limited by diffusion phenomena for the time regime investigated. On the other hand, the damage depth of OSG materials is low and the modified layer is limited to the near-surface region. The OSG damage depth saturates at 70 nm for O_2, and 30 nm for both N_2 and H_2 after a plasma exposure time of 40 s.

Ion sampling measurements performed on a similar ICP system in our laboratory show that the plasma potential is around 20-30 eV for the discharge

conditions used here. If we ignore ion-neutral collisions which will reduce the corresponding ion impact energies, the ion penetration at these energies in silica materials is limited to a few nanometers.[17] From the deep modification of OSG and nanoporous silica as a result of exposure to ashing discharges, we conclude that diffusion of neutral species is an important mechanism in the damage process. From the dependence of damage depth on overall porosity we conclude that the diffusion processes are enhanced by the presence of nanopores in the materials. The fact that saturation of the damage depth is only observed for OSG suggests that plasma-driven reactions in the subsurface region are governed not only by overall porosity but also pore interconnectivity. Assuming that the plasma only reacts with the matrix and all nanopores (assumed to be vacuum cavities) are isolated, the damage thickness is expected to be inversely proportional to the mass density. Based on this, we may expect that the damage saturates at 96 nm and 119 nm for 32 % and 45 % porous NPS materials, respectively. This estimate is not consistent with the experimental observations. A possible reason is that interconnected pores enable long-range migration of reactive species from the surface to the deep bulk region. During the transport in connected pores, recombination of radicals does not occur at a high rate, and reactions with carbon, i. e. Si-C bond breaking and carbon oxidation can take place deep inside the nanoporous material and chemically modify the material. Although the reactive species for O_2 and H_2 discharges are completely different, the porosity dependence of the damage thickness is similar for the two types of discharges (see Fig. 5.2 (b)) after 10 s plasma exposure. For these conditions the damage depths increase exponentially with porosity at the same power. This indicates

a universal behavior for diffusion of reactive species through interconnected pores. Oxygen radicals appear much more reactive than hydrogen-related species. The activation energy for the reaction is lower in the case of oxygen, resulting in a higher reaction rate.

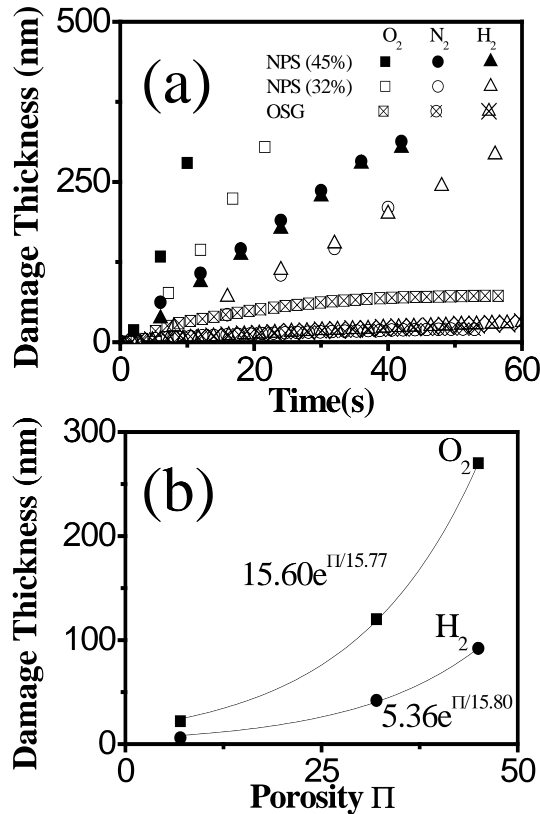

Figure 5.2: *(a) Damage thickness as a function of process time of O_2, N_2, or H_2 discharges; (b) Influence of porosity on damage layer thickness after 10 s of either O_2 or H_2 discharge treatments. Discharges were generated using a source power of 500 W, pressure 100 mTorr, and total gas flow rate 50sccm. Damage thickness was determined with the 1 % HF dipping method and ellipsometry.*

Photoresist Stripping Efficiency: To evaluate different stripping processes, the ratio between the damage (discussed in next section) and resist removal is an important parameter to consider and provides a measure of the process efficiency. Although the absolute damage of NPS materials by an oxygen plasma for a given exposure time is the worst, oxygen discharges are more efficient for stripping photoresist from the

ULK materials studied here since the photoresist stripping rate in O_2 is very high. The efficiency also depends on the porosity as shown in Fig. 5.3. The photoresist thicknesses of actual masking layers and the thickness of dielectric materials are both a few hundred nanometers. The data plotted in Fig.5.3, indicate that the whole bulk of the dielectric material is damaged by all ashing processes before the photoresist has been removed. We must keep in mind, however, that this analysis overestimates the damage to the low k and ULK materials in actual device structures. For actual device structures the dielectric materials would not be directly exposed to the discharge for most of the duration of the plasma ashing process. Nevertheless, low k and ULK ash damage due to direct exposure is a significant concern, and the investigation of alternative approaches is desirable.

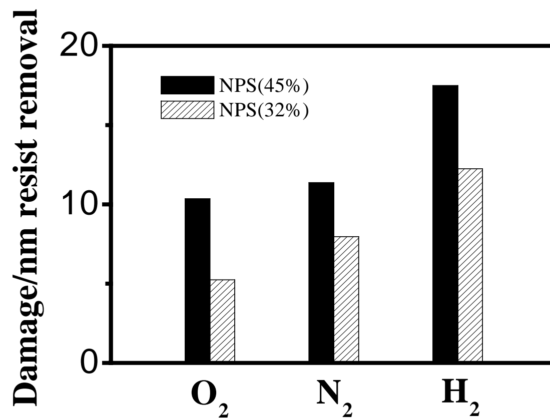

Figure 5.3: *Process efficiency defined as NPS damage thickness per nm photoresist removal for different direct discharges examined in this work. Discharges were generated with source power 500 W, pressure 100 mTorr, and total gas flow rate 50 sccm.*

Surface Characterization Employing XPS: To clarify the mechanism of stripping process-induced modifications of OSG and NPS materials, surface analysis of direct

plasma-treated specimens was performed using XPS**.** The intensities of C 1s and Si 2p spectra obtained with NPS material (32 % porosity) after O_2, N_2 or H_2-based stripping processes are summarized in Fig.5.4 as a function of processing time. Figure 5.4 shows that O_2, N_2 or H_2 stripping processes introduce densification and carbon depletion. Figure 5.4 shows that O_2 is the most damaging ashing process. Carbon is depleted near the surface within 2 s exposure to the oxygen discharge. Since the probing depth of XPS is about 10nm,[5.20] the carbon depletion extends to at least 10 nm from the surface, even though the time of the exposure to the direct O_2 plasma is only two seconds. The removal of the carbon groups can cause the collapse of the SiO-matrix. This produces a denser material. Consistent with this expectation, densification accompanied carbon depletion and is evident in the XPS data of Fig. 5.4.

Figure 5.4 shows that use of H_2 discharges minimizes the modifications of the NPS material relative to using O_2 and N_2 discharges. However, even for H_2 discharges, complete removal of carbon in the near-surface region is observed after long (40 s) plasma exposure time. For N_2 discharge treatments we observed that the drop of the C1s intensity for long plasma exposure times is accompanied by nitrogen incorporation into the NPS material. Overall, we conclude that the XPS data obtained with ULK materials after different time exposures to O_2, N_2 or H_2 discharges are consistent with the results of the damage thickness measurements based on selective HF etching of the damaged layer and subsequent ellipsometric thickness measurement.

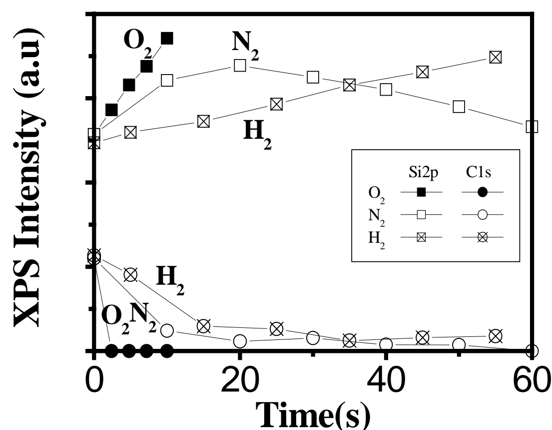

Figure 5.4: *Si2p and C1s intensities obtained using XPS with plasma-treated NPS films as a function of process time. Results for direct O_2, N_2 or H_2 plasma treatments are shown. Carbon depletion and densification are observed for all ashing processes. Discharges were generated with source power 500 W, pressure 100 mTorr, and total gas flow rate 50 sccm.*

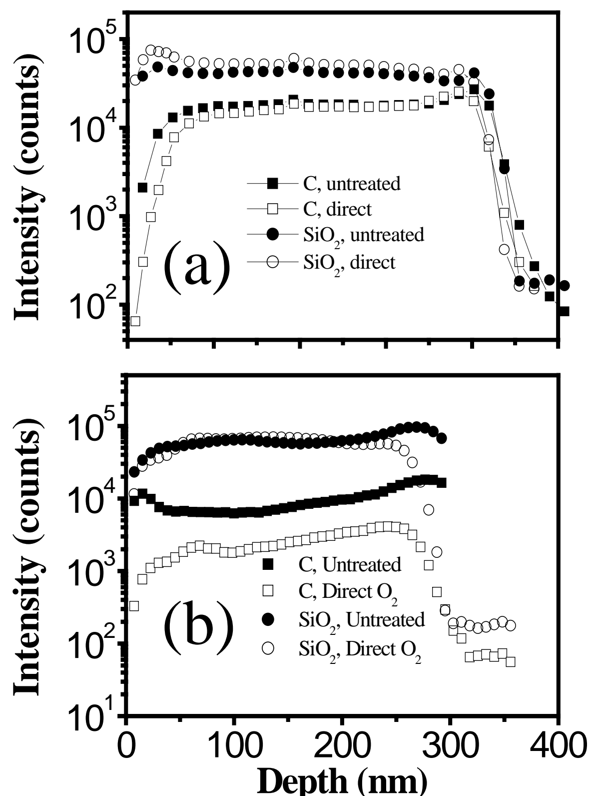

Figure 5.5: *TOF SIMS depth profiles of OSG(a) and 3 2% NPS (b) material after 30 s direct plasma exposure employing O_2. The intensities obtained with untreated materials are shown for comparison. Discharges were generated with source power 500 W, pressure 100 mTorr, and total gas flow rate 50 sccm.*

Characterization of Bulk Modifications Using Dynamic SIMS: Information on plasma-induced bulk modifications of the dielectric materials was obtained using dynamic SIMS. Representative results are shown in Fig. 5.5 for OSG and NPS materials after 30 s O_2 exposure, along with data obtained for untreated materials. Carbon depletion (reduced C signal) and densification (increased SiO_2 signal) were verified in the SIMS studies. For OSG, the materials modifications are restricted to the near-surface region, and can be explained by the low porosity of this material. In this case, significant carbon loss was seen to a depth of ~70 nm from the surface, consistent with the damage thickness determined using the HF dipping method. For the highly porous dielectric (32 % porous NPS), carbon loss was observed throughout the bulk of the material. This shows that a 30 s exposure to a direct O_2 discharge is sufficient to modify the entire bulk of the NPS material. At the same time, thickness shrinkage is evident in Fig. 5.5 for the 32 % NPS material. Thickness shrinkage is not seen for the OSG material. The carbon loss amounts to about 50 % in the bulk of the O_2 plasma treated NPS material relative to that measured for a control. This implies that the HF etching method will etch carbon-containing SiO_2 material, as long as either the C content is reduced sufficiently, and/or Si-C bonds in the matrix are broken. Essentially, the SIMS measurements shows that oxygen replaces easily C of the SiC groups in the matrix, but that residual carbon is present in the dielectric material after oxygen plasma attack. This is consistent with the XPS measurements, which showed residual carbon content of the NPS material after part of the damaged layer had been removed using HF.

The SIMS data on the dielectric materials modifications caused by exposures to direct N_2 or H_2 discharges were found to be similar to those obtained with O_2 plasmas, albeit at lower modification rates. For the sake of brevity, we will not show these data.

5.3.2. Remote Plasma Photoresist Stripping and ULK Damage Effects:

During photoresist removal by an ashing process, C-C bonds which are the primary bonds in the photoresist backbone, must be broken and volatile compounds formed by reaction with the reactants. The bond energies of C-C bonds and Si-C bonds are comparable (3.71 eV).[5.21] Therefore, it is not surprising that the aggressive approach to photoresist removal realized by direct plasma exposure, where the attack of the photoresist by reactive neutrals is assisted by ion bombardment, can be highly damaging to carbon containing silica-based ULK materials. During direct plasma exposure, Si-C bonds may be broken by ion bombardment. This explains the unacceptable damage to the NPS material, regardless if O_2, N_2 or H_2 discharges are employed for photoresist stripping. To reduce physical bombardment damage, the photoresist-coated ULK film needs to be shielded from direct plasma exposure. We previously described a small gap structure that prevents direct ion bombardment of surfaces during processing and that has been used to study aspects of gas-surface interactions that are characteristics of remote plasma processing.[5.16] In the current work, a roof that is large relative to the sample size was used to shield the sample and enable interaction with reactive neutrals.

Damaged Layer Thickness: Figure 5.6 shows the damaged layer thickness of NPS materials with two different porosities as a result of exposure to O_2, N_2, and H_2 remote plasmas. The damage levels measured after O_2 remote plasma exposure are comparable to those measured after direct plasma exposure, indicating that the reactive species present in the afterglow of O_2 discharges are able to damage Si-C bonds even without assistance by ion bombardment. Since the energy flux incident on the surface for the remote plasma exposure is much lower as compared with direct plasma exposure, we conclude that the activation energy of the reaction between oxygen radicals and Si-C bonds is low and the energy carried by the reactive species is sufficient to activate a reaction with the carbon species. Although the damage levels seen for nanoporous silica materials for direct and remote O_2 plasma exposure are similar, the photoresist removal rate decreases to 20 nm/min for remote plasma exposure. A possible explanation is a higher activation energy of the overall chemical reaction that results in photo resist removal – breaking C-C bonds and forming volatile CO and CO_2 species by reaction with atomic O - relative to damaging Si-C bonds by O atom attack. We conclude that both direct and remote O_2 plasma photoresist stripping introduces unacceptable damage levels in nanoporous ULK materials.

Use of remote N_2 discharges for photoresist ashing shows greatly reduced damage levels of nanoporous ULK materials, whereas the damage levels seen for remote H_2 discharges can no longer be measured using our approach. At the same time, the photoresist removal rates for both remote N_2 and H_2 discharges are impractically small if the substrates are held at room temperature. Since remote N_2

discharges still introduces damage of the NPS materials, the remainder of this article is focused on increasing the photoresist removal rates for remote H_2 discharges while minimizing the amount of NPS damage.

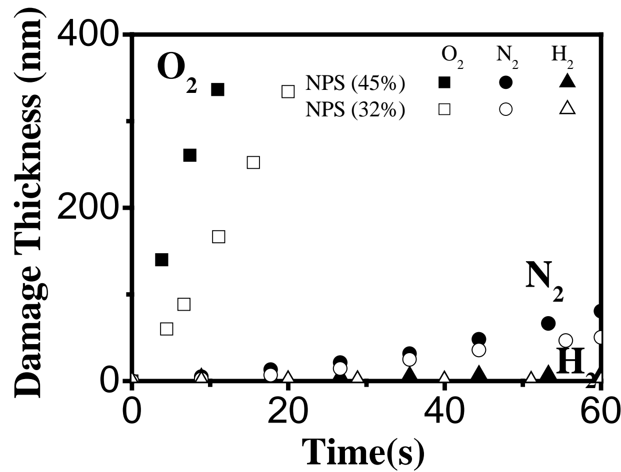

Figure 5.6: *Thickness of damaged layers produced in NPS materials as a result of remote plasma exposures using O_2, N_2 or H_2 discharges. Discharges were generated with at a source power level of 1000 W, pressure of 100 mTorr, and total gas flow rate of 50 sccm.*

Temperature Dependence: One possible way to increase the photoresist stripping rate is to increase the substrate temperature. By raising the substrate temperature to 260 ^{0}C for a remote H_2 discharge, the ashing rate of photoresist could be increased to ~100 nm/min. To evaluate the influence of photoresist polymer structure on ashing rate, we studied ashing of both 193 nm and 248 nm photoresists in remote H_2 discharges. For 248 nm photoresist, the polymer backbone contains aromatic rings, which is stable in the plasma environment due to C=C bonds in the ring.[5.21] Because of high UV absorption of C=C, these polymers are not suitable at 193 nm photolithography, which is required for the integreation of future device.[5.22, 5.23]

Instead of the aromatic ring structure, 193 nm photoresist materials consists a polymethylmethacrylate backbone with lactone- and adamantine-based substituents. In Fig. 5.7 the temperature dependence of the ashing rates of both 248 nm and 193 nm photoresist materials is shown for remote H_2 discharges. The photoresist ashing rates start to increase rapidly once the substrate temperature exceeds 150 ^{0}C. This corresponds approximately to the glass transition temperature (T_g) of these polymers.[5.24] If the temperature is below T_g, polymers are rigid and the chain mobility is small. As the substrate temperature rises above T_g, the segmental mobility of the polymer increases. Thus, a higher reaction rate with the plasma is expected for photoresists once the temperature is above T_g. Figure 5.7 shows that the ashing rate of the aromatic ring containing 248 nm photoresist increases at a much slower rate with temperature than the ashing rate of the 193 nm photoresist material in the remote H_2 plasma. Figure 5.7 also shows that the damage layer thickness of the NPS material remains below 10 nm as the substrate temperature is increased up to 300 ^{0}C. Apparently, the residual carbon groups in the nanoporous silica material are stable at high substrate temperature, and the attack due to the remote H_2 plasma is minimized.

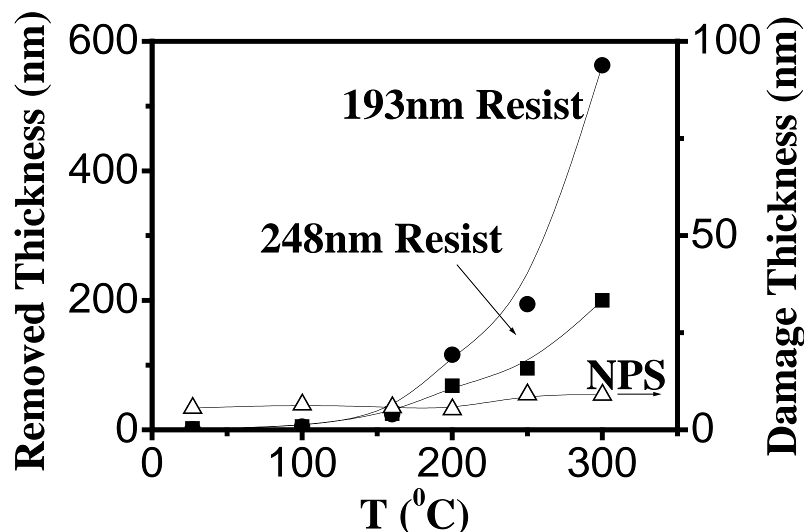

Figure 5.7: *The effect of substrate temperature on removed photoresist thickness and nanoporous ULK material damage layer thickness after 1 minute exposure to a remote H_2 plasma. Discharges were generated using 1000 W source power, a pressure of 100 mTorr, and a total gas flow rate of 50 sccm.*

Surface Characterization Using XPS: When NPS materials were exposed to remote O_2, N_2 or H_2 discharges, pronounced differences in damage layer thickness were seen (see Fig. 5.6). XPS was used to examine the plasma exposed NPS materials and clarify the reasons for these differences. Figure 5.8 shows C 1s and Si 2p spectra obtained with NPS materials after 60 s exposure to either O_2 or H_2 remote plasmas. The spectra of an untreated sample are shown for comparison. Figure 5.8 shows that for a remote O_2 plasma the carbon was nearly completely removed and that significant densification of the NPS was introduced (as made evident by the increased Si 2p intensity). This confirms that a remote O_2 plasma strongly modifies the properties of carbon containing ULK materials. When the NPS material was exposed to a remote H_2 discharge, a small reduction of the carbon intensity was observed. The

Si 2p intensity remained essentially the same as the one obtained with an untreated NPS film. It is possible that the reduced carbon signal may be due primarily to loss of surface carbon, and thus no correlated densification of the SiO-matrix is seen in this case.

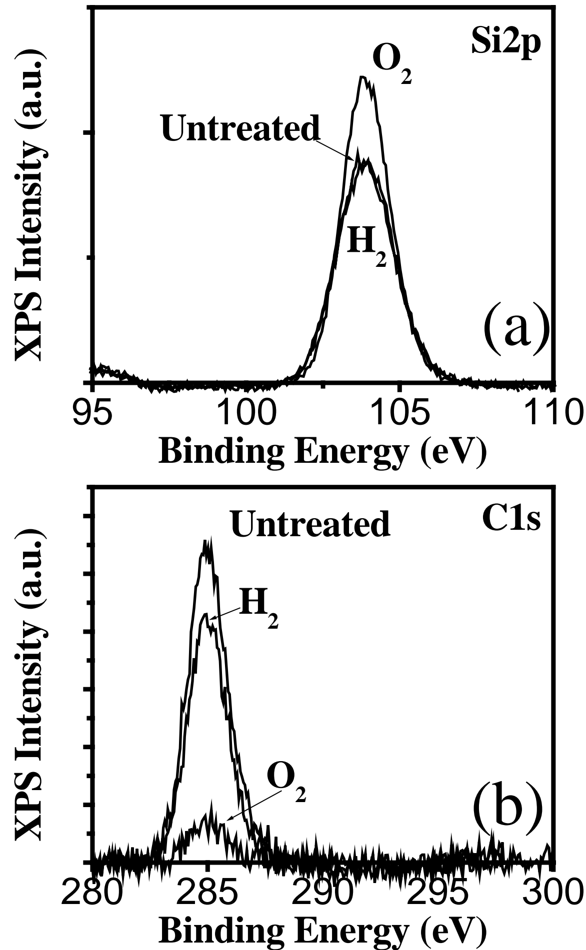

Figure 5.8: (a) *Si2p and (b) C1s XPS spectra obtained with 32% porous NPS films after either 1 minute exposure to remote O_2 or H_2 plasmas. The substrate temperature was maintained at 260^0C. For comparison, XPS data obtained with an untreated NPS film are also shown. Discharges were generated using 1000 W source power, a pressure of 100 mTorr, and a total gas flow rate of 50 sccm.*

Bulk Characterization Using Dynamic SIMS: To improve our understanding of the NPS damage mechanism and reveal deep penetration of reactive species into the

porous structure as a result of exposure to remote plasmas useful for photoresist ashing, we performed characterization of the NPS composition as a function of depth using dynamic SIMS. The results are shown in Fig. 5.9. The following observations stand out: Firstly, we note shrinkage of the NPS material by about 70 nm thickness after remote O_2 treatment at elevated temperature relative to a control. Secondly, severe carbon depletion throughout the bulk of the NPS material is apparent in Fig. 5.9. Third, a strong increase of the Si related signal is consistent with a significant increase of the SiO matrix density. The severe carbon reduction seen throughout the bulk of the NPS material shows that reactions between long-lived oxygen radicals produced in the plasma and the NPS material takes place at elevated substrate temperature and that elimination of ion bombardment is not sufficient to prevent these reactions for the present process conditions. Since the carbon content is reduced throughout the bulk of the NPS material to a fairly constant, we conclude that the oxygen-carbon interaction is not limited by the porous matrix of the NPS material for the film thickness investigated in this work.

The SIMS profiles obtained with NPS material after exposure to a remote H_2 plasma are essentially the same as those measured for untreated films. The absence of NPS materials modifications in this case is consistent with the damage thickness study and XPS characterization reported above.

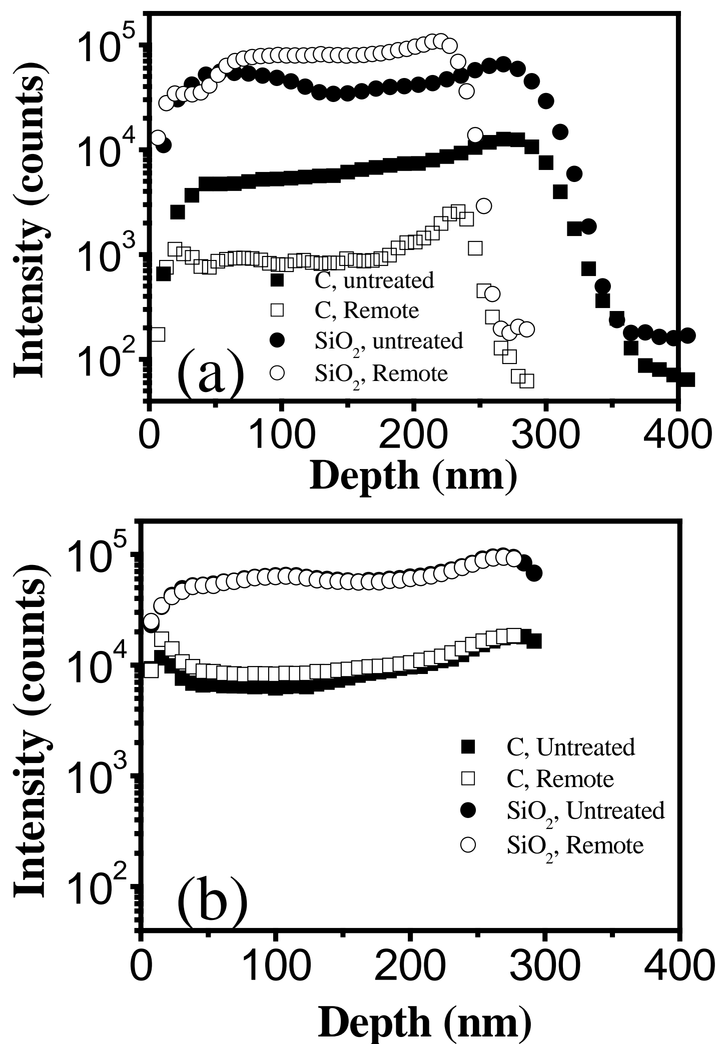

Figure 5.9: *Dynamic SIMS depth profiles of 32 % NPS materials after 30 s exposure to remote(a) O_2 or (b) H_2 plasmas at a substrate temperature of 260 ^{0}C. For comparison, dynamic SIMS data obtained with an untreated NPS film are also shown. Discharges were generated using 1000 W source power, a pressure of 100 mTorr, and a total gas flow rate of 50 sccm.*

Transmission Electron Microscopy (TEM). NPS films after exposure to remote O_2 and H_2 discharges along with an untreated control were also characterized by TEM. All samples were thinned by hand-polishing to avoid the damage caused by conventional ion sputtering sample preparation techniques. The results are shown in Fig. 5.10. The TEM image of an untreated film is shown in Fig. 5.10 (a). The initial film thickness obtained by TEM is 290 nm indicated. A NPS film after exposure to a remote H_2 plasma is shown in Fig. 5.10 (b). Essentially, the thickness of the material is 284~290 nm, close to the value of the control. Figure 5.10 (c) shows that the thickness after a remote O_2 treatment is reduced to 191nm, consistent with the thickness value obtained by SIMS. Because of the small pore size (2~3 nm diameter),[25] it is difficult to quantify the pore diameter from these images. Overall, it appears that the pores are more visible in images Fig. 5.10 (a) and (b), and comparable. This is further evidence that the pore morphology remains unchanged by the remote H_2 plasma process. The image shown in Fig. 5.10 (c) may be interpreted as indicating a pore size decrease as the film density increases as a result of the remote O_2 plasma treatment. The SiO matrix is densified as a result of carbon removal by oxidation, and the NPS material changes to become more similar to SiO_2, with a higher mass density. One may expect that the pore volume is reduced as the matrix collapses, consistent with the smaller pores seen in Fig. 5.10 (c).

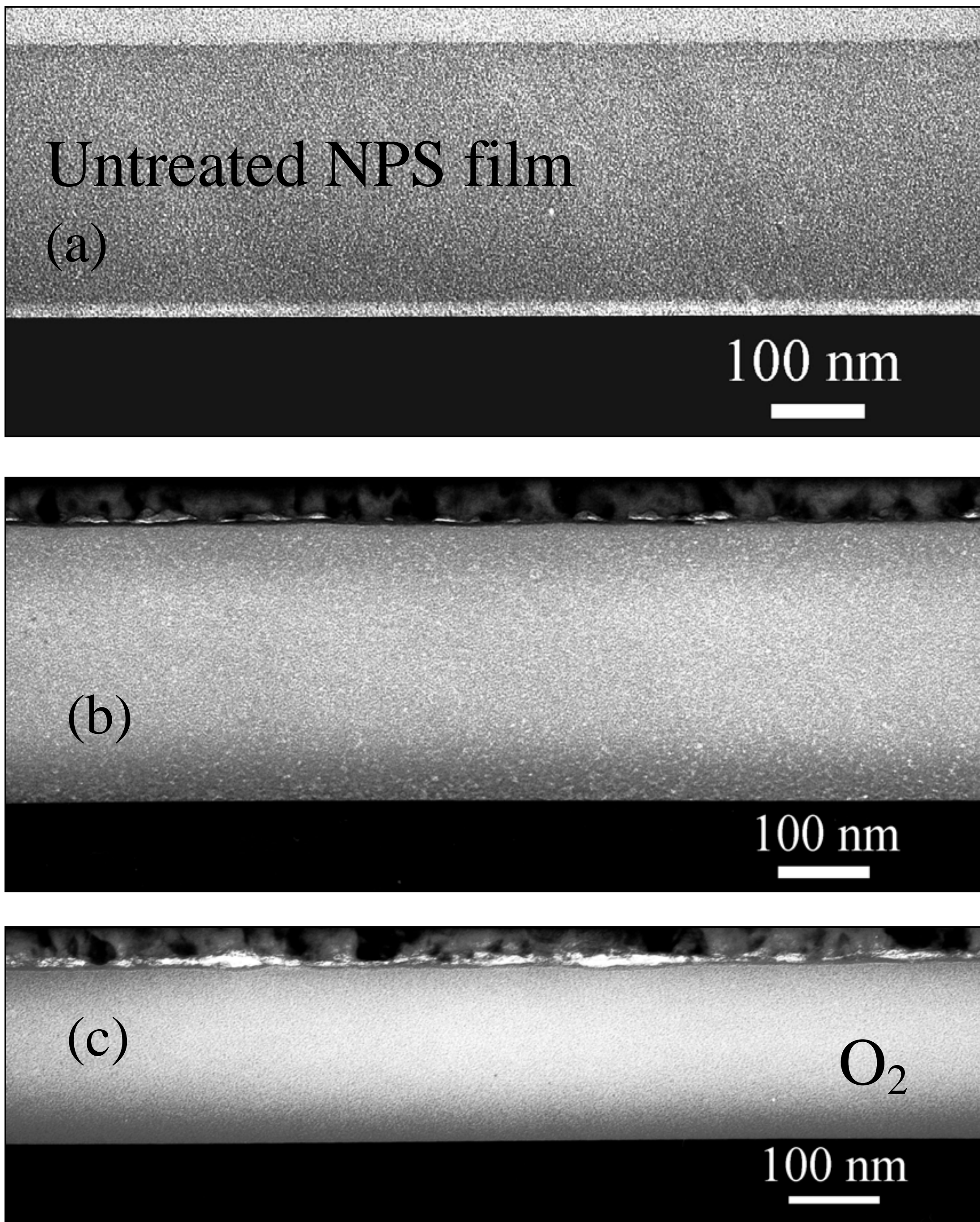

Figure 5.10: C*ross-sectional images of NPS films obtained by TEM. (a) untreated; (b) after 1 minute exposure to a remote H_2 plasma at a substrate temperature of 260^0C; (c) after 1 minute exposure to a remote O_2 plasma at a substrate temperature of 260^0C. Discharges were generated using 1000W source power, a pressure of 100mTorr, and a total gas flow rate of 50sccm.*

Atomic Force Microscopy (AFM): Nanoporous silica materials have a higher surface roughness as compared with SiO_2.[5.9] This may be explained by the presence of nanopores. The surface roughness qualitatively reflects the pore size (a few nanometers) if the surface is relatively smooth at a micrometer length scale. The RMS roughness obtained by AFM is plotted in Fig. 5.11. Figure 5.11 shows that exposure of NPS at elevated substrate temperature to a remote H_2 plasma does not modify the surface and the surface roughness remains about 1.2 nm. The surface roughness drops to 0.7 nm after exposure of NPS at the same substrate temperature to a remote O_2 discharge. This is possibly due to the reduction of the pore size seen in the TEM cross-sectional images. However, the surface of TEM cross sectional images shows a rougher surface for the NPS material after exposure to a remote O_2 discharge than the surface roughness seen after exposure to a remote H_2 discharge. It is possibly that this inconsistency may be explained by the deposition of a metal layer on the NPS surface during sample preparation for the TEM measurements.

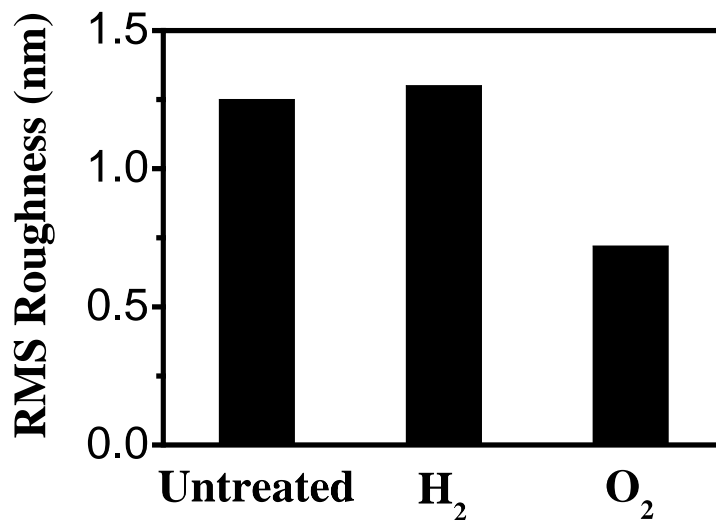

Figure 5.11: *RMS roughness results obtained by AFM measurements employing NPS films exposed to H_2 and O_2 remote plasma ashing processes. An untreated control is shown for comparison. Discharges were generated using 1000 W source power, a pressure of 100 mTorr, and a total gas flow rate of 50 sccm.*

Ashing Results Obtained Using Actual Etched Trench Structures: Actual trench structures were patterned using plasma etching employing a photoresist mask. The mask was subsequently removed using the remote plasma ashing approaches described above. The photoresist pattern was transferred using C_4F_8/90% Ar inductively coupled discharges for 1 minute. The discharges were generated using 1000W source power, a pressure of 100 mTorr, and a total gas flow rate of 50 sccm. An additional RF power supply at 13.56 MHz was used to bias the substrates at –125 V to enable directional etching of the dielectric materials. A scanning electron microscopy (SEM) cross-sectional image obtained with the etched trench structure is shown in Fig. 5.12 (a). The ULK film with a thickness of ~410 nm was completely etched using 20 % of overetching. The sidewalls of the etched trenches are sloped,

which is related to the deposition of fluorocarbon material on the sidewall. On top of the lines of ULK material, the 248 nm photoresist mask is located, with a thickness of 250 nm. To remove the remaining photoresist mask**,** the etched trench structures were exposed to remote O_2 or H_2 plasmas at an elevated substrate temperature (260 ^{0}C). To guarantee complete removal of the photoresist mask, the etched trench structures were exposed for a length of time that was 30% greater than the nominally required ashing time (based on the thickness of the photoresist mask and measured photoresist ashing rates). The SEM images show that the resist films were successfully removed using both O_2 and H_2 remote plasmas. The thickness of the NPS material exposed to the remote H_2 discharge remained essentially the same as measured after plasma etching with the photoresist mask still in place. On the other hand, the thickness of the NPS layer was reduced by about 50 nm if photoresist ashing was performed using an remote O_2 discharge. The trenches became wider after the ashing process, which is possibly related to the removal of fluorocarbon material present at the trench sidewalls. A remote O_2 discharge is more effective for the removal of FC residues which leads to wider trenches as compared with remote H_2 plasma processing. Additionally, the ultra low k material will be densified and the lateral width of the structure reduced as a result of oxygen species attack of the NPS matrix.

Overall, the results of removing photoresist from actual plasma etched structures are consistent with the characterization of blanket NPS films described in this work. The structure investigation shows that remote O_2 discharges are not suitable to strip photoresist from porous low k structures, whereas use of remote H_2 discharges is promising if the substrate temperature is above 250 ^{0}C.

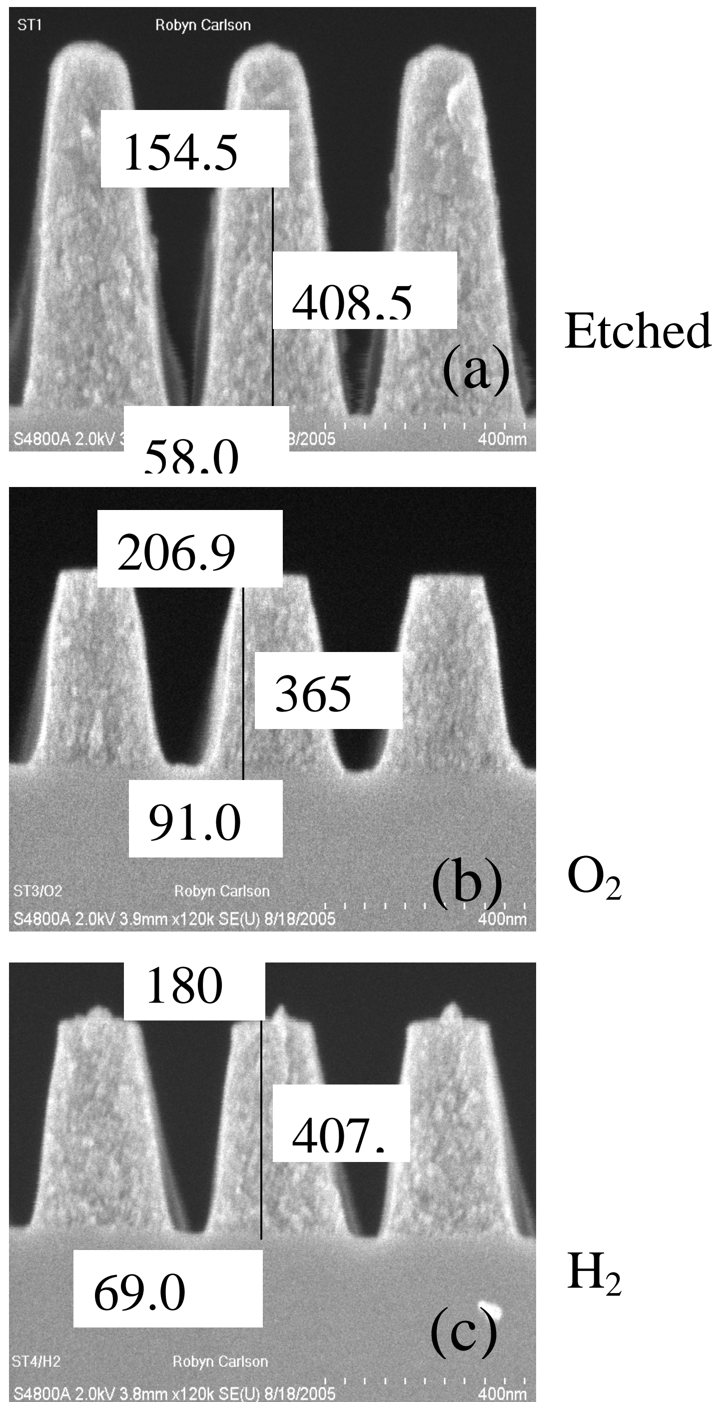

Figure 5.12: *Cross-sectional scanning electron microscopy images of NPS trench structures after: (a) directional etching using C4F8/90%Ar and employing a selfbias voltage of –125V;(b)1 minute remote O_2 discharge ashing;(c)3.5 minute remote H_2 discharge ashing. Discharges were generated using 1000W source power, a pressure of 100mTorr, and a total gas flow rate of 50sccm.*

5.4 SUMMARY AND CONCLUSIONS

Plasma induced modifications of nanoporous ultra-low k dielectric materials as a result of exposure to various plasma processes useful for removing photoresist masks from plasma etched structures were studied using complementary methods. The most significant ashing plasma-induced modifications seen for the carbon containing nanoporous silica materials examined in this work are carbon depletion, and densification of the SiO_2 matrix. From this work it appears that carbon depletion is connected with a reorganization of the silica matrix and a reduction of the pore size, resulting in a densification of the NPS material. Direct plasma exposure of the NPS materials induces unacceptable damage, regardless if O_2, N_2 or H_2 discharges were employed. Use of O_2, N_2 and H_2 based remote discharges for photoresist removal was also investigated. For remote O_2 discharges, NPS damage levels were still unsatisfactory. By employing remote H_2 discharges, the damage layer thickness of NPS materials could be reduced to a value of about 1 nm for substrate temperatures ranging from room temperature to greater than 250 ^{0}C. Simultaneously, for substrate temperatures greater than 250 ^{0}C, the photoresist ashing rates could be increased to values above 100 nm/min.

Acknowledgements

Financial support of this work by the Semiconductor Research Corporation's Center for Advanced Interconnect Sciences and Technology (CAIST) is gratefully acknowledged. We also thank International SEMATECH and Texas Instruments for supply of ULK materials.

Chapter 6: Studies Of Plasma Surface Interactions During Short Time Plasma Etching of 193nm and 248nm Photoresist Materials

To be submitted to J. Vac. Sci. Technol. A., 2005

Xuefeng Hua, S. Engelmann G.S. Oehrlein, P. Jiang, P. Lazzeri, E. Iacob and M. Anderle

ABSTRACT

As the device dimensions scale to 100 nm, the use of photoresist materials suitable for lithographic patterning at 193nm. The molecular structure of 193nm photoresist materials is significantly different from that of 248nm photoresist materials,[6.1,6.2] which leads to a number of undesirable consequences, including pronounced surface and line edge roughness during plasma etching.[3-5] In this article, we present an investigation of the mechanisms for the surface/line edge roughening of photoresist materials during plasma etching using C_4F_8/90% Ar discharges. We emphasized in our study short exposure times (the first few seconds) of the photoresist materials and structures to the plasma, a time regime that has not been well studied. Rapid modifications were observed for both 193nm and 248nm photoresists during short time exposure. During the first seconds of plasma exposure, photoresist material densification and hydrogen depletion are important processes. It is also found that rough surfaces develop within a few seconds exposure to the C_4F_8/90% Ar discharges. Plasma exposure leads to the formation of rough edges on the top of trench sidewalls in photoresist trench and line structures. During prolonged exposure to the plasma, the roughness is transferred to produce striations on the sidewalls. After an initial stage, the roughening rate remains constant for 193nm photoresist, whereas for 248nm photoresist

the roughening rate is negligible. This difference is possibly related to the preferential removal of carbonyl groups for the 193nm photoresist material, which has been revealed by x-ray photoelectron spectroscopy and seconday ion mass spectroscopy.

6.1 INTRODUCTION

For the fabrication of sub-100 nm structures, photolithography employs exposure at 193nm wavelength rather than at 248 nm to produce photoresist mask patterns. This change in exposure wavelength necessitates changes in the polymer structure used for the photoresists. The aromatic ring structure on which 248 nm photoresists are based and that retains the image characteristics when exposed to energetic ion bombardment accompanying plasma etching of dielectrics is not suitable for 193nm photolithography because of the high absorption of C=C bonds at 193nm.[6.1,6.2] A significant modification of the photoresist polymer structure is required to enable exposure at 193 nm wavelength.[6.3,6.4] Polymethacrylates are highly transparent at 193 nm and are thus used in the design of 193nm photoresist. Alicyclic structures such as adamantane and norbornane are also incorporated in the structure to enhance the etch resistance.[6.3] Typical molecular structures of the 193 nm and 248 nm photoresist polymers employed in the current work are shown in Fig. 6.1.[6.5] 193 nm photoresist consists of methyl adamantyl methacrylate (MAMA) and alpha methacryloyloxy gamma butyrolactone (α GBLMA), which contain that contains adamantane and lactone groups respectively as indicated. In 248 nm photoresist, polyhydroxy styrene (PHOST) is used.

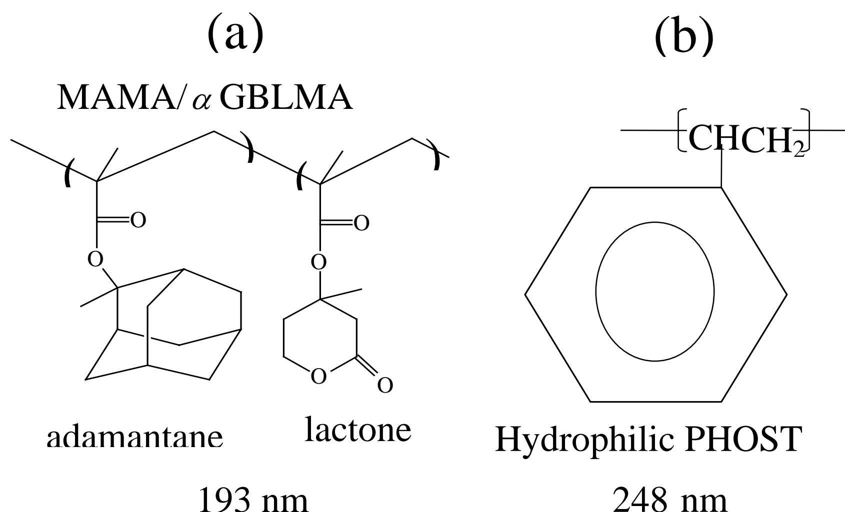

Figure 6.1: *Molecular structures of (a) 193nm and (b) 248nm photoresists.*

Due to these structural changes, 193 nm photoresist materials can exhibit less etching resistance and more severe surface roughening relative to 248 nm photoresist in plasma etching environments, in particular fluorocarbon dischargeswhich are widely used for the transfer of the photoresist pattern into dielectric films. [6.6-6.14] Surface roughness may produce roughness of feature sidewalls that can be transferred into the films being etched.[6.15-6.18] These problems need to be solved to achieve successful fabrication of integrated circuits with sub-100 nm critical dimensions. However, the mechanisms causing these problems have remained unclear because of the complexity of the plasma-polymer materials interactions. One major challenge in the study of plasma surface interactions with fluorocarbon discharges is to obtain reliable data on surface modifications for short plasma exposure times. This task is made difficult by the fact that for fluorocarbon discharges the time to achieve stable plasma characteristics can range up to 30 s.[6.6] This time scale of plasma stabilization is often much greater than the time required to achieve steady-state surface conditions for a blanket surface exposed to a plasma. This situation makes it difficult to employ conventional plasma processing

approaches to obtain clear information on the initial stages of the plasma-polymer interaction. To improve our understanding of plasma-surface interactions, we employed for this work a shutter approach describe in a previous publication.[6.19] Using the shutter approach, we were able to expose 193 nm and 248 nm photoresists to stable fluorocarbon-based plasmas for short times (fractions of second to several seconds) in a highly controlled fashion.

In this work, we studied fluorocarbon plasma etching of 193 and 248nm photoresists with the shutter approach. Details of the shutter approach will be described in the section of experimental setup and procedures. Plasma induced modifications of these polymers will be discussed for both structures and blanket films in the section of results and discussions.

6.2 EXPERIMENTAL SETUP AND PROCEDURES

The inductively coupled high-density plasma-etching reactor used for this study has been described in a previous publication.[6.20] A planar coil is placed on top of a quartz window and powered through an L-type matching network by a 13.56 MHz, 0-2000 W power supply to generate plasma which is confined to a narrow region 2-3 cm below the window by induced electromagnetic fields. The ion bombardment energy at the substrate electrode (300 mm diameter) is controlled by applying a RF bias voltage using another 13.56 MHz power supply (0-1000 W). The wafers are located at the center of the electrode that is cooled by circulation of a cooling liquid to 15 ^{0}C. Total gas flow into the reactor was set at 50 sccm. An operating pressure of 10 mTorr was maintained by using an automatic throttle valve in the exhaust line. Before each experiment, the chamber was

cleaned using an O_2 plasma, followed by a 3 minute chamber seasoning using the conditions for the next experiment. After that, the sample is loaded and the experiment of interest is conducted. A thin metal mesh is installed around the discharge region to ensure stable processing conditions and reproducibility. The temperature of the vessel wall was kept constant at 50 ^oC using heating straps.

The materials used in this work are 193 nm and 248 nm photoresists. For patterned samples, the photoresist materials - 300 nm and 410 nm thickness for 193 nm and 248 nm lithography, respectively - were spin-coated on ~80 nm thick bottom antireflection coating (BARC) layer, underneath which there is organosilicate glass layer. Line and trench patterns were formed in the photoresist materials by lithographic exposure and development. The structures were directly exposed to C_4F_8/90% Ar plasmas without initially etching the BARC layer using a plasma etching process, as is done conventionally. The reason is that we were interested in initial stages of the modifications of the photoresist materials and structures as a result of exposure to C_4F_8/90% Ar discharges. After plasma treatments, scanning electron microscopy (SEM) was used to characterize the profile evolutions of patterned samples. We also studied plasma exposure of blanket films of 193 nm and 248 nm photoresists. Single wavelength (632.8 nm) ellipsometry was employed to measure the time-dependent etching rates and the surface modification as a result of plasma etching. Surface morphology was analyzed with atomic force microscopy (AFM). X-ray photoelectron spectroscopy (XPS) analysis was performed at 90^0 take-off angle using a nonmonochromatized Mg K-alpha X-ray source (1253.6 eV) to obtain the photoemission spectra of partially etched samples after sample transfer in air. The pass energy of the hemispherical analyzer was fixed at 20 eV.

Secondary ion mass microscopy was employed to obtain additional information on chemical transformations.

For plasma processing of nanoscale layers, the total length of the substrate-plasma interaction time decreases to a few seconds and less. For short plasma-substrate interaction times, transient plasma effects, including electrical matching, plasma stabilization, and changes in plasma composition due to changing plasma-wall interactions play a more important role than for longer plasma processes. Our ability to control plasma induced nanoscale surface modifications of a substrate is reduced relative to larger length scales. For instance, Figure 6.2 (a) shows the temporal behaviors of the OSG etch rate and of the fluorocarbon deposition rate for fluorocarbon plasma using typical conditions, where the substrate is in contact with the plasma during all phases of the plasma process, including initialization of the discharge, biasing of the substrate, desired plasma processing by plasma/substrate interaction and plasma extinction. Constant etching or deposition rates are achieved after about 30 s for our experimental conditions. This reflects that during the initial period (first 30 s in our experimental conditions), the plasma properties change as a function of time and substrate processing is poorly controlled. To increase the control of plasma processes, it is desirable to use a stabilized plasma for processing and prevent interference due to the initial transients. We use a moving shutter containing slits in close contact with the substrate, to control the interaction time of stabilized gas discharges with the substrate for nanoscale layer/nanostructure processing. During the initial time interval (~30s), when the plasma properties change significantly, the substrate is shielded by the opaque portion of the shutter to prevent interaction with the evolving plasma. Once the plasma is fully

developed, the shutter is translated across the sample at a chosen speed and the substrate is exposed to the plasma (see Fig.6.3). The plasma-substrate interaction time t is determined by slit width w and shutter traveling speed v according to $t = \frac{w}{v}$.

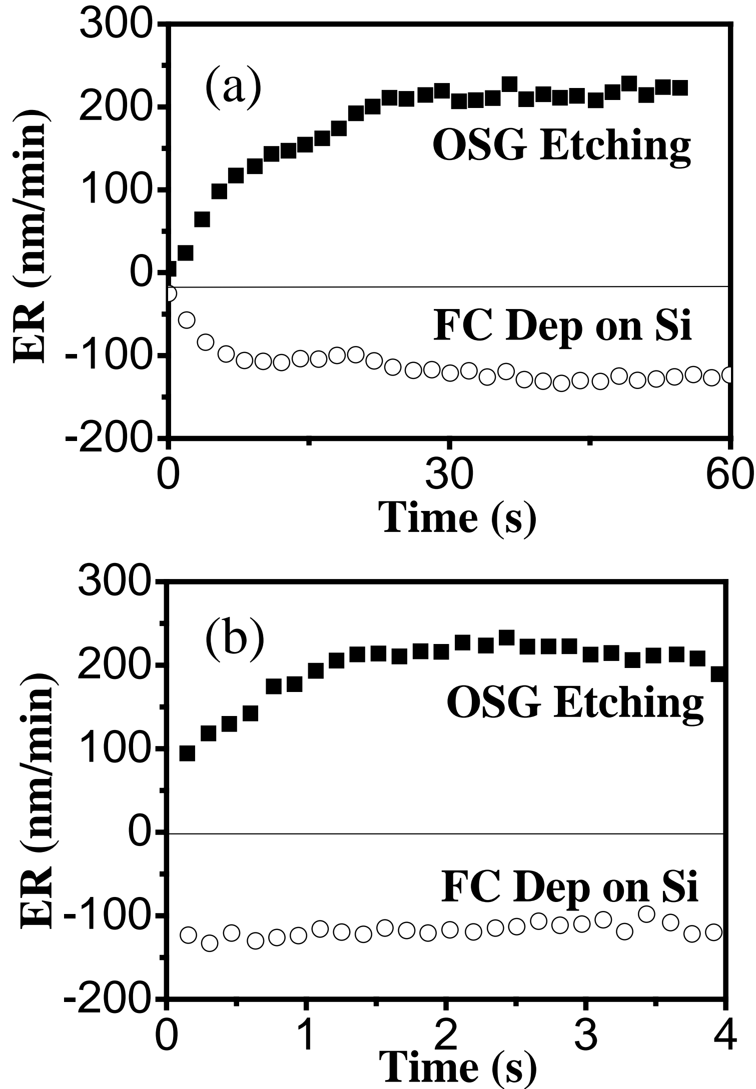

Figure 6.2: *OSG Etching/FC Deposition results: (a) conventional exposure; (b) shutter approach. Discharges were generated with 1000 W source power, a pressure of 10 mTorr, and total gas flow rate 50 sccm with a fixed bias voltage –125 V.*

The results of OSG ER and FC deposition rate with a stable plasma are plotted in Fig. 6.2 (b). The OSG etching rate no longer changes after about 2 s, whereas the fluorocarbon deposition rate was essentially constant throughout the entire experiment. The time to achieve a constant etching rate of the OSG material is determined by the plasma surface interaction mechanism, rather than by time constant of reactor processes, e.g. plasma-reactor wall interactions. These results indicate that for conventional fluorocarbon plasma etching and film deposition processes, , the time to achieve stable plasma properties is much greater than the times required to reach steady state surface etching and film deposition rates. The present shutter approach provides therefore the opportunity to study fundamental plasma-surface interactions in a time-regime that is not accessible using the conventional plasma processing approach.

The shutter employed in this work was made of silicon. The silicon etching rate in the fluorocarbon plasma environment is small, and a possible influence of etching product by interaction of the discharges with the shutter can be considered to be minor. The slits were generated by masking and using a wet etching approach for silicon using a dilute mixture of HF and nitric acid. The shutter was amounted directly on the substrate and positively contacted the substrate at several points. The movement of the shutter was controlled by a motor through a gear mechanism and vacuum feed through. In this work, we use a 18 mm wide slit, with which the perturbation on sheath topography is minor.[19] In addition to the uniform exposure of a complete substrate achieved with slits in the shutter, we have produced gradients of exposure time across a sample using the shutter approach. In the simplest case a sample is initially covered by the shutter and

subsequently exposed to the plasma once the plasma properties have stabilized, as shown in Fig. 6.3 (b). The exposure time varies continuously across the sample.

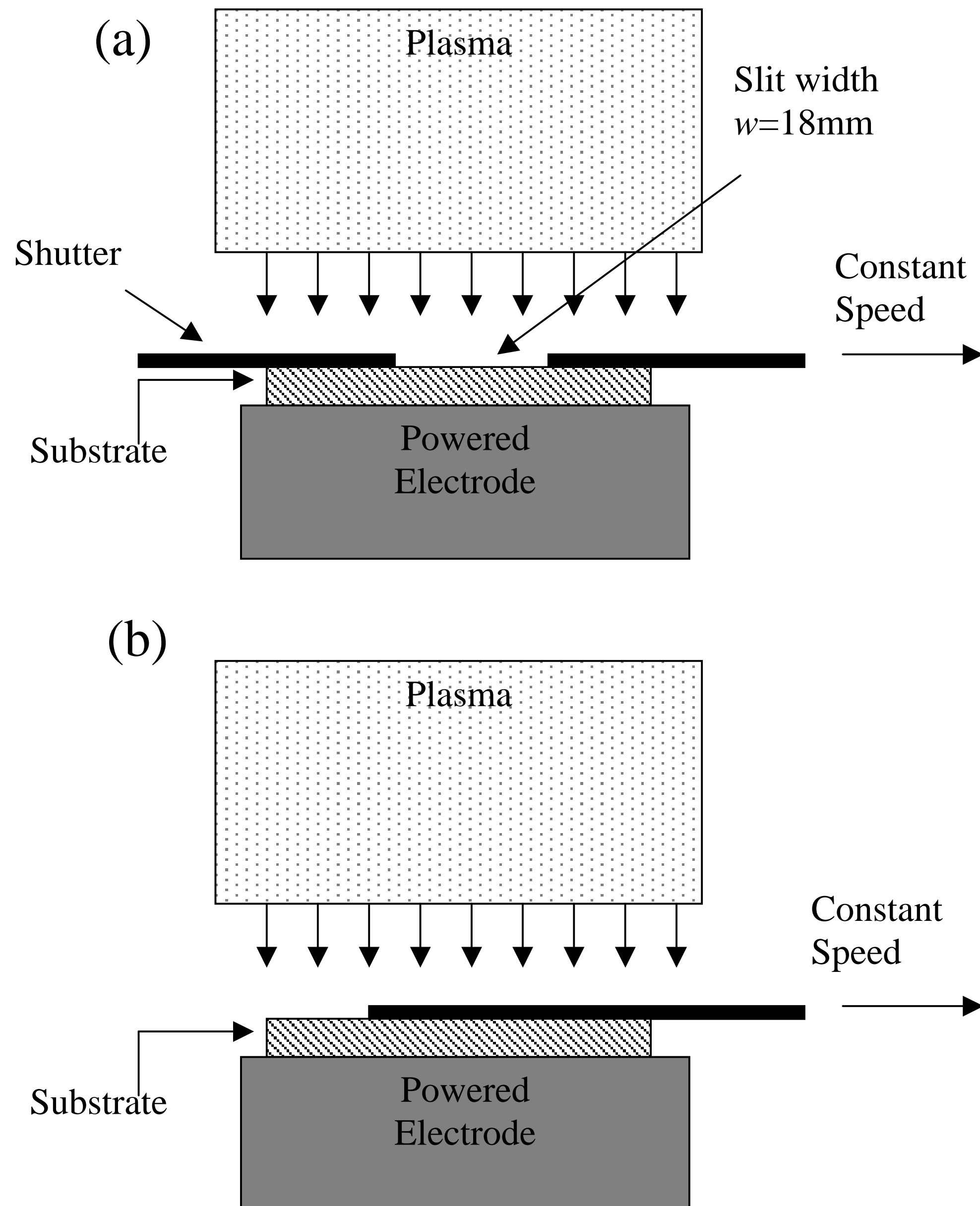

Figure 6.3: *Concept of moving shutter: (a) Shutter containing a 18 mm wide slit to control the interaction of a substrate with a plasma. (b) Solid shutter that is used to generate gradients of exposure time across a sample.*

6.3 RESULTS AND DISCUSSIONS

6.3.1Temporal Evolutions of 193 nm and 248 nm Photoresist Patterns

a. Trench and Line Evolution

Figure 6.4 shows SEM cross-sections of 193 nm (images (a) through (d)) and 248 nm (images (e) through (h)) photoresist patterns after plasma etching for various times using C_4F_8/90% Ar discharges. All samples were uniformly exposed to a stable plasma for different times. A 18 mm wide slit in a silicon shutter was used to expose the samples. Changes in processing characteristics due to sheath perturbations and their dependence on slit size have been discussed in a previous publication, and are minor with this slit size.[19] For scanning electron microscopy, the samples were tilted to maximize the information that could be obtained from the study of the surface, trench/line and sidewall portions of the samples. Both the surface and sidewall roughness of etched 193 nm photoresist samples is greater than that of 248 nm photoresist patterns after comparable plasma treatments. Even a brief plasma exposure of ~1.6s introduces significant roughness in the 193 nm photoresist pattern (Fig. 6.4 (b)). The roughness increased for all times investigated here (up to 60 s), and the roughening rate is clearly much higher for the 193 nm photoresist patterns. Images of features etched for 60 s, showed development of sloped sidewalls and striations on the sidewalls for both 193 nm and 248 nm photoresists.

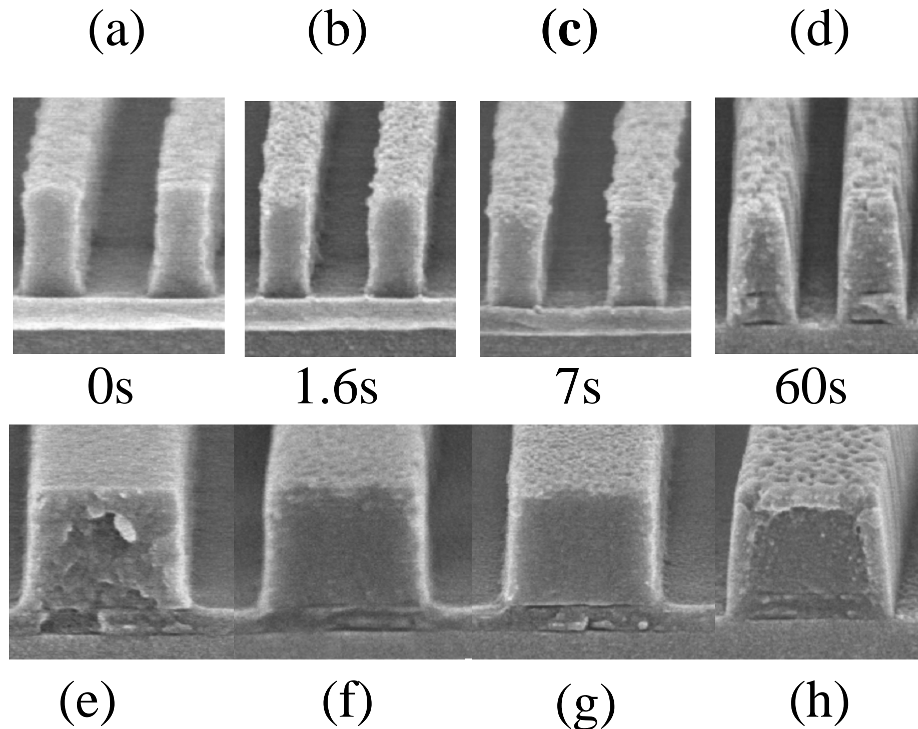

Figure 6.4: *Photoresist mask evolution during C_4F_8/90%Ar etching: (a) 0s, (b) 1.6s, (c)7s, and (d) 60s for 193 nm photoresist etching; (e) 0s, (f) 1.6s, (g)7s, and (h) 60s for 248 nm photoresist. Discharges were generated using 1000 W source power, a pressure of 10mTorr, and 50sccm as total gas flow rate with a fixed bias voltage –125V.*

The quantitative values of etch rate, trench and line widths obtained in these and additional experiments are summarized in Figs. 6.5 (a), (b) and (c), respectively. Dramatic changes of the etch rates (Fig. 6.5 (a)) and the trench and line widths (Fig. 6.5 (b) for 193 nm photoresist and Fig. 6.5 (c) for 248 nm photoresist) can be observed during the first 20 seconds of plasma exposure. The temporal evolutions of trench and line widths are consistent with the time scale of the changes seen for the ER. For both 193 nm and 248 nm photoresist patterns a decrease of the trench width is observed, which may be caused by fluorocarbon deposition on the trench sidewalls. Figure 6.5 (a) shows that the etch rates of both types of photoresists are high during the initial phase, and then

drop to a steady-state value. Possible explanations of this are (a) the properties of the photoresist polymers may be different near the surface as compared to the bulk of the photoresist, e.g. due to moisture uptake from ambient and different polymer characteristics for chains ending at the surface, and (b) a strong plasma-induced modification of the photoresist material which reduces its etching rate, e.g. graphitization.[6.21-6.23] Another interpretation could be that the etching of the photoresist polymers is easier if the fluorocarbon coverage of the surface is not complete. Overall, these results demonstrate the dynamic nature of these changes, and the need for time-resolved measurements of these effects.

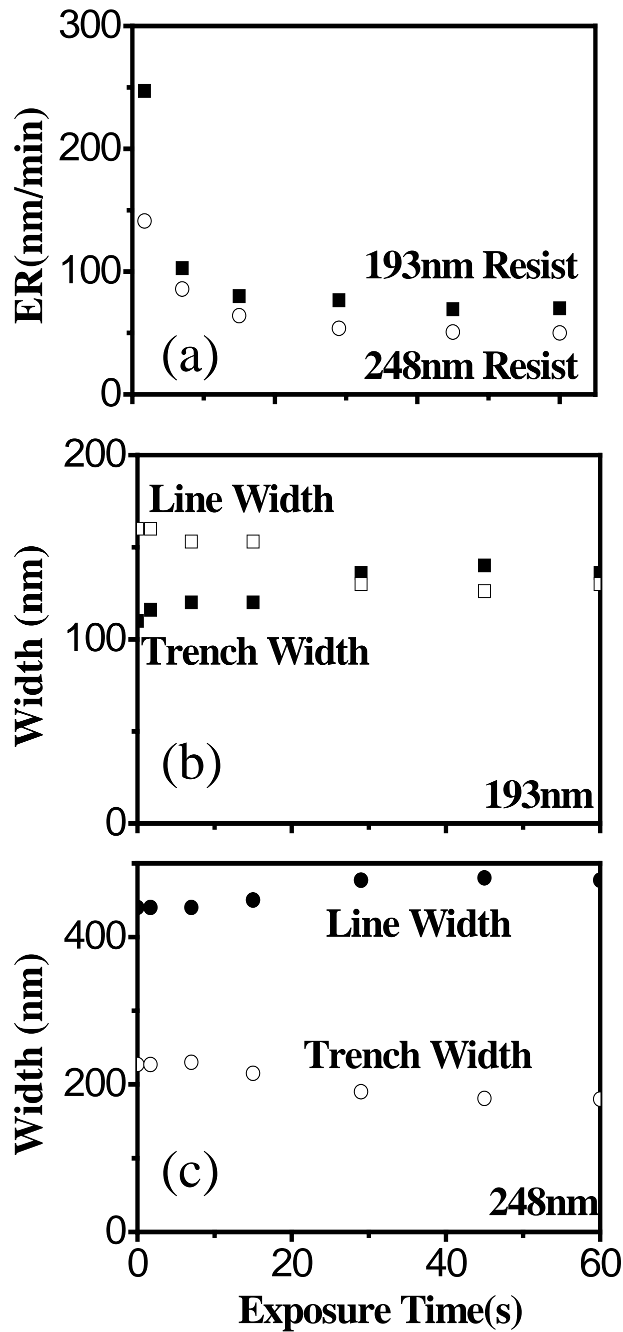

Figure 6.5: *(a)193 and 248 nm photoresist etch rates, (b) Trench/Line width evolution of 193 nm photoresist feature and (c) Trench/Line width evolution of 248 nm photoresist feature during pattern transfer. Discharges were generated using 1000 W source power, a pressure of 10mTorr, and 50sccm as total gas flow rate with a fixed bias voltage –125V.*

b. Formation of Striations in Sidewalls of Photoresist Structures

As seen above, striations were formed on the sidewalls of both photoresist structures. Formation of striations and their subsequent transfer into dielectric films has been studied by many investigators, e.g. for a recent study see reference 6.24. It is important to control the sidewall roughness during the fabrication.

SEM images of the top surfaces and trench sidewalls of plasma exposed 193 nm and 248 nm photoresist features of are shown in Figs. 6.6 and 6.7, respectively. The samples were tilted for SEM analysis to show the surface morphology of both horizontal and vertical surfaces. A “standing wave” pattern is visible on the sidewalls of as received 193 nm and 248 nm photoresist patterns (horizontal lines in Figs. 6.6 (a) and 6.7 (a)), which were generated by the photolithographic process. These standing wave patterns disappeared after short plasma-photoresist interactions times. Significant surface modifications of the photoresist lines are introduced during plasma etching that vary with plasma processing time and surface location. It appears that surface roughness and sidewall roughness are of similar magnitude. The species incident on the sidewalls are mainly neutrals while the top surface is exposed to energetic ion bombardment. Ion bombardment of the trench sidewalls can be caused by the arrival of ions deflected to the trench sidewalls by negative charging. [6.25-6.27] Different mechanisms are expected to control the modification of the surface and sidewall of the photoresist line, respectively. The initial stages of surface roughening will be discussed in more detail below.

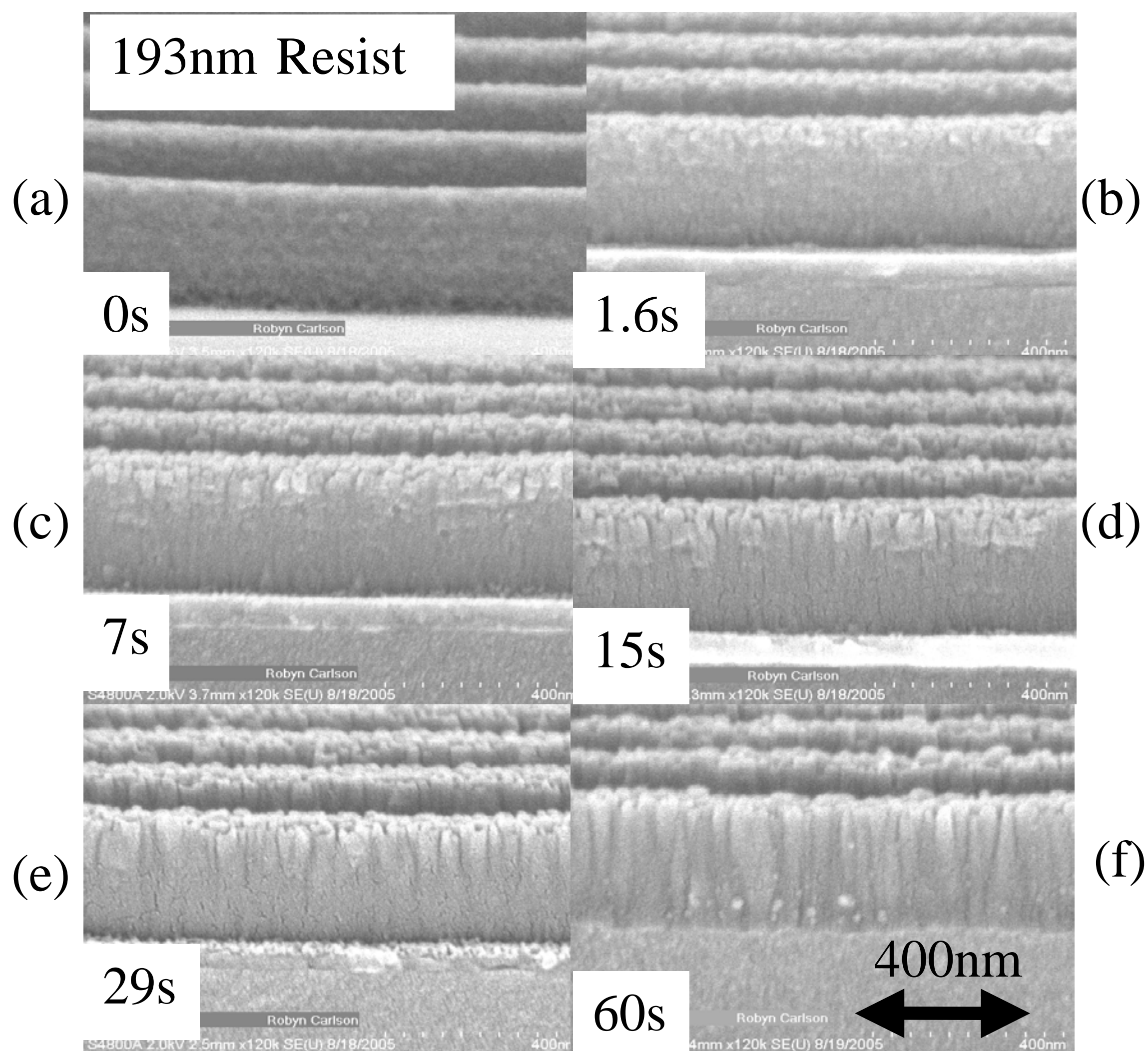

Figure 6.6: *Striation evolution on the sidewall of 193 nm photoresist mask during pattern transfer with C_4F_8/90%Ardischarges: (a) as received, (b) 1.6s, (c) 7s, (d) 15s, (e) 29s and (f) 60s.Discharges were generated using 1000 W source power, a pressure of 10mTorr, and 50sccm as total gas flow rate with a fixed bias voltage –125V.*

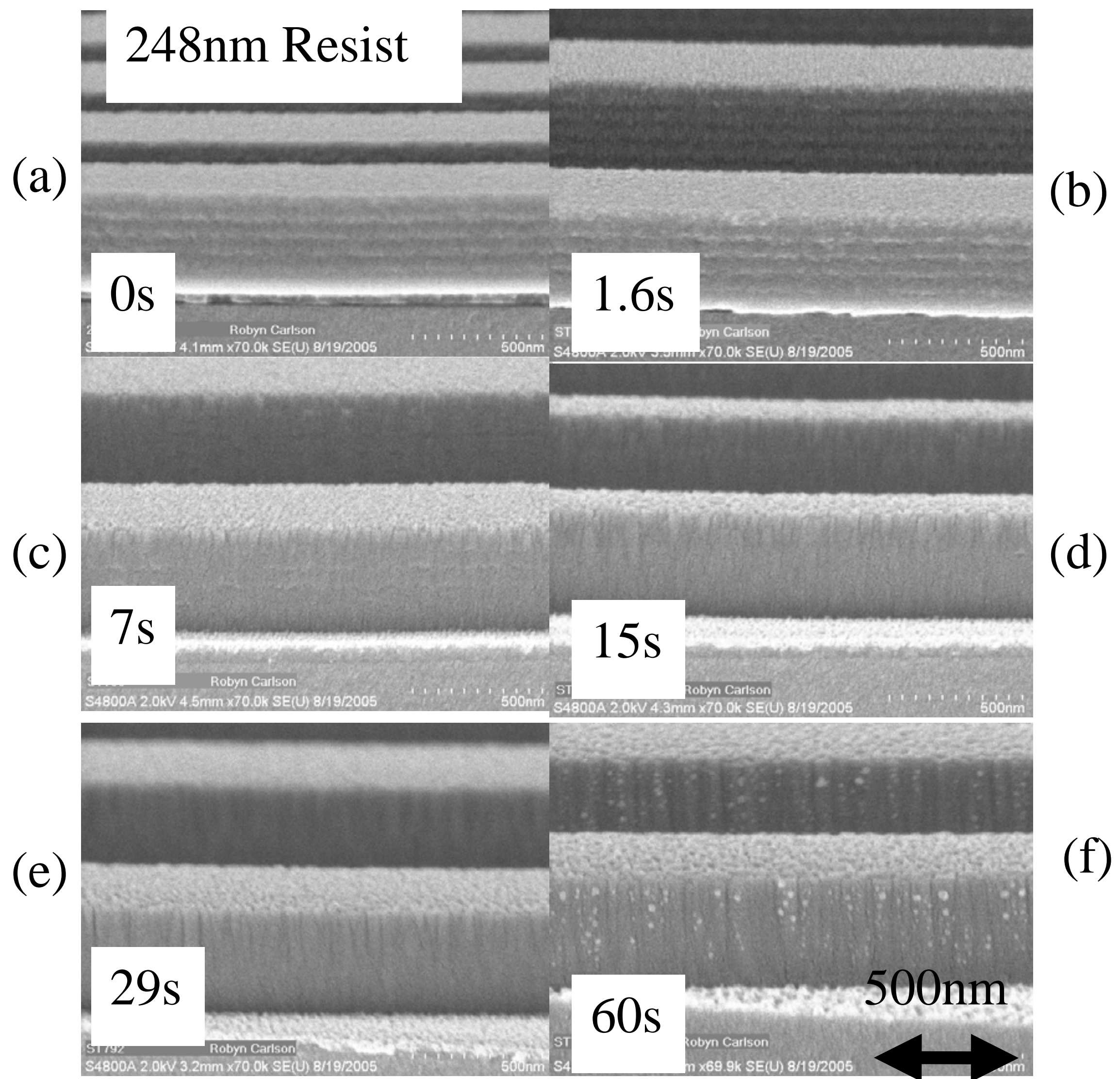

Figure 6.7: *Striation evolution on the sidewall of 248 nm photoresist mask during pattern transfer with C_4F_8/90%Ardischarges: (a) as received, (b) 1.6s, (c) 7s, (d) 15s, (e) 29s and (f) 60s. Discharges were generated using 1000 W source power, a pressure of 10mTorr, and 50sccm as total gas flow rate with a fixed bias voltage –125V.*

Figures 6.6 and 6.7 display important information on the kinetics of the formation of "striations" along the sidewalls of the photoresist lines as a result of plasma exposure. For a short plasma exposure time (~1.6 s), primarily surface roughness is visible and no features that extend from the top to the bottom of the photoresist sidewalls are visible in the images shown in Figs. 6.6 (b) and 6.7 (b). As the plasma exposure time is increased, increasingly longer and more clearly defined stripes are formed on the photoresist line sidewalls. Ultimately striations extend from the top to the bottom of the photoresist line sidewalls. The orientation of the striations is nearly vertical, indicating that ion bombardment plays a role in the striation formation mechanism. Although the polymer structure of 193 nm and 248 nm photoresists are quite different, the evolution of striations as a function of time and depth is similar for features formed from either material. This indicates that the formation of striations is a consequence of the plasma etching process and appears to be caused by initial surface roughening followed by ion induced transfer of the rough edges into the feature sidewalls. Since fluorocarbon deposition at the feature sidewalls accompanies the ion-induced etching for the C_4F_8/Ar etching process employed here, non-uniform fluorocarbon film deposition may contribute to the generation of striations at the photoresist sidewalls. The width of striations formed on features after 60 s etching with C_4F_8/90% Ar discharges are ~40 nm and ~60 nm for 193 and 248 nm photoresists, respectively. This means that during the plasma etching process, more striations are formed per unit length along 193 nm photoresist lines than for 248 nm photoresist features. This finding is consistent with the increased surface

roughness seen for 193 nm photoresist material. The molecular structure plays an important role in determining the striation size.

The striation lengths and the striation growth rates for both materials are summarized in Figs. 6.8 (a) and (b), respectively. The striation length is defined as the distance from the top of photoresist line to the end of the observable striation on the sidewall. The striation growth rate is obtained by dividing the striation length by the total process time. These data on striation evolution do not take into account the fact that the photoresist line height is simultaneously reduced by etching. Figure 6.8 shows that the initially striations grew more quickly in features formed from the 193 nm photoresist material, consistent with the fact that plasma exposure introduces severe roughness on 193 nm photoresist compared with 248 nm photoresist as shown by SEM images in Figs. 6.4, 6.6 and 6.7. However, for long exposure times the striation was transferred deeper for the 248 nm photoresist structure than 193 nm photoresist. This may be explained by the different feature dimensions formed in the two materials. Due to the smaller width of the trenches formed in the 193 nm photoresist, it is more difficult for plasma species to penetrate the trench depth, which reduces the interaction of the reactive species with the trench sidewall, resulting in low striation growth rate.

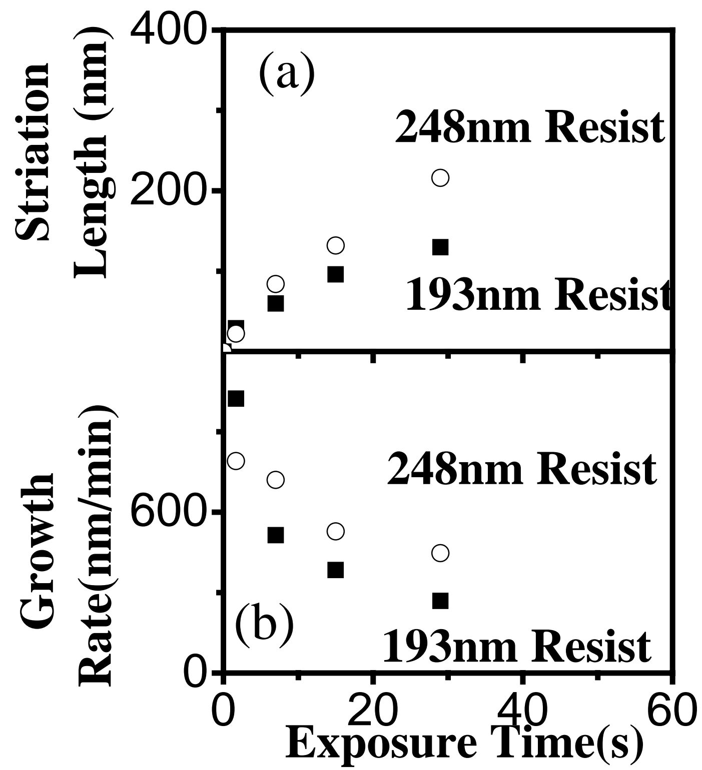

Figure 6.8: *Quantitative results of striation evolution during 193 nm and 248 nm photoresists etching with C_4F_8/90%Ar plasma* shown in Figs. 6.6 and 6.7.

The rapid generation of striations for short exposure times is possibly due to the more fragile molecular structure of the 193 nm photoresist material relative to the 248 nm photoresist material. The striation growth rates are extremely high initially, equal to almost three times the value of the photoresist etching rates shown in Fig. 6.5 (a). Reduced ion bombardment is expected on the sidewalls, which typically results in lower etching rates for fluorocarbon discharges. The high striation growth rates are inconsistent with simple pattern transfer of micromasks into blanket photoresist films. In addition, the random orientation of the striations seen for short plasma exposure times suggests that these features are not a result of directional etching. The sidewalls of the photoresist features are exposed to ion bombardment at grazing angles. Additional information on the mechanism of striation formation can be obtained from a comparison of SEM images obtained with photoresist lines after short plasma exposure with images of untreated photoresist lines. This is shown in Figs. 6.9 (a) and (b), and (c) and (d), for 193 nm and 248 nm photoresist structures, respectively. Figure 6.9 compares the widths of the trenches at the top of the photoresist lines. For the 193 nm photoresist material, the width of the trench between the two photoresist lines was reduced from 127 nm to 107 nm after 1.6 s plasma etching (see Figs. 6.9(a) and (b)). The reduction may be due to a distortion of the photoresist material on the top due to ion bombardment, fluorocarbon deposition or both. The reduction of the trench width of 248 nm photoresist feature is 5nm after 1.6 s plasma etching (see Figs. 6.9(c) and (d)). Minor surface roughening of 248 nm photoresist is a plausible explanation. This difference in trench width reduction indicates that a photoresist material change near the top of the photoresist lines rather than

fluorocarbon deposition is the dominant factor in photoresist lineshape distortion observed for short plasma etching times. Fluorocarbon deposition also takes place on the trench sidewalls during the plasma etching process and may contribute to the increase of the linewidths shown in Figs. 6.9 (b) and (d). The irregularly shaped photoresist profile after initial distortion along with fluorocarbon coverage on the corners will prevent locally grazing angle ion bombardment of the photoresist sidewalls.

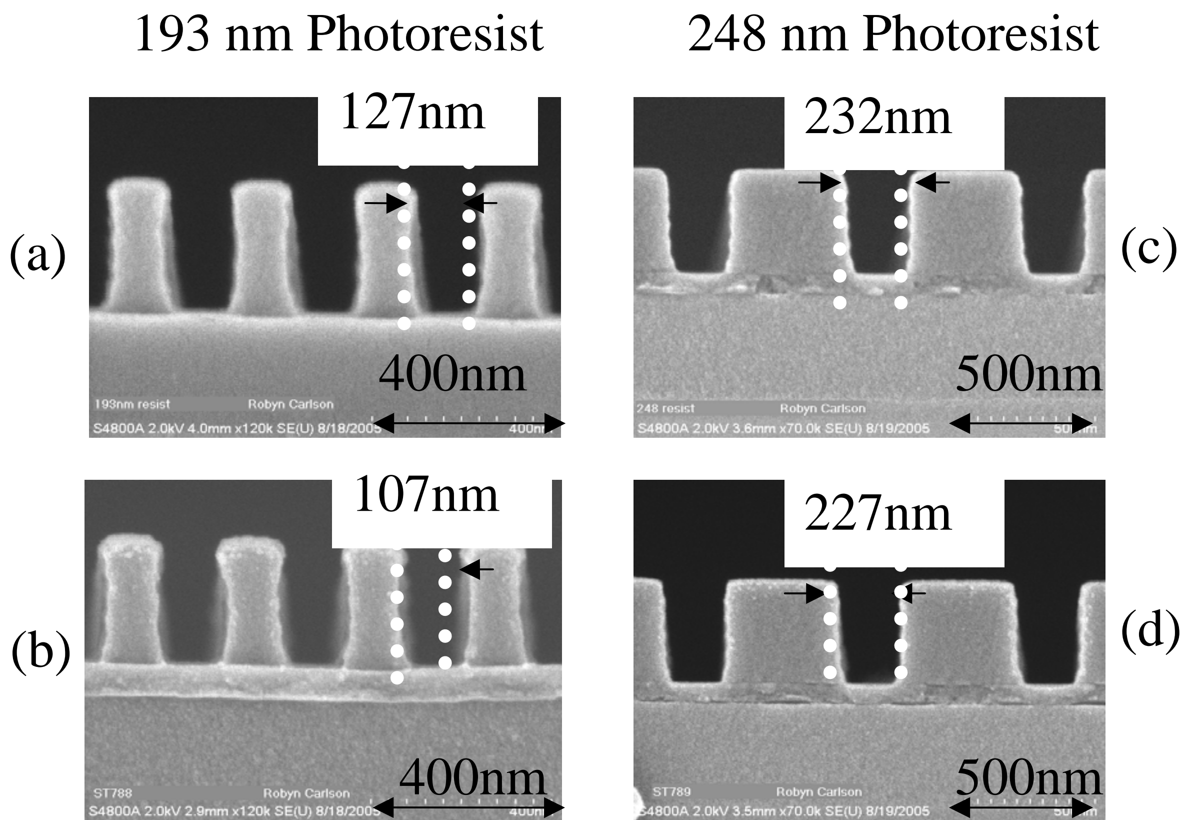

Figure 6.9: *Comparisons of SEM cross-section images of 193 and 248 nm photoresists between short time etching (1.6s) and untreated samples: (a) as received 193 nm photoresist, (b) 193 nm photoresist feature after 1.6s etching, (c) as received 248 nm photoresist, (d) 248 nm photoresist feature after 1.6s etching. Discharges were generated using 1000 W source power, a pressure of 10mTorr, and 50sccm as total gas flow rate with a fixed bias voltage –125V.*

6.3.2 Surface Modifications of Photoresist Films During Argon Sputtering

The chemical modifications of photoresist surfaces for short plasma exposure times were characterized. Blanket films were processed using argon plasmas and subsequently studied using x-ray photoemission spectroscopy (XPS). Argon rather than fluorocarbon discharges were used for this initial study of ion induced damage to the photoresist materials, since fluorocarbon deposition and related surface modifications mask changes of the C-C or C-O related signals in the C 1s spectra. Carbon 1s spectra of both 193 and 248 nm photoresist materials after exposure to an argon plasma are shown in Figs. 6.10 (a) and (b), respectively. For 193 nm photoresist, the C=O peak intensity vanishes and the C-C/C-H peak intensity decreases slightly as a result of sputtering. We conclude that physical sputtering causes rapid removal of C=O bonds from the 193 nm photoresist material. Figure 6.10 (b) shows that the aromatic ring structure associated with the 248 nm photoresist is destroyed by argon plasma induced sputtering. The C-C/C-H related intensity also drops slightly.

The integrated C 1s intensity for both materials as a function of argon sputtering time shows that both materials lose mass density. One possible interpretation is formation of surface roughness. The integrated C1s peak intensity of the 193 nm photoresist decreases more than that of the 248 nm photoresist as a function of sputtering time.

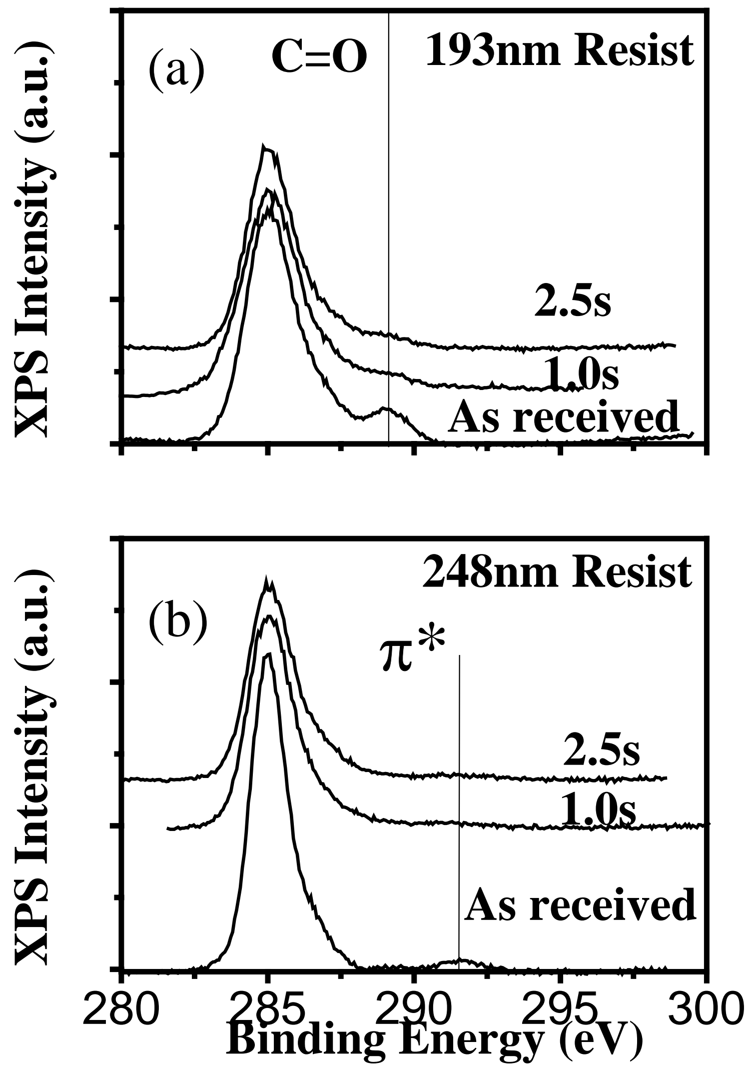

Figure 6.10: *XPS C1s spectra of 193 nm and 248 nm photoresists after short time argon sputtering. Discharges were generated using 600 W source power, a pressure of 10mTorr, and 50sccm as total gas flow rate with a fixed bias voltage –125V.*

6.3.3 Surface Roughness of Blanket Photoresist Films for C_4F_8/Ar Discharges

To improve our understanding of the plasma-induced surface modifications, the changes of blanket photoresist surfaces were determined as a function of processing time for C_4F_8/Ar discharges. For these studies, different surface portions of a single sample were exposed to the discharge for different amounts of time using the shutter. This approach enables characterization of the evolution of surface roughness and surface chemistry of photoresist materials as a function of exposure time to the same discharge. We applied ellipsometry, atomic force microscopy (AFM) and time-of-flight SIMS to the characterization of the plasma-exposed photoresist films. We do not report XPS data obtained with C_4F_8/Ar plasma treated photoresist materials since fluorocarbon deposition and fluorination were the dominant effects seen. The study of similar modifications has been reported previously.[6.5]

a. Ellipsometric Characterization

A rotating compensator ellipsometer in the polarizer-compensator-sample-analyzer (PCSA) configuration with a 632.8 nm He/Ne laser was used to determine thin film etching rates and the introduction of surface modifications after the plasma etching process. Both 248 nm and 193 nm photoresist films were exposed to C_4F_8/90% Ar plasma for times of up to 80 s. Figure 6.11 shows the removed photoresist thickness and the corresponding photoresist etching rate for both materials as a function of plasma exposure time. The 193 nm photoresist material exhibits a higher etching rate than the 248 nm photoresist for the C_4F_8/90% Ar discharge used. For both materials, the initially very high etching rates decrease as a function of time and stabilize at much lower values

after about 30 s. A total thickness of about 20 nm is removed for both the 193 nm and 248 nm photoresists at the point where the etching rate has dropped close to the steady-state etch rate value. This indicates two different plasma surface interaction regimes for each photoresist material.

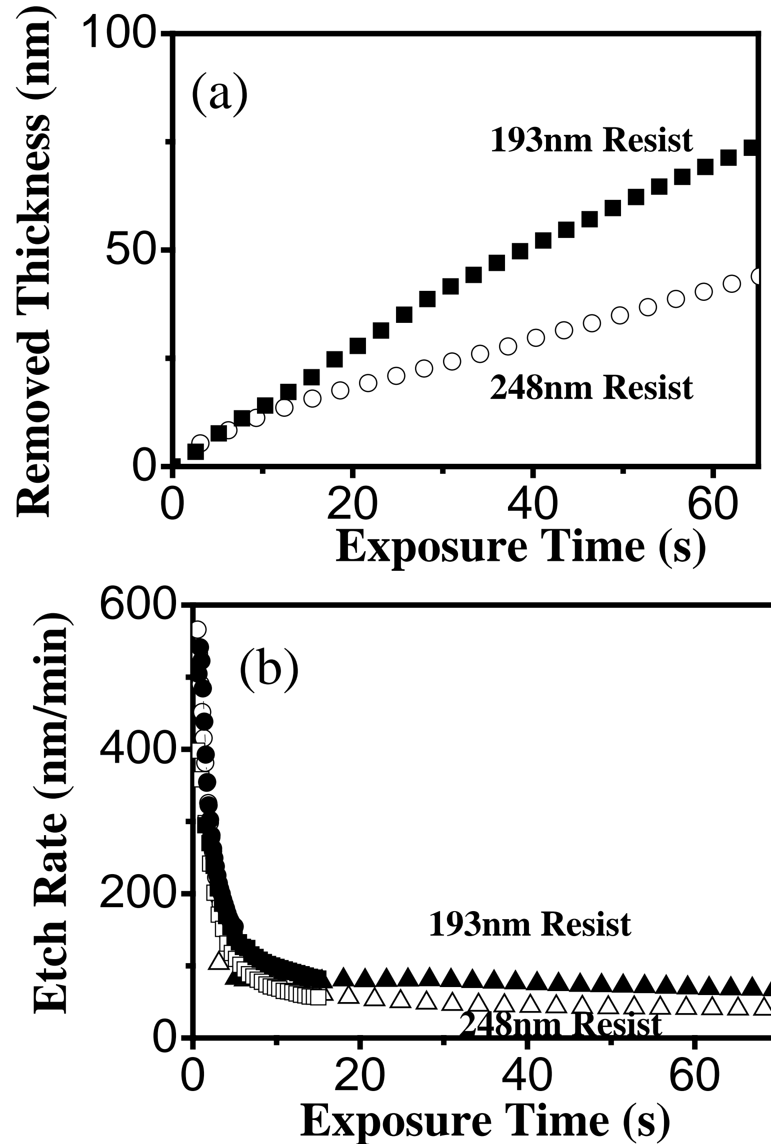

Figure 6.11: *(a) Thickness removal and (b) etch rate of blanket 193 nm or 248 nm photoresist films during fluorocarbon plasma etching with combinatorial approach shown in Fig.6.3 (b). Discharges were generated using 1000 W source power, a pressure of 10mTorr, and 50sccm as total gas flow rate with a fixed bias voltage –125V.*

The effective refractive index (632.8 nm) obtained using a single-layer model of the photoresist films is summarized in Fig. 6.12 as a function of plasma exposure time. The temporal behavior of the effective refractive index of 193 nm photoresist is very different from that of 248 nm photoresist. For both materials the refractive index initially increases as a result of plasma exposure. This may be interpreted as a densification of the photoresist material caused by the plasma exposure, and can be due to hydrogen loss from the photoresist materials, cross-linking, and graphitization.[6.21-6.23] After about 30 s plasma exposure, the refractive index of the 193 nm photoresist material starts to decrease and ultimately drops below that of untreated 193 nm photoresist. The decrease of the refractive index can be explained by fluorination of the photoresist material, surface roughening or both. A similar decrease is not seen for the refractive index of the 248 nm photoresist material. This indicates that formation of a less dense material due to severe roughening is the reason for the refractive index decrease seen for the 193 nm photoresist for long plasma exposure times. These observations are consistent with the less severe surface roughening reported for 248 nm photoresist above.

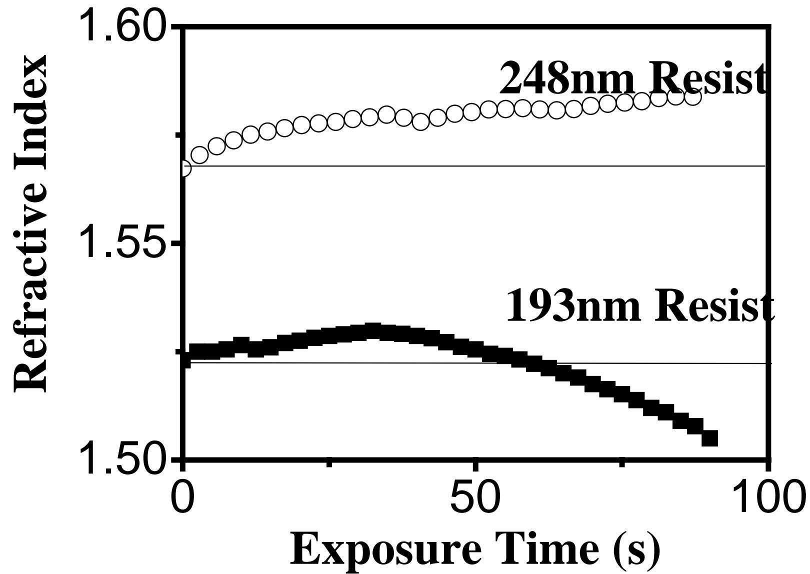

Figure 6.12: *Effective refractive index evolution of 193 nm or 248 nm photoresists during C_4F_8/90%Ar plasma etching. Discharges were generated using 1000 W source power, a pressure of 10mTorr, and 50sccm as total gas flow rate with a fixed bias voltage –125V.*

b. Surface Roughness Evolution

It is well-known that severe surface roughness of 193 nm photoresist materials can be introduced by fluorocarbon based plasma etching because of the more fragile polymer structure of these materials.[6.5,6.24] Similar substrates as the ones analyzed using ellipsometry were investigated using AFM. The time evolution of RMS roughness is reported in Fig. 6.13. The roughness of the 248 nm photoresist increases initially, but then stabilizes quickly and the RMS value remains overall fairly low. On the other hand, for the 193 nm photoresist the RMS roughness continued to increase for the longest plasma exposure times investigated (up to 60 s). Figure 6.13 shows that in this case the RMS roughness increases after about 20 s linearly with exposure time. The AFM results obtained for both 193 nm and 248 nm photoresists are consistent with the ellipsometric data, which showed a stable refractive index for the 248 nm photoresist, whereas the

refractive index of the 193 nm photoresist decreased continuously after about 30 s. The initial roughening rate (first 10 s, see inset in Fig. 6.13) is higher than seen at later times, indicative of diverse mechanisms possibly related to different material properties. This is consistent with the rapid photoresist etching rate measured for short plasma exposure times. The increase of the refractive index for short plasma exposure times suggests that densification is the dominant material transformation of the photoresist during this period. This is followed by a period where surface roughening of the 193 nm photoresist material dominates.

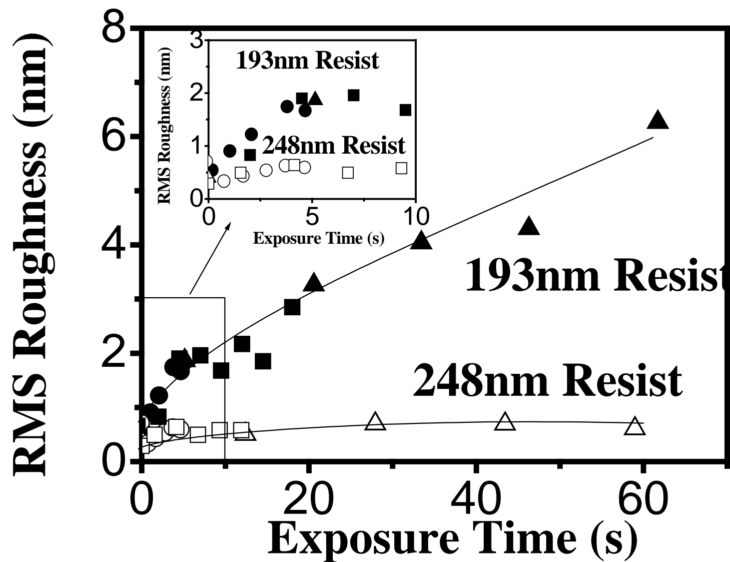

Figure 6.13: *Time evolution of RMS roughness of 193 nm or 248 nm photoresists during C_4F_8/90%Ar plasma etching. Discharges were generated using 1000 W source power, a pressure of 10mTorr, and 50sccm as total gas flow rate with a fixed bias voltage –125V.*

Figure 6.14 shows the relationship between the RMS roughness and etching depth. The RMS roughness increases at an approximately constant rate with etching depth for each material, albeit at different rates. Additionally, it appears that this surface roughening mechanism becomes operative after about 10 nm of material have been removed from either photoresist film. This may imply that the plasma-polymer interaction is different for the first 10 nm of the material as compared to the interaction with the bulk material.

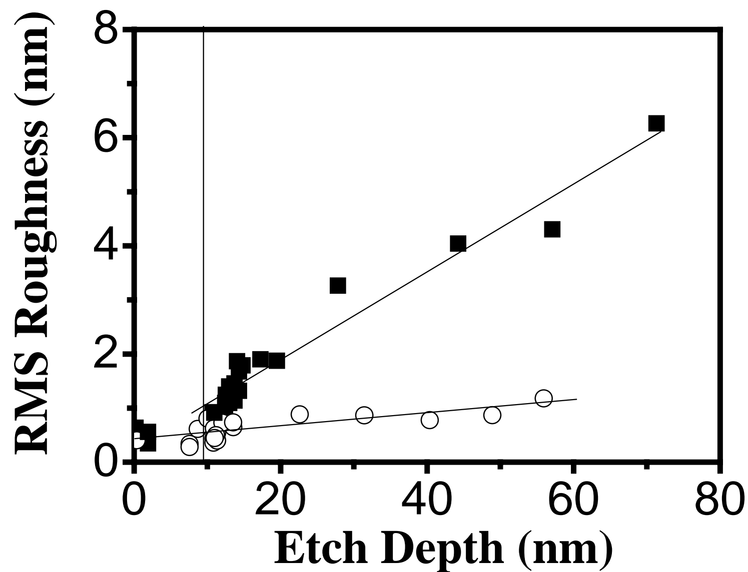

Figure 6.14: *RMS roughness evolution as a function of etch depth during the etching of193 and 248 nm photoresists with C_4F_8/90%Ar discharges. Discharges were generated using 1000 W source power, a pressure of 10mTorr, and 50sccm as total gas flow rate with a fixed bias voltage –125V.*

c. ToF SIMS Data

Chemical information is essential for the understanding of surface roughening of photoresist materials during plasma etching process. TOF SIMS was used to study changes in the chemical nature of the 193 nm and 248 nm photoresist materials as a function of exposure time to fluorocarbon plasmas. The results are summarized in Fig. 6.15. For both photoresists, FC coverage (indicated as C_2F_5O and $C_6F_{13}O$) is significant immediately once the substrate is exposed to the plasma (Fig. 6.15(a)). A variation of the FC intensity on 193 nm photoresist was observed while the one on 248 nm photoresist was nearly constant. This implies that the plasma/materials interactions reach a steady-state in terms of fluorocarbon species more quickly on 248 nm photoresist than for 193 nm material. This difference should be reflected in different temporal behavior of other surface properties, e.g. it is consistent with the surface roughening behavior, where 248 nm photoresist surface saturates at a minor RMS roughness and 193 nm photoresist surface continuously roughens. The percentage of oxygen content in 193 nm photoresist material is higher than for 248nm photoresist (see Fig. 6.1), and less fluorocarbon coverage may be expected for the 193 nm photoresist during fluorocarbon plasma etching. The fact that a higher fluorocarbon coverage is seen for the 193 nm photoresist material during the initial exposure may be explained by the rough surface of the 193 nm photoresist material enhancing fluorocarbon deposition. For long plasma etching times, a very rough surface is formed and oxygen from the sub-surface region photoresist region is released. This could lead to a reduction of the FC coverage. [28] This occurs after about 5 s (see Fig. 6.15 (a)). The SIMS signals related to the polymer structure and indicated as MAMA and GBLMA for 193 nm photoresist and C_4H_9O for 248 nm photoresist in Fig. 6.15, are reduced in intensity as a result of the plasma exposure. The intensities of these groups drop to background level within about 0.2 second exposure.

In addition to the polymer shown in Fig. 6.6, the photoresist system typically contains a certain amount (~3%) of photoacid generator (PAG) required for pattern formation. PFBS is used as PAG in 193 nm photoresist material and iodonium-triflate is identified as the PAG used in 248 nm photoresist formulation. We show the temporal evolution of the PAG for both photoresists during plasma etching in Fig. 6.15 (c). The PFBS PAG is completely damaged by 1 s of plasma exposure. PAG enrichment is

observed for the 248 nm photoresist after 1 s of plasma exposure. The intensity of SO_3 remains above the noise level for long exposure time in this case. This difference confirms that the full 248 nm photoresist system is more stable in the fluorocarbon plasma etching environment than a fully formulated 193 nm photoresist system.

To clarify the contribution of the chemical modifications of the photoresist materials to surface and line edge roughening, further characterization is necessary. For instance, the absolute loss of particular groups can be evaluated using depth profiling. These data may be correlated with the surface roughness data. This kind of research is in progress and will ultimately provide a molecular level understanding of the factors that contribute to roughness formation in advanced photoresist materials and structures.

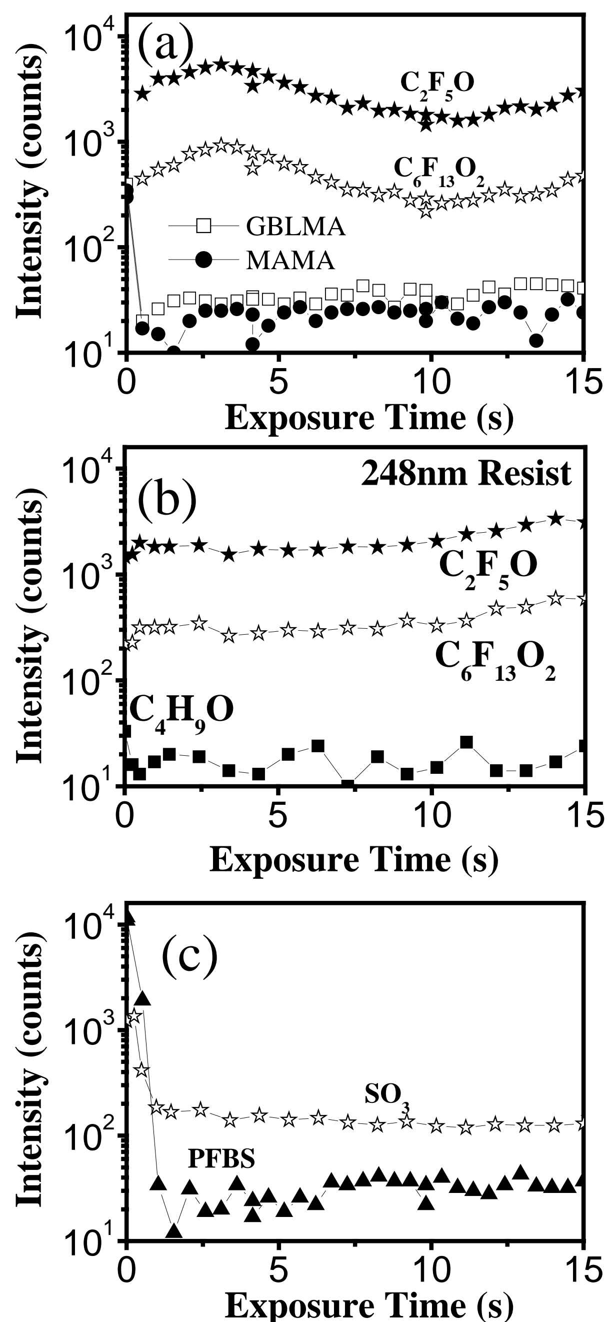

Figure 6.15: *Chemical signature evolutions during plasma etching of (a) 193nm and (b) 248nm photoresists. C_2F_5O and $C_6F_{13}O$ represent the FC coverage on the surface, GBLMA and MAMA is copolymer for 193nm photo resist while C_4H_9O indicates the information for 248nm photoresist. (c) PAG information can be found as PFBS and SO_3 for 193nm and 248nm photoresist respectively. C_4F_8/90%Ar discharges were generated using 1000 W source power, a pressure of 10mTorr, and 50sccm as total gas flow rate with a fixed bias voltage –125V.*

6.4 CONCLUSIONS

We have studied the initial phases of the interaction of fluorocarbon plasmas with 193 nm and 248 nm photoresists materials and structures. We employed a shutter to control the plasma-substrate interaction time. During this time frame, rapid surface roughening, and material densification/graphitization were observed upon plasma exposure. For photoresist line and trenche structures surface roughness is introduced near the top of the photoresist lines initially. The rough edges on the top of the photoresist lines can be transferred into the sidewalls of the photoresist lines to form striations that extend from the top to the bottom of the lines. For 248 nm photoresist, surface roughening, material densification, and other modifications saturate for exposure times of 20 s and longer. Conversely, for the 193 nm photoresist material the surface roughness continues to increase even for the longest plasma exposure times investigated (90 s). While a molecular level understanding of this difference in behavior of the two photoresist materials is lacking at this time, the present work shows that a systematic study of the interaction of plasmas with different polymer structures is possible, and will be required to understand the fundamental factors resulting in the loss of photoresist line shape during plasma processing.

ACKNOWLEDGEMENTS

The authors gratefully acknowledge support of this work by Department of Energy (Contract No. DE-FG0200ER54608), National Science Foundation (under award No. DMR-0406120) and by Maryland Technology-Development Corporation (TEDCO). We thank C. Stolz for collaboration during the initial phase of the shutter project, R.

Dabrowsky for assistance with design and building of the motor-driven shutter assembly, and Texas Instruments for the patterned substrates.

Chapter 7:General Conclusions

The work in thesis presents a mechanistic study of plasma processing of conventional SiO_2 material, nanoporous silica materials and advanced polymers used as a mask for nano-structure formation. With C_4F_8/Ar discharges, major factor controlling SiO_2 etching is identified. Porosity introduced in Si-O matrix completely changes the interactions with plasma for both polymerization conditions (fluorocarbon plasmas) and nonpolymerization discharges (O_2, N_2 or H_2 discharges). The etching behaviors of polymers with fluorocarbon plasmas strongly depend on the molecular structures.

In chapter 2, it is shown that the ion induced defluorination is one of key factors in SiO_2 etching with fluorocarbon based plasmas. The F/C ratio of fluorocarbon film is maintained constant if low bias voltage is applies. If the bias voltage is above the etching threshold, etching of the substrate takes place, accompanied with fluorine loss of fluorocarbon film on the surface. It is suggested that both fluorine and carbon atoms are required to be mobile during etching. The idea is further confirmed by the study of argon sputtering of fluorocarbon films. In pure argon discharges, fluorine loss of deposited fluorocarbon films is observed if not RF bias power is applied, but no significant fluorocarbon film removal occurs. The ion energy in this case is of the order of 10 eV, which is sufficient to break C-F bonds (5.18eV). To remove deposited fluorocarbon films, the RF bias voltage is required to exceed -10V, in which the ion energy is in the range of 30 to 40eV, an energy sufficient to displace carbon atoms in graphite.

Based on this fact, the etch rate is expected to correlate with the total fluorocarbon species flux that adsorbs on the surface. A measure of this quantity is given by the value of the fluorocarbon deposition rate measured without an RF bias applied. The data of chapter 2 show that the etch rate increases with the deposition rate given the same defluorination of fluorocarbon films. It is found that the ion-induced defluorination is strongly related to plasma properties. In fluorocarbon radical dominated discharges, the fluorocarbon flux is high enough to maintain the F/C ratio even with energetic ion bombardment. The fluorocarbon films become highly fluorine deficient for discharges containing a high proportion of argon is an RF bias is applied simultaneously for energetic ion bombardment of the surface. Both FC deposition rate and the defluorination of the deposited FC film need to be considered in a description of the overall etching reaction.

Once fluorine or carbon atoms are free, they can interact with the substrate. Depending on the chemical composition of the substrate, the stoichiometry of the fluorocarbon film on the surface varies. For SiO_2 etching, oxygen from the substrate assists carbon removal. The F/C ratio is higher at the interface between fluorocarbon film and SiO_2 surface than the one between the fluorocarbon film and plasma. An opposite gradient of the F/C ratio is observed for Si etching.

When porosity is introduced in the Si-O matrix, as pursued for ultra-low dielectric constant materials, the plasma-induced modification of the dielectric becomes much more pronounced. Overall, the penetration depth of species, either neutrals or ions, increases relative to SiO_2, especially for interconnected pores. The materials modifications depend strongly on plasma properties. For highly

polymerization conditions, e.g. pure C_4F_8 discharges, significant fluorocarbon deposition occurs in the porous structure, even at depths of 30nm below the surface. The fluorocarbon deposition along with ion bombardment results in enlarged pores near the surface, which reduces the interfacial area between porous structure and plasma species. The porous structure is not stable in the energetic plasma environment, and the structure is reorganized to minimize the interfacial energy during the plasma process. This severe fluorocarbon deposition eliminates the difference between SiO_2 and porous silica, and the etching behaviors become essentially the same. Fluorocarbon accumulation on NPS materials increases with their porosity, indicating that the fluorocarbon film precursors are abundant in pure C_4F_8 discharges.

For C_4F_8/90% Ar discharges which are characterized by a low polymerization rate, the fluorocarbon surface coverage is nearly constant as a function of porosity. This leads to a reduced fluorocarbon film thickness for highly porous NPS materials. The etching rate strongly increases with porosity in this case. It is found that the direct ion induced reactions are possible in the subsurface region because of connected pores. As a result, a rough surface is produced during the etching of nanoporous silica in C_4F_8/90% Ar discharges. The degree of roughness that is introduced depends on overall porosity, and surface roughness is not produced for dense materials like SiO_2 or OSG. The roughness scale (~30nm for 30% NPS) is much greater than the pore size (~2-3nm).

Plasma-based ashing processes are required to remove photoresist masks from the NPS material using O_2, N_2 or H_2 discharges. An important stability of nanoporous

materials exposed during the ashing process is observed. Residual carbon groups present in the NPS material are eliminated and the thickness of layers is reduced during direct exposure to O_2, N_2 or H_2 discharges, where low energy ion bombardment of the NPS material takes place. The loss of carbon groups from the silica matrix is likely connected with a collapse of the material and pore size reduction. The damaged layer thickness increases with overall porosity, which may be explained by pore interconnectivity. Interconnected pores form free paths for reactants from the surface to deep into the bulk of the low k material. The damage of the NPS material can by reduced if N_2 or H_2 remote discharges are used to remove the photoresist mask at elevated temperature. Satisfactory photoresist ashing rates and essentially no damage of the NPS material can be achieved if a remote H_2 discharge and a substrate temperature above 250^0C are employed.

In the last chapter, we use a shutter approach to study plasma interactions with advanced photoresist mask materials. These materials are exposed at 193nm and 248nm lithographic wavelengths. The shutter approach enables to study the photoresist polymers with process plasmas for a very short exposure times and obtain novel insights on the plasma surface interactions that are essential to nanoscale manufacturing. Rapid material removal along with densification of the photoresist materials is observed for both blanket 193nm and 248nm photoresist films during the first few seconds of plasma exposure. For the more fragile 193 nm photoresist material this is followed by significant surface roughening. Surface roughening is likely related to the selective removal of certain groups from the polymer backbone, e.g. the removal of carbonyl groups from the 193 nm photoresist has been observed in

the present work. The degree of surface roughening depends strongly on molecular structure, and is minor for the 248nm photoresist material which is based on aromatic rings. Surface roughening introduces important problems during structure etching. The distortion of the surface regions of photoresist lines caused by plasma exposure leads to irregularly shaped photoresist line tops. We have shown how the rough edges associated with these can be transferred along the sidewall of photoresist lines to form striations extending along the whole of the sidewall.

The shutter approach developed in this thesis enables the exploration of plasma surface interactions for short plasma exposure times. This is believed to an essential regime for nanoscale manufacturing. The study of nanoporous silica suggests that the reduction of pore interconnectivity is one promising solution to minimize the modification of this kind of nanomaterial during plasma etching or plasma ashing. The results of the photoresist work presented here suggests that the design of the molecular structure of advanced photoresists is the key to control image stability during plasma-based pattern transfer. These topics are currently under investigation by the "Plasma Team" at the University of Maryland, College Park with the overall goal of improving our understanding and control of plasmas to enable efficient and precise formation of nanostructures.

References:

Chapter 1:

[1.1] B. Chapman, *Glow discharge Process*, (John Wiley& Sons, Inc. 1980).

[1.2] M.A. Lieberman, A.J. Lichtenberg, *Principles of Plasma Discharges and Materials Processing*, (John Wiley & Sons, Inc., New York, 1994).

[1.3] D. M. Manos and D. L. Flamm (Eds), *Plasma Etching*, (Academic Press Inc., 1988)

[1.4] R. J. Shul and S. J. Pearton (Eds.) *Handbook of Advanced Plasma Processing Techniques*, (Springer, 2000).

[1.5] N. Ikegami, A. Yabata, T. Matsui, J. Kanamori, and Y. Horiike, Jpn. J. Appl. Phys., **36**, 2470 (1997).

[1.6] M. Schaepkens, and G. S. Oehrlein, J. Electronchem. Soc., **148**, C211 (2001).

[1.7] Y. Iijima, Y. Ishikawa, C. L. Yang, M. Chang, and H. Okano, Jpn. J. Appl. Phys., **36**, 5498 (1997).

[1.8] G. Kokkors, E. Gogolides, and A. G. Boudouvis, Microelectronic Engineering, **58**, 599 (2001).

[1.9] J. W. Coburn and E. Kay, IBM J. Res. Dev. **23**, 33 (1979).

[1.10] C. Y. Chang and S. M. Sze, *ULSI Technology*, (The Magraw-Hill Companies, Inc. 1996).

[1.11] Xi Li, Li ling, Xuefeng Hua, Masanaga Fukasawa, Gottlieb S. Oehrlein, Marcos Barela and Harold M. Anderson, J. Vac. Sci. Technol. A **21**, 284 (2003).

[1.12] X.Li, L.Ling, Xuefeng Hua, G.S.Oehrlein, Y.Wang, A.Vasenkov and M.Kushner, J. Vac. Sci. Technol. A **22**, 500 (2004).

[1.13] X.Li, L.Ling, Xuefeng Hua**,** G.S.Oehrlein, Y.Wang and H.M.Anderson, J.Vac.Sic.Technol A **21,** 1955 (2003).

[1.14] Xi Li, Xuefeng Hua, Li ling, Gottlieb S. Oehrlein, Marcos Barela and Harold M. Anderson, J. Vac. Sci. Technol. A, **20**, 2052 (2002).

[1.15] A.Vasenkov, X.Li, G.S.Oehrlein, and M.Kushner, J. Vac. Sci. Technol. A **22**, 511 (2004).

[1.16] G.I.Font, W.L. Morgan and G.Mennenga, J. Appl Phys. **91**,3530 (2002).

[1.17] T. E. F. M. Standaert, M. Scharpkens, N. R. Rueger, P. G. M. Sebel, G. S. Oehrlein, and J. M. Cook, J.Vac. Sci. & Technol. **A 16**, 239 (1998).

[1.18] M. Schaepkens, T. E. F. M. Standaert, N. R. Rueger, P. G. M. Sebel, G. S. Oehrlein, and J. M. Cook, J. Vac. Sci. Technol. **A 17**, 26 (1999).

[1.19] E.Gogolides, P. Vauvert, G. Kokkoris, G. Turban, and A. G. Boudouvis, J. Appl. Phys., **88**, 5570 (2000).

[1.20] D. Zhang, and M. J. Kushner, J. of Vac. Sci. Technol. A, **18**, 2661 (2000).

[1.21] J. W. Coburn and H. F. Winters, J. of Vac. Sci. Technol, **15**, 327 (1978).

[1.22] P. S. Ho, J. Leu, and W. W. Lee (Eds), *Low dielectric Constant Materials for IC Applications,* Spring Series in Advanced Microelectronics, Vol. 9, (Springer, Herdelberg, 2002).

[1.23] H. Ito, IBM J. Res. Dev. **45,** 683 (2001).

[1.24] T. Kajita, Y. Nishimura, M. Yamamoto, H. Ishii, A. Soyano, A. Kataoka, M. Slezak, M. Shimizu, P. Varanasi, G. Jordhamo, M. Lawson, R. Chen, W. Brunsvold, W. Li, R. Allen, H. Ito, H. Truong, and T. Wallow, Proc. SPIE **4345,** 712 (2001).

[1.25] J.A. O'Neill and J. Singh, J. Appl. Phys. **77**, 497 (1995).

[1.26] M. Schaepkens, R.C.M. Bosch, T. Standaert, G.S. Oehrlein, and J.M. Cook, J. Vac. Sci. & Tech. **A16**, 2099 (1998).

[1.27] K. W. Guarini, C. T. Black, K. R. Milkove, and R. L. Sandstrom, J. Vac. Sci. & Tech. **B**, 2784 (2001).

[1.28] K. W. Guarini, C. T. Black, Y. Zhang, H. Kim, E. M. Sikorski, and I. V. Babich, J. Vac. Sci. & Tech. **B**, 2788 (2002).

[1.29] G. S. Oehrlein, Xuefeng Hua, C. Scholz, and J. Ping, J. Vac. Sci. & Technol. B (in press).

Chapter 2:

[2.1] T. E. F. M. Standaert, C. Hedlund, E. A. Joseph, G. S. Oehrlein, and T. J. Dalton, J. Vac. Sci. & Technol. A 22, 53 (2004).

[2.2] D. Humbird, D. B. Graves, X. Hua, and G. S. Oehrlein, Appl. Phys. Lett. 84, 1073 (2004)

[2.3] Xi Li, Li Ling, X. Hua and G. S. Oehrlein, Y. Wang, A. V. Vasenkov and M. J. Kushner, J. Vac. Sci. Technol. A 22, 500 (2004).

[2.4] A. V. Vasenkov, Xi Li, G. S. Oehrlein, and M. J. Kushner, J. Vac. Sci. Technol. A 22, 511 (2004).

[2.5] G.S.Oehrlein,S.W.Robey,J.L.Lindstrom, K.K.Chan, M.A.Jaso, and G.J.Scilla, J.Electrochem.Soc 136, 2501(1989).

[2.6] G.S.Oehrlein, Y.Zhang, D. Vender, and O.Joubert, J. Vac. Sci. Technol. A 12,333(1994).

[2.7] M. Schaepkens, and G. S. Oehrlein, J. Electronchem. Soc. 148, C211 (2001).

[2.8] Da Zhang and Mark J. Kushner, J. Appl. Phys. 87, 1060(2000).

[2.9] T. E. F. M. Standaert, M. Schaepkens, N. R. Rueger, P. G. M. Sebel, G. S. Oehrlein, and J. M. Cook, J. Vac. Sci. Technol. A 16, 239 (1998).

[2.10] H. Hayashi, S. Morishita, T. Tatsumi, Y. Hikosaka, S. Noda, H. Nakagawa, S. Kobayashi, M. Inoue, and T. Hoshino, J. Vac. Sci. Technol. A 17, 2557 (1999).

[2.11] K. Takahashi, and K. Tachibana, J. Appl. Phys. 89, 893 (2001).

[2.12] M. Nakamura, M. Hori, T. Goto, M. Ito, and N. Ito, J. Vac. Sci. Technol.A 19, 2134 (2001).

[2.13] E.Gogolides, P. Vauvert, G. Kokkoris, G. Turban, and A. G. Boudouvis, J. Appl. Phys. 88, 5570 (2000).

[2.14] Xuefeng Hua,X.Wang, D.Fuentevilla,G.S.Oehrlein,F. G. Celii,K. H. R. Kirmse, J. Vac. Sci. Technol. A 21, 1708 (2003)

[2.15] Xi Li, Li ling, Xuefeng Hua, Masanaga Fukasawa,Gottlieb S. Oehrlein, Marcos Barela and Harold M. Anderson, J. Vac. Sci. Technol. A 21, 284 (2003).

[2.16] X.Li, L.Ling, Xuefeng Hua, G.S.Oehrlein, Y.Wang and H.M.Anderson, J.Vac.Sic.Technol A 21, 1955 (2003).

[2.17] J. Dulak, B. J. Howard, and Ch. Steinbrüchel, J. Vac. Sci. Technol. A 9, 775 (1991).

[2.18] J. W. Butterbaugh, D.C. Gray and H.H.Sawin, J. Vac. Sci. Technol.B 9, 1461 (1991).

[2.19] D.C. Gray, H.H.Sawin and J. W. Butterbaugh, J. Vac. Sci. Technol. A 9, 779 (1991).

[2.20] W.W.Stoffels, E. Stoffels and K. Tachibana, J. Vac. Sci. Technol. A 16, 87 (1997).

[2.21] W.H.Chang, I. Bello and W.M.Lau, J. Vac. Sci. Technol. A 11, 1221(1993).

[2.22] I. Bello, W.H.Chang and W.M.Lau, J. Vac. Sci. Technol. A 12, 1221(1994).

[2.23] Erick R.Fuoco and Luke Hanley, J. Appl. Phys. 92, 37 (2002).

[2.24] Da Zhang and Mark J. Kushner, J. Vac. Sci. Technol. A 19, 524(2000).

[2.25] H. J.Steffen, D. Marton and J. W. Rabalais, Phys. Rev. Lett. 68, 1726 (1992).

[2.26] G.S.Oehrlein and H.L.Williams, J.Appl.Phys. 62, 662 (1987).

[2.27] G.S.Oehrlein, S.W.Robey, and M.A.Jaso., Mater. Res. Soc. Symp. Proc. 98, 229 (1987).

[2.28] T. E. F. M. Standaert, P.J.Matsuo, S.D.Allen, G.S.Oehrlein and T.J.Dalton, J. Vac. Sci. Technol. A 17, 741 (1999).

[2.29] M. Schaepkens, T. E. F. M. Standaert, N. R. Rueger, P. G. M. Sebel, G. S. Oehrlein, and J. M. Cook, J. Vac. Sci. Technol. A 17, 26 (1999).

Chapter 3:

[3.1] G.S. Oehrlein, K. Maex, Y.-C.Joo, S.Ogawa, and J.T. Wetzel, Materials, Technology and Reliability for Advanced Interconnects and Low-k Dielectrics. (Warrendale, Materials Research Society Symposium Proceedings Vol. 612, 2001)

[3.2] G.S.Oehrlein,S.W.Robey,J.L.Lindstrom, K.K.Chan, M.A.Jaso, and G.J.Scilla, J.Electrochem.Soc 136, 2501(1989).

[3.3] G.S.Oehrlein, Y.Zhang, D. Vender, and O.Joubert, J.Vac.Sci.Technol.A 12,333(1994).

[3.4] N.R.Rueger, J.J.Beulens, M.Schaepkens, M.F.Doemling, J.M.Mirza, T.E.F.M.Standaert, and G.S.Oehrlein, J.Vac.Sci.Technol.A 15,1881(1997).

[3.5] M.Schaepkens, T.E.F.M.Standaert, N.R.Rueger, P.G.M.Sebel, G.S.Oehrlein and J.M.Cook, J.Vac.Sci.Technol.A17, 26(1999).

[3.6] T.E.F.M.Standaert C.Hedlund, E.A.Joseph, G.S.Oehrlein and T.J.Dalton, (to be published)

[3.7] T. E. F. M. Standaert, P. J. Matsuo, X. Li, G. S. Oehrlein, T.-M. Lu, R. Gutmann, C. T. Rosenmayer, J. W. Bartz, J. G. Langan, and W. R. Entley, J. Vac. Sci. Technol. A 19, 435 (2001).

[3.8] T. E. F. M. Standaert, M. Schaepkens, N. R. Rueger, P. G. M. Sebel, G. S. Oehrlein, and J. M. Cook, J. Vac. Sci. Technol. A 16, 239 (1998)

[3.9] Miyako Matsui, Fumihiko Uchida, Masayuki Kojima, Takafumi Tokunaga, Fumiko Yano, and Masaki Hasegawa, J. Vac. Sci. Technol. A 20, 117 (2002)

[3.10] Yicheng Wang and J. K. Olthoff, J. Appl. Phys. 85, 6358 (1999)

[3.11] Yicheng Wang, R. J. Van Brunt, and J. K. Olthoff, J. Appl. Phys. 83, 703 (1998)

[3.12] X.Li, X.Hua,L.Ling, G.S.Oehrlein, Marcos Barela and Harold M. Anderson, (accepted for publication)

[3.13] G.I.Font, W.L. Morgan and G.Mennenga, J. Appl Phys. 91,3530 (2002)

Chapter 4:

[4.1] The National Technology Roadmap for Semiconductors: Technology Needs, SIA, Semiconductor Industry Association, 1997 Edition.

[4.2] Alfred Grill and Deborah A. Neumayer, J. Appl. Phys. 94, 6697 (2003).

[4.3] Wen-li Wu, William E. Wallace, Eric K. Lin, Gary W. Lynn, Charles J. Glinka, E.

Todd Ryan, and Huei-Min Ho, J. Appl. Phys. 87, 1193 (2000).

[4.4] Akira Uedono, Zhi Quan Chen, Ryoichi Suzuki, Toshiyuki Ohdaira, Tomohisa Mikado, Shiomi Fukui, Atsushi Shiota, and Shin-ichi Kimura, J. Appl. Phys. 90, 2498 (2001).

[4.5] Anurag Jain, Svetlana Rogojevic, Shom Ponoth, William N. Gill, Joel L. Plawsky, Eva Simonyi, Shyng-Tsong Chen, and P. S. Ho, J. Appl. Phys. 91, 3275 (2002).

[4.6] E. Huang, M. F. Toney, W. Volken, D. Mecerreyes, P. Brook, H. C. Kim, C. J. Hawker, J. L. Hedrick, V. Y. Lee, T. Magbitang, R. D. Miller, and L. B. Lurio, Appl. Phys. Lett. 81, 2232 (2002)

[4.7] T. E. F. M. Standaert, E. A. Joseph, G. S. Oehrlein, A. Jain, W. N. Gill, P. C. Wayner, Jr., and J. L. Plawsky, J. Vac. Sci. Technol. A 18, 2742 (2000).

[4.8] Arvind Sankaran and Mark J. Kushner, Appl. Phys. Lett. 82, 1824 (2003).

[4.9] Yasuhiro Morikawa, Naoki Mizutani, Masanori Ozawa, Toshio Hayashi, Wei Chen, and Taijiro Uchida, J. Vac. Sci. Technol. B 21(4), 1344 (2003).

[4.10] Steven A. Vitale and Herbert H. Sawin, J. Vac. Sci. Technol. A 20, 651 (2002).

[4.11] A. Das, T. Kokubo, Y. Furukawa, H. Struyf, I. Vos, B. Sijmus, F. Iacopi, J. Van. Aelst, Q. T. Le, L. Carbonell *et al*, Microelectronic Engineering, Volume 64, Issues 1-4, 351-360, 2002.

[4.12] M. Schaepkens, and G. S. Oehrlein, J. Electronchem. Soc. 148, C211 (2001).

[4.13] Xi Li, Li Ling, Xuefeng Hua, Gottlieb S. Oehrlein, Yicheng Wang, and H. M. Anderson, J. Vac. Sci. Technol. A 21, 1955 (2003).

[4.14] Xi Li, Li Ling, Xuefeng Hua, Masanaga Fukasawa, Gottlieb S. Oehrlein, Marcos Barela, and Harold M. Anderson, J. Vac. Sci. Technol. A 21, 284 (2003).

[4.15] Xi Li, Xuefeng Hua, Li Ling, Gottlieb S. Oehrlein, Marcos Barela, and Harold M. Anderson, J. Vac. Sci. Technol. A 20, 2052 (2002).

[4.16] Xuefenghua, G. S. Oehrlein, (to be submitted).

[4.17] I.T.Jilliffe, Principal Component Analysis, Springer-Verlag, New York, 2002

[4.18] T. M. Mayer, R. A. Barker, and L. J. Whitman, J. Vac. Sci. Technol. 18, 349 (1981).

[4.19] G. S. Oehrlein, S.W. Robey, J. L. Lindstrom, K. K. Chan, M. A. Jaso, and G. J. Scilla, J. Electrochem. Soc 136, 2501(1989).

[4.20] T. E. F. M. Standaert, M. Scharpkens, N. R. Rueger, P. G. M. Sebel, G. S. Oehrlein, and J. M. Cook, J.Vac. Sci. & Technol. A 16, 239 (1998).

[4.21] T. E. F. M. Standaert, C. Hedlund, E. A. Joseph, G. S. Oehrlein, and T. J. Dalton, J. Vac. Sci. Technol. A 22, 53 (2004)

[4.22] Xuefeng Hua, X. Wang, D. Fuentevilla, G. S. Oehrlein, F. G. Celii, and K. H. R. Kirmse, J. Vac. Sci. Technol. A 21, 1708 (2003).

[4.23] M. Schaepkens, T. E. F. M. Standaert, N. R. Rueger, P. G. M. Sebel, G. S. Oehrlein, and J. M. Cook, J. Vac. Sci. Technol. A 17, 26 (1999).

[4.24] H.P.C.E. Kuipers, H. C. E. van Leuven and W. M. Visser, Surf. Interface Anal. 8, 235 (1986).

[4.25] L. Griffiths and L. Bradley, Appl. Spectrosc. 46, 1426 (1992).

[4.26] Ronald C. Chatelier, Heather A. W. St John, Thomas R. Gengenbach, Peter Kingshott and Hans J. Griesser, Surf. Interface Anal. 25, 741 (1997).

[4.27] P. L. J. Gunter, and J. W. Niemantverdriet, J. Vac. Sci. Technol. A 13, 1290 (1995).

[4.28] D. Briggs, M.P. Seah, Practical Surface Analysis, vol.1, John Wiley & Sons (1990).

[4.29] R. D. Miller, International Sematech/Ultralow-k workshop, June 6-7, 2002.

[4.30] D.W. Gidley, J.N. Sun, Y.F. Hu, W.E. Frieze, and S. Yang, Materials Research Society Spring Meeting, (vol. 726, Q10.5), April 2002 in San Francisco.

Chapter 5:

[5.1] P. S. Ho, J. Leu and W. W. Lee (Eds.), *Low dielectric Constant Materials for IC Applications,* Spring Series in Advanced Microelectronics, Vol. 9, (Springer, Herdelberg, 2002).

[5.2] R.J.O.M. Hoofman, G.J.A.M. Verheijden, J. Michelon, F. Iacopi, Y. Travaly, M.R. Baklanov, Zs. Tökei and G.P. Beyer, Microelectronic Engineering, **80**, 337 (2005).

[5.3] Y. Furukawa, R. Wolters, H. Roosen, J.H.M. Snijders and R. Hoofman, Microelectronic Engineering, **76**, 25 (2004).

[5.4] P. Y. Mabboux and K. K. Gleason, J. Electrochem. Soc, **152**, F7 (2005).

[5.5] I. Fisher, W. D. Kaplan, and M. Eizenber, J, Appl. Phys., **95**, 10 (2004).

[5.6] The *International Technology Roadmap for Semiconductors* (ITRS), (Semiconductor Industry Association, 2004).

[5.7] F. Iacopi, S. H. Brongersma, B. Vandevelde, M. O'Toole, D. Degryse, Y. Travaly and K. Maex, Microelectronic Engineering, **75**, 54 (2004).

[5.8] Xuefeng Hua, C. Stolz, G. S. Oehrlein, P. Lazzeri, N. Coghe, M. Anderle, C. K. Inoki, T. S. Kuan, and P. Jiang, J. Vac. Sci. Technol. A. **23**, 151 (2005).

[5.9] P. Lazzeri, X. Hua G. S. O ehrlein, M. Barrozi, E. Iacob, and M. Anderle, J. Vac. Sci. Technol. B. **23**, 1491 (2005)

[5.10] Y. Wang, R. Kumar, X. Zhou, J. Pan, and J. Chai, Thin Solid Films, **473**, 132, (2005).

[5.11] H. Cui, R. J. Carter, D. L. Moore, H. Peng, D. W. Gidley, and P. A. Burke, J. Appl. Phys. **97** , 113302 (2005).

[5.12] H. J. Lee, C. L. Soles, D. W. Liu, B. J. Bauer, E. K. Lin, W. L. Wu and A. Grill, J. Appl. Phys. **95**, 2355 (2004).

[5.13] Wen-li Wu, William E. Wallace, Eric K. Lin, Gary W. Lynn, Charles J. Glinka, E. Todd Ryan, and Huei-Min Ho, J. Appl. Phys. **87**, 1193 (2000).

[5.14] Xuefeng Hua, X. Wang, D. Fuentevilla, G. S. Oehrlein, F. G. Celii, and K. H. R. Kirmse, J. Vac. Sci. Technol. A, **21**, 1708 (2003).

[5.15] S. G. Park, H. Y. Song, N and B. H. O, J. Vac. Sci. Technol. B, **19**, 1841 (2001).

[5.16] L. Zheng, L. Ling, Xuefeng. Hua, G. S. Oehrlein, and E. A. Hudson, J. Vac. Sci. Technol. A, **23**, 634 (2005).

[5.17] M. Nastasi, J. Mayer, and J. Hirvonen, *Ion-solid interaction: fundamentals and applications*, (Cambridge, New York, Cambridge University Press, 1996).

[5.18] Q.T. Le, M. R. Baklanov, E. Kesters, A. Azioune, H. Struyf, W. Boullart, J. J. Pireaux, and S. Vanhaelemeersch, Electrochemical and Solid State Letters, **8**(7), F21 (2005).

[5.19] S. Fujimura, K. Shinagawa, M. T. Suzuki, and M. Nakamura, J. Vac. Sci. Technol. B, **9**, 357 (1991).

[5.20] D. Briggs, M.P. Seah, *Practical Surface Analysis*, (John Wiley & Sons 1990), Vol. 1.

[5.21] L.Ling, Xuefeng Hua, X. Li, G.S.Oehrlein, E.A.Hundson, J. Vac. Sci. Technol. B,

22, 2594 (2004).

5.22 H. Ito, IBM J. Res. Dev. **41,** 69 (1997).

5.23 E. Reichmanis, O. Nalamasu, F.M. Houlihan, T.I. Wallow, A.G. Timko, R. Cirelli, G. Dabbagh, R.S. Hutton, A.E. Novembre, and B.W. Smith, J. Vac. Sci. Technol. B, **15**, 2528 (1997).

5.24 C. L. Soles, E. K. Lin, J. L. Lenhart, R. L. Jones, Wen-li Wu D. L. Goldfarb and M. Angelopoulos, J. Vac. Sci. Technol. B, **19**, 2690 (2001).

5.25 A. Das, T. Kokubo, Y. Furukawa, H. Struyf, I. Vos, B. Sijmus, F. Iacopi, J. Van. Aelst, Q. T. Le, and L. Carbonell, Microelectronic Engineering, **64**, 351 (2002).

Chapter 6:

6.1 H. Ito, IBM J. Res. Dev. **45,** 683 (2001).

6.2 T. Kajita, Y. Nishimura, M. Yamamoto, H. Ishii, A. Soyano, A. Kataoka, M. Slezak, M. Shimizu, P. Varanasi, G. Jordhamo, M. Lawson, R. Chen, W. Brunsvold, W. Li, R. Allen, H. Ito, H. Truong, and T. Wallow, Proc. SPIE **4345,** 712 (2001).

6.3 H. Ito, IBM J. Res. Dev. **41,** 69 (1997).

6.4 E. Reichmanis, O. Nalamasu, F.M. Houlihan, T.I. Wallow, A.G. Timko, R. Cirelli, G. Dabbagh, R.S. Hutton, A.E. Novembre, and B.W. Smith, J. Vac. Sci. Technol. B, **15,** 2528 (1997).

6.5 L.Ling, Xuefeng Hua, X. Li, G.S.Oehrlein, E.A.Hundson, J. Vac. Sci. Technol. B, **22**, 2594 (2004).

6.6 M. Schaepkens, R.C.M. Bosch, T. Standaert, G.S. Oehrlein, and J.M. Cook, J. Vac. Sci. & Tech. **A 16**, 2099 (1998).

[6.7] T. E. F. M. Standaert, M. Scharpkens, N. R. Rueger, P. G. M. Sebel, G. S. Oehrlein, and J. M. Cook, J.Vac. Sci. & Technol. **A 16**, 239(1998).

[6.8] J. W. Coburn and H. F. Winters, Journal of Vacuum Science & Technology **15** (2), 327(1978).

[6.9] H. F. Winters and J. W. Coburn, Surface Science Reports **14,** 161 (1992).

[6.10] D. Zhang, and M. J. Kushner, J. of Vac. Sci. Technol. A, **18**, 2661 (2000).

[6.11] D. Humbird, and D.B. Graves, J. Appl. Phys. **96**, 65 (2004).

[6.12] T.E.F.M.Standaert, C.Hedlund, E.A.Joseph, G.S.Oehrlein and T.J.Dalton, J. Vac. Sci. Technol. A **22**, 53 (2004).

[6.13] M. Schaepkens, and G. S. Oehrlein, J. Electronchem. Soc. **148**, C211 (2001).

[6.14] H. Hayashi, S. Morishita, T. Tatsumi, Y. Hikosaka, S. Noda, H. Nakagawa, S. Kobayashi, M. Inoue, and T. Hoshino, J. Vac. Sci. Technol. A **17**, 2557 (1999).

[6.15] T. Kudo, E. Alemy, R. Dammel, W. Kim, T. Kudo, S. Lee, S. Masuda, D. McKenzie, M. Rahman, A. Romano, M. Padmanaban, J. Chun, J. Jun, S. Lee, K. Shin and H.Kim, J. Photopolym. Sci. Technol. **15**, 549 (2002).

[6.16] M. Padmanaban, E. Alemy, R. Dammel, W. Kim, T. Kudo, S. Lee, D. Rahman, W. Chen, R. Sadjadi, W. Livesay and M. Ross, J. Photopolym. Sci. Technol. **15**, 521 (2002).

[6.17] T. Kudo, J. Bae, R. Dammel, W. Kim, D. McKenzie, M. Rahman, M. Padmanaban, Proc. SPIE, **4345**, 179 (2001).

[6.18]E. A. Hudson, Z. Dai, Z. Li, S. Kang, S. Lee, W. Chen, and R. Sadjadi , Proc. Of International Symposium on Dry Process, Tokyo, Institute of Electrical Engineers of Japan, 253 (2003).

[6.19] G. S. Oehrlein, Xuefeng Hua, C. Scholz, and J. Ping, J. Vac. Sci. & Technol. B (in press)

[6.20] Xuefeng Hua, X. Wang, D. Fuentevilla, G. S. Oehrlein, F. G. Celii, and K. H. R. Kirmse, J. Vac. Sci. Technol. A **21**, 1708 (2003).

[6.21] O. Joubert, C. Fiori, J. C. Oberlin, P. Paniez, J. Pelletier, M. Pons, T. Vachette, and A.Weill, J. Appl. Phys., **69**, 1697 (1991).

[6.22] Y. Koval, J. Vac. Sci. Technol. B, **22**, 843 (2004).

[6.23] V. Picq, J. M. Ramillon, and E. Balanzat, Nucl. Instr. And Meth. In Phys. Res. B, **146**, 496 (1998).

[6.24] D. L. Goldfarb, A. P. Mahorowala, G. M. Gallatin, K. E. Petrillo, K. Temple, M. Angelopoulos, S. Rasgon, H. H. Sawin, S. D. Allen, M. C. Lawson, and R. W. Kwong, J. Vac. Sci. Technol. B, **22**, 647 (2004).

[6.25] M. Shaepkens, and G. S. Oehrlein, Appl. Phys. Lett. **72** , 1293 (1998).

[6.26] I. W. Rangelow, J. Vac. Sci. Technol. A, **21**, 1550 (2003).

[6.27] M. Watanabe, D. M. Shaw, and G. J. Collins, Appl. Phys. Lett. **79**, 2698 (2001).

[6.28] Xuefeng Hua and G. S. Oehrlein (unpublished).